

Ionic Liquid Crystal Polymers for Display Devices

A Study of Mesogenic Diallylamine-Terminated Polymers

Alan R. Roper

Doctor of Philosophy

University of York

Chemistry

September 2016

Abstract

Exploration into the development and synthesis of ionic polymeric liquid crystal devices for potential use in touch screens and smart windows considered the potential of amine-based functional groups for tunable polymerisations and bulk compound properties. Through consideration of the nature of the functional group as well as the motif, it would be possible to control the polymerisation rate, as well as thermal and potentially conductive properties of the compounds used in the ultimate device. In this study, three different functional groups, as well as three different motifs were considered across a small range of spacer chain lengths, which also allowed an investigation into a possible odd/even effect on liquid crystal properties.

Table of Contents

Abstract.....	2
Table of Contents	3
Table of Figures.....	7
Acknowledgements.....	18
Author’s Declaration	18
1: Introduction	19
1.1: Target Technologies.....	19
1.2: An Introduction to Liquid Crystals	19
1.2.1: Thermotropic Liquid Crystals	20
1.3: Liquid Crystal Polymers and Polymerization in Organized Media	27
1.3.1: Main Chain Liquid Crystal Polymers.....	28
1.3.2: Side Chain Liquid Crystal Polymers	28
1.4: Ionic Liquid Crystals	29
1.5: Synthesis of Polymers	32
1.5.1: Free Radical Polymerisation.....	32
1.5.2: UV-polymerisation	33
1.5.3: The process of polymerisation.....	34
1.5.4: Polydispersity	36
1.5.5: Types of Polymer	37
1.5.6: Co-Polymer Systems	40
1.5.7: Polymerizable End Groups	45
1.6: Touchscreens	52
1.6.1: Resistive Touchscreens	52
1.6.2: Surface Acoustic Wave (SAW).....	54
1.6.3: Infrared (IR).....	54
1.6.4: Capacitive Touchscreens.....	54
1.7: Smart Windows.....	56
1.8: Compensation Films.....	58
1.9: Films	62
1.9.1: Film Thickness	62
1.10: Pixels	63
1.11: Mixtures	63
2: Aims	65
2.1: An Overview of the Technologies	65
2.2: Technological Requirements.....	65

2.2.1: Smart Windows.....	65
2.2.2: Compensation Films.....	66
2.2.3: Touch Screens	67
2.3: Summary of Requirements	67
3: Experimental.....	69
3.1: General Techniques	69
3.1.1: Materials	69
3.1.2: Thin Layer and Column Chromatography	69
3.1.3: Nuclear Magnetic Resonance Spectroscopy (NMR)	69
3.1.4: Mass Spectrometry	70
3.1.5: Polarised Optical Microscopy	70
3.1.6: Ultra-Violet Differential Scanning Calorimetry (UV-DSC)	70
3.1.7: Differential Scanning Calorimetry (DSC)	71
3.1.8: Fourier-Transform Infra-Red Spectroscopy (FT-IR).....	71
3.1.9: Ultra Violet Spectroscopy	71
3.1.10: X-Ray Spectroscopy.....	72
3.2: Generic Synthetic Procedures.....	72
3.2.1: Preparation 1	72
3.2.2: Preparation 2	73
3.2.3: Preparation 3	73
3.2.4: Preparation 4	74
3.2.5: Preparation 5	74
3.2.6: Preparation 6	75
3.2.7: Salt syntheses.....	75
3.3: Proposed mechanisms	75
3.3.1: Preparation 1	75
3.3.2: Preparation 2	76
3.3.3: Preparation 3	77
3.3.4: Preparation 4	77
3.3.5: Preparation 5	78
3.3.6: Preparation 6	79
3.4: Abbreviations.....	80
4: Syntheses	82
4.1: Syntheses of Di-functionalised Compounds for Polymerization Studies.....	82
4.1.1: Compound 1 (Bis-1,10-diallylaminodecane) (Preparation 1)	82
4.1.2: Compound 2 (Decane-1,10-bis-diallylammonium chloride) (Direct Acidification).....	82

4.1.3: Compound 3 (N^1, N^1, N^{12}, N^{12} -tetraallyldodecanediamide) (Preparation 2)	83
4.2: Intermediate Bromide Syntheses	83
4.2.1: Synthesis of Biphenyl Bromide Compounds	83
4.2.2: Synthesis of Terphenyl Bromide Compounds.....	87
4.3: Diallylamine-Terminated Compound Syntheses.....	90
4.3.1: Synthesis of Biphenyl Amine Compounds	90
4.3.2: Synthesis of Terphenyl Amine Compounds	94
4.4: Synthesis of Ester Compounds.....	98
4.4.1: Synthesis of Bromo-terminated Benzoate Ester Compounds	98
4.4.2: Synthesis of Amino-terminated Benzoate Ester Compounds.....	100
4.4.3: Deprotection of Benzoate Esters	103
4.4.4: Synthesis of Ester Motifs	105
5: Thermal Studies of Compounds.....	110
5.1: Analysis of Bromo-terminated Biphenyl Intermediates (Compounds 4-8)	110
5.2: Analysis of Bromo-terminated Terphenyl Intermediates (Compounds 9 to 13)	116
5.3: Analysis of Diallylamino-Terminated Biphenyl Compounds (Compounds 14-18).....	129
5.4: Analysis of Diallylamine-terminated Terphenyl Compounds (Compounds 19 to 23)	135
5.5: Analysis of Ester-based Compounds (39 to 43)	145
5.6: Comparison of the Impact of Motifs on Thermal Behaviours	146
6: Salt syntheses and Analyses.....	147
6.1: Selection of Compounds to Be Acidified.....	147
6.2: Salt Syntheses	147
6.2.1: Direct Acidification Procedure	147
6.2.2: Solution Addition Procedure.....	148
6.2.3: Metathesis/Salt Replacement Procedure	150
6.3: Thermal Analysis of Biphenyl Salts	150
6.3.1: Observations of the Effects of Salt Introduction to Biphenyl-Terminated Compounds	151
6.3.2: Conclusion of Biphenyl Salt Studies and Further Study.....	152
6.4: Syntheses of Terphenyl Salt Compounds	152
6.5: Thermal Analysis of Terphenyl Quaternary Diallylammonium Salts	153
6.5.1: Analysis of the Chloride Salt	153
6.5.2: Analysis of the Acrylate Salt.....	154
6.5.3: Analysis of the Hexafluorophosphate Salt.....	154
6.6: Effects of Salt Introduction	154
6.7: Investigation of Salt Mixtures	155

6.7.1: Chloride Salt Mixtures.....	155
6.7.2: Acrylate Salt Mixtures.....	164
6.7.3: Hexafluorophosphate Salt Mixtures.....	171
6.8: Overall Observations from the Impact of Salt Introduction	182
7: UV-Polymerization Studies	183
7.1: Photoinitiator Studies	183
7.1.1: Initial Polymerization Studies	183
7.1.2: Initiator compatibility	187
7.1.4: Selection of Initiator for Polymerisation of Monomers.....	195
7.2: UV-Polymerisation Analysis	195
7.2.1: Initiator Test.....	196
7.3 Comparison of Polymerisations in Phases	204
8: Conclusions	207
9: References	210

Table of Figures

Figure 1.1: Possible liquid crystal phases formed upon heating. The orientations of the molecules are shown relative to the director (n).....	20
Figure 1.2: A representation of the nematic liquid crystal phase composed of calamitic molecules, showing their general alignment with the director, n	21
Figure 1.3: Photomicrograph showing the schlieren texture of the nematic phase with 4- and 2-brush defects (x100).	21
Figure 1.4: A simplified representation of the Smectic A liquid crystal phase, showing their directional alignment and the formation of very diffuse layers.	22
Figure 1.5: a) Arrangement of the smectic layers forming a focal conic defect and b) photomicrograph of a focal conic defect showing the ellipse and hyperbola.	23
Figure 1.6: A representation of the Smectic C liquid crystal phase, showing the tilt of the molecules, and alignment and layer formation.....	23
Figure 1.7: Photomicrograph of a smectic C phase showing a broken focal conic texture and schlieren exhibiting only 4-brush defects.	24
Figure 1.8: A representation of incident X-rays on a crystal lattice at angles θ , showing the layer spacing, d	25
Figure 1.9: A representation of a crystal lattice being studied by X-ray, with the scattering effect shown.....	26
Figure 1.10: A cartoon representation showing the sharp small angle diffractions, as well as the diffuse wide angle diffractions. The rotation difference between the 'brackets' at wide angles in (b) and (c) show the tilt angle of the smectic C phase (c).....	27
Figure 1.11: A generic view of a main chain liquid crystal polymer.	28
Figure 1.12: A generic example of a terminally attached side chain liquid crystal polymer.	28
Figure 1.13: A generic example of a laterally attached side chain liquid crystal polymer.	29
Figure 1.14: Structures of example ionic liquid crystal compounds, where R , R_1 and R_2 are organic groups, and X^- is the associated anion, e.g. Cl^-	29
Figure 1.15: The generic structures of quaternary ammonium and phosphonium salt ionic liquid crystal salts, where R represents an organic group.	30
Figure 1.16: Structure of a methacrylate terminated ionic liquid crystal (the compound displayed a smectic A phase between $60^\circ C$ and $52^\circ C$).	31
Figure 1.17: Structure of a fan-shaped acrylate terminated ionic liquid crystal (the compound displayed a hexagonal columnar phase between $20^\circ C$ and $50^\circ C$).	31
Figure 1.18: Structure of a diene-terminated ionic liquid crystal. The polymer formed with a bicontinuous cubic nanostructure exhibited the highest conductivities.....	32
Figure 1.19: (left) Benzoyl Peroxide, (right) AIBN.	33

Figure 1.20: Formation of initiator radical from a peroxide initiator compound.....	35
Figure 1.21: Transfer of radical character from the initiator to the monomeric substrate.	35
Figure 1.22: Cleavage of AIBN in radical initiation.....	35
Figure 1.23: Radical propagation in polymerisation of vinyl containing monomers.....	35
Figure 1.24: Chain combination termination in radical polymerisation.	35
Figure 1.25: Termination of polymerisation by initiator combination.	36
Figure 1.26: Termination of polymerisation by disproportionation.	36
Figure 1.27: A cartoon representation of an elastomer, where the blue circles represent the monomers, the blue lines represent the bonding along the polymer backbone, and the red lines represent the flexible cross-linkages.	38
Figure 1.28: A cartoon representation of a network polymer. The red cross-linkers may be composed of the same monomers as the blue backbone.....	39
Figure 1.29: A cartoon representation of a statistical co-polymer with a random distribution of the different incorporated groups.	40
Figure 1.30: A cartoon representation of an alternating co-polymer showing the AB-repeating pattern of components through the polymer backbone.....	41
Figure 1.31: A cartoon representation of a block co-polymer showing the separation of the different monomers when they are incorporated into the polymer backbone.....	41
Figure 1.32: A representation of a lamellar structure formed in a mixed solvent system.....	42
Figure 1.33: A simple representation of bicontinuous cubic phases in different solvent environments.....	42
Figure 1.34: A representation of columnar phases in different solvent environments.	43
Figure 1.35: A representation of the cubic micellar structure in different solvent environments. .	43
Figure 1.36: A cartoon representation of a graft co-polymer, showing the different groups in red grafted to the polymer backbone.	44
Figure 1.37: A cartoon representation of a graft co-polymer, with lateral chains associated with their preferred solvent environments.	45
Figure 1.38: Structure of a generic acrylate polymerisable unit.	46
Figure 1.39: Structure of 4-Biphenyl-4-(6-acryloxyhexyloxy)benzoate Cr 70°C SmC 80°C N 95°C Iso.	46
Figure 1.40: Generic structure of diacrylate mesogens synthesised by Broer.	47
Figure 1.41: The general structure of an epoxide, where R ¹ and R ² are organic groups.....	48
Figure 1.42: A reaction scheme for the reaction of epichlorohydrin with bisphenol A.	48
Figure 1.43: A reaction scheme for the reaction of an epoxide terminated polymer with an amine based cross-linker.	48

Figure 1.44: Radical polymerisation of a diallylamino-functional unit to form 6 and 7 membered rings where R is a radical initiator and R ₁ is an attached organic unit.....	49
Figure 1.45: Radical polymerisation of a diallylamino-functional unit to form 5 and 6 membered rings where R is a radical initiator and R ₁ is an attached organic unit.....	50
Figure 1.46: Generic structures of (a) a diallylamino-functional group, (b) a diallylamide and (c) a quaternary diallylammonium salt.....	51
Figure 1.47: Co-ordination of four-wire touchscreen components.....	53
Figure 1.48: Co-ordination of wire connections on the back layer of a 5-wire resistive touchscreen, also showing the patterning applied to the lower ITO layer.	53
Figure 1.49: A schematic representation of a capacitive touchscreen. The etching on the ITO layers could be combined onto a single layer.	56
Figure 1.50: A generic structure of a smart window assembly.	56
Figure 1.51: Transmissive state of an aligned PDLC showing the alignment of director fields.	57
Figure 1.52: An unaligned, scattering PDLC showing the alignment of director fields.	58
Figure 1.53: Light passing through a birefringent material with an angle (45°) between them.	60
Figure 1.54: Light passing through a birefringent material (bottom) and through a birefringent compensation layer (top), with angle 45°.....	60
Figure 1.55: The orientation of the different plates used in compensation films, displaying the in-plane, out-of-plane and oblique retardance of the A-, C- and O-plates.....	61
Figure 1.56: A phase diagram for the mixture of 5CB and 8OCB.....	64
Figure 2.1: Generic structures for target compounds to be synthesised, where n = 8-12.....	68
Figure 3.1: A simplified schematic of a polarising optical microscope (top). The slide may be present (lower blow-up) in a heating or cooling stage.....	70
Figure 3.2: A simplified schematic of a UV-DSC calorimeter.	71
Figure 3.3: A simplified representation of how incident X-rays interact with a crystal lattice, with the layer spacing d and angle of incidence θ	72
Figure 3.4: A reaction scheme of Preparation 1 in the synthesis of Compound 1 where n = 10.	72
Figure 3.5: A reaction scheme of Preparation 1 for the synthesis of various target compounds, where n = 8, 9, 10 or 12, and m = 2 or 3.....	73
Figure 3.6: A reaction scheme of the first step of Preparation 2, showing the synthesis of the acid chloride intermediate.	73
Figure 3.7: A reaction scheme of the second step of Preparation 2, showing the conversion of the intermediate acid chloride into the target amide compound.	73
Figure 3.8: A reaction scheme of Preparation 3, showing the mono-addition of the aromatic motif to flexible spacer chain, where n = 8, 9, 10 or 12, and m = 2 or 3.....	74

Figure 3.9: A reaction scheme of Preparation 4, showing the Mitsunobu reaction between 11-bromo-1-undecanol and an aromatic motif, where $m = 2$ or 3 .	74
Figure 3.10: A reaction scheme of Preparation 5, showing the deprotection of an ethyl protected benzoate ester to the corresponding carboxylic acid, where $n = 8 - 12$.	75
Figure 3.11: A reaction scheme of Preparation 6, showing the formation of a benzoate ester <i>via</i> a Steglich Esterification reaction, where $n = 8 - 12$.	75
Figure 3.12: A proposed reaction mechanism followed through Preparation 1, showing the movement of electrons (denoted by blue arrows) and charges.	76
Figure 3.13: A proposed reaction mechanism followed through the first step of Preparation 2, showing the movement of electrons (denoted by blue arrows) and charges.	76
Figure 3.14: A proposed reaction mechanism followed through the second step of Preparation 2, showing the movement of electrons (denoted by blue arrows) and charges.	77
Figure 3.15: A proposed reaction mechanism followed through Preparation 3, showing the movement of electrons (denoted by blue arrows) and charges.	77
Figure 3.16: A proposed reaction mechanism followed through Preparation 4, showing the movement of electrons (denoted by blue arrows) and charges.	78
Figure 3.17: A proposed reaction mechanism followed through Preparation 5, showing the movement of electrons (denoted by blue arrows) and charges.	79
Figure 3.18: A proposed reaction mechanism followed through Preparation 6, showing the movement of electrons (denoted by blue arrows) and charges.	80
Figure 4.1: Structure of Compound 1 (Bis-1,10-diallylaminodecane).	82
Figure 4.2: Structure of Compound 2 (Decane-1,10-bis-diallylammonium chloride).	82
Figure 4.3: Structure of Compound 3 (N^1, N^1, N^{12}, N^{12} -tetraallyldodecanediamide).	83
Figure 4.4: Structure of Compound 4 (4-Cyano-4'-(8-bromooctyloxy)biphenyl).	84
Figure 4.5: Structure of Compound 5 (4-Cyano-4'-(9-bromononyloxy)biphenyl).	84
Figure 4.6: Structure of Compound 6 (4-Cyano-4'-(10-bromodecyloxy)biphenyl).	85
Figure 4.7: Structure of Compound 7 (4-Cyano-4'-(11-bromoundecyloxy)biphenyl).	86
Figure 4.8: Structure of Compound 8 (4-Cyano-4'-(12-bromododecyloxy)biphenyl).	87
Figure 4.9: Structure of Compound 9 (4-Cyano-4''-(8-bromooctyloxy)terphenyl).	87
Figure 4.10: Structure of Compound 10 (4-Cyano-4''-(9-bromononyloxy)terphenyl).	88
Figure 4.11: Structure of Compound 11 (4-Cyano-4''-(10-bromodecyloxy)terphenyl).	89
Figure 4.12: Structure of Compound 12 (4-Cyano-4''-(11-bromoundecyloxy)terphenyl).	89
Figure 4.13: Structure of Compound 13 (4-Cyano-4''-(12-bromododecyloxy)terphenyl).	90
Figure 4.14: Structure of Compound 14 (4'-Cyano-4-(8- <i>N,N</i> -diallylaminoctyloxy)biphenyl).	91
Figure 4.15: Structure of Compound 15 (4'-Cyano-4-(9- <i>N,N</i> -diallylaminoctyloxy)biphenyl).	92
Figure 4.16: Structure of Compound 16 (4'-Cyano-4-(10- <i>N,N</i> -diallylaminoctyloxy)biphenyl).	92

Figure 4.17: Structure of Compound 17 (4'-Cyano-4-(11- <i>N,N</i> -diallylaminoundecyloxy)biphenyl).	.93
Figure 4.18: Structure of Compound 18 (4'-Cyano-4-(12- <i>N,N</i> -diallylaminododecyloxy)biphenyl).	.94
Figure 4.19: Structure of Compound 19 (4''-Cyano-4-(8- <i>N,N</i> -diallylaminooctyloxy)terphenyl).....	95
Figure 4.20: Structure of Compound 20 (4''-Cyano-4-(9- <i>N,N</i> -diallylaminononyloxy)terphenyl).....	95
Figure 4.21: Structure of Compound 21 (4''-Cyano-4-(10- <i>N,N</i> -diallylaminodecyloxy)terphenyl).	...96
Figure 4.22: Structure of Compound 22 (4''-Cyano-4-(11- <i>N,N</i> -diallylaminoundecyloxy)terphenyl).97
Figure 4.23: Structure of Compound 23 (4''-Cyano-4-(12- <i>N,N</i> -diallylaminododecyloxy)terphenyl).98
Figure 4.24: Structure of Compound 24 (Ethyl 4-((8-bromooctyl)oxy)benzoate).98
Figure 4.25: Structure of Compound 25 (Ethyl 4-((9-bromononyl)oxy)benzoate).99
Figure 4.26: Structure of Compound 26 (Ethyl 4-((10-bromodecyl)oxy)benzoate).....	99
Figure 4.27: Structure of Compound 27 (Ethyl 4-((11-bromoundecyl)oxy)benzoate).100
Figure 4.28: Structure of Compound 28 (Ethyl 4-((12-bromododecyl)oxy)benzoate).100
Figure 4.29: Structure of Compound 29 (Ethyl 4-((8-diallylamino)octyl)oxy)benzoate).101
Figure 4.30: Structure of Compound 30 (Ethyl 4-((9-diallylamino)nonyl)oxy)benzoate).101
Figure 4.31: Structure of Compound 31 (Ethyl 4-((10-diallylamino)decyl)oxy)benzoate).....	102
Figure 4.32: Structure of Compound 32 (Ethyl 4-((11-diallylamino)undecyl)oxy)benzoate).102
Figure 4.33: Structure of Compound 33 (Ethyl 4-((12-diallylamino)dodecyl)oxy)benzoate).103
Figure 4.34: Structure of Compound 34 (4-((8-diallylamino)octyl)oxy)benzoic acid).103
Figure 4.35: Structure of Compound 35 (4-((9-diallylamino)nonyl)oxy)benzoic acid).104
Figure 4.36: Structure of Compound 36 (4-((10-diallylamino)decyl)oxy)benzoic acid).....	104
Figure 4.37: Structure of Compound 37 (4-((11-diallylamino)undecyl)oxy)benzoic acid).....	105
Figure 4.38: Structure of Compound 38 (4-((12-diallylamino)dodecyl)oxy)benzoic acid).....	105
Figure 4.39: Structure of Compound 39 (4-cyanophenyl 4-((8-(diallylamino)octyl)oxy)benzoate).106
Figure 4.40: Structure of Compound 40 (4-cyanophenyl 4-((9-(diallylamino)nonyl)oxy)benzoate).107
Figure 4.41: Structure of Compound 41 (4-cyanophenyl 4-((10-(diallylamino)decyl)oxy)benzoate).108
Figure 4.42: Structure of Compound 42 (4-cyanophenyl 4-((11-(diallylamino)undecyl)oxy)benzoate).108
Figure 4.43: Structure of Compound 43 (4-cyanophenyl 4-((12-(diallylamino)dodecyl)oxy)benzoate).109
Figure 5.1: DSC thermogram (10 °C min ⁻¹) showing the melting behaviour of Compound 4.....	111
Figure 5.2: DSC thermogram (10 °C min ⁻¹) showing the melting behaviour of Compound 5.....	111

Figure 5.3: DSC thermogram (10 °C min ⁻¹) showing the melting behaviour of Compound 6.....	112
Figure 5.4: DSC thermogram (10 °C min ⁻¹) showing the melting behaviour of Compound 7.....	112
Figure 5.5: DSC thermogram (10 °C min ⁻¹) showing the melting behaviour of Compound 8.....	113
Figure 5.6: Graph showing the transition temperatures as a function of methylene spacer length for Compounds 4-8.....	113
Figure 5.7: Photomicrographs (x100) showing examples of the nematic schlieren texture observed for a) 5 at 61.4 °C b) 6 at 62.2 °C and c) 8 at 65.1 °C view through crossed polarisers.....	115
Figure 5.8: X-ray diffraction showing the diffraction pattern for the nematic phase of Compound 5.....	116
Figure 5.9: DSC thermogram (10 °C min ⁻¹) showing the melting behaviour of Compound 9.....	117
Figure 5.10: DSC thermogram (10 °C min ⁻¹) showing the melting behaviour of Compound 10.....	118
Figure 5.11: DSC thermogram (10 °C min ⁻¹) showing the melting behaviour of Compound 11.....	118
Figure 5.12: DSC thermogram (10 °C min ⁻¹) showing the melting behaviour of Compound 12.....	119
Figure 5.13: DSC thermogram (10 °C min ⁻¹) showing the melting behaviour of Compound 13.....	119
Figure 5.14: Graph showing the transition temperatures (°C) for Compounds 9-13.....	120
Figure 5.15: Photomicrographs (x100) showing a) Compound 9 in a nematic phase at 165 °C, b) Compound 10 at the N-SmA phase transition, c) mosaic texture of the B phase of Compound 10 at 137.4 °C, d) SmA-B phase transition for Compound 11 and e) B phase of Compound 11 at 142.3°C.....	122
Figure 5.16: Graph showing the layer spacing (Å) as a function of temperature (°C) for Compound 9.....	123
Figure 5.17: Plot showing the diffraction peaks as a function of temperature for Compound 9.....	123
Figure 5.18: Diffraction patterns for Compound 9 showing a) aligned nematic phase with diffuse diffraction peaks and b) B phase showing sharp diffraction peaks.....	124
Figure 5.19: Plot showing the layer spacing (Å) as a function of temperature for Compound 10.....	124
Figure 5.20: Plot showing the diffraction peaks as a function of temperature for Compound 10.....	125
Figure 5.21: Diffraction patterns for Compound 10 showing a) aligned smectic A phase with 100 and 200 peaks and b) B phase showing sharp diffraction peaks including 100, 111, 200 and 300 peaks.....	125
Figure 5.22: Plot showing the layer spacing (Å) as a function of temperature for Compound 11.....	126

Figure 5.23: Plot showing the diffraction peaks as a function of temperature for Compound 11.....	126
Figure 5.24: Diffraction patterns for Compound 11 showing a) aligned smectic A phase with 100 and 200 peaks and b) B phase showing good alignment and c) crystalline state at low temperature showing strong correlation of the layered structure.....	126
Figure 5.25: Plot showing the layer spacing (Å) as a function of temperature for Compound 12.....	127
Figure 5.26: Plot showing the diffraction peaks as a function of temperature for Compound 12.....	127
Figure 5.27: Plot showing the layer spacing (Å) as a function of temperature for Compound 13.....	128
Figure 5.28: Plot showing the diffraction peaks as a function of temperature for Compound 13.....	129
Figure 5.29: DSC thermogram (10 °C min ⁻¹) showing the melting behaviour of Compound 15.....	130
Figure 5.30: DSC thermogram (10 °C min ⁻¹) showing the melting behaviour of Compound 16.....	131
Figure 5.31: DSC thermogram (10 °C min ⁻¹) showing the melting behaviour of Compound 18.....	131
Figure 5.32: Photomicrographs (x100) showing the smectic A focal conic textures of a) Compound 16 and b) Compound 18.....	133
Figure 5.33: Layer spacing (Å) as a function of temperature (°C) for Compounds 15, 16 and 18.....	134
Figure 5.34: Plot showing the diffraction peaks as a function of temperature for Compound 15.....	134
Figure 5.35: Plot showing the diffraction peaks as a function of temperature for Compound 16.....	134
Figure 5.36: Plot showing the diffraction peaks as a function of temperature for Compound 18.....	135
Figure 5.37: Diffraction pattern of the smectic A phase for Compound 18.....	135
Figure 5.38: DSC thermogram (10 °C min ⁻¹) showing the melting behaviour of Compound 19.....	136
Figure 5.39: DSC thermogram (10 °C min ⁻¹) showing the melting behaviour of Compound 20.....	137
Figure 5.40: DSC thermogram (10 °C min ⁻¹) showing the melting behaviour of Compound 21.....	137
Figure 5.41: DSC thermogram (10 °C min ⁻¹) showing the melting behaviour of Compound 22.....	138
Figure 5.42: DSC thermogram (10 °C min ⁻¹) showing the melting behaviour of Compound 23.....	138

Figure 5.43: Graph showing the transition temperatures (°C) for Compounds 19-23.....	139
Figure 5.44: Photomicrographs (x100) showing a) smectic A phase b) smectic A – crystal B phase transition and c) crystal B phase mosaic texture for Compound 22.....	140
Figure 5.45: Plot showing the layer spacing (Å) as a function of temperature (°C) for Compound 19.....	141
Figure 5.46: Plot showing the diffraction peaks as a function of temperature (°C) for Compound 19.....	141
Figure 5.47: Diffraction patterns showing a) smectic A phase and b) crystal B phase for Compound 19.....	142
Figure 5.48: Graph showing the layer spacing (Å) as a function of temperature (°C) for Compound 20.....	142
Figure 5.49: Plot showing the diffraction peaks as a function of temperature (°C) for Compound 20.....	143
Figure 5.50: Graph showing the layer spacing (Å) as a function of temperature (°C) for Compound 21.....	144
Figure 5.51: Plot showing the diffraction peaks as a function of temperature (°C) for Compound 21.....	144
Figure 5.52: Diffraction patterns showing a) Smectic A phase and b) B phase for Compound 21.....	144
Figure 5.53: Graph showing the layer spacing (Å) as a function of temperature (°C) for Compound 22.....	145
Figure 5.54: Plot showing the diffraction peaks as a function of temperature for Compound 22.....	145
Figure 5.55: DSC thermogram (10 °C min ⁻¹) showing the melting behaviour of Compound 40.....	146
Figure 6.1: Structure of the salt of Compound 16, where X represents the anion.	151
Figure 6.2: Structure of the salt of Compound 17, where X represents the anion.	152
Figure 6.3: An example of the crystal textures observed from studies of biphenyl salt compounds.	152
Figure 6.4: Structure of the salt of Compound 22, where X represents the anion.	153
Figure 6.5: DSC thermogram of heat flow (mW ⁻¹) as a function of temperature (°C) for a 3:1 mixture of Compound 22 : chloride salt.	157
Figure 6.6: Photomicrographs of the 3:1 mixture showing the textures of the smectic A phase close to the transition at 180 °C (left) and the smectic A phase further into the phase at 170 °C (right) (x100 optical zoom).....	158
Figure 6.7: DSC thermogram of heat flow (mW ⁻¹) as a function of temperature (°C) for a 2:1 mixture of Compound 22 : chloride salt.	158

Figure 6.8: Photomicrographs showing the smectic A texture of the 2:1 mixture of Compound 22 and its chloride salt at close to the clearing point at 180 °C (left) and further into the phase at 170 °C (right) (x100 optical zoom).	159
Figure 6.9: DSC thermogram of heat flow (mW^{-1}) as a function of temperature ($^{\circ}\text{C}$) for a 1:1 mixture of Compound 22 : chloride salt.	160
Figure 6.10: Photomicrographs showing the smectic A texture of the 1:1 mixture of Compound 22 and its chloride salt 185 °C showing different regions of the slide between left and right (x100 optical zoom).	161
Figure 6.11: DSC thermogram of heat flow (mW^{-1}) as a function of temperature ($^{\circ}\text{C}$) for a 1:2 mixture of Compound 22 : chloride salt.	161
Figure 6.12: Photomicrographs showing the smectic A texture of the 1:2 mixture of Compound 22 and its chloride salt at close to the clearing point at 185 °C (left) and further into the phase at 180 °C (right) (x100 optical zoom).	162
Figure 6.13: Photomicrograph of the smectic B phase of the 1:2 mixture of Compound 22 and its chloride salt at 128 °C.	162
Figure 6.14: DSC thermogram of heat flow (mW^{-1}) as a function of temperature ($^{\circ}\text{C}$) for a 1:3 mixture of Compound 22 : chloride salt.	163
Figure 6.15: Photomicrographs showing the smectic A texture of the 1:3 mixture of Compound 22 and its chloride salt at close to the clearing point at 185 °C (left) and further into the phase at 170 °C (right) (x100 optical zoom).	164
Figure 6.16: Transition temperatures (●- clearing point, ●-smectic A to smectic B) as a function of concentration (wt %)of the chloride salt of Compound 22 with the parent Compound 22.	164
Figure 6.17: DSC thermogram of heat flow (mW^{-1}) as a function of temperature ($^{\circ}\text{C}$) for a 3:1 mixture of Compound 22 : acrylate salt.	165
Figure 6.18: Photomicrographs showing the smectic A texture of the 3:1 mixture of Compound 22 and its acrylate salt at close to the clearing point at 170 °C (left) and further into the phase at 160 °C (right) (x100 optical zoom).	166
Figure 6.19: Photomicrographs showing the smectic B texture of the 3:1 mixture of Compound 22 and its acrylate salt at close to the clearing point at 125 °C (left) and further into the phase at 101 °C (right) (x100 optical zoom).	167
Figure 6.20: DSC thermogram of heat flow (mW^{-1}) as a function of temperature ($^{\circ}\text{C}$) for a 2:1 mixture of Compound 22 : acrylate salt.	167
Figure 6.21: Photomicrographs showing the smectic A texture of the 2:1 mixture of Compound 22 and its acrylate salt at close to the clearing point at 170 °C (left) and the smectic B phase at 125 °C (right) (x100 optical zoom).....	168

Figure 6.22: DSC thermogram of heat flow (mW^{-1}) as a function of temperature ($^{\circ}\text{C}$) for a 1:1 mixture of Compound 22 : acrylate salt.	169
Figure 6.23: DSC thermogram of heat flow (mW^{-1}) as a function of temperature ($^{\circ}\text{C}$) for a 1:2 mixture of Compound 22 : acrylate salt.	170
Figure 6.24: DSC thermogram of heat flow (mW^{-1}) as a function of temperature ($^{\circ}\text{C}$) for a 1:3 mixture of Compound 22 : acrylate salt.	171
Figure 6.25: Transition temperatures (●- clearing point, ●-smectic A to smectic B) as a function of concentration (wt %)of the chloride salt of Compound 22 with the parent Compound 22.	172
Figure 6.26: DSC thermogram of heat flow (mW^{-1}) as a function of temperature ($^{\circ}\text{C}$) for a 3:1 mixture of Compound 22 : hexafluorophosphate salt.....	173
Figure 6.27: Photomicrographs showing the smectic A texture of the 3:1 mixture of Compound 22 and its hexafluorophosphate salt at close to the clearing point at 191°C (left) and further into the phase at 191°C (right) (x100 optical zoom).....	174
Figure 6.28: Photomicrographs showing the smectic A texture of the 3:1 mixture of Compound 22 and its hexafluorophosphate salt at 185°C (left) in the smectic B phase at 165°C (right) (x100 optical zoom).	174
Figure 6.29: DSC thermogram of heat flow (mW^{-1}) as a function of temperature ($^{\circ}\text{C}$) for a 2:1 mixture of Compound 22 : hexafluorophosphate salt.....	175
Figure 6.30: Photomicrographs showing the smectic A texture of the 2:1 mixture of Compound 22 and its hexafluorophosphate salt at close to the clearing point at 190°C (left) and further into the phase at 185°C (right) (x100 optical zoom).....	176
Figure 7.1: Structures of Compound 1 (top left), Compound 2 (top right) and Compound 3 (bottom).....	184
Figure 7.2: Slide showing the discolouration of photopolymerised Compound 2.	185
Figure 7.3: Structures of Irgacure 184 (left) and Irgacure 369 (right).	186
Figure 7.4: UV-DSC trace for the photopolymerisation of Compound 2 using 6 wt % Irgacure 184.	186
Figure 7.5: Structure of Compound 22.	188
Figure 7.6: UV-Vis absorption spectrum of Compound 22.....	188
Figure 7.7: UV-Vis absorption spectrum and structure of Irgacure 184.....	189
Figure 7.8: UV-Vis absorption spectrum and structure of Irgacure 369.....	190
Figure 7.9: UV-Vis absorption spectrum and structure of Irgacure 651.....	191
Figure 7.10: UV-Vis absorption spectrum and structure of Irgacure 819.....	191
Figure 7.11: UV-Vis absorption spectrum and structure of Irgacure 907.....	192
Figure 7.12: UV-Vis absorption spectrum and structure of Irgacure 1700.....	193
Figure 7.13: UV-Vis absorption spectrum and structure of Irgacure 1800.....	193

Figure 7.14: UV-Vis absorption spectrum and structure of Irgacure 2959.....	194
Figure 7.15: UV-Vis absorption spectrum and structure of Darocure 4265.	195
Figure 7.16: UV-Vis absorption spectrum and structure of CGI1300.	195
Figure 7.18: UV-DSC profile for the polymerisation of Compound 2 initiated by CGI1300.....	198
Figure 7.19: UV-DSC profile of the polymerisation of Compound 22 initiated by CGI1300 at 194 °C, isotropic liquid phase.	199
Figure 7.20: UV-DSC profile of the polymerisation of Compound 22 initiated by CGI1300 at 199 °C, isotropic liquid phase.	200
Figure 7.21: UV-DSC profile of the polymerisation of Compound 22 initiated by CGI1300 at 174 °C, smectic A phase.	202
Figure 7.22: UV-DSC profile of the polymerisation of Compound 22 initiated by CGI1300 at 169 °C, smectic A phase.	203
Figure 7.23: UV-DSC profile of the polymerisation of Compound 22 initiated by CGI1300 at 120 °C, smectic B phase.	204
Figure 7.24: UV-DSC profile of the polymerisation of Compound 22 initiated by CGI1300 at 100 °C, smectic B phase.	205
Figure 7.25: Initiation time and completion time as a function of temperature for the polymerisation of the chloride salt of Compound 22.	206
Figure 7.26: Rate of polymerisation as a function of temperature for the polymerisation of Compound 22.....	207

Acknowledgements

I would like to thank my supervisors, Professor John Goodby and Doctor Stephen Cowling, for their constant guidance and support throughout the duration of my PhD, as well as for their patience in helping correct this thesis. I would also like to thank the Materials group, who have aided me in various ways, including assistance with the developments of syntheses, teaching me how to use specific instrumentation, reminding me that everything is achievable, letting me use their equipment, chemicals and laboratory space and generally helping me throughout the past four years. They are as follows, in no particular order: Dr. Richard Mandle, Dr. Edward Davies, Dr. Emily Bevis, Dr. Katrina Bakker, Dr. Mark Sims, Dr. Kirsty Davey, Dr. Abdel Belaisaoui, Dr. Xiang Xia, Dr. Wen Cai, Dr. Tiantian Ma, Dr. Charlie Wand, Dr. Linda Mcallister, Dr. Tingjun Zhong, Dr. David Stewart, Dr. Saleesh Nambalan Sivaraman, Dr. Sarah Kirchhecker, Dr. Iman Khazal, Imelda Silalahi, Julia Sarju, Craig Archbold, Richard Booth, Harry Toynton, Christopher Cabry, Jing Tseng, Dr. Isabel Saez, Dr. Martin Bates, Prof. Duncan Bruce and Prof. Peter Raynes. I would also like to extend thanks to the students who spent time in the laboratory in the course of their MChem, BSc and summer placement projects.

I would also like to thank the EPSRC and Merck for funding. I would also like to thank Iain Gardiner for support from Merck, as well as Julian Vaughn-Spickers for arranging the annual CASE Conferences for the students funded by the company.

Finally, I would like to thank my family for their unwavering support, as well as my girlfriend, Elizabeth, and her family, for allowing me into their family and offering support for the last three years.

Author's Declaration

I hereby declare that I am the sole author of the thesis. Work presented has been conducted by the author in conjunction with the supervision of Prof. John Goodby and Dr. Stephen Cowling, and in conjunction with Merck Chilworth.

All work presented has been conducted by the author, and any external input has been accurately referenced and acknowledged. This work has not previously been presented for an award at this, or any other, University.

1: Introduction

1.1: Target Technologies

In recent years, both smart windows and touch-screen technologies have dramatically increased in popularity, going from rare and expensive technologies to common and, in the case of touch-screens, everyday devices. The increased usage of both of these technologies means that they occupy a growing industry, and refinement is always required to allow for greater efficiency, lower production costs and greater functionality.

Modern smart window technology allows the transmission of light through a large area to be modulated via the application of an electric field. Typically, such devices utilize a polymer dispersed liquid crystal (PDLC) in which a host liquid crystal is encapsulated in a polymer network. Application of a voltage across the glass *via* transparent electrodes causes the material to reversibly change from transparent to opaque. However, due to the polymer network, this method requires a large electric field to induce re-orientation of the liquid crystal, thereby necessitating a large driving voltage, high energy consumption, and low efficiency due to the disperse nature of the electric field.^{1,2} A potential development in this area is the introduction of conductive polymer chains with attached mesogens³, which would facilitate the electric field to penetrate the polymer and address the liquid crystal and hence reduce voltage demands.⁴ This, in turn, could make the operation of smart windows cheaper and more environmentally friendly.

In the case of touch-screens, current developmental goals include: the variation of pressure leading to different behaviours; the concept of touch feedback so that the screen mimics the feeling of what is presented; and increased efficiency and reducing manufacturing costs.

1.2: An Introduction to Liquid Crystals

Mesogenic compounds exhibit liquid-crystalline behaviour as they show some of the properties of both liquids and crystalline solids, such as the ability to flow in combination with ordered structural features. As a consequence of their partial ordering, liquid crystals exhibit anisotropic physical properties, for example optical anisotropy (birefringence) and dielectric anisotropy.

Liquid crystals fall into two primary categories: materials that form a liquid crystalline phase as a function of temperature and in the absence of solvent, which are called thermotropic liquid crystals; and materials that only form mesophases as a function of concentration in the presence of a suitable solvent that are dubbed lyotropic liquid crystals. The remainder of this report will focus primarily on the phases and properties of thermotropic liquid crystals for the diallylamine terminated compounds, yet in the cases of quaternary diallylammonium salts, lyotropic behaviours could be considered.

1.2.1: Thermotropic Liquid Crystals

Upon heating, most materials that are solid at room temperature reach a point at which the crystalline lattice breaks down to give an isotropic liquid phase. This point is called the melting point. However, for materials that show liquid-crystalline behaviour, the transition from the solid state to the isotropic liquid phase is punctuated by one or more thermodynamically stable mesophases, these can be broadly divided into two classes: the nematic phase and the smectic phases for calamitic or rod-like molecules (see Figure 1.1); and discotic nematic and columnar phases for disc-shaped molecular systems. The nematic and smectic phases are the most relevant to the work undertaken during this project and therefore will be discussed in the following sections.

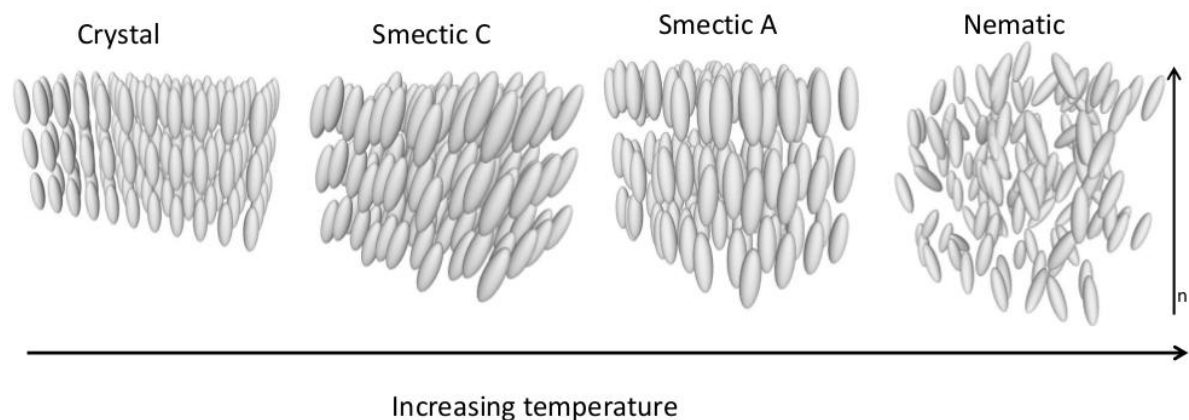


Figure 1.1: Possible liquid crystal phases formed upon heating. The orientations of the molecules are shown relative to the director (n).

1.2.1.1: The Nematic Phase

The nematic phase is the least ordered liquid-crystalline phase and shows only orientational ordering of the constituent molecules. Therefore, in this phase, there is a general alignment of the molecular long axes with respect to the director (n).⁵ However, it is important to note that there are as many molecules pointing in an 'up' direction as there are in an opposing 'down' direction in the nematic phase, i.e., $n=-n$, which means that the nematic phase shows no bulk polar properties, see Figure 1.2. The degree of orientational order within the phase is given by the order parameter (S) (Equation 1.1):

$$S = \frac{1}{2} \langle 3 \sin^2 \theta - 1 \rangle \quad \text{Equation 1.1}$$

The angular brackets account for an average across all of the constituent molecules. A typical value of S for a nematic phase tends to fall between 0.4 and 0.7.

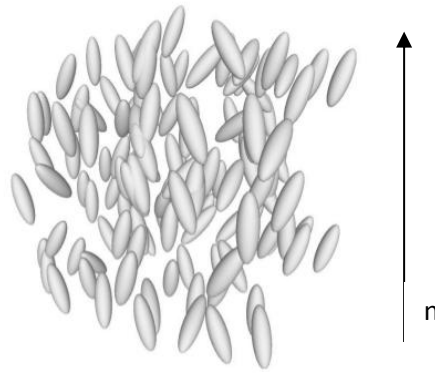


Figure 1.2: A representation of the nematic liquid crystal phase composed of calamitic molecules, showing their general alignment with the director, n .

Although the molecules are in dynamic motion, when cooling towards the smectic phases, small areas displaying smectic A or smectic C-like ordering within the nematic phase can exist. These are known as cybotactic clusters.⁶ The identifying feature of the nematic phase under optical microscopy, when viewed through cross-polarisers (x100 to x200), is the ‘*schlieren*’ texture, which typically exhibits defect lines and singularities which have a ‘brush-like’ appearance. These point defects exist as 4- or 2-brush defects (Figure 1.3). These ‘brushes’, which appear as patches of darkness, occur where the light is extinguished by the polarizers owing to the fact that the polarisation direction of light has been unaffected by the liquid crystal due to the local director being either parallel to the polariser or analyser. This means that the light can pass through the first polariser, yet since it is unchanged, it will be unable to pass through the analyser, which is set at 90 degrees from the first. Due to the fluidity of the phase and the presence of impurity particles, Brownian motion is often observed in nematic liquid crystals when examined under the optical microscope.

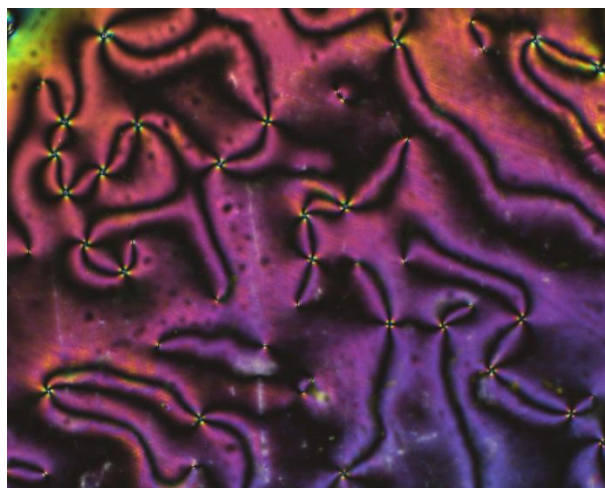


Figure 1.3: Photomicrograph showing the schlieren texture of the nematic phase with 4- and 2-brush defects (x100).

1.2.1.2: The Smectic A Phase

In the smectic A phase, molecules are arranged in diffuse layers with their long axis perpendicular to the layer normal, see Figure 1.4. In the plane parallel to the smectic layer there is short-range order of around 2 nm, with this order decreasing above this distance. Each molecule rotates about its long axis rapidly (on the order of 10^{11} times per second), and about its short axis around a million times a second.⁷ X-ray diffraction experiments have shown that there is sinusoidal distribution of the centres of masses of the molecules, i.e., the layers are not well defined in the smectic A phase.⁸

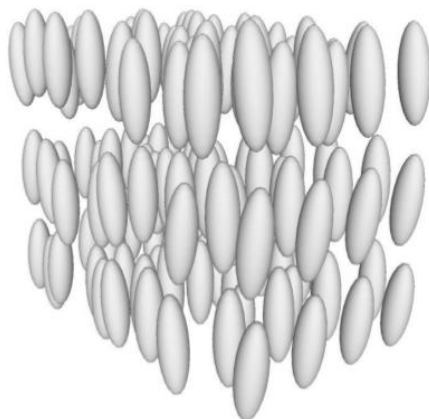


Figure 1.4: A simplified representation of the Smectic A liquid crystal phase, showing their directional alignment and the formation of very diffuse layers.

The smectic A phase is more ordered compared to the nematic phase, yet the rapid rotation of the molecules means that there is significantly less order than in the solid state. However, as molecules within this phase rotate rapidly, they are able to easily realign during a reaction, which facilitates more rapid polymerisation than observed in other phases, such as the nematic and isotropic phases.

The smectic A phase appears significantly different to the nematic phase by polarised optical microscopy where no schlieren texture is observed. Instead, the smectic A phase shows characteristic focal conic and homeotropic domains.⁹ The focal conic defect shows characteristic defect lines, which are known as the ellipse and hyperbola. A classic focal conic defect texture is shown in Figure 1.5.¹⁰

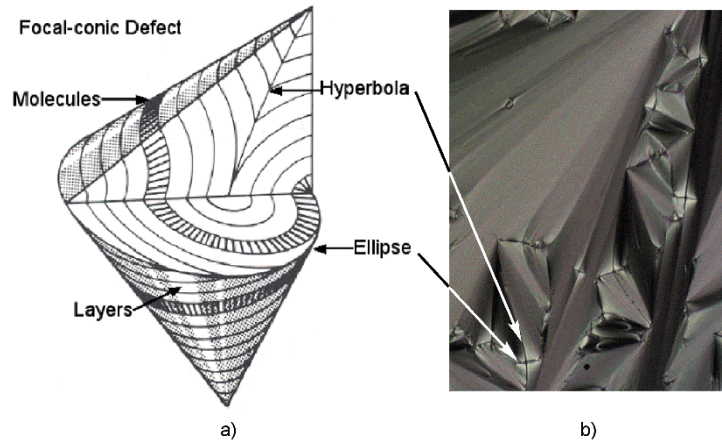


Figure 1.5: a) Arrangement of the smectic layers forming a focal conic defect and b) photomicrograph of a focal conic defect showing the ellipse and hyperbola.

1.2.1.3: The Smectic C Phase

The structure of the smectic C phase is similar to that of the smectic A phase, with the exception of the constituent molecules being tilted at an angle with respect to the layer normal, see Figure 1.6. The tilt is regular throughout a given domain, maintaining the angle and arrangement between layers. However, over a greater range, molecules are more randomly arranged. Within layers, the molecules pack locally in hexagonal arrangements, yet this is not a far-reaching arrangement extending over a distance of the order 2 nm *i.e.* a few molecular entities.

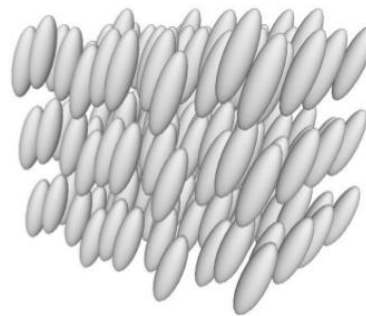


Figure 1.6: A representation of the Smectic C liquid crystal phase, showing the tilt of the molecules, and alignment and layer formation.

The tilt angle of the molecules is temperature dependent, and if formed from cooling of a smectic A phase, the relationship between the tilt angle and temperature can be described with the use of the following formula (Equation 1.2):¹¹

$$(\theta)_T = (\theta)_0(T_{A-C} - T)^\alpha \quad \text{Equation 1.2}$$

where θ_T is the tilt angle at temperature T °C; θ_0 is a constant; T_{A-C} is the SmA-SmC transition temperature; T is the temperature; and α is an exponent, theoretically predicted to be 0.5 from Landau theory.

Using polarised optical microscopy the smectic C phase has a distinctive appearance consisting of a broken focal conic texture and a *schlieren* texture where only 4-brush defects are observed. The broken nature of the focal conic texture arises from tilt domains where the molecules orient in differing directions within the focal conic itself causing a patchy appearance. This becomes more pronounced as the tilt angle increases with decreasing temperature. Figure 1.7 shows a broken focal conic texture and *schlieren* texture for a smectic C phase.

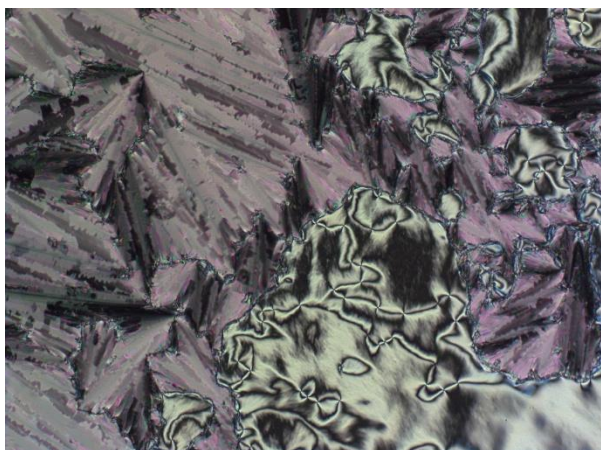


Figure 1.7: Photomicrograph of a smectic C phase showing a broken focal conic texture and schlieren exhibiting only 4-brush defects.

1.2.1.4: Birefringence

The optical anisotropy, or birefringence, is the optical property of a material that induces differing refractive indices based on the polarisation of incident light.^{12,13} The principal refractive indices are those for the ordinary and extraordinary rays, the former being measured for the electric vector of light vibrating perpendicular to the optical axis, whereas the latter is concerned with the vibration along the optic axis. A qualitative value for the optical anisotropy can be obtained from the following Equation 1.3:

$$\Delta n = n_e - n_o \quad \text{Equation 1.3}$$

where n_e is the refractive index of the extraordinary vector, and n_o is that of the ordinary refractive index. Hence, for positive birefringence, the extraordinary refractive index tends to be greater than the ordinary refractive index, yet these converge towards the clearing point, and thereafter in the isotropic liquid phase there is no difference between the two, meaning the birefringence is lost. The birefringence of a compound is directly related to the number of pi electrons that are in the core of the molecule, i.e. a biphenyl compound is of higher birefringence than a cyclohexyl phenyl compound, but lower than a corresponding toluene. A desirable trait of a mesogenic compound is to have a moderate to high birefringence, which allows for a thinner layer to be practical in devices, and thereby allowing for easier processing. Further to the optical anisotropy, if a material is ionic then conductivity can be anisotropic, that is the conductivity will be different in different directions.

1.2.1.5: X-ray Analysis of Liquid Crystalline Phases

From the observation of the semi-organised nature of the liquid crystal phases discussed, it was supposed that certain techniques used for the analysis of crystal structures would be of interest in the analysis of liquid crystalline phases. However, the weak ordering of the molecules in liquid crystal phases means that there are challenges to be overcome in the analysis of a wide range of these phases, such as the low numbers of diffraction peaks that may be witnessed and whether the samples are aligned or not.

Analysis is conducted using the Bragg Law (Equation 1.4),¹⁴ which concerns the nature of constructive interference reflected from different yet adjacent planes within a structure separated by a distance defined as d .

$$n\lambda = 2d \sin \theta \quad \text{Equation 1.4}$$

Here, the angle θ is the incident angle of X-ray irradiation onto the layer of the structure, with λ the wavelength of the X-rays used. The natures of d and θ are presented in Figure 1.8 below.

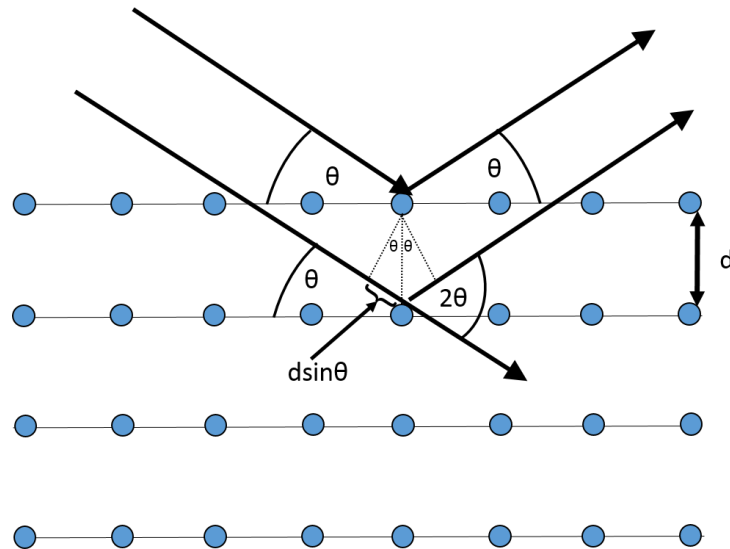


Figure 1.8: A representation of incident X-rays on a crystal lattice at angles θ , showing the layer spacing, d .

The incident X-rays meet the parallel planes of the crystal which are separated by distance d at an angle of θ . The path difference of the X-rays is $2d\sin\theta$, with the extra distance being traversed on the left hand side being presented as $d\sin\theta$, which will also be taken into account on the reflected rays on the right of the figure, creating the overall path distance described. This path difference will be equivalent to $n\lambda$, an integral multiple of the wavelength of the X-ray.

An alternate way of describing the Bragg Law is through the identification of the scattering vector q , which is presented below in Equation 1.5.¹⁵

$$|q| = |k_i - k_f| = \frac{(4\pi \sin \theta)}{\lambda} \quad \text{Equation 1.5}$$

The scattering vector, q , relates to the path difference of the X-ray of known wavelength through the sample. This is shown in Figure 1.9 below.

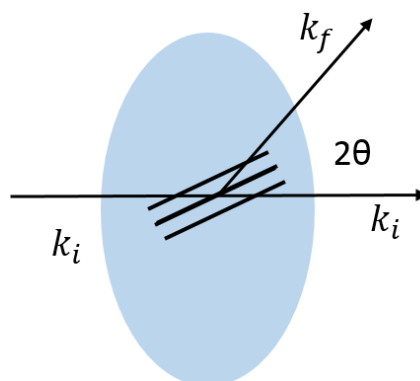


Figure 1.9: A representation of a crystal lattice being studied by X-ray, with the scattering effect shown.

The vectors of the incident and scattered X-rays are k_i and k_f respectively, with the angular difference between them being 2θ . The intensity of the scattered X-rays is zero at all times other than when Bragg's Law is satisfied. By evaluating the angle between the incident and scattered rays, the only unevaluated variables are n , an integer value, and d , the layer spacing within the sample. Through calculation of the scattering angle and knowledge of the wavelength used in the study, it is therefore possible to calculate the layer spacings in a phase.

The nature of Smectic A and Smectic C phases allows for analysis of the layer spacings by X-ray diffraction in a manner similar to that of crystal compounds, with some slight alterations.¹⁶ The intensity peaks generated from detection in scattering experiments for liquid crystal phases tend to be weaker and broader than corresponding crystal peaks. There is also the question of alignment of the sample in the scattering experiment. There is a difference between the outputs of aligned and unaligned samples, where the patterns generated will be impacted by this.

Alignment of the liquid crystal will dictate how much information can be obtained about the structure of a phase. Unaligned samples of nematic, smectic A and smectic C phases which feature random orientation, give rise to powder patterns akin to circular rings about the scattering profile (Figure 1.10a). The inner ring represents the layer spacing (end to end interaction) and the outer ring represents the distance between the molecules (distance between molecules laterally). Aligned samples will feature more discrete patterns akin to brackets. Depending on the nature of the phase, these sets of brackets may be perpendicular to one another as in the case of both the nematic and smectic A phases (Figure 1.10b), or the wide angle diffraction may be at angles to the small angle diffraction representing the tilt of the molecules as in the smectic C phase (Figure 1.10c). The nematic phase shows diffuse small angle and wide angle diffraction peaks representing the fluid nature of the phase whereas the smectic phases exhibit much sharper and

more intense small angle diffraction peaks. Sometimes it is also possible to observe the 2nd order diffraction peak for the smectic phase where the layer spacing is exactly half the 1st order diffraction peak.¹⁷



Figure 1.10: A cartoon representation showing the sharp small angle diffractions, as well as the diffuse wide angle diffractions. The rotation difference between the 'brackets' at wide angles in (b) and (c) show the tilt angle of the smectic C phase (c).

1.3: Liquid Crystal Polymers and Polymerization in Organized Media

Polymeric liquid crystals can display properties of both liquid crystals, such as optical and conductive anisotropy, whilst exhibiting polymeric properties, such as glass- or rubber-like behaviour. The behaviour and physical properties of liquid-crystalline polymers is often dependent on the molecular weight of the polymer, but this can be controlled by factors such as the temperature and corresponding phase in which they are formed, as well as the composition or presence of copolymers, and the means by which the mesogenic sub-units are potentially attached to the polymer backbone.¹⁸

The phase the polymer is formed in tends to be stabilised in the liquid crystal polymer. Furthermore, in the case of network polymer formation, the choice of mesophase in which the monomer is polymerized also determines the rate of polymerization with more ordered mesophases tending to give faster rates of polymerization, *i.e.* monomers in smectic phases tend to polymerise more rapidly than nematics, which in turn will polymerize more rapidly than the isotropic liquid. The degree of polymerisation also differs between phases, with the nature of the polymerizable groups also having a bearing on this. Interestingly, in mono-functionalised compounds polymerisation occurs to a greater extent in the isotropic and nematic phases, whereas in compounds with multiple polymerizable groups the reverse is observed, where greater degrees of polymerisations are achieved in more organised phases where the polymerizable moieties are forced to pack together.

From the polymerisation of mesogenic compounds, there are two main ways in which the mesogenic unit can be incorporated within a polymer chain: main chain or side chain. The polymer will also have different properties based on this positioning of the mesogen. This dramatically affects the bulk physical properties of the material due to alignment of strands between one

another, changing properties such as tensile strength. The relative alignments of the mesogens within the polymer, and their freedom to re-orientate, also affect physical properties of the polymer.

1.3.1: Main Chain Liquid Crystal Polymers

In main chain liquid crystal polymers (Figure 1.11), the mesogenic units are incorporated along the backbone of the polymer, separated by spacer linkages, which may vary in length and identity. The flexibilities of the spacer linkages dramatically affect the capability of the mesogens to self-organize, so the relative stability of liquid crystal phases can be tuned by the identity of the spacer groups. Main chain liquid crystal polymers tend to lack smectic phases, and instead prefer formation of nematic phases.¹⁹ Common examples of main chain polymers include polyesters, polyethers, polyamides and polycarbonates.

Main chain liquid crystal polymers can be useful for physical properties aside from optical behaviour due to the self-organization of the mesogenic units. For instance, if they are processed properly, they can possess very high tensile strengths, such as in spider silk or Kevlar.²⁰

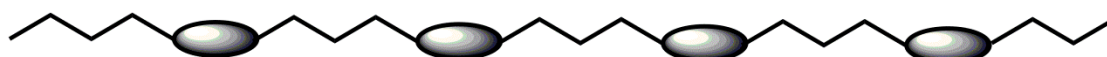


Figure 1.11: A generic view of a main chain liquid crystal polymer.

1.3.2: Side Chain Liquid Crystal Polymers

In contrast to main chain liquid crystal polymers, side chain liquid crystal polymers have pendant mesogenic units that are suspended from the backbone of the polymer by linkers. This offers two possibilities for their attachment: terminal (or end on) (Figure 1.12) or lateral attachment (Figure 1.13).²¹

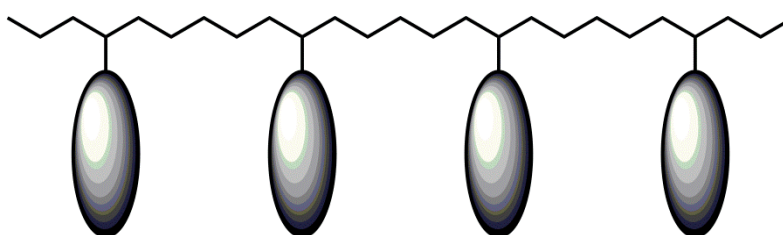


Figure 1.12: A generic example of a terminally attached side chain liquid crystal polymer.

In side chain polymers, the phase behaviour is largely governed by nature of these peripheral units where it is common to observe smectic phase behaviour with end-on attachment of the pendant groups and nematic phase behaviour with lateral attachment of the pendant groups. As with low molar mass materials, the behaviour of the polymer may be affected by the application of an electric field, altering the direction of the director to which the mesogens align, meaning that optical properties can be switched.¹⁹ However, due to the comparatively higher viscosities, the

response times observed for liquid crystal polymers tend to be greater than in lower molar mass materials.

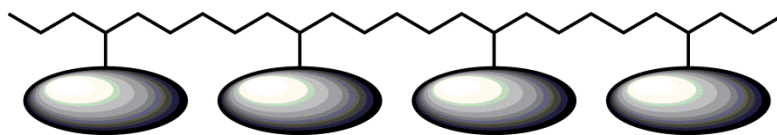


Figure 1.13: A generic example of a laterally attached side chain liquid crystal polymer.

1.4: Ionic Liquid Crystals

Ionic liquid crystals possess mesogenic motifs with ionic character, such as N-substituted imidazole salts. Like ionic liquids, these ionic liquid crystals are generally non-flammable, non-volatile and highly conductive,²² however due to their liquid crystalline nature, the conductivity can be anisotropic, which is potentially a very useful property for applications in thin film assemblies.^{23,24} Ionic liquid crystals are presently of great interest as bio-sensors for these reasons. Another property of these compounds is that they have a preference for forming stable smectic phases, as the ionic character tends to drive the formation of lamellar structures.^{23,24}

Many ionic liquid crystals incorporate the ionic character within the motif, such as in the case of imidazolium salts (Figure 1.14) synthesised by the Seddon and Bruce groups.²⁵ In these cases, the motif, rather than being benzene-derived, is centred around an imidazolium group, with an anion associated loosely to the dissociated cationic charge within the heteroaromatic ring. The generic structure of these compounds is that of the imidazolium group, with an aliphatic chain attached to one of the nitrogens, with another organic group attached at the other nitrogen, though this may be a hydrogen in the case of simpler structures. The chain may also feature alternative terminal groups, such as halogenation.

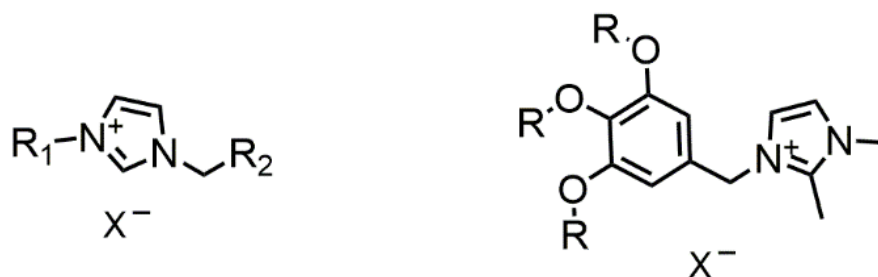


Figure 1.14: Structures of example ionic liquid crystal compounds, where R, R₁ and R₂ are organic groups, and X⁻ is the associated anion, e.g. Cl⁻.

The mesomorphic behaviours of these compounds depends strongly on the overall structure but also show a strong dependency on the nature of the anion (X⁻). The self-organisation is driven by nanosegregation of the ionic motifs and the chains attached to them.

As already stated, the liquid crystalline phases formed vary in nature dependent upon the shape of the overall molecule, as well as the ratio of the chain to the motif, i.e. the volume ratio between the ionic and non-ionic regions. The ionic compounds can be rod-like giving rise to smectic phases, or wedge-like giving rise to columnar phases.

In addition to their thermotropic behaviours, ionic liquid crystals can act as lyotropic liquid crystals when mixed with ionic liquids. As well as the effects that the anionic species has on phase behaviour it is also possible to change the cationic moieties and examine the effect that this has on phase behaviour. Figure 1.15²⁶ shows the structure of compounds where the cationic species was changed from imidazolium to quaternary amine and phosphonium salts.



Figure 1.15: The generic structures of quaternary ammonium and phosphonium salt ionic liquid crystal salts, where R represents an organic group.

These fan-shaped structures formed bicontinuous cubic phases with conductive channels for the anions to flow through. The phase behaviour was dictated by the shape of the molecule but the size of the cationic group governed the temperature range of the phase. The ammonium salt exhibited a wider temperature range of the phase (42-82 °C) when compared with the phosphonium salt (32-49 °C).

The association between the imidazolium ring and the corresponding anion is fairly weak, partially due to the dissociation of the positive charge about the heteroaromatic ring, as well as due to the cavity size for the anion to reside being rather small. The loose binding of the anion promotes conductivity through the bulk material.²⁵ The nature of the anion, however, also influences the nature of the conductivity, with anisotropic conductivity reduced with increased size of the anion.²⁵ It is generally assumed that the conductivity is predominantly due to the anions present, in part based on the impact of the anion on the anisotropic conductivity, as well as the belief that the mobility of the anions will be considerably greater than that of the cations. The anions are assumed to be more mobile due to the formation of channels for the anions to flow through, as well as the formation of structures from the cations which will rigidly define their position and prevent their carriage of charge.

In addition to the low molecular mass compounds discussed, ionic compounds containing terminal polymerizable groups, such as methacrylates (Figure 1.16),²⁷ acrylates (Figure 1.17)²⁸ and dienes

(Figure 1.18)²⁹ have been investigated. Many of these polymeric materials have been used in thin films and have exhibited some interesting conductivities depending on the nature of the mesophase that the compound was polymerised from.

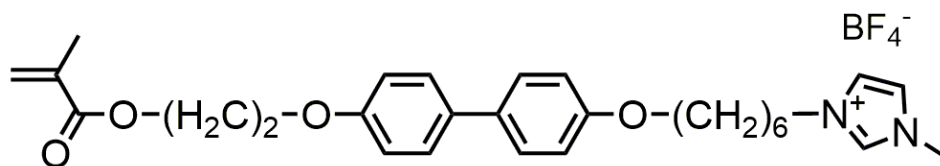


Figure 1.16: Structure of a methacrylate terminated ionic liquid crystal (the compound displayed a smectic A phase between 60°C and 52°C).

When the compound in Figure 1.16 was irradiated with UV on a glass substrate while in the smectic A phase, the resultant polymer formed was found to be a conductive 2-dimensional film.

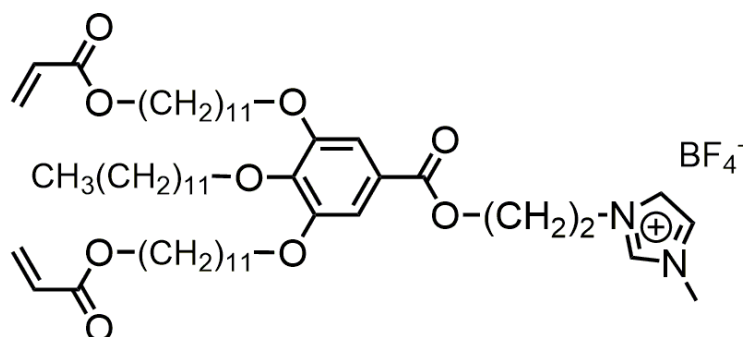


Figure 1.17: Structure of a fan-shaped acrylate terminated ionic liquid crystal (the compound displayed a hexagonal columnar phase between 20°C and 50°C).

The fan-shaped compound presented in Figure 1.17, studied by Yoshio, Kato *et al.*,²⁸ developed two different anisotropically conductive polymer films. These films consisted of one-dimensional channels that formed parallel or perpendicular to the surface of the film. Similar to the rod-like example (shown in Figure 1.16),²⁷ the polymer was obtained through UV polymerization, with a hexagonal columnar phase exhibited between 20 °C and 50 °C. The different films were formed with respect to different substrates, with the perpendicular form being associated with amine-functionalised substrates, and the parallel equivalents being obtained from the shearing of the film having first been polymerized between two glass slides.

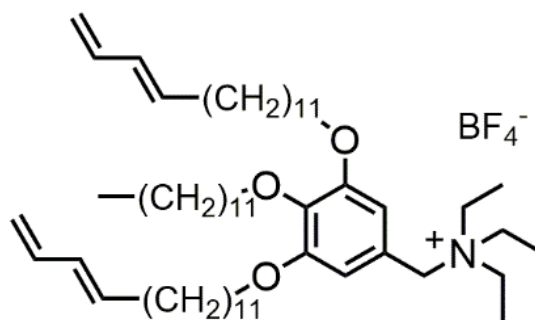


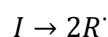
Figure 1.18: Structure of a diene-terminated ionic liquid crystal. The polymer formed with a bicontinuous cubic nanostructure exhibited the highest conductivities.

The diene-functionalised compound presented in Figure 1.18 formed three-dimensionally and one-dimensionally conductive films *via* photofixation of bicontinuous and columnar phases. The film that resulted from the photofixation of bicontinuous cubic phases exhibited greater degrees of ionic conductivity than the resultant films polymerized from the columnar and isotropic phases.²⁹

The formations from the identified ionic liquid crystals result in anisotropic ionic conductivity, i.e. directionally oriented conductivity throughout the substrate, which could allow for ionic conductivity throughout a display.

1.5: Synthesis of Polymers

1.5.1: Free Radical Polymerisation



The process of free radical polymerisation³⁰ readily allows the formation of long polymers from simple monomers with unsaturated regions, *e.g.* a terminal alkene group, such as in the case of polystyrene. The double bond is affected by the presence of a radicalised initiator, binding the initiator to the substrate, and causing the radical to reform at the opposite end of the bond. Free radical polymerisation requires the presence of an initiator, which will fragment when irradiated by an external source, such as by heat (thermal, such as benzoyl peroxide), ultra-violet irradiation (UV, such as AIBN, Figure 1.19), or another method (*e.g.* redox reactions, such as iron and hydrogen peroxide). Furthermore, these initiators can be designed so that they react only under specific conditions. For example, in UV polymerisation the initiator can be selected such that polymerisation can only occur under specific ranges of UV wavelengths, for example Irgacure 184 will predominantly only radicalise between 222nm and 245nm. Consequently, the choice of initiator is of importance. Selection of an appropriate initiator takes into account the pigmentation of the monomer so that the absorption wavelengths of both the medium and initiator are different, as well as considering the potential for side-reactions with the monomer. As it is often desirable to polymerise from certain mesophases to yield specific properties, care must be taken to ensure that

the initiator remains stable at the temperatures used during polymerisation. In the case of this study, only UV-polymerisations will be extensively considered.



Figure 1.19: (left) Benzoyl Peroxide, (right) AIBN.

1.5.2: UV-polymerisation

UV-polymerisation will, of course, have several different factors from other types of polymerisation, such as thermally induced polymerisation. As has previously been mentioned, there are issues of stability of the monomers to consider in the choice of approach needed to be taken, yet there are significant other factors that must be considered. With thermal polymerisation, there is a chance of monomer decomposition at increased temperatures, whereas UV-polymerisation will not suffer from these issues, but rather from questions over stability from UV-irradiation.

UV-Initiated polymerisation has positives, as well as drawbacks.³¹ UV light used to initiate a polymerisation is not always able to penetrate the bulk of a sample, meaning that UV-polymerisation is limited to surfaces and thin films. In addition, pigmented compounds can absorb UV-irradiation, further decreasing its penetration into the sample and decreasing polymerisation. UV-polymerisation requires an initiator to be present, which is sometimes present in the polymer formed. This can adversely affect the polymer's properties, such as tensile strength and conductivity.

UV-polymerisations can be conducted at any temperature at which the monomer is stable. This is of particular interest in the case of liquid crystals, where the rate of polymerisation and the physical properties of the polymer can be controlled by polymerising from different mesophases. UV-polymerisation is efficient in terms of energy and space. The medium to be polymerised can be free-standing, as only a UV-bulb is required for the polymerisation, rather than a full heating unit in the case of thermal polymerisation.

Another issue encountered with UV-polymerisation is the issue of unregulated heating of the sample. The exposure to an ultraviolet light source will cause further heating of a sample as it is a high energy input into a system. This could prove disadvantageous if the polymerisation is conducted at a temperature approaching a phase transition, with the further energy provided to the system potentially causing the substrate to transition into a different phase, for example if you attempt to polymerise a substrate in the nematic phase, the extra heating from the UV source could cause the sample to clear into the isotropic liquid phase. This would be problematic for several reasons, such as variation of reaction kinetics, the properties of the polymer formed, or even the decomposition of less stable substrates, especially at higher temperatures.

A further complication to be considered is the compatibility of the monomer with the initiator, that being the overlap of UV absorbance at different wavelengths. It is desirable for there to be as minimal an overlap between the optimal wavelengths for absorption (λ_{max}) of both initiator and monomer. With a vastly greater concentration of monomer compared to initiator, similar peak absorbance values will lead to the UV light being absorbed by the monomer and not by the initiator, meaning that the radicals required for the reaction will either not be produced, or will be generated at a dramatically inferior rate. This means that the choice of initiator and wavelength of light used is of great importance, but generally UV light sources for polymerisation emit across a wide range of wavelengths, so the main aspects of control are the λ_{max} s of the substrate (which is generally non-negotiable) and the initiator. Irgacure 184 predominantly absorbs in the region of 222nm to 245nm, whereas CGI1300 absorbs in the regions of 219nm to 250nm, as well as in the region of 320nm. If the monomer to be polymerised strongly absorbs UV-irradiation at 320nm, then it would be inadvisable to choose CGI1300 as an initiator in the system. Alternatively, if the UV absorption profile of the monomer shows a strong absorbance in the region of 240nm, the wavelengths necessary to radicalise Irgacure 184 would be strongly absorbed by the monomer, and therefore the initiation of the reaction would be hindered.

1.5.3: The process of polymerisation

UV-polymerisation occurs in three distinct phases: initiation, propagation and termination. The principles of each of these stages are outlined in the sections that follow.

1.5.3.1: Initiation

Incident ultraviolet irradiation causes homolytic cleavage of a bond within the photoinitiator. Depending on the identity of the initiator, this could be the O-O bond of a peroxide (Figure 1.20), or the C-N=N single bonds in an azo compound such as azobisisobutyronitrile (AIBN). Since the cleavage is homolytic, one electron is proposed to go in each direction (in AIBN (Figure 1.22), this happens both sides, and the diradical dinitrogen forms the triple bond), forming a pair of radicals, which can both interact with the monomeric species. Another possibility, however, is recombination of the photoinitiator, whereby the two radical units reform the initial compound. Further to this, there are possible side reactions, where radicals can degrade, react with solvents and also form more stable radicals that do not react with the monomer. This means that less than 100% of the initiator initiates any subsequent reaction, and therefore the efficiency of the initiation must be considered. This efficiency will depend on the conditions of the reaction, such as the concentration of the initiator and monomer, the solvent used, any impurities that might be present, and the temperature of the reaction.

The photoinitiator radical formed as a result of irradiation can then interact with the double bond in the unsaturated monomer (Figure 1.21),^{20,32} causing cleavage of the π -bond, transferring radical

character to the other end of the bond. This results in the formation of a reactive monomeric compound, which allows the polymer to form and grow.

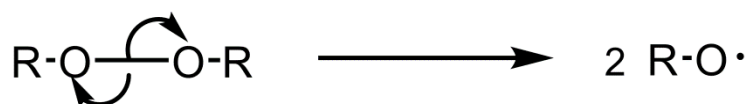


Figure 1.20: Formation of initiator radical from a peroxide initiator compound.

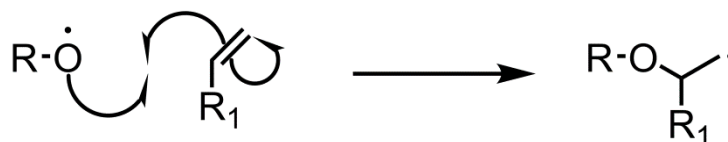


Figure 1.21: Transfer of radical character from the initiator to the monomeric substrate.

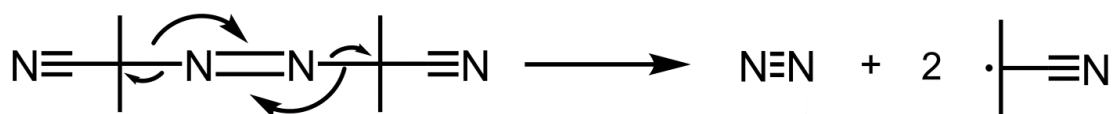


Figure 1.22: Cleavage of AIBN in radical initiation.

1.5.3.2: Propagation

The monomer radical is able to react with another monomer species in the same fashion as the initiation, moving the radical character further down the chain (Figure 1.23).^{20,32} With each reaction, another unit is added to the polymer chain, which can then react further. Theoretically, this could continue until all monomer molecules have reacted to form one long polymer chain. However, it is far more likely that numerous different initiations will have created numerous chains. In addition, termination of chains may be halted at various chain lengths, resulting in a chain length distribution.

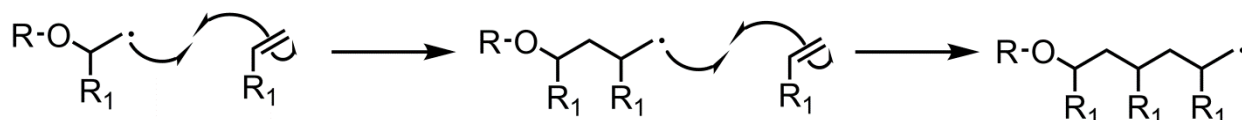


Figure 1.23: Radical propagation in polymerisation of vinyl containing monomers.

1.5.3.3: Termination

The termination of the radical polymerisation can occur in one of several different ways.³² Two chains of growing polymer can react together (Figure 1.24), with the radicals extinguished in the process of forming a new bond between the active ends.

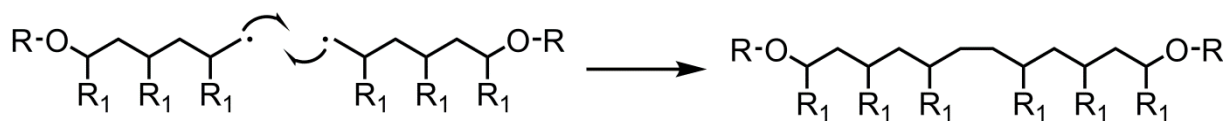


Figure 1.24: Chain combination termination in radical polymerisation.

Another possibility is that the reactive radical site can react with an unreacted initiator radical, which will produce a similar result (Figure 1.25).

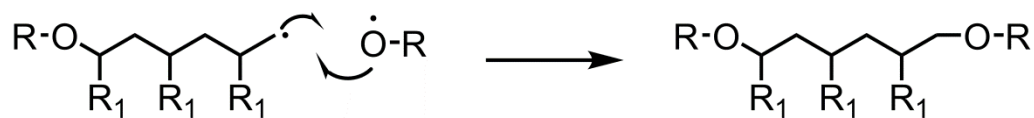


Figure 1.25: Termination of polymerisation by initiator combination.

A radical is also able to abstract a unit from another molecule (Figure 1.26), for example the abstraction of a hydrogen atom from another reactive polymer chain. This leads to the loss of radical character in both chains in a process called disproportionation.



Figure 1.26: Termination of polymerisation by disproportionation.

Another way for polymerisation to terminate is by loss of the radical to the surroundings, such as to the solvent or any impurity in the mixture, such as oxygen. It is because of this potential unregulated termination that inert gaseous environments are often used in the process of UV-DSC (scanning calorimetry), such as using a nitrogen atmosphere to prevent radical losses to oxygen.

1.5.4: Polydispersity

The nature of polymerisations is semi-controlled, meaning that the length of chain produced in most polymerisations is random. The chains produced will be a statistical distribution about an average chain length, yet the actual chain lengths may differ from this average themselves by significant margins. The dispersity is calculated by the ratio of different mass averages. These different mass averages represent the mass fraction (q_i) and number fraction (p_i). If each macromolecule has a given mass denoted by M_i and their number given as N_i , then their total mass can be given by $M_i N_i$. This means that their number fraction can be quantified in the following Equation 1.6:³³

$$p_i = N_i / \sum N_i \quad \text{Equation 1.6}$$

where N_i represents the number of macromolecules for a given mass, and $\sum N_i$ is the total number of macromolecules. In turn, the weight fraction can be given as follows in Equation 1.7:

$$q_i = N_i M_i / \sum N_i M_i \quad \text{Equation 1.7}$$

where M_i is the given mass of the macromolecules in question.

Taking these individual samples for specified masses, number average molar mass (M_n) can be determined as follows (Equation 1.8):

$$M_n = \sum p_i M_i \quad \text{Equation 1.8}$$

as well as the weight average molar mass (Equation 1.9):

$$M_w = \sum q_i M_i \quad \text{Equation 1.9}$$

which considers the full sample range of macromolecules in the sample. This allows the final evaluation of polydispersity to be determined below (Equation 1.10):

$$M_w/M_n \quad \text{Equation 1.10}$$

which is the ratio between the averages the weight average and number average masses. This means that for a perfectly monodisperse polymer,³⁴ the ratio will be 1.

The M_w and M_n are only relevant for linear polymer systems, and are irrelevant in the case of networks. The formation of networks creates an environment which is, essentially, a single molecule rather than numerous long chains.

Linear polymers form into an array of long chains of linked molecules, with the length of these chains varying due to the random nature of their formation. In the formation of networks, all monomer molecules are reacted into the singular framework, which creates a singular macromolecular unit. Since there is only one macromolecular architecture produced, it is therefore impossible to have any variation in mass between components of the mixture.

1.5.5: Types of Polymer

1.5.5.1: Elastomers

Elastomers are synthetic polymers which simulate the natural properties of rubber.³⁵ One noteworthy example of an elastomer is styrene-butadiene, which, when reinforced with carbon black, is used in the manufacture of tyres,³⁶ and is one of the most commonly used elastomers.

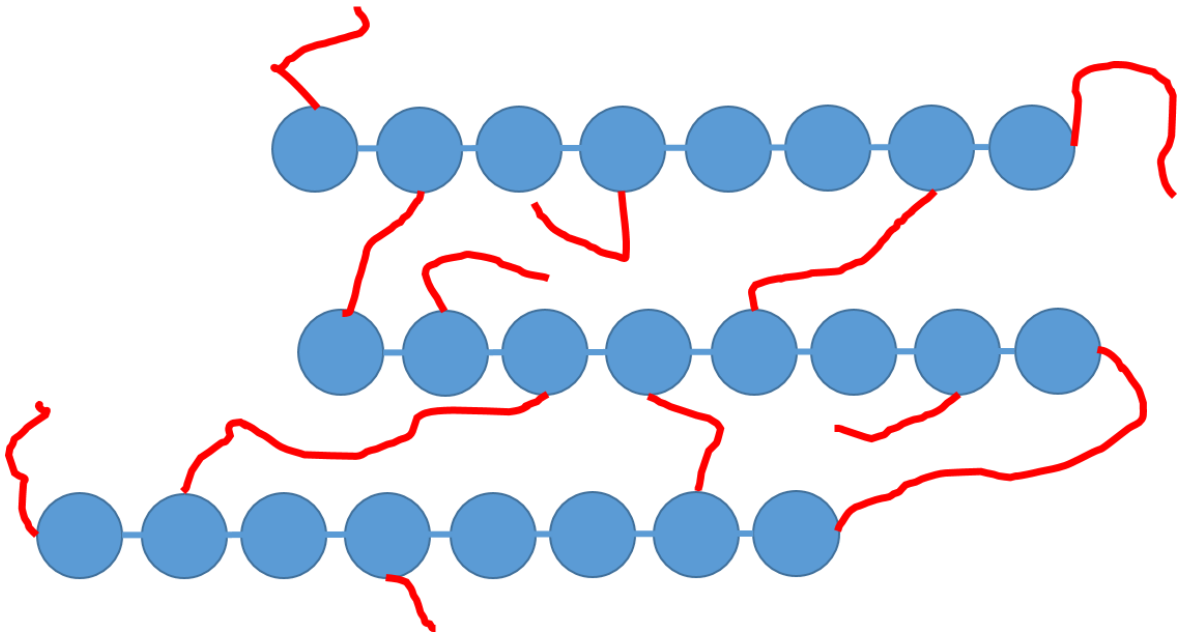


Figure 1.27: A cartoon representation of an elastomer, where the blue circles represent the monomers, the blue lines represent the bonding along the polymer backbone, and the red lines represent the flexible cross-linkages.

The above representation is of a typical elastomer. The connections between different chains are flexible cross-linkages. These linkages and their flexible nature lead to the connection between different polymer strands, which are allowed to move in relation to one another. This can allow for the deformation of the elastomer by compression, and more importantly in stretching, mimicking the properties of natural rubbers. There are five principal characteristics of elastomers:³⁷

1. Material exhibits the elastomeric state at temperatures above their glass temperature
2. Material is capable of rapid extension and contraction compared to other polymers
3. Material possesses high modulus strength when stretched
4. Material has little to no crystallinity
5. Large molar mass molecule, or ease of molecule to be cross-linked

One of the most important factors to consider for elastomers is the glass transition temperature (T_g). This characteristic property is the thermal boundary of a material, below this temperature the material behaves in a manner similar to that of a glass, whereas above this temperature the material becomes softer and more rubber-like, allowing for it to be more easily deformed, even stretched into wires or fibres (ductile behaviour). This state exists between T_g and T_m (the melting temperature).

The glass transition of an elastomer is generally below ambient temperatures, such as for natural rubber at 200 K, significantly below the standard ambient temperature (approximately 298 K for a standard room temperature of 25 °C). If the glass transition is exceeded (but not the melting

transition) before the polymer formation and cross-linking, the resultant product will potentially be an elastomer.

Rigid polymers and fibres resist deformation with high modulus and low elongations. For elastomers, deformation is generally readily achieved with minimal applied stress, this being the exhibition of elasticity.³⁸

1.5.5.2: Networks

A network polymer is a large architecture that, rather than forming into an array of linear chains through polymerization, formed a singular macromolecule. Since this exists as a singular molecular entity, there is no polydispersity to be considered.³⁹

The significant difference between an elastomer and a network is that the cross-linkage between the chains within an elastomer are constructed from the same or similar units as the main chains. Network polymers can be found in compensation and retardation films in display devices.⁴⁰

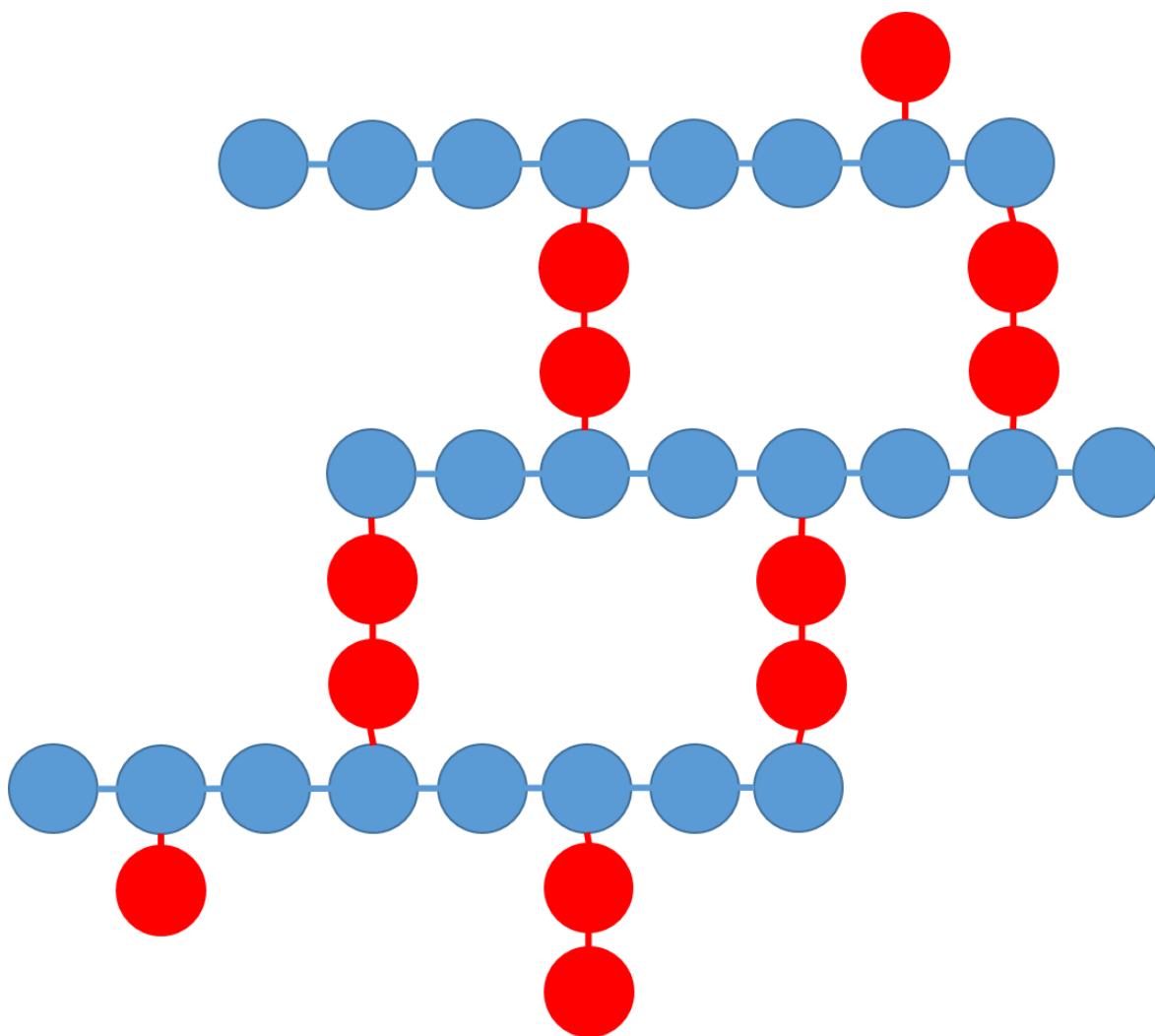


Figure 1.28: A cartoon representation of a network polymer. The red cross-linkers may be composed of the same monomers as the blue backbone.

These connections between the different chains are more robust than those seen in elastomers, creating a variation in bulk physical properties. The cross-linkers may or may not be composed of the same entities found in the backbones (i.e. the red groups may or may not be identical in nature to the blue groups).

Networks exhibit greater rigidity than elastomers, yet abide by a similar principle of cross-linked polymer chains. It is, however, the nature of this cross-linking that generates the difference between the systems.

1.5.6: Co-Polymer Systems

There are numerous different ways in which co-polymers may be formed, even from binary component systems. These include statistical, alternating, block and graft co-polymers, which can be composed of two or more different monomers in combination. The synthesis of these can be different for the different categories, and the properties of each can differ greatly due to the different architectures, as well as the different properties of the monomers themselves.

1.5.6.1: Statistical Co-Polymers

The formation of this class of co-polymer (shown in Figure 1.29) is random in nature, forming a disorganised series of components along the polymer backbone. The properties of the polymer are variable depending on the nature of the monomers, as well as how the polymer is formed randomly.⁴¹



Figure 1.29: A cartoon representation of a statistical co-polymer with a random distribution of the different incorporated groups.

This class of co-polymer is formed *via* the polymerisation of a mixture of both the red and blue monomers, which must be miscible for this to occur. The pattern of the red and blue constituent monomers in the resultant polymer is not predetermined, and will not be repeated throughout the chain. There is no discrimination between the reactivities of the polymerisable groups, which enables the production of the statistical co-polymer rather than a block co-polymer.

1.5.6.2: Alternating Co-Polymers

This form of co-polymer features a repeating A-B-A-B pattern, with an alternation of the constituent monomers throughout the chain. The properties of the polymer are determined by the nature of the monomer units.⁴²

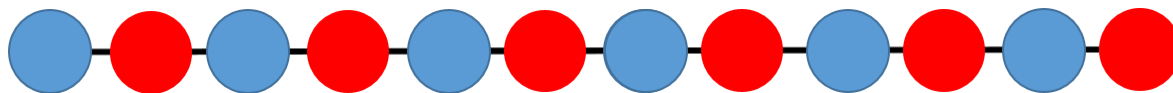


Figure 1.30: A cartoon representation of an alternating co-polymer showing the AB-repeating pattern of components through the polymer backbone.

The alternating blue-red pattern is consistent throughout the polymer, and is formed from an equimolar mixture of the different monomers. The pattern can be formed through the continued addition of monomers, or through the compatibility of the reactive groups that react to form between each monomer along the length of the backbone. This would be the case if, for example, the red monomer was a diol-based compound, and the blue monomer being an equivalent di-acid compound, leading to ester formation only between red and blue, rather than between red and red or blue and blue.

1.5.6.3: Block Co-Polymers

Block co-polymers are formations of clusters of a type of monomer within the backbone, or, in some cases, one end of the polymer being one monomer joined together, with the other end being composed of another monomer.⁴³

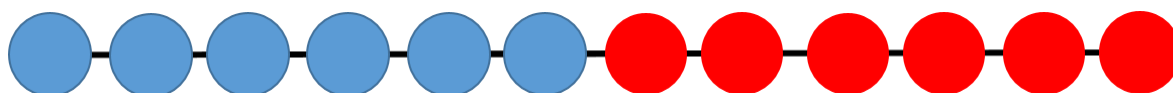


Figure 1.31: A cartoon representation of a block co-polymer showing the separation of the different monomers when they are incorporated into the polymer backbone.

The above figure represents a simple block co-polymer system, yet as previously stated, this may possess more than two component monomers, and may also feature another chain of blue monomers attached the other side of the red chain.

The properties of block co-polymers can be interesting, with the behaviours of the red and blue monomers differing greatly. For an example, the blue monomers may be hydrophilic, with the red monomers being hydrophobic. This means that a block co-polymer can form an amphiphilic layer similar to that observed in the membrane of a cell, with the hydrophilic end of the chain interacting with the aqueous environment, and the hydrophobic end of the chain interacting with an organic environment. It is possible to create micellar structures, such as for drug encapsulation, with customised hydrophilic and hydrophobic groups that can have optimised properties for the environments they are designed to operate in. Depending on the ratio of one of the blocks to the other different self-organised structures can be observed through microphase segregation. The structures observed thermotropically are analogous to those formed in oil/water systems where different ratios of solvent drive the self-organisation by inducing different curvature into the system to minimise the hydrophobic/hydrophilic interactions.

The following assumes that the polymer is a block copolymer with equal proportions of hydrophobic and hydrophilic units. The different structures that are observed are dictated by the ratio of aqueous to organic solvent and the curvature that is induced to minimise contact of the unit that dislikes the majority solvent. An equal ratio of solvent (i.e. 50:50) results in a balanced environment with no curvature of the polymer layer, and a lamellar (layered) environment, with each solvent encapsulated like a sandwich between the layers of polymer (Figure 1.32).⁴⁴

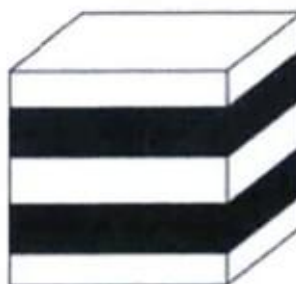


Figure 1.32: A representation of a lamellar structure formed in a mixed solvent system.

When a solvent is in a small majority over the other (e.g. 60:40), a bicontinuous cubic (sometimes gyroidal) phase may form, which allows for channels of a certain solvent within larger frameworks, with the two solvents kept separate in different channels, see Figure 1.33 showing the normal and inverse structures for the bicontinuous cubic phase.⁴⁴

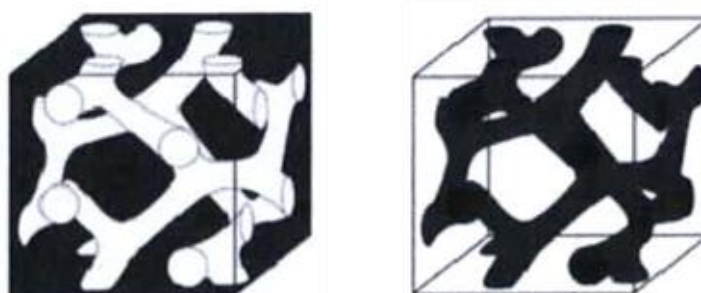


Figure 1.33: A simple representation of bicontinuous cubic phases in different solvent environments.

With an increase in the ratio of the solvents (e.g. 70:30), a columnar phase can be formed, with increased curvature compared to the bicontinuous cubic phase, leading to essentially a network of pipes through the more prevalent environment, see Figure 1.34.⁴⁴



Figure 1.34: A representation of columnar phases in different solvent environments.

At greater ratios (75:25 and beyond), a micellar cubic arrangement will form, wherein the minority solvent is encapsulated within micelles which are suspended within the majority solvent, see Figure 1.35.⁴⁴

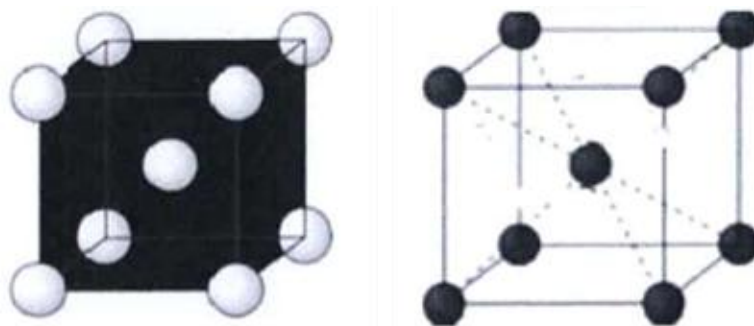


Figure 1.35: A representation of the cubic micellar structure in different solvent environments.

1.5.6.4: Graft Co-Polymers

Similar to block co-polymers, graft co-polymers can possess distinct regions within the bulk frame. However, in graft co-polymers, the template includes not just the potential for a mixed component backbone, but also for a variety of peripheral chains that are attached to the main backbone via subsequent reactions.⁴⁵

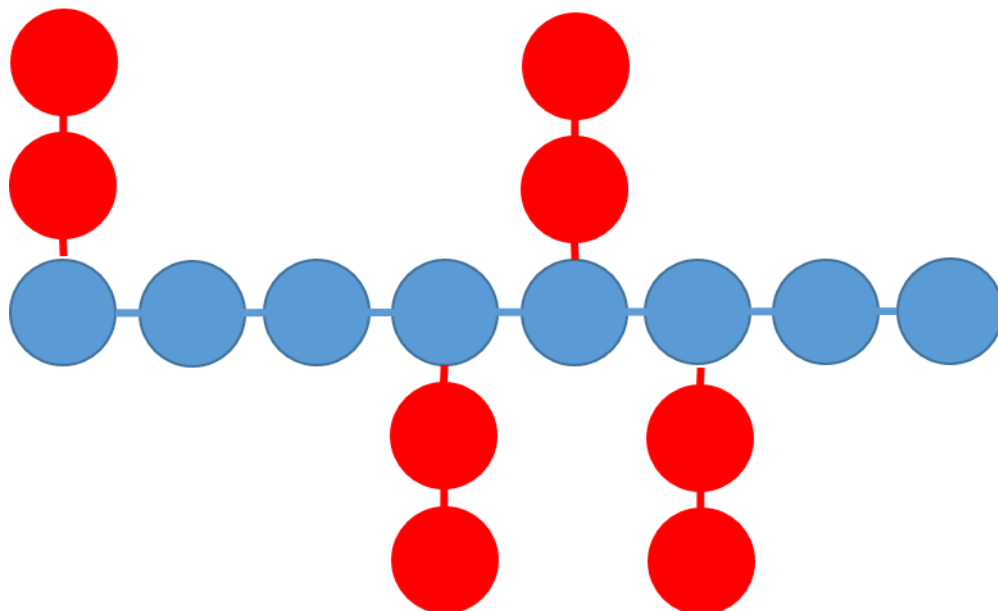


Figure 1.36: A cartoon representation of a graft co-polymer, showing the different groups in red grafted to the polymer backbone.

Figure 1.36 (above) shows the structure of a simple graft co-polymer, with red chains grafted to the main blue backbone. However, it is possible to attach different chains along the length of the backbone, as well as composing the backbone of more than one monomer, such as forming it in the style of any of the previously mentioned co-polymers (statistical, alternating and block).

As shown previously for the block co-polymers, it is possible to mix different varieties of behaviours within the bulk polymer dependent upon the natures of the monomers. If the grafted chains differed from one another, they would behave in different fashions from one another, preventing the alignment of them along the same side of the chain. This could also lead to different solvent properties of the polymer. For example, if the backbone has varied interactions with solvents, but is assumed to be neutral, the different grafted chains will align on different sides of the polymer, as shown in Figure 1.37 below.

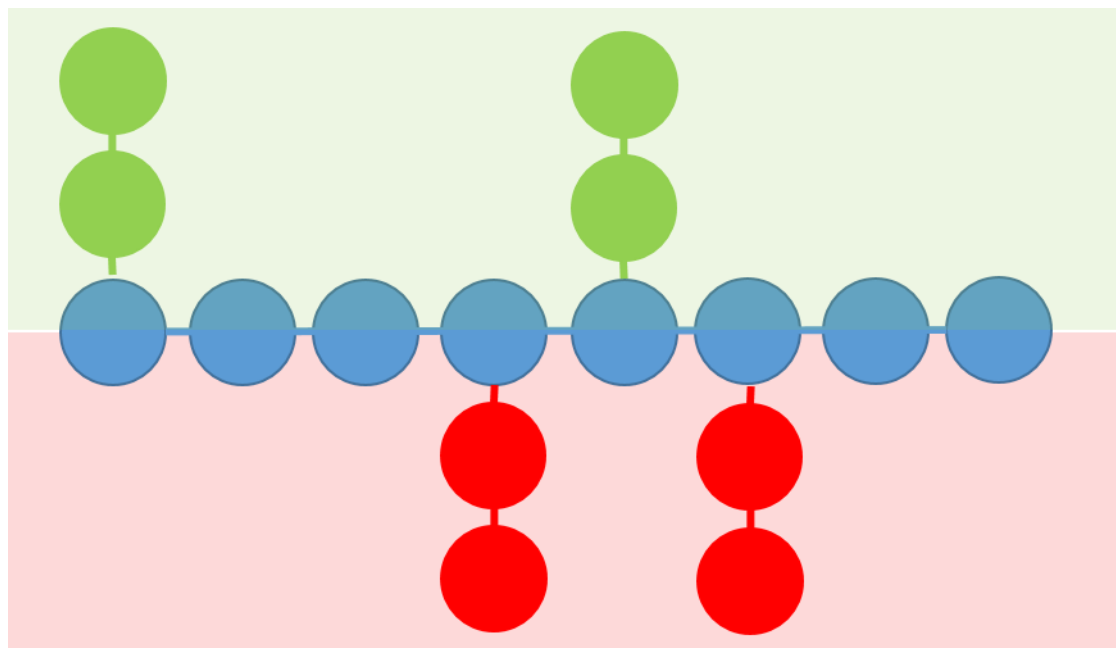


Figure 1.37: A cartoon representation of a graft co-polymer, with lateral chains associated with their preferred solvent environments.

In the above image, the half the red groups have been replaced with green graft chains, which have different solvent miscibilities than the red chains. When exposed to different solvent environments, the chains align on alternating sides of the molecule to allow like with like matching. This, however, can only readily occur should the bonds along the polymer backbone allow for rotation, or if the grafted chains allow for flexibility and bending of the polymer to allow alignment with the solvents.

1.5.7: Polymerizable End Groups

In order to make polymeric liquid crystals, the monomers possessing a polymerizable functional group, which could potentially be of a variety of groups, must be used. Simple units such as an alkene can allow for polymerisation, such as in polystyrene (discussed previously) from the monomer styrene. However, other unsaturated units can offer greater control of behaviours, such as increased or decreased polymerisation rates. These more complex monomers also allow the means of polymerisation (thermal, UV) to be varied, depending on their structure. The polymerisable group must be compatible with the rest of the molecule to prevent side reactions or degradation. It may also influence the overall mesogenic properties of the compound, both in its monomeric and polymeric forms. Furthermore, the size of all the functional groups will influence the allowable proximity of the molecules to one another, and so will affect the formation of liquid crystalline phases, potentially stabilising or destabilising them. In the monomeric form, the size of the polymerizable group in relation to the mesogenic motif will affect the packing of the molecules, potentially altering phase behaviour.

1.5.7.1: Acrylates

Acrylates (their generic structure is shown in Figure 1.38 where R is an organic group) are a well-tested, well understood functional group for use in UV polymerisations.⁴⁶

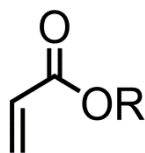


Figure 1.38: Structure of a generic acrylate polymerisable unit.

Mesogenic compounds incorporating acrylates have been studied by Broer *et al*,⁴⁷ among others, with both mono- and di-functionalised compounds being investigated. Many of the monomers investigated exhibit smectic C and nematic phases. A typical example is the mono-acrylate compound 4-biphenyl-4-(6-acryloxyhexyloxy)benzoate (Figure 1.39).

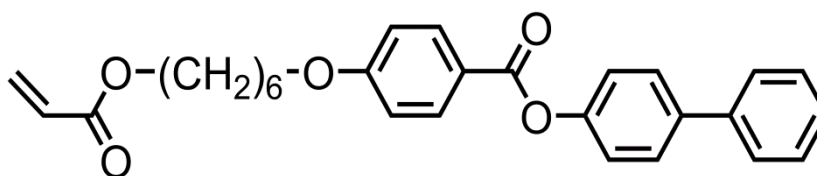


Figure 1.39: Structure of 4-Biphenyl-4-(6-acryloxyhexyloxy)benzoate

Cr 70°C SmC 80°C N 95°C Iso.

Investigations into polymerisation in the different phases for 4-biphenyl-4-(6-acryloxyhexyloxy)benzoate showed different polymerisation rates dependent upon the phase type in which polymerisation was achieved; with significantly faster rates observed between 70 and 95 °C (where mesogenic behaviour was observed).⁴⁷ However, the reported exotherms obtained from UV-DSC studies suggested a greater degree of conversion at the higher temperatures above the clearing point at around 100 °C. This was due to the greater fluidity in the system.

In the case of a difunctionalised compound studied (1,4-phenylene bis{4-[6-(acryloyloxy)hexyloxy]benzoate}) (Figure 1.40),⁴⁸ the results obtained were rather different compared to the mono-acrylate compound (Figure 1.39). Both greater rate and greater conversion were observed when the difunctionalised acrylate was polymerised below the clearing point. Further research considered the order change observed upon polymerisation. It was discovered that, despite a decrease in order parameter (0.7 to 0.6), it was still possible to have highly ordered systems with polymerisation close to a phase transition, with more ordered systems originating at the transition from the smectic C phase than from the nematic phase. Through optical microscopy, it was determined that cross-linking in the polymer network lead to retention of orientation at high temperatures.

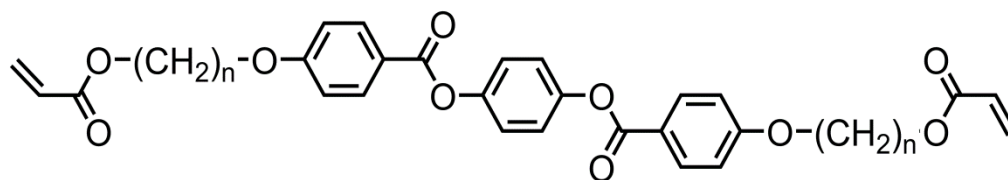


Figure 1.40: Generic structure of diacrylate mesogens synthesised by Broer.

n	Cr		Smectic C		Nematic		Isotropic
4	•	107	•	-	-	165	•
5	•	92	•	-	-	170	•
6	•	108	(•	86)	•	155	•
7	•	83	•	93	•	158	•
8	•	82	•	108	•	149	•
9	•	101	•	109	•	148	•
10	•	87	•	112	•	137	•
11	•	87	•	118	•	138	•

Table 1.1: Transition temperatures (°C) for diacrylate mesogens presented in Figure 1.40.

One situation that could be problematic with acrylate polymers is that of “in phase auto-polymerisation” for compounds with very high transition temperatures. Acrylates are prone to undergo thermal polymerisation, which can be very rapid and potentially very dangerous.

1.5.7.2: Epoxides

Another class of polymerisable compounds include epoxides, which have the general structure presented in Figure. The group is generally reactive due to the strained nature of the system that contains the oxygen bound by two weak single bonds.³⁷



Figure 1.41: The general structure of an epoxide, where R¹ and R² are organic groups.

Epoxides are generally used in thermosetting polymers, and can act as polymerisable materials as well as cross-linkers for network polymer systems.

The inclusion of epoxides in polymers can be either at the end of the polymer chains (structuroterminal) or within the chain (structuropendant). Epoxy resins utilise the structuroterminal epoxide as well as hydroxyl groups in structuropendant positions. An example of an epoxide polymerisation is the reaction of bisphenol A with epichlorohydrin,⁴⁹ where the epoxide can be found in both positions, as shown in Figure 1.42.

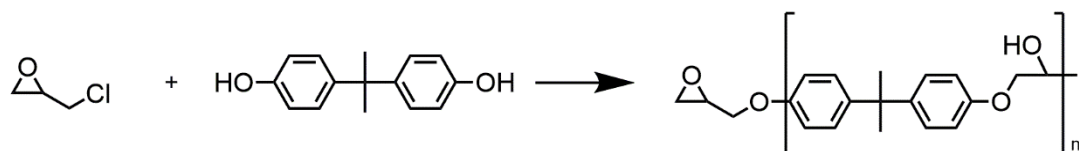


Figure 1.42: A reaction scheme for the reaction of epichlorohydrin with bisphenol A.

The structuroterminal epoxide group can further react to form cross-linkages with another cross-linking agent, such as aliphatic amines to form intractable network structures at low costs and ambient temperatures (see Figure 1.43).³⁷

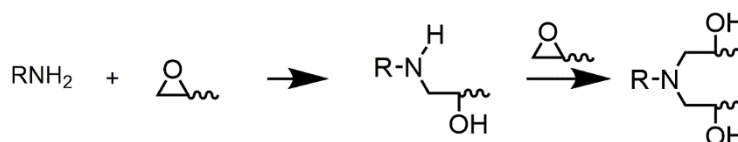


Figure 1.43: A reaction scheme for the reaction of an epoxide terminated polymer with an amine based cross-linker.

1.5.7.3: Diallylamines

Diallylamines and their derivatives were initially studied by Butler *et. al.* in the late 1940s (see Figure 20 for the generic structures).^{20,50,51} They are a less studied functional unit than acrylates, but are still useful in polymerisations.

With an additional region of unsaturation in the monomer, behaviour in polymerisations will obviously be different from mono-unsaturated functional groups such as acrylates.^{20,50,51} Diallylamine containing units have been seen to exhibit lower melting and clearing points than their analogues that possess terminal acrylate or methacrylate units. In terms of polymerisation, it was seen that the mechanism involved intramolecular cyclisations to form a linear, yet rigid, polymer backbone.

Initial studies in this are from Butler *et.al.* concerned free radical polymerisation of quaternary diallylammonium salts in solution.²⁰ Cyclisation along the polymer backbone (Figures 1.44 and 1.45 show the mechanisms proposed for this cyclisation polymerisation) formed predominantly 5-membered rings, with 6- and 7-membered rings being less favoured.⁵² It transpired that the 5-membered rings were preferred as the mechanism required to produce these allowed greater orbital overlap, thus facilitating a more rapid reaction. This orbital overlap outweighed the stability of a 6-membered ring in the product.

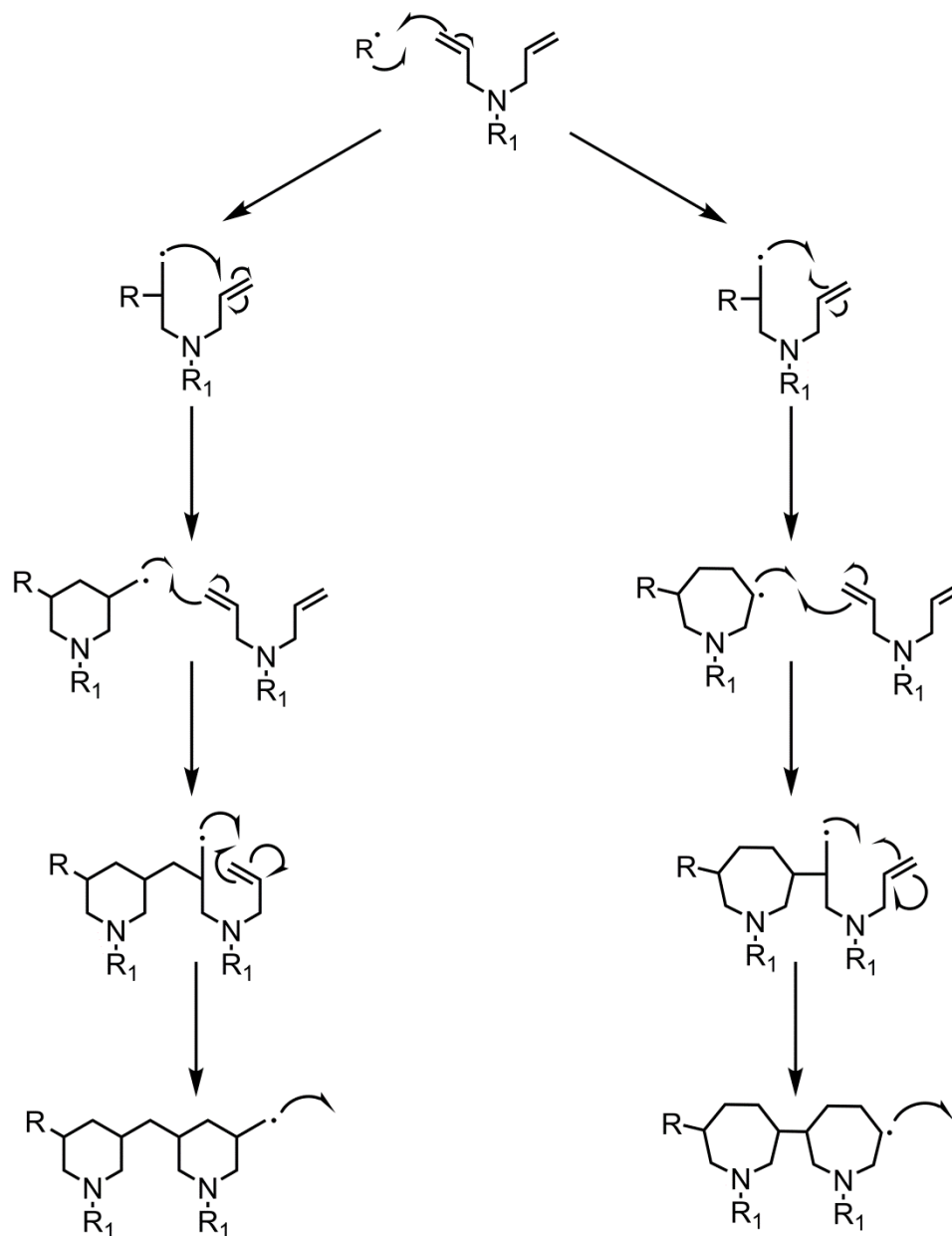


Figure 1.44: Radical polymerisation of a diallylamino-functional unit to form 6 and 7 membered rings where R is a radical initiator and R_1 is an attached organic unit.

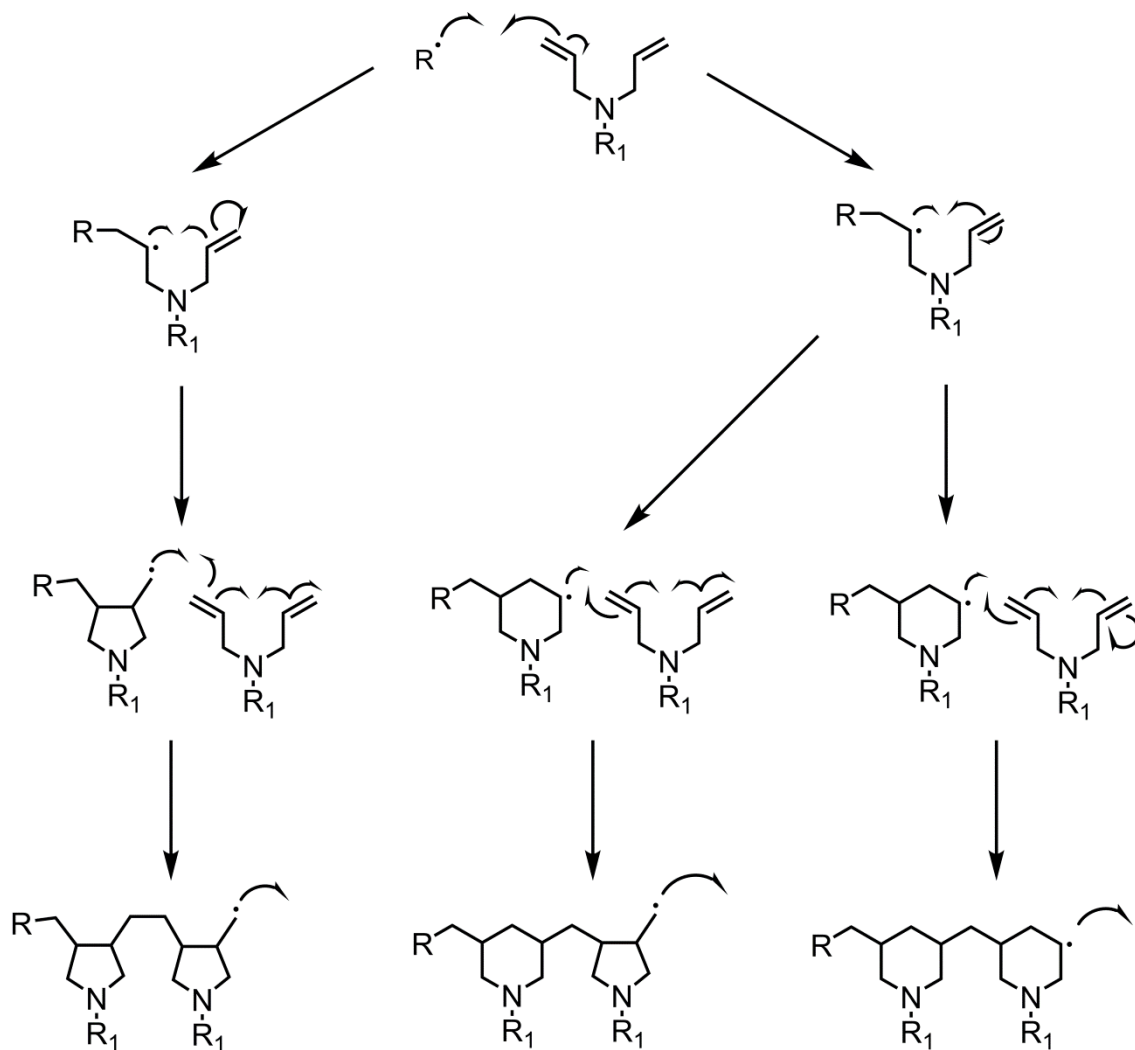


Figure 1.45: Radical polymerisation of a diallylamino-functional unit to form 5 and 6 membered rings where R is a radical initiator and R_1 is an attached organic unit.

The formation of the 5-membered ring occurs in preference to the 6-membered ring due to the nature of the radical.⁵² The secondary radical formed in the formation of the 6-membered ring could be seen as more favourable due to greater stability due to greater levels of inductive effects to the radical site, yet the greater stability reduces the rate at which it will react. Within the system, the reactive group that interacts with the radical is held in close proximity, being a constituent of the same terminal group in the same molecule. The normally disfavoured primary radical is less stable and will react faster and more readily than the secondary radical. Due to the combination of close proximity of the reactive groups to one another with the relative instability of the radical, the 5-membered ring is formed in preference through a kinetic favourability. It is also worth considering the effects of the R-group associated with the nitrogen within the diallylamino-functional unit, as the electronic effects of this group will no doubt have some influence over the formation of the radicals in the initiation of this reaction.⁵³

1.5.7.4: Differing Diallylamine-derived Units

Three possible derivatives that could be considered are diallylamines themselves, as well as the related quaternary salts, and also the diallylamides (structures displayed in Figure 1.46). Their differing electronic character has a significant impact upon their polymerisable behaviours, and indeed this was seen with initial studies conducted by Hall *et al.*⁵³ Hall found that the difference in polymerisation rates observed was due to the electron donating properties of the diene groups. The diallylamine functional group (Figure 1.46(a)) possesses a nitrogen atom, which donates electron density into the diene group. This destabilises the radical formation and disfavours the radical reaction pathway. The diallylamide (Figure 1.46(b)) possesses a carbonyl group, which allows mesomeric withdrawal of electrons from the reactive diene units that increases the radical stability to a small extent. However, in the case of the quaternary salt (Figure 20(c)), the nitrogen has a formal positive charge due to the acceptance of a proton from the acid, which further withdraws electrons from the diene. As a result, radical formation from the quaternary salt is more favoured in comparison to the situation with the diallylamide.

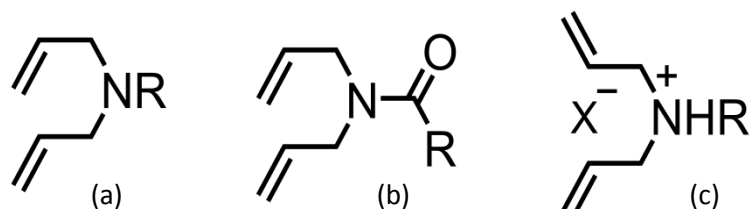


Figure 1.46: Generic structures of (a) a diallylamino-functional group, (b) a diallylamide and (c) a quaternary diallylammonium salt.

Unlike the previously mentioned acrylates, these compounds are less intensively studied, but initial research shows that they are similarly useful in terms of polymerisation. Diallylamines are cost effective compared to acrylates, and the diallylammonium salts allow for some interesting physical properties. For example, the use of a salt-based backbone could allow for conductivity by free movement of the counter-ion along the backbone, with conductivity potentially being tuneable through the nature of the counter-ion and its interaction with the ammonium-based cation, dependent upon the electrostatic attractions and the sterical hindrances upon mobility. Varying the counter-ion allows other physical properties such as hydrophobicity to be altered. The work of Hall *et al* has previously shown that copper sheets coated in polymerised quaternary diallylammonium salts corrode at vastly differing rates due to the nature of the counter-ion. For example, PF₆⁻ leads to hydrophobic behaviour and minimal corrosion of the copper plate.⁵³ Conversely, chloride counter-ions result in hydrophilic and porous behaviour, exposing the plate to moisture so that corrosion occurs at a rate similar to untreated copper.

Another area of interest in terms of the counter-ion selection is the use of polymerizable counter-ions, for example acrylates, which may co-polymerise with the diene-based backbone. This may

give rise to several interesting scenarios, such as free acrylates left un-polymerised, two different polymer backbones being formed, or even the acrylates being polymerised into the same chain. Further to the conductive potential, as well as the tuneable physical properties and cost effective nature of the quaternary diallylammonium salts, other positive factors include the formation of a strong polymer backbone, as well as the excellent adhesive properties and the low shrinkage volume observed.

1.6: Touchscreens

Touchscreen technologies belong to four predominant different categories: capacitive, resistive, infrared and surface acoustic wave.⁵⁴ These different technologies are summarized in the following sections. The main touchscreen of interest in recent years is the capacitive touchscreen, yet all are relevant in modern technologies.

1.6.1: Resistive Touchscreens

Resistive touchscreens are an attractive prospect due to their capability to work with almost any stylus, as they do not require electrical conductivity and capacitance for their operation.⁵⁵ They operate using two thin, transparent layers of resistive material that are held apart. One of the layers has a conductive layer of connections along the inner-facing side, and when the upper layer is pressed then the two layers make contact at a specific point, creating a pair of voltage dividers, meaning that the location of the touch can be read and then processed by software. Despite advantages such as low production costs and resistance to liquid contaminants (meaning that the technology is widely used in hospitals), the resistive touchscreens suffer due to poor contrast due to extra layers and the gap between layers. Further to this, the screens are likely to suffer damage from sharp materials.⁵⁶ The positional location of the touch input is determined via alternating voltage along the X and Y axes which produces the co-ordinates for the software to process the input. Resistive touchscreens can be divided into two primary areas: 4-wire and 5-wire.

1.6.1.1: 4-Wire Resistive Touchscreens

4-wire systems utilise both layers within a system, yet of the 4 wires, only 3 are utilised at any one time.^{54,55} The lower layer has an applied voltage along an axis which, when touched, probes the voltage from the upper layer, the voltage giving the position along the axis for generation of the X co-ordinate (see Figure 1.47). The process then flips to determine the Y co-ordinate, where the upper layer has the applied voltage which is read off by the lower layer. Due to the flexing of the upper layer, however, the lifetime of the ITO is reduced as it is also flexed, and may lead to cracking.⁵⁶ Damage to the ITO layer leads to irregularities in the resistive readings reducing the accuracy of detection.

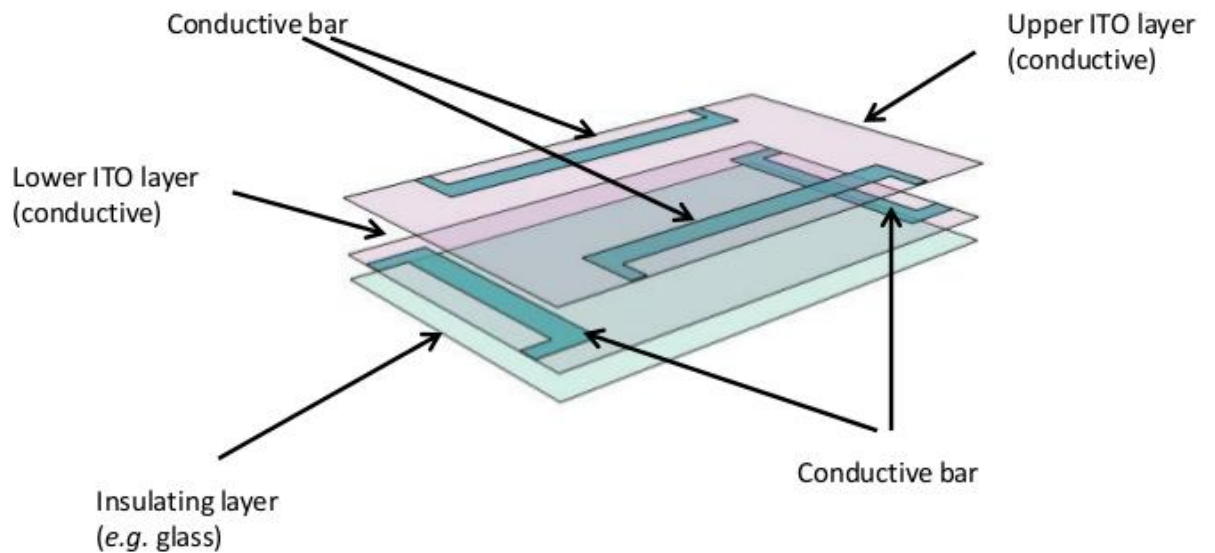


Figure 1.47: Co-ordination of four-wire touchscreen components.

1.6.1.2: 5-Wire Resistive Touchscreens

In a 5-wire system, 4 wires are connected to the corners (A, B, C and D) of the back layer, whereas the fifth is connected across the front layer to act as a voltage probe, as shown in Figure 1.48.^{54,55}

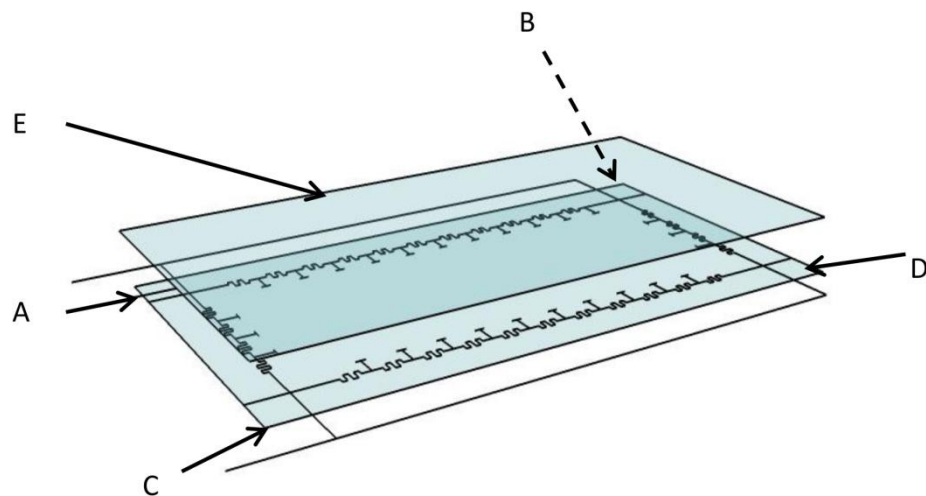


Figure 1.48: Co-ordination of wire connections on the back layer of a 5-wire resistive touchscreen, also showing the patterning applied to the lower ITO layer.

A voltage is applied to the wires connected to corners A and B, whereas C and D are grounded, allowing a flow of charge uniformly along the downward (Y) axis of the layer. When a pressure is applied to the front layer, the voltage at the point of contact is measured, so the Y co-ordinate is noted. The charge is then applied at A and C, with B and D grounded, so that the X co-ordinate is determined. In this system, the issue of cracks in ITO is reduced, as though they may still occur they will no longer cause non-linearity in measurements.

Between each of the corners, there is a pattern etched into the ITO to prevent the non-linear conduction of charge, normalising the voltage across the system.

Both systems of resistive touchscreens mentioned are based around the principle that the readable voltage between an applied voltage and a grounded region (across a potential difference) reduces regularly, and so with the known voltage reading acquired, it is thus easily possible to identify the position of touch.

1.6.2: Surface Acoustic Wave (SAW)

SAW technologies make use of ultrasonic waves passing over the touchscreen panel, the waves being partially absorbed at the point of touch. This change in the wave is registered, and is then passed on to the software. Similar to the issues faced with resistive screens, damage from sharp objects can be a major issue, yet unlike the resistive technologies there can be significant problems with surface contaminants, as these can also register as touches.⁵⁴

1.6.3: Infrared (IR)

Infrared touchscreens rely on an X-Y grid of IR LEDs and opposing detectors, allowing for the co-ordination of X and Y feedback to confirm the position of interaction. This form of touchscreen does not require full contact with the screen, and the 'stylus' used requires no special properties, allowing for universal usage, whether by finger, pen or any other device. The matrix of LEDs and detectors is placed in the frame above the screen, and therefore there is no extra requirement in the manufacture of the screen compared to regular displays, meaning that there is no major issue of damage to the system. A major drawback, however, is the possible false readings due to dirt on the display registering by blocking co-ordinated positions on the IR grid. Also, with no requirement for direct contact with the screen, haptic (sensory) feedback is negated. A further issue is that infrared radiation from external sources may cause interference with operation if detected, thereby providing a false negative in feedback.⁵⁴

1.6.4: Capacitive Touchscreens

Unlike resistive touchscreens, the 'stylus' must be a conductive medium, such as a finger, or more occasionally a specific glove or stylus. Capacitive touchscreens consist of an insulating layer such as a glass, which is coated in a transparent conductive layer, usually indium tin oxide (ITO,) yet this is becoming increasingly scarce and expensive and in some areas it is being replaced by new technologies. The capacitive layer can be included within the display, which allows a more direct interface between the user and the display. Changes in capacitance that occur at the point of contact between the display and stylus are detected by receptor circuits in the corners of the touchscreen. These relay data collected to controller software for processing.^{54,57}

1.6.4.1: Surface Capacitive Touchscreens

In this form of capacitive touchscreen, only one side of the insulating medium is treated with a conductive coating, and has a small voltage applied creating a uniform electrostatic field. When a finger touches the uncoated face of the surface, it creates a capacitor system, with the glass being the dielectric medium.⁵⁴ The location of touch is determined indirectly by noting the change in capacitance at the four receptors at the corners of the screen. Since the detection control relies only on the capacitance change and no deformation of parts, such as in the case of resistive touchscreens, these systems can be made very rigid and durable. Despite these advantages they may suffer from poor resolution and false signal generation.⁵⁷

1.6.4.2: Projected Capacitive Touchscreens

This category of touch screen, see Figure 1.49, has become increasingly common in recent years since the advent of 'smart' mobile telephones.⁵⁷ They provide better performance than their surface capacitance and resistive counterparts in terms of resolution, and retain the durability desired. The formation of the conductive system is by etching one or two layers of conductive material into an X-Y grid of electrodes. In the case of self-capacitance, individual electrodes are probed, rather than the intersections, leading to poor recognition of multiple touch points.⁵⁴ In a mutual-capacitance system, far better multiple contact recognition is achieved by patterning electrodes into two separated layers, scanning each intersection individually. The chief drawbacks of projected capacitive touchscreens concern their cost and their sensitivity. The materials required for their construction are expensive in comparison to resistive touchscreen counterparts, though their cost is dropping. Sensitivity is a key issue in terms of the change in capacitance that must be recorded, which is in the realm of femtofarads. Such sensitivity means that it is easily possible for interference to create false signals, or for a close proximity finger, which does not touch the screen, to register as making contact. This phenomenon, known as electromagnetic interference (EMI), has led to initial projected capacitive touchscreens being limited to far smaller screen sizes than their resistive counterparts, for example.

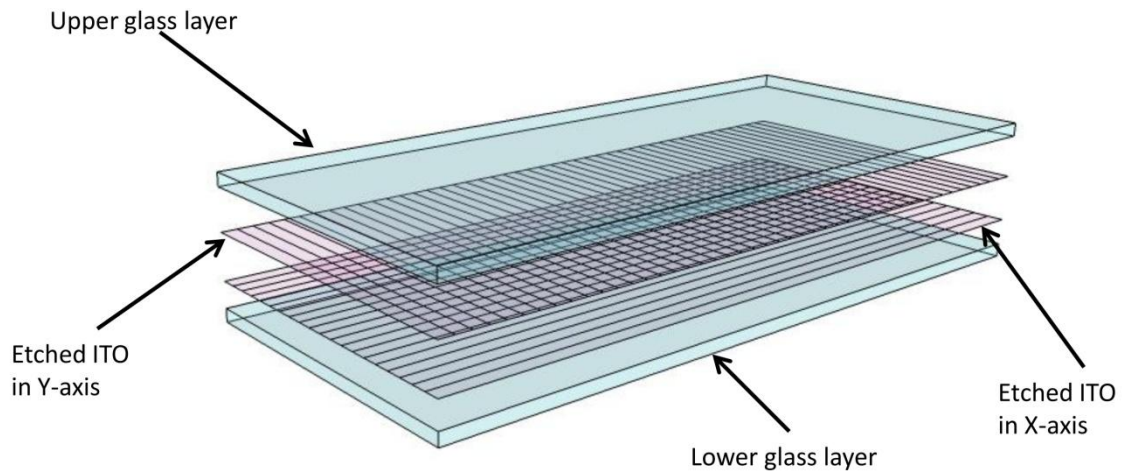


Figure 1.49: A schematic representation of a capacitive touchscreen. The etching on the ITO layers could be combined onto a single layer.

1.7: Smart Windows

Smart window technologies (Figure 1.50) focus on the ability to switch between transparent and opaque states, driven by an electric field. Current technologies rely on a polymer dispersed liquid crystal (PDLC) system, where if a field is applied to the window, then the PDLCs will align, allowing light to pass through the window. When the electric field is removed, the PDLCs return to an unaligned state, prompting scattering of light.^{58,59}

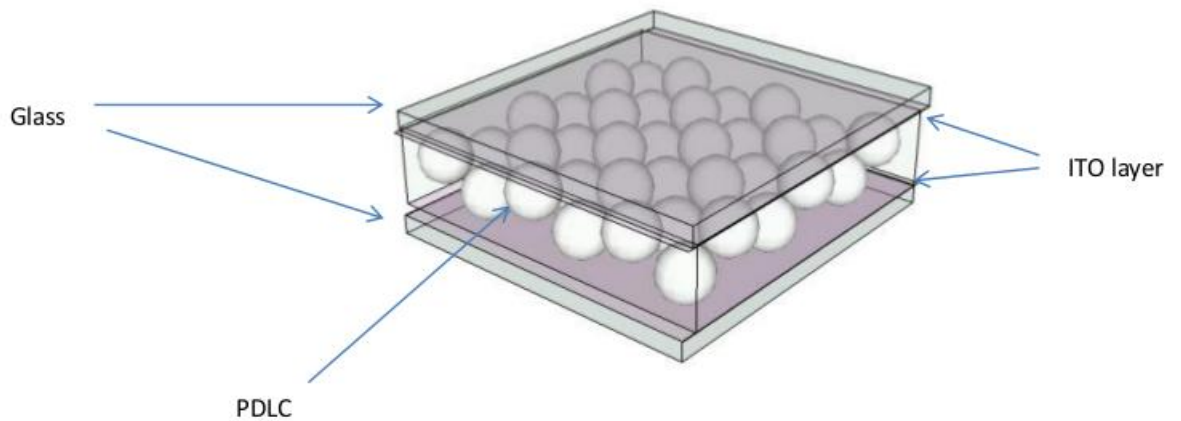


Figure 1.50: A generic structure of a smart window assembly.

Inside the glass of the window there is a thin transparent conductive layer usually composed of ITO, which is next to the cavity filled with PDLCs, allowing for the generation of the electric field. As previously stated, ITO is increasingly expensive due to the scarcity of the materials required to produce it, therefore more cost efficient technologies are desirable, including nano-soldered silver.⁶⁰ However, if it was possible to replace the overall system, wherein the liquid crystalline

material was also the conducting medium, this would be cheaper and would save energy and space. This would remove the need for many layers, and for the large electric field to be generated across the PDLC layer to be replaced by a smaller charge across the liquid crystalline polymer network. The PDLC technology requires the generation of an electric field between the encapsulating layers of ITO-coated glass, whereas a polymer or network replacement based on an ionic liquid crystal would allow direct transmission of the electric charge. This would be a more efficient approach as the charge would be in closer proximity to the mesogen, allowing a shorter range to be influence over, and thus a smaller electric field being required.

Figures 1.51 and 1.52 show the different states of a PDLC. Figure 1.51, showing the aligned director fields, generates a transmissive state which allows transmission of light (and infrared) through the smart window. However, if the electric field is changed, the direct fields are unaligned, Figure 1.52, which leads to scattering of incident light. Light will still pass through a smart window in the scattering state, yet will not allow clear vision of images either side. The scattering state causes a scattering of incident light, which can be reflected back out of the window, or through the cavity.

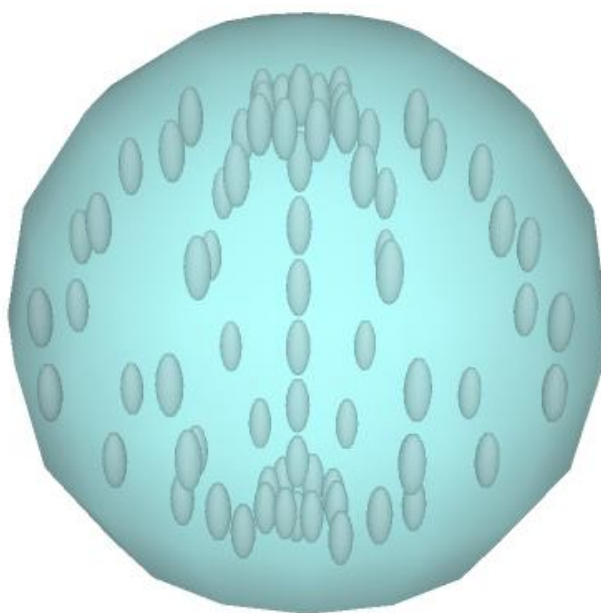


Figure 1.51: Transmissive state of an aligned PDLC showing the alignment of director fields.

Smart windows are currently used as projection screens, as well as skylights and regular windows. They facilitate light and heat regulation in offices, and are also used as privacy screens in some hospitals and hotels.^{61,62} Advantages over conventional curtains as privacy screens in hospitals include the comparative ease of cleaning and their durability. Advertising industries have also made use of smart window technologies in mobile displays, and automotive manufacturers, such as Ferrari, have begun using them in the production of car sunroofs.⁶²

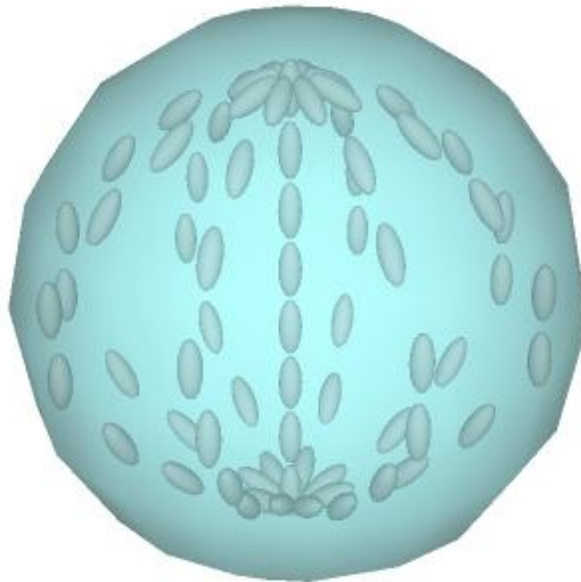


Figure 1.52: An unaligned, scattering PDLC showing the alignment of director fields.

1.8: Compensation Films

Compensation films aim to allow for better contrast and wider viewing angles in displays such as in laptop screens. Uncompensated screens tend to possess poor viewing angles or very poor colour contrast (or both) due to the varied path lengths through the liquid crystal components of the screen. Due to the different path lengths at the different angles, this can mean that the impact upon the transmitted light can be dramatic in certain areas, far more so than in others.^{63,64,65}

A phase shift for polarised light is determined by the path length of light through a birefringent material, as well as the degree of birefringence in relation to the wavelength of light. The retardation of the light is often expressed as a distance in nanometres or in terms of a fraction of the wavelength of light (which is often approximated to 550 nm).

Upon observation of a greyscale image, there will be an inversion in the shades observed after an increase in angle. Low luminescent areas will appear lighter in tone than high luminescent regions, causing an inversion in what is seen between dark and light. This phenomenon is caused by the liquid crystal retardation of the different grey levels with different viewing angle dependences.^{63,64,65}

Another situation arises due to the imperfection of cross-polarisers, which, when at an angle away from perpendicular (that is 0° , 90° , 180° , 270°), the effective angle between the polarisers is not 90° . At an angle such as 135° , light polarised by the lower polariser is not orthogonal to the upper polariser, and so will be able to pass through, remaining visible to an extent, and so light is seen at these angles when they should be in a dark state. It is possible to compensate this by using either

a combination of uniaxial plates (+C plate e.g. homeotropic liquid crystal, and A-plate e.g. planar liquid crystal)⁶³ or by using a biaxial compensation plate.

In order to properly compensate a display, the retardation must be addressed. With variation of angle, the degree of retardation changes, so for example the degree of retardation of the ordinary component may increase with the increasing angle. To counteract this, the compensation film must have an opposing effect, by retarding the extraordinary component to an equal degree, effectively cancelling the retardation and negating the phase shift. This is accomplished by using opposing birefringence, so using a negatively birefringent material as compensation for positively birefringent materials. The birefringence of the material does not need to be equal and opposite to effectively compensate because the phase shift is also dependent upon the distance travelled through the medium, so therefore if the birefringence of the compensator is greater than that of the liquid crystal medium, a thinner layer must be used.

If a birefringent material 1 μm thick (t) is taken as an example, see Figure 1.27, then viewing from a 45° angle (θ) would result in a path length (l_p) (Equation 1.11 and 1.11a) of:

$$l_p = t / \cos \theta \quad \text{Equation 1.11}$$

$$l_p = 1 / \cos 45 \quad \text{Equation 1.11a}$$

giving a path length of 1.41 μm . This means that the light has travelled an additional 0.41 μm through a birefringent medium, which will lead to a phase shift of the light. If the wavelength of light is assumed to be 550 nm as previously stated as an approximation then it is possible to calculate the difference in retardation between the viewing angles.

The number of wavelengths each wave of polarised light passes through a medium can be given by the following equations (Equation 1.12 and Equation 1.13):

$$m_e = d \times n_e / \lambda_0 \quad \text{Equation 1.12}$$

for the extraordinary component, where m_e is the number of wavelengths completed through the path length (d). The wavelength of the light is denoted by λ_0 and n_e is the refractive index of the extraordinary wave. In the case of the ordinary component, which is at 90° to the extraordinary component, the equation is:

$$m_o = d \times n_o / \lambda_0 \quad \text{Equation 1.13}$$

where m_o is the number of wavelengths completed by the ordinary wave and n_o is the corresponding refractive index. In the case of a birefringent material, n_e and n_o will differ, whereas the distance and wavelength will remain the same. This difference means that the number of

wavelengths completed will differ, causing a phase shift between the ordinary and extraordinary waves. By subtraction of m_o from m_e , the phase difference is given by Equation 1.14:

$$m_e - m_o = d \times \Delta n / \lambda_o \quad \text{Equation 1.14}$$

which gives the difference in number of wavelengths between the components of the waves. If the term for the wavelength is removed from the equation, then the outcome is the retardation. Using these equations, it is clear that a greater path length will lead to a greater retardation experienced by the light. Retardation affects the polarisation of light, where a half wavelength change leads to the polarisation being perpendicular to the original polarisation. If the birefringence is simply assumed to be 1, then the retardation will be 1.41 for the 45° angle, so there is a difference of 0.41, leading to 0.745 wavelengths greater phase shift. The phase shift of approximately $\frac{3}{4}$ of a wavelength will lead to the transmitted light being circularly polarized.

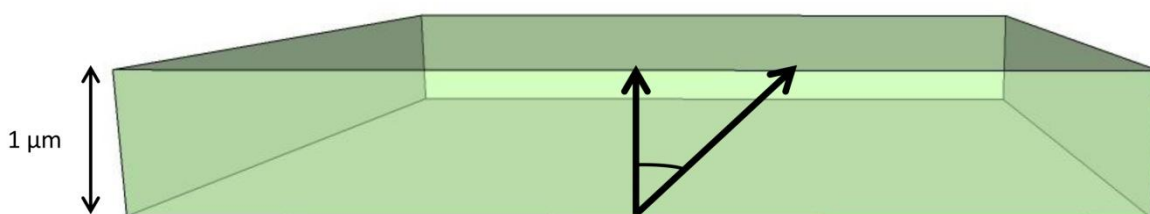


Figure 1.53: Light passing through a birefringent material with an angle (45°) between them.

In order to compensate for this change in polarisation, the opposite effects must be applied to the light. Taking a compensation layer with thickness $0.5 \mu\text{m}$ will lead to the light travelling $0.707 \mu\text{m}$, but if the birefringence of this material is -2 , that would mean that the phase shift difference between the light perpendicular to the material and the light at 45° would be -0.745 wavelengths, neutralising the effect of the initial material, see Figures 1.53 and 1.54.

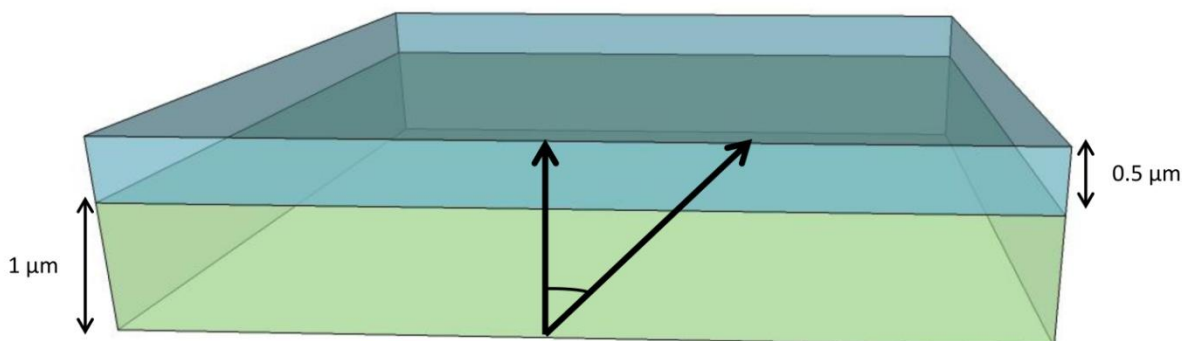


Figure 1.54: Light passing through a birefringent material (bottom) and through a birefringent compensation layer (top), with angle 45° .

The process of compensation can be accomplished by stretching polymers, polymerisation of liquid crystalline materials in an organised phase or the growth of birefringent crystals. The compensation of a device accounting for a variety of incident angles of light as well as considering the mechanism of the device itself leads to a complex issue. These complications are resolved using either a singular compensation film, or through combinations of compensation films. There are three significant components of compensation films, these being A-plates, C-plates and O-plates, defined by their symmetry.⁶⁶ Each of these plates exhibit uniaxial birefringence, but combinations of these can be used to create a film with biaxial character. Further to the symmetry consideration of these plates, there is also the nature of the birefringence that has to be accounted for. If the plate exhibits positive birefringence, it is considered positive, with the opposite being negative (exhibiting negative birefringence).

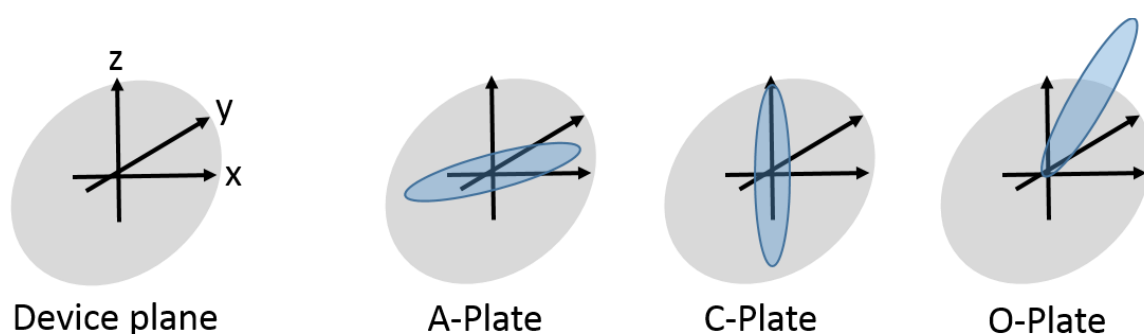


Figure 1.55: The orientation of the different plates used in compensation films, displaying the in-plane, out-of-plane and oblique retardance of the A-, C- and O-plates.

The above Figure (1.55)⁶⁶ shows the orientation of each type of plate. The A-plate has its extraordinary axis (n_e) parallel to the plane of the device, the C-plate has its n_e perpendicular to the plane of the device and the O-plate has its n_e oblique to the plane of the device.

Due to its orientation, the C-plate will have no impact on the normal incident rays, instead only impacting the off-axis rays. This influence on only the off-axis rays leads to their use in the compensation for out-of-plane retardance. Contrary to this, the A-plate is perpendicular to this and will compensate for in-plane retardance. In most devices, there will be a combination of plates, such as the combination of C- and O-plates in twisted nematic liquid crystal displays (TN-LCDs).⁶⁷ Another example is that of in plane switching (IPS) devices being compensated by two positive A-plates combined perpendicular to one another, contributing a similar bulk impact similar to that of a negative C-plate (a plate which is aligned as a C-plate but composed of a negative birefringence material).⁶⁸

The construction of a film from combined plates, such as that mentioned for IPS devices created from the combination of A-plates, can be formed from two perpendicular liquid crystal polymer layers. If the film is composed of ionic liquid crystal polymer layers, it could therefore be possible

to combine conductive layers in the manner of a grid for a touchscreen device (such as in Figure 1.49).

1.9: Films

Conductive liquid crystal polymer films need to be polymerised onto a substrate (usually an ITO treated piece of glass) which has been prepared to allow alignment for the liquid crystal. The process of alignment generally involves rubbing the substrate to create grooves along one direction in order to encourage the orientation of the molecules and hence the bulk material. This process allows the film to be aligned parallel to or perpendicular to the polarisers, as well as to form a more uniform arrangement to prevent formation of defects and different alignments within the medium.

The coating process is done in several ways, most commonly through spin coating or through use of rollers, which allow for a uniform spread and depth of the monomer on the substrate before polymerisation. This uniformity is highly important both in the final film formation as well as in the polymerisation process, as it allows more even polymerisation rates and no monomer remaining in the final system. A uniform depth is necessary in a film due to reasons comparable to those mentioned in the section on compensation films, where if there is a greater thickness in one area, the light passing through will have experienced a greater effective birefringence and will suffer a greater retardation and thus a difference in phase when compared to in other regions of the film, changing the appearance of what is transmitted.

1.9.1: Film Thickness

The thickness of the film is of paramount importance to its operation, as well as its synthesis. As mentioned previously, the film can be prepared using spin coating and the use of rollers.

For use in display screens or compensation films, a uniform thickness is required. If there is variation in the thickness, then light from a backlight will be differently affected at different points, leading to different levels of retardation of light, meaning the display will be affected. The outcome of this would be irregular displays, and the information broadcast by them would no longer be useful or readable.

In a similar fashion, different film thicknesses in compensation films would lead to similar problems. However, another issue is that the film thicknesses would have to be controlled overall, not just in uniformity. This means that the overall path of light would be known, allowing for the degree of retardation to be understood. This would be something that would need to be known in order to create a display screen, but the creation of a compensation layer would also depend on this.

Moving away from the optical effects of film thickness, for a conducting film, the resistance of the film would also be affected by the dimensions used. This is the same for wires, where the cross-sectional area of a wire has an impact on the conductivity of the overall wire. Defects in film thickness would lead to deviations in conductivity, and to unpredictable behaviour. This would be an even greater issue when using capacitive and resistive touchscreens. For capacitive screens, this would lead to different densities of charge in the screen leading to inaccurate readings of capacitance change and incorrect evaluation of the X and Y co-ordinates. A similar problem may arise with resistive screens.

One of the most important aspects of regular film thicknesses, however, is in their construction. This is of particular relevance for UV-polymerised screens as the external irradiation has to penetrate through, meaning that with different thicknesses, there will be different depths of penetration and different degrees of polymerisation within the film. This could lead to incomplete polymerisation, leaving pockets of monomer which will have negative structural impacts on the overall system.

1.10: Pixels

For displays, pixels are what transmit light through the liquid crystal layer. Pixels are composed of three sources of light (red, green and blue) that appear as white when all are viewed at maximum together. The layer of pixels is in the backlight behind the primary polariser, meaning polarised light of three colours reaches the liquid crystal layer. The orientation of the liquid crystals will then affect the light through their birefringence, meaning that, if the light is unaffected, then it will be extinguished by the upper polariser and that colour will not be seen. Light can be partially extinguished to create different colours through various combinations of the different colours at varying intensities.⁶⁹

1.11: Mixtures

When mixing different materials, the melting points can be dramatically altered. An obvious everyday situation is that of water and sodium chloride (salt). The melting points of both systems are dramatically different, with salt being much higher than water.⁷⁰ However, when these components are mixed in various ratios, the melting point of the combined system is significantly lowered, which is used in winters to clear ice as the melting point is lowered and this causes the ice to melt. A similar situation can be observed in the case of liquid crystals, where mixtures can be used to vary the phase transition temperatures and the phases observed.

Commercial liquid crystal mixtures are developed using the same principle as the mixing of salt and ice. Figure 1.56 shows a phase diagram based on the mixing of 5CB with 8OCB. In this phase there is a depression of the melting point upon mixing. The segment across the bottom of the

phase diagram is where solid 5CB and 8OCB are in equilibrium with each other. The two domains under the melting point curve represent points where either solid 5CB (segment on the left side of the phase diagram) or solid 8OCB (segment on the right side of the phase diagram) are in equilibrium with a nematic phase comprised of both 5CB and 8OCB. However, the nematic to isotropic phase transition behaves as an ideal liquid and a linear progression in this transition is seen from one side to the other in the phase diagram. The point at which the melting point reaches a minimum is the eutectic point where both solid 5CB and solid 8OCB are in equilibrium with the nematic phase comprised of both.⁷¹

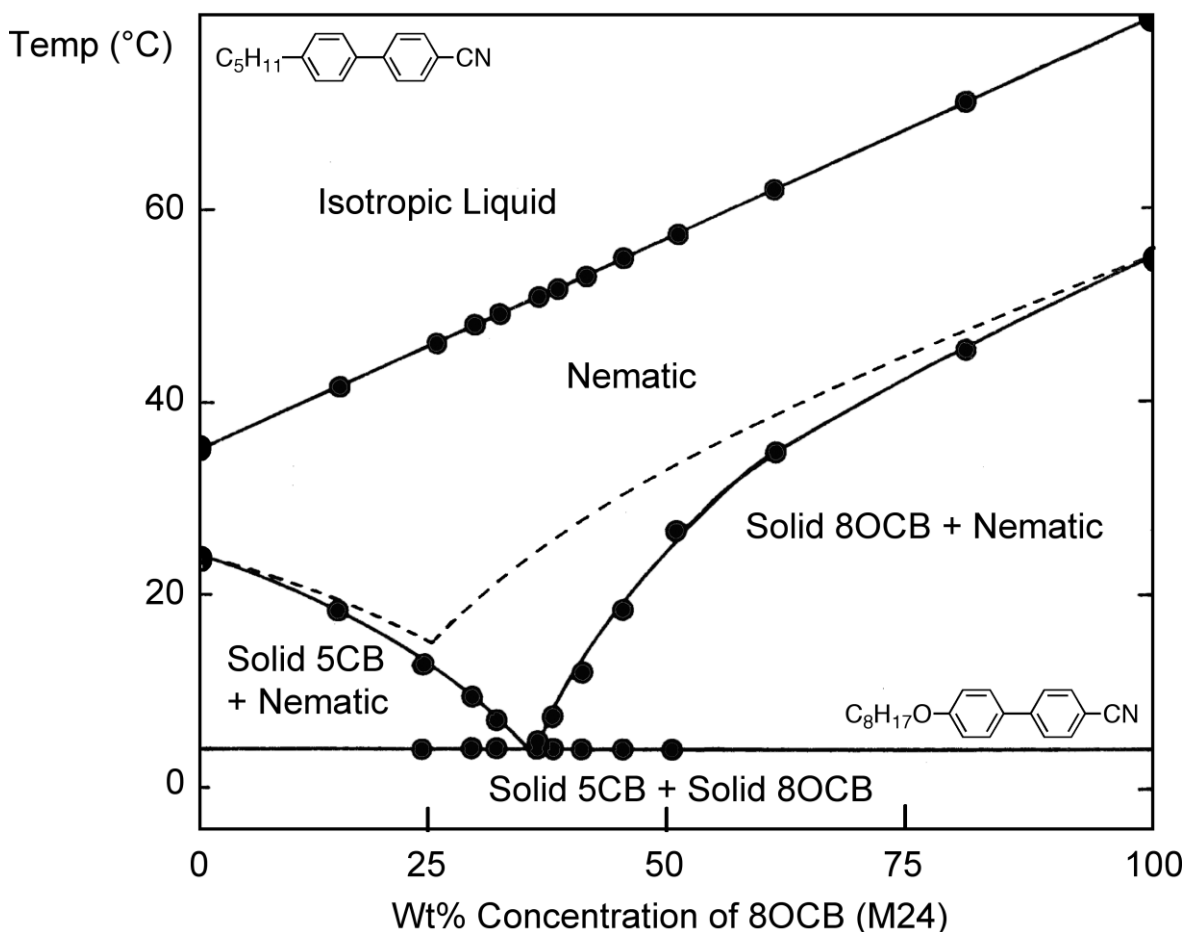


Figure 1.56: A phase diagram for the mixture of 5CB and 8OCB.

Liquid crystals are generally mixed together for use in displays to tailor properties such as viscosity, dielectric anisotropy, birefringence and elastic constants. In a similar manner, liquid crystal monomers are mixed together to tailor the properties of polymers for film applications. In these mixtures, additives such as cross-linkers may be added that are not liquid-crystalline themselves and it is important to understand the effect they will have on both physical properties and also phase transition temperatures. Further to this, chirality can be induced into the polymers through the addition of chiral dopants.

2: Aims

The aims of the project, on a general scale, are to synthesise compounds which would assist in the refinement of the technologies discussed in the introduction, those being smart windows, touch screens and compensation films.

In order to refine the targets of the compounds to be synthesised, it was necessary to look in detail at the requirements for these technologies.

2.1: An Overview of the Technologies

As stated, the technologies to be considered are smart windows, touch screens and compensation films. However, it is worth considering that the touch screen and compensation film technologies could be combined due to the construction of the touch screen device.

Each different technology will have some different specific requirements, yet will not have any conflicts with one another in terms of requirements, which will therefore not prevent the use of the same compounds across the different technologies.

2.2: Technological Requirements

Each of the different technologies considered has an array of requirements for operation. The different technologies will have similar requirements, and they could be considered on separate bases, but the objective was to design a material that could satisfy more than one need in the creation of designer films.

2.2.1: Smart Windows

Based on the operation of smart windows and what can be improved, a conductive liquid-crystalline polymer could be employed in the role to potentially increase efficiency of the device.

In order to suit the technology, a product would need to be a birefringent conductive polymer that can be formed into uniform thickness films. The polymer would need to possess a liquid-crystalline phase over a wide range, with a degree of order at low temperatures for winter and night time operation in exterior windows, yet at the same time will need to have a significantly higher transition temperature out of this phase due to the heat they will be exposed to in direct sunlight in summer operation.

The temperature ranges considered could allow for different compounds to be used in different environments, whether that is for deployment in different countries (the temperatures experienced in Iceland will differ dramatically from those experienced in Italy) or for the deployment between exterior and interior windows. The interior windows will only be exposed to a small temperature range, existing around an ambient temperature experienced within an office.

It is clear that the thermal behaviours for a compound would either have to include a very broad transition, or that a variety of analogous compounds could be used, each exhibiting different but comparable thermal transitions.

Another key aspect of the material would be that it would have to polymerise to form the film. This could be accomplished by the incorporation of a reactive functional group, such as an acrylate or diallylamine, the latter being used in this case. This is due to the desire for conductivity, which is another required property of the ultimate polymer film.

The conductivity is desired to allow for the more direct exposure of the motif to an electric charge without the generation of a strong electric field across a cavity, reducing the energy demands required to realign the medium and switch the window's state from scattering to transmissive.

In summary, the desired material(s) would be one, or a family, possessing a broad liquid-crystalline phase range at temperatures above and below standard ambient temperatures, as well as being readily polymerisable and incorporating ionic character to allow for electric conductivity.

2.2.2: Compensation Films

Compensation films require being made into uniform thin films, with birefringence being exhibited. In order to accomplish this, there are several demands to be made of the target compound.

In order to allow for the uniform thin film, the compound would have to incorporate a polymerisable group, such as the previously mentioned diallylamine group. A further consideration to be made is also that the monomer would preferably polymerise *via* a UV-initiated polymerisation. UV-polymerisation is desired to prevent the deformation of the monomer, as well as preventing thermal transitions and realignment, which could ruin the properties of the film.

Another consideration would be that the compound should exhibit a rather significant birefringence to allow for the construction of thinner films (which can still compensate the display medium), with the thinner films more easily UV-polymerised. This is due to the penetration of UV-irradiation through the substrate, with reduced penetration at greater depths within the substrate. Thermal polymerisation gives a more uniform polymerisation through thicker films, yet this is undesired as it may cause changes to the films structure during the polymerisation process.

The general requirements for compensation films are that they need to be birefringent thin films that are polymerisable producing a uniform thickness. This would necessitate the compound being liquid-crystalline in nature, allowing for alignment prior to the polymerisation. The compound would also need a functional group that also allows for compatibility with UV-polymerisation.

2.2.3: Touch Screens

In the case of touch screens, there are some additional criteria which need to be considered.

In the case of capacitive touch screens, the polymer film needs to exhibit anisotropic conductivity, along the direction of the polymer backbone. This is necessary for their operation in the X-Y grid system previously as previously described. It would also be desirable for the film to be fairly rigid and robust due to the continued application of force to the screen, because any permanent cracking or other deformation would render it no longer of use.

Further to this, the film is required to be a thin film to minimise the overall size of the display, with size efficiency being highly important for compact, portable devices. The film would also have to be uniform to prevent changes in the resistivity of the material as a conductor, with the bulk of the material having to retain high purity in order to prevent the interference of the conduction of charge across the medium.

If the target material were to be applied to a resistive touch screen, similar properties would be required, with the film needing to be mildly flexible to allow for the deformation of the upper screen to form a contact point on the lower screen. However, in the case of a 5-wire resistive touch screen, the upper screen would not necessarily require anisotropic conductivity. Similar to the capacitive example, the film would have to be a uniform thin thickness throughout, with a high degree of purity in order to maintain uniform conductivity.

2.3: Summary of Requirements

The compounds synthesised would, in all cases, need to readily polymerise into controlled films, exhibiting a high degree of purity, and the capability to polymerise to a significant extent and remain rigid.

For the examples of smart windows and touch screens, target materials would have to allow for conductivity, which also, though not needed, would not be “a negative” in the case of a compensation film.

Further to this, both the compensation films and smart windows would have to be made from birefringent materials. However, in the case of a touch screen, this could have a negative impact if the film were constructed in such a way that the mesogenic nature causes undesired corruption of the presented image. It is possible, however, to avoid this compensation, such as the choice of alignment of the birefringent material, as well as self-compensation of the films used (that is their birefringent effects would cancel one another out). Of more interest, though, is the combination of the touch screen films and the compensation films, meaning that each case would benefit from being birefringent.

Overall, the demands on a targeted material are that it is polymerisable, conductive, and liquid-crystalline, and which features stable liquid-crystalline phases over a broad range about the ambient temperatures experienced.

The figure below (Figure 2.1) shows the generic target structures for the requirements of the applications.

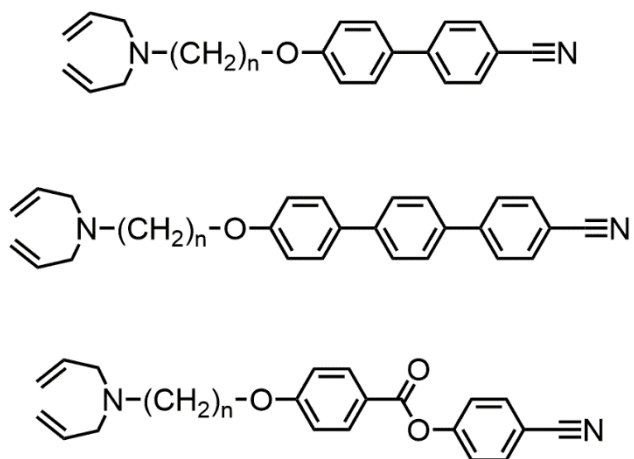


Figure 2.1: Generic structures for target compounds to be synthesised, where $n = 8-12$.

3: Experimental

3.1: General Techniques

3.1.1: Materials

All solvents used in syntheses were purchased from Fisher with the exception of anhydrous solvents, which were obtained from Sigma-Aldrich. All solvents were used without purification.

Reagent materials and catalysts were appropriated from Sigma-Aldrich, Tokyo Chemical Industries (Belgium), Apollo Scientific, Fisher and Alfa Aesar unless specifically stated. These were used without purification. N-(3-Dimethylaminopropyl)-N'-ethylcarbodiimide hydrochloride (EDAC) was purchased from CarboSynth, and was similarly used without purification.

3.1.2: Thin Layer and Column Chromatography

Thin layer chromatography (TLC), where appropriate, was used to follow the progress of reactions, as well as to assess solvent suitability for use in separations via column chromatography. TLC plates, silica coated aluminium (Kieselgel 60 F-254), were purchased from Merck, and visualised using ultraviolet light (254nm or 365nm wavelength from a UVGL-58 Handheld UV Lamp supplied by UVP), or alternatively oxidised using potassium permanganate solution in the case of non-UV active compounds present in the reaction mixture, the stain being applied, and then the plate being heated to visualise the products.

Column chromatography, used for separations, was conducted using flash grade silica gel (Fluka, 70-230 mesh, 63-200µm particle size), with increased flow facilitated by vacuum flash techniques. Prior to each separation, suitability of solvent was determined using comparisons *via* TLC.

3.1.3: Nuclear Magnetic Resonance Spectroscopy (NMR)

¹H and ¹³C NMRs were recorded on a JEOL ECX or ECS spectrometer at 400 MHz (¹H) and 100.5 MHz (¹³C), processed using JEOL Delta NMR Processing and Control Software. Chemical shifts are quoted in ppm, with the residual protic solvent used as a reference standard, for which the chemical shifts were defined. Multiplicities of peaks were described using the following abbreviations:

s – singlet	dd – doublet of doublets
d – doublet	ddd – doublet of doublet of doublets
t – triplet	dt – doublet of triplets
quart – quartet	tt – triplet of triplets
quint – quintet	ttt – triple, triple triplet
sex – sextet	m – multiplet
sept – septet	

3.1.4: Mass Spectrometry

Analysis by mass spectrometry was conducted using electrospray ionisation (ESI) unless otherwise stated. For this ionisation, a Bruker microTOF MS-Agilent series 1200LC spectrometer was used for the analysis.

3.1.5: Polarised Optical Microscopy

For observation by polarized-light transmission microscopy, a Zeiss Axioskop 40 Pol microscope was used (x100 magnification), see Figure 3.1, using a Mettler FP82HT furnace, controlled by a Mettler FP90 control unit. Images were recorded using an Infinity X-21 digital camera attached to the unit.

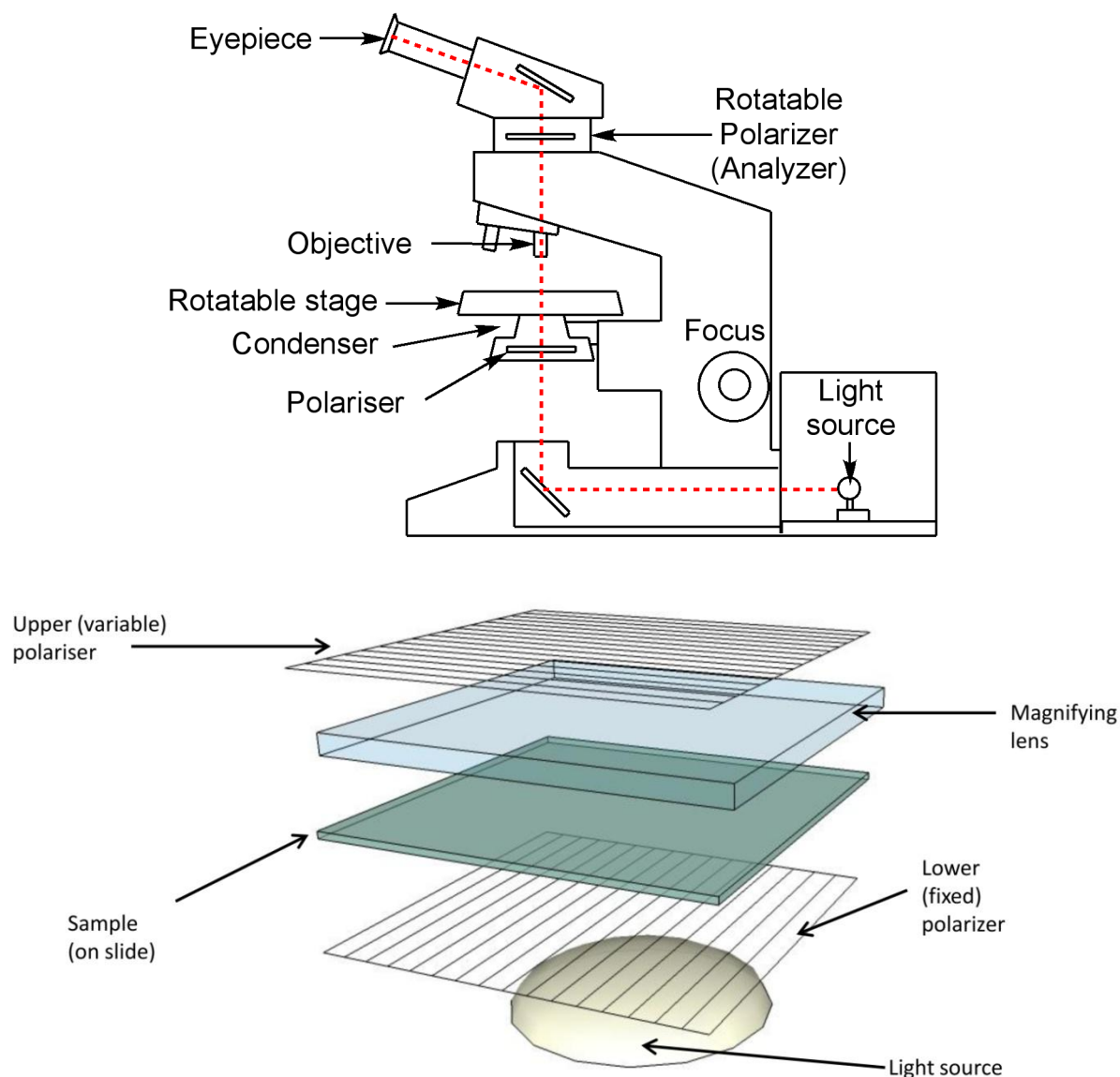


Figure 3.1: A simplified schematic of a polarising optical microscope (top). The slide may be present (lower blow-up) in a heating or cooling stage.

3.1.6: Ultra-Violet Differential Scanning Calorimetry (UV-DSC)

UV-DSC studies⁷² were conducted under an atmosphere of nitrogen, with temperature regulated to specified temperatures. The UV-DSC instrument used (see Figure 3.2) was a Mettler Toledo

DSC822° with a Hamamatsu Lightningcure LC5 UV light source connected *via* fibre-optic cables. The data was processed using Star^e Software. Results were standardised using an empty pan in the reference position.

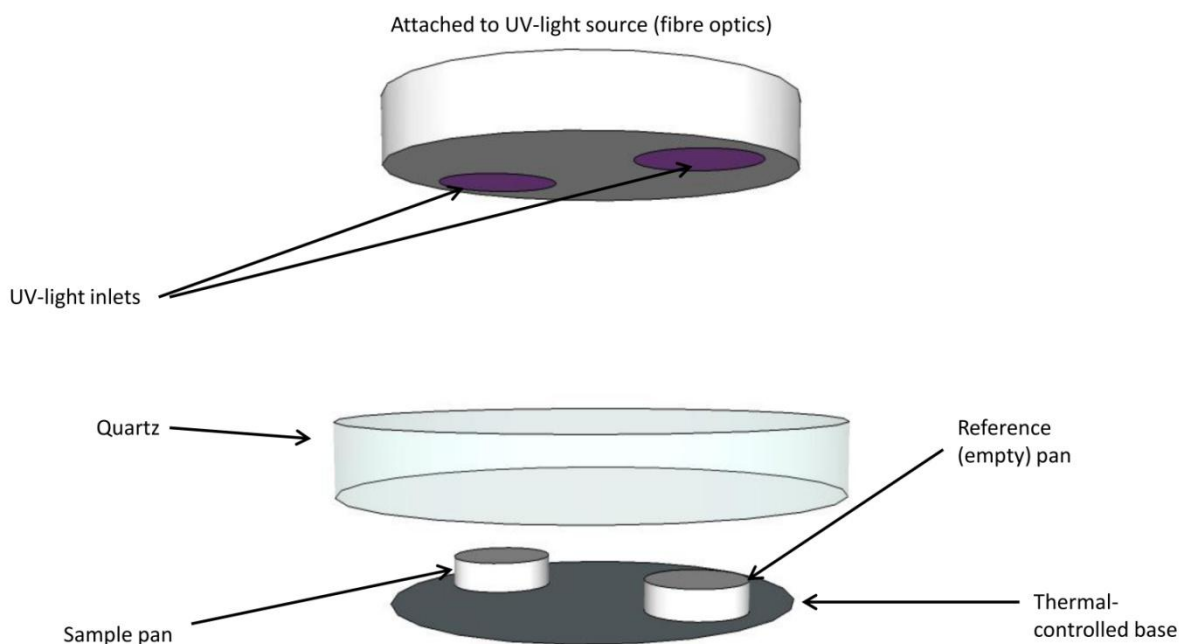


Figure 3.2: A simplified schematic of a UV-DSC calorimeter.

3.1.7: Differential Scanning Calorimetry (DSC)

DSC studies were conducted under an atmosphere of nitrogen. The machine used was a Mettler Toledo DSC822^e with a 32 slot Mettler TSO801RO sample robot. A HAAKE EK90/MT cooling unit was also attached for lower temperature ranges and more rapid cooling of the system. Samples were run in 20 μ L aluminium pans (Mettler ME-51119810 AL Light). Before each analytical run, a standard of indium of known mass was run and checked against reference values (mass 6.39 mg, onset temperature = 156.55 °C, transition energy = 28.45 kJ.mol⁻¹).

3.1.8: Fourier-Transform Infra-Red Spectroscopy (FT-IR)

IR studies were conducted to further corroborate the identities of the compounds synthesised. These experiments were performed using a Shimadzu IR Prestige-21 FT-IR. Samples were presented neat for analysis.

3.1.9: Ultra Violet Spectroscopy

UV analyses of certain compounds were conducted in order to explore the absorbance maxima in comparison with possible photoinitiators for the polymerisation procedures. Comparison of values for λ_{max} allowed for selection of a photoinitiator that had minimised overlap with the compounds to be studied, thereby allowing for more rapid and efficient polymerisations.

3.1.10: X-Ray Spectroscopy

The majority of final compounds, as well as many intermediates, were analysed *via* X-ray diffraction scanning across a range of temperatures by Dr. Stephen Cowling. This allowed for the studies of the different phases observed, noting the crystal structure, as well as the structures of liquid crystal phases and the layer spacing observed in the Smectic A and Smectic C phases.

It is possible to calculate the layer spacing through application of the Bragg equation (1.4)¹⁴

$$n\lambda = 2d\sin\theta \quad \text{Equation 1.4}$$

where n is an integer, λ is the wavelength of the X-rays, d is the layer spacing and θ is the incident angle of the beam (see Figure 3.3).

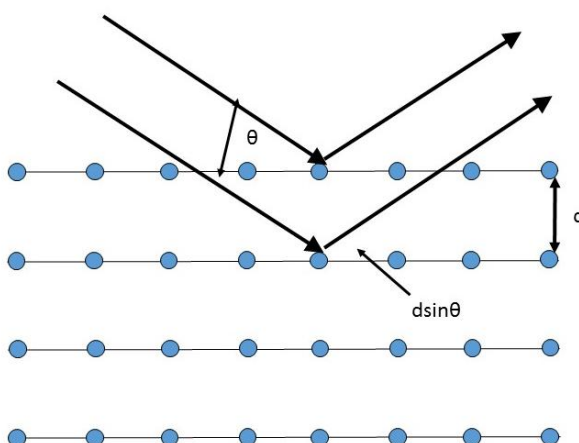


Figure 3.3: A simplified representation of how incident X-rays interact with a crystal lattice, with the layer spacing d and angle of incidence θ .

With the emitted wavelength known, it is thus possible to calculate the layer spacing by knowing the value of θ , which is determined by the relative positioning of the detector.

3.2: Generic Synthetic Procedures

Syntheses of different compounds were conducted generally by a small number of different syntheses which were freely adaptable for different purposes.

3.2.1: Preparation 1

A modified Williamson alkylation reaction was used for numerous purposes, see Figures 3.4 and 3.5, generally in the final step of syntheses, as well as in initial investigations into the role of the terminal amine unit.⁷³

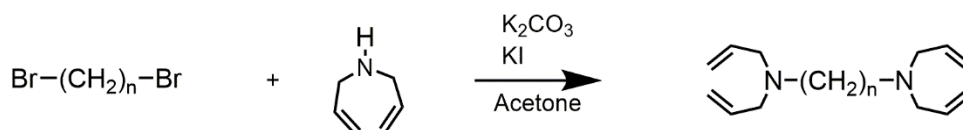


Figure 3.4: A reaction scheme of Preparation 1 in the synthesis of Compound 1 where $n = 10$.

The reaction proceeded with by the substitution of a terminal bromide with diallylamine in solution in the presence of potassium carbonate, as well as a small quantity of potassium bromide, generally using acetone as a solvent and the reaction heated under reflux conditions. Purification of the final compounds was performed by filtration to remove the potassium carbonate and potassium bromide before the removal of the solvent. The resultant mixture was then subjected to column chromatography, with the initial fractions being eluted with hexane, and the final compounds being eluted using a gradient of DCM to ethyl acetate.

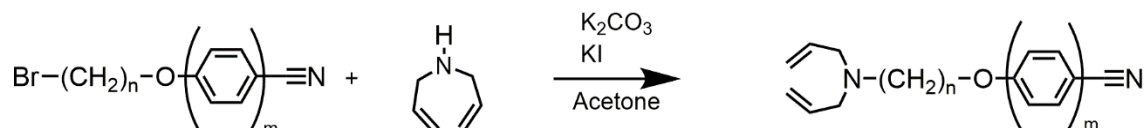


Figure 3.5: A reaction scheme of Preparation 1 for the synthesis of various target compounds, where $n = 8, 9, 10$ or 12 , and $m = 2$ or 3 .

3.2.2: Preparation 2

The amide synthesis was conducted *via* a different pathway, using two synthetic steps in the overall synthesis.⁷⁴ Firstly, an acid chloride was synthesised using the associated diacid and oxalyl chloride as presented in Figure 3.6.

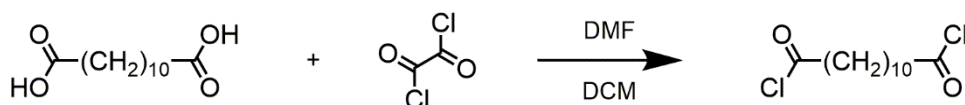


Figure 3.6: A reaction scheme of the first step of Preparation 2, showing the synthesis of the acid chloride intermediate.

After 10 h stirring under a nitrogen atmosphere, diallylamine was introduced with trimethylamine, and the reaction left to continue for a further 8 h (see Figure 3.7). The reaction mixture was then purified *via* column chromatography with the products eluted using DCM.

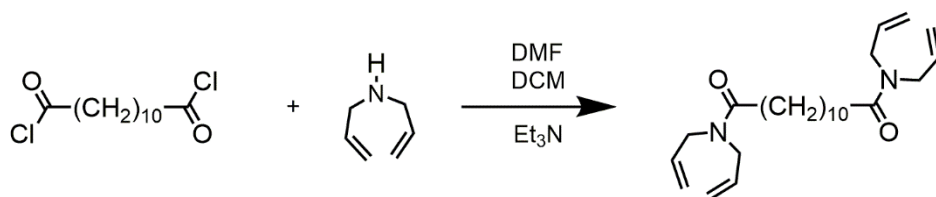


Figure 3.7: A reaction scheme of the second step of Preparation 2, showing the conversion of the intermediate acid chloride into the target amide compound.

3.2.3: Preparation 3

In a similar way to preparation 1, the introduction of the aromatic motif could be performed using a modified Williamson reaction to form an ether linkage (see Figure 3.8).⁷³ The reaction between the dibromide starting material and the aromatic alcohol of the motif was conducted in acetone, heated under reflux conditions and in the presence of potassium carbonate. After 20 h, the reactions were monitored by TLC, and if deemed complete, were removed from heating and

filtered to remove potassium carbonate, before being concentrated and purified by column chromatography. The initial fractions of unreacted dibromide were eluted using hexane, before the products were eluted with 50:50 DCM:hexane. Previous work conducted by Davis et. al^{75, 76} and Itahara and Tamura⁷⁷ also utilised a similar synthetic procedure in the formation of their bromo-terminated alkoxybiphenyls for the specified chain lengths.

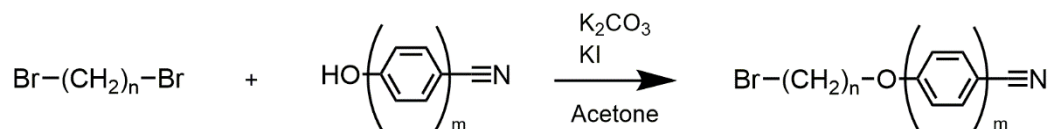


Figure 3.8: A reaction scheme of Preparation 3, showing the mono-addition of the aromatic motif to flexible spacer chain, where $n = 8, 9, 10$ or 12 , and $m = 2$ or 3 .

3.2.4: Preparation 4

An alternative to preparation 3 was performed using a Mitsunobu reaction between a bromoalcohol and a phenol (see Figure 3.9).⁸¹ The reactions were performed in dried THF in the presence of triphenyl phosphine. With the reagents and triphenyl phosphine in solution under an atmosphere of nitrogen, DIAD was added dropwise to prevent the heating of the reaction system. The reaction was monitored by TLC, and upon completion, the solvent was removed under reduced pressure before the resultant mixture was purified by column chromatography. The fractions were eluted via a gradient elution using hexane and DCM, with the final fractions eluted with ethyl acetate. Products were then subsequently recrystallized from ethanol.

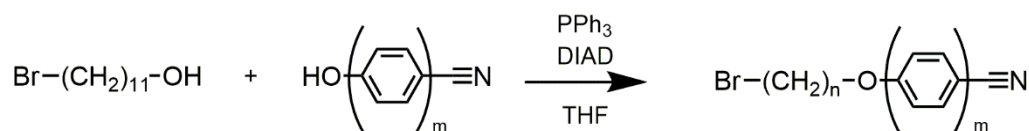


Figure 3.9: A reaction scheme of Preparation 4, showing the Mitsunobu reaction between 11-bromo-1-undecanol and an aromatic motif, where $m = 2$ or 3 .

3.2.5: Preparation 5

The deprotection of protected benzoic acids was conducted in a two-step procedure (see Figure 3.10).⁸² Firstly, the starting materials were dissolved in a solvent mixture of water, methanol and acetonitrile (1:9:40 ratio respectively). The reaction proceeded under reflux conditions for 20 h in the presence of potassium hydroxide before being cooled to -20°C and treated with acetyl chloride, added dropwise to a pH of 1. The mixture was then filtered and the solution dried to obtain the quaternary ammonium salt.

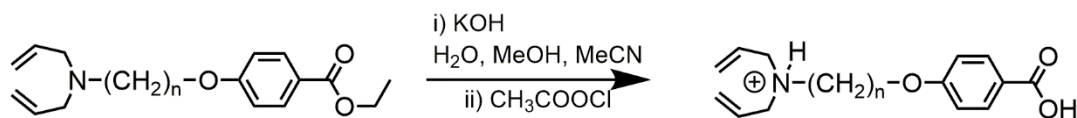


Figure 3.10: A reaction scheme of Preparation 5, showing the deprotection of an ethyl protected benzoate ester to the corresponding carboxylic acid, where $n = 8 - 12$.

3.2.6: Preparation 6

The synthesis of the ester compounds was conducted *via* a Steglich esterification in DCM (see Figure 3.11).⁸⁰ The reagents were dissolved with EDAC and a catalytic quantity of DMAP. The reactions were conducted at ambient temperature for 14 h (or until complete, confirmed by TLC), before purification by column chromatography, and eluted with hexane.

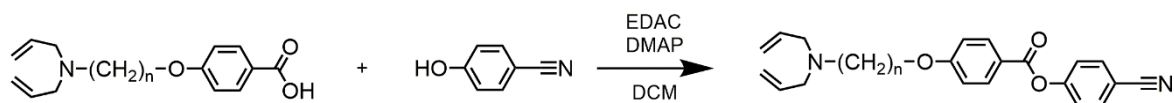


Figure 3.11: A reaction scheme of Preparation 6, showing the formation of a benzoate ester *via* a Steglich Esterification reaction, where $n = 8 - 12$.

3.2.7: Salt syntheses

From the final diallylamine compounds obtained, it was possible to acidify the basic amines in order to form the quaternary ammonium salts. This was done through two routes as follows.

3.2.7.1: Direct acidification

The target amino-compound was first dissolved in DCM before being treated with a stoichiometric amount of either HCl (in 1M etherific solution) or a carboxylic acid in DCM. The mixture was stirred for one hour before the solvent was removed under reduced pressure.

3.2.7.2: Metatheses

From the existing chloride salt, it was possible to replace the associated anion. The salt was dissolved in DCM and shaken with a solution of the other anion (generally an aqueous solution). The aqueous and DCM layers were then separated, and the organic layer was washed with water before being dried in the presence of magnesium sulfate. This was then filtered, and the solvent removed to isolate the alternative salt compound.

3.3: Proposed mechanisms

3.3.1: Preparation 1

The proposed mechanism for Preparation 1 is that of a Williamson Ether synthesis, which is initiated by the abstraction of the hydrogen associated with the amine by the basic conditions. Subsequent to this, the negatively charged nitrogen interacts with the electron-deficient, partially positive terminal carbon bonded to the leaving group, in this case a bromine. The bromine

receives the electron density from the bond and acts as a leaving group, allowing the formation of the carbon-nitrogen bond.

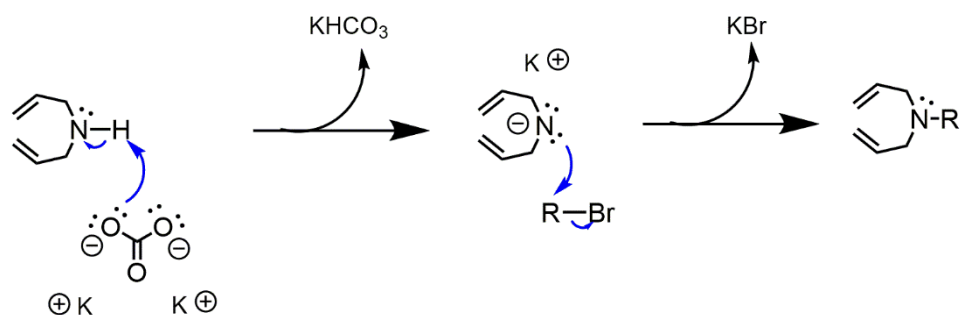


Figure 3.12: A proposed reaction mechanism followed through Preparation 1, showing the movement of electrons (denoted by blue arrows) and charges.

3.3.2: Preparation 2

Unlike Preparation 1, Preparation 2 was conducted over subsequent steps, with the formation of a reactive acid chloride prior to conversion to the amide. Therefore, the reaction features different mechanistic pathways for each step of the reaction.

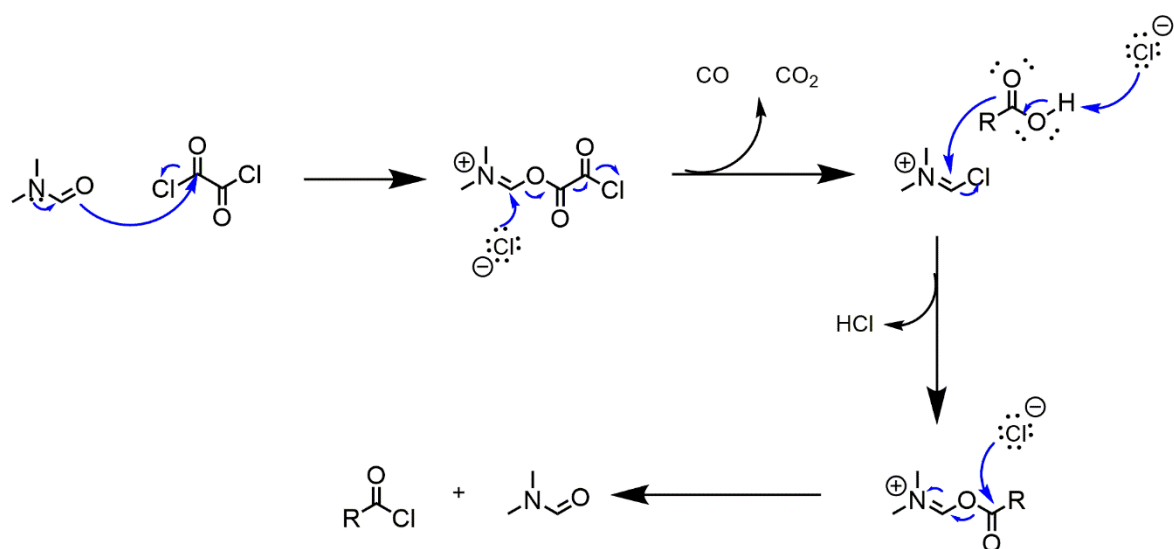


Figure 3.13: A proposed reaction mechanism followed through the first step of Preparation 2, showing the movement of electrons (denoted by blue arrows) and charges.

The first mechanism shows the generation of the acid chloride in the presence of DMF, which acts as a catalyst in the reaction, and is shown to be reformed in the final step of the mechanism. From this point, the reaction is then continued from the intermediate acid chloride to form the target amide. The second mechanism shows the reaction of the lone pair of electrons present on the nitrogen from the amine and the electron-deficient carbon of the acid chloride. The carbon is electron deficient due to both the inductive effects of the adjacent chlorine and the oxygen. The next step of the mechanism shows the loss of the chlorine as a suitable leaving group, which then abstracts the hydrogen associated with the nitrogen, removing the charge from the molecule.

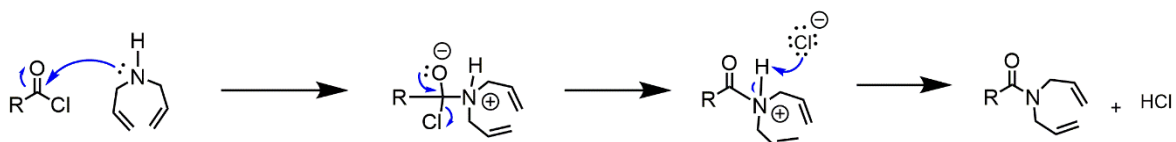


Figure 3.14: A proposed reaction mechanism followed through the second step of Preparation 2, showing the movement of electrons (denoted by blue arrows) and charges.

3.3.3: Preparation 3

In a similar manner to Preparation 1, the reaction mechanism presented is that of a Williamson Ether formation, in this case unmodified to allow the synthesis of an ether. The key difference in the mechanism is the nature of the functional group being reacted, with an alcohol used in this situation, which reacts in a similar manner to the amine.

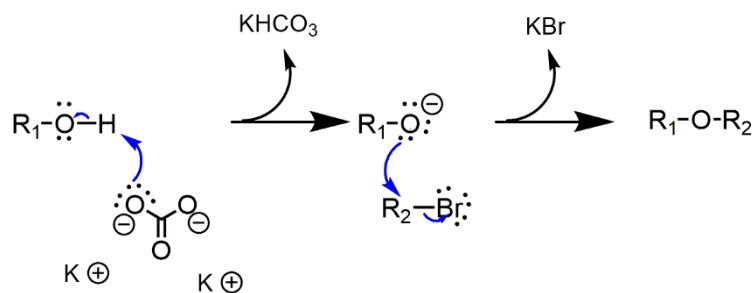


Figure 3.15: A proposed reaction mechanism followed through Preparation 3, showing the movement of electrons (denoted by blue arrows) and charges.

3.3.4: Preparation 4

The mechanism proposed for Preparation 4 is that for the Mitsunobu reaction. The mechanism shows the generation of a reactive group from the interaction of DIAD and triphenyl phosphine, the reactive group generated then interacting with the alkyl alcohol, promoting nucleophilic attack (such as from another alcohol) and the inversion of stereochemistry of the reactive carbon. The reaction also generates triphenyl phosphine oxide as a by-product.

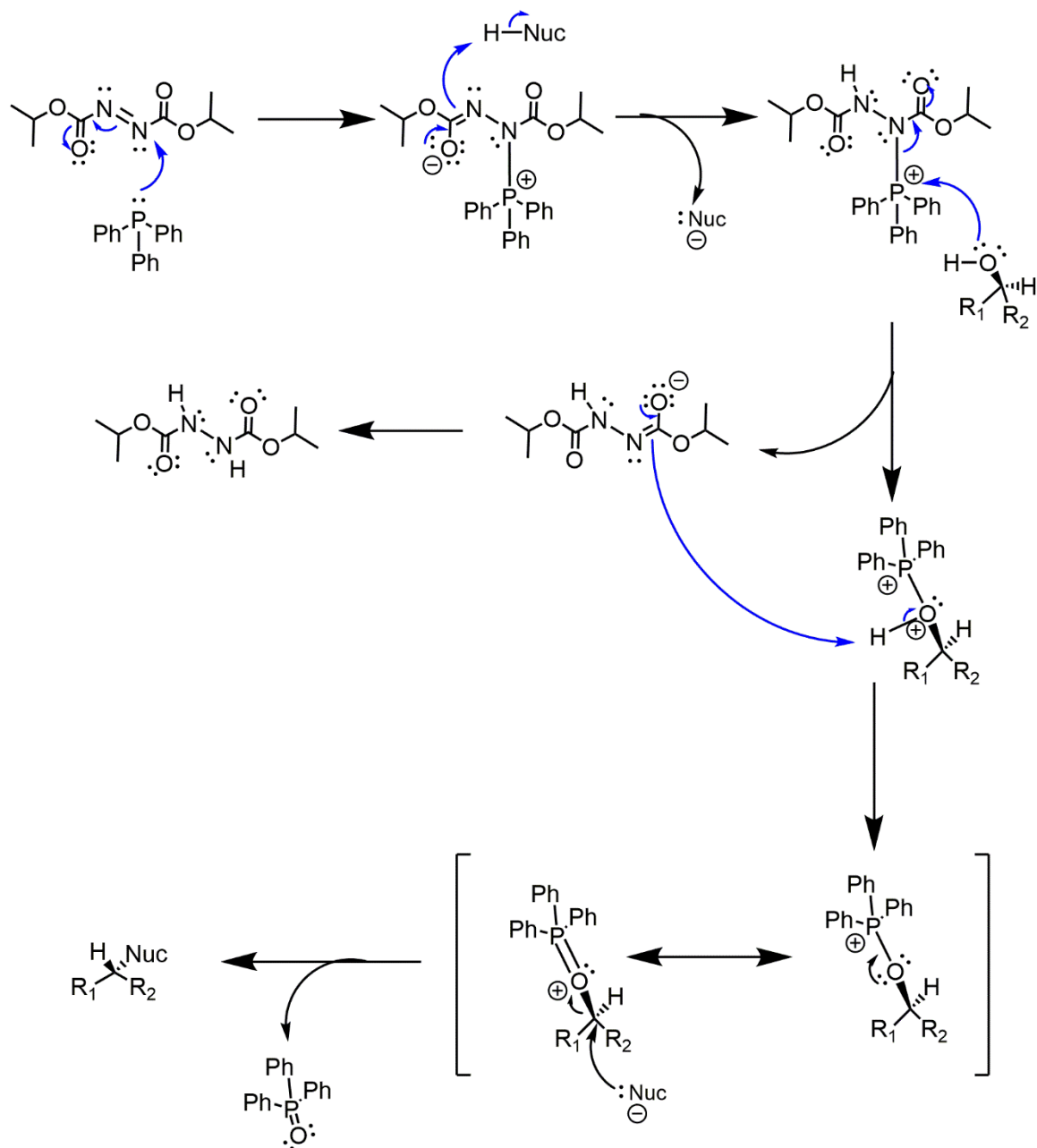


Figure 3.16: A proposed reaction mechanism followed through Preparation 4, showing the movement of electrons (denoted by blue arrows) and charges.

3.3.5: Preparation 5

The proposed mechanism for Preparation 5 shows the deprotection of an ester in basic conditions (shown by the presence of the hydroxide anion). This hydroxide anion attacks the electron-deficient carbonyl carbon, with rearrangement of charge into the associated oxygen. A reversible scenario is then established wherein the now negatively charged oxygen interacts with the aqueous solvent. The carbonyl group is reformed with the loss of the alkyl chain as a alcohol, as well as the reformation of the base.

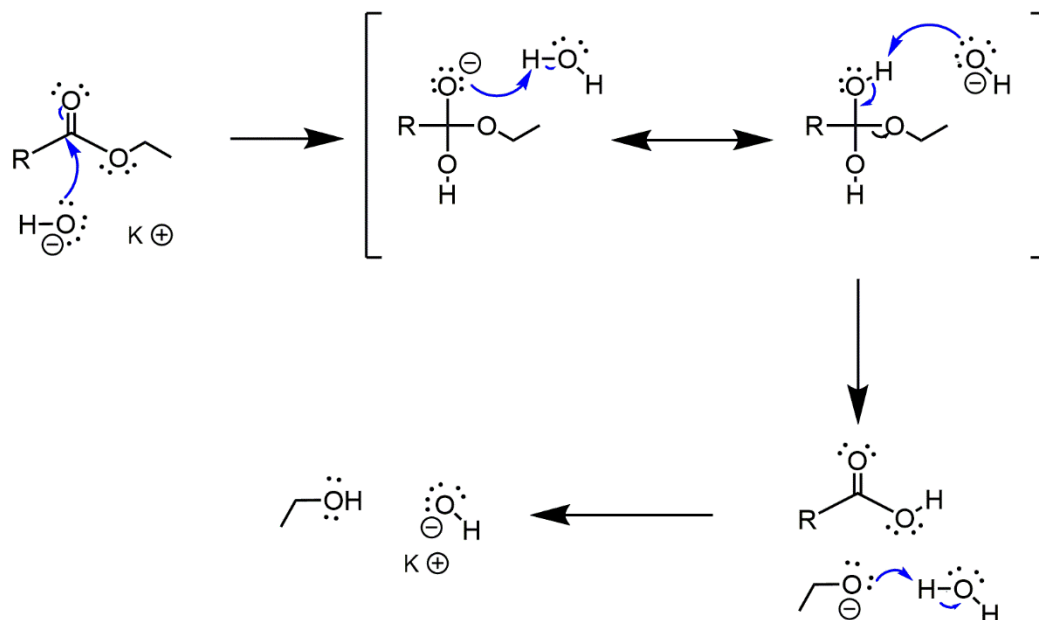


Figure 3.17: A proposed reaction mechanism followed through Preparation 5, showing the movement of electrons (denoted by blue arrows) and charges.

3.3.6: Preparation 6

The proposed mechanism for Preparation 6 is that for a Steglich Esterification, which is initiated by the interaction of the carboxylic acid with EDAC. The EDAC initially acts as a base and abstracts the acidic hydrogen, before reacting at the imido-carbon (which is electron deficient) with the negatively charged oxygen. The carbonyl carbon (which is also electron deficient) is attacked by the DMAP, which causes the loss of the oxygen from the acid, and forms a resonant structure where aromaticity is lost within the pyridine ring. The carbonyl carbon is activated to react with the alcohol, with the passage of charge around the pyridine ring reforming aromaticity and the DMAP is reformed and lost, with the ester newly formed.

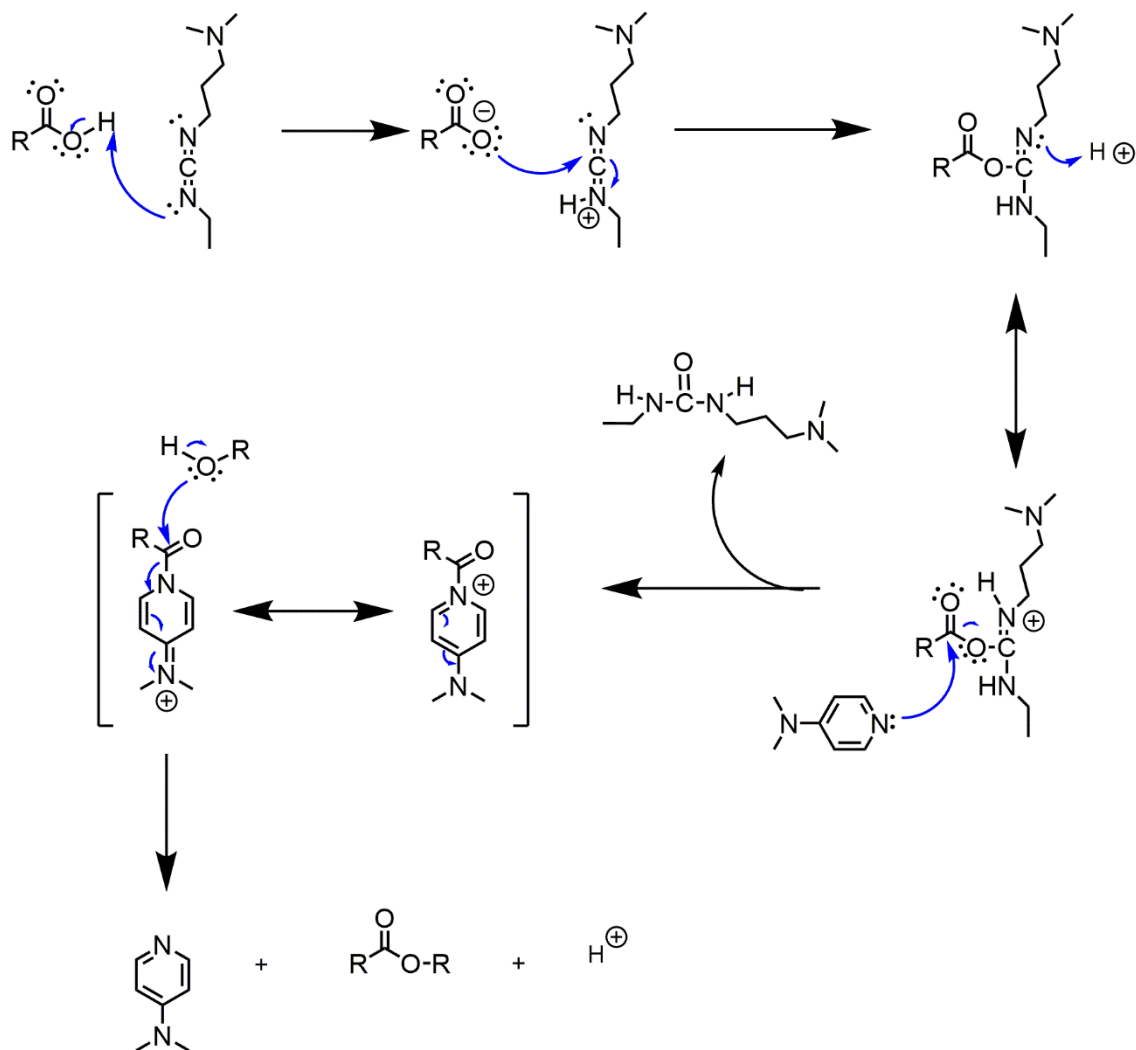


Figure 3.18: A proposed reaction mechanism followed through Preparation 6, showing the movement of electrons (denoted by blue arrows) and charges.

3.4: Abbreviations

Throughout the thesis will be included numerous abbreviations for different commonly used chemicals and solvents, in addition to those for various techniques. The following is a list of common abbreviations and what they represent.

DCM – Dichloromethane, a common solvent.

DIAD – Diisopropyl azodicarboxylate, used in the Mitsunobu Reaction presented in Preparation 4 and the corresponding mechanism.

DMAP – Dimethyl amino pyridine, used in the Steglich Esterification reaction outlined in Preparation 6 and the corresponding mechanism.

DMF – Dimethyl formamide.

DSC – Differential scanning calorimetry, a technique used to analyse the heat-flow through a compound with variation of temperature applied to the sample, allowing analysis of phase transitions.

EDAC – 1-Ethyl-3-(3-dimethylaminopropyl)carbodiimide, used in the Steglich Esterification reaction outlined in Preparation 6 and the corresponding mechanism.

FT-IR – Fourier transform infrared spectroscopy, used to analyse functional groups in a synthesised compound.

M/z – Used to denote the molecular mass derived from mass spectrometry, showing the molecular ion peak.

NMR - Nuclear magnetic resonance, used as an analytical technique to confirm the identity and structure of compounds synthesised.

TLC – Thin layer chromatography, an analytical tool to investigate the differing polarities of compounds in a mixture, which will interact differently with the silica plate in different solvent environments, allowing for analysis of how to separate different components.

UV- Ultraviolet, a high energy section of the electromagnetic spectrum, in this case used in polymerisations, as well as in UV-DSC, the study of polymerisations, as well as in UV-Spectroscopy, analysing the electronic nature of compounds and their interaction with different wavelengths of visible and ultraviolet light.

4: Syntheses

4.1: Syntheses of Di-functionalised Compounds for Polymerization Studies

The first compounds to be considered for synthesis are those for the study of the polymerization of diallylamine and diallylamine-derived functional groups.

4.1.1: Compound 1 (Bis-1,10-diallylaminodecane) (Preparation 1)

1,10-dibromodecane (10.00 g, 33.3 mmol) was added to ethanol (60ml) with diallylamine (6.45 g, 66.4 mmol) and potassium carbonate (9.70 g, 70.2 mmol). The mixture was stirred under reflux (10 h) before cooling to room temperature and filtration. The solvent was then removed under reduced pressure and then the product mixture purified by column chromatography. The initial fraction (1,10-dibromodecane) was eluted using hexane, with the solvent mixture then being replaced with DCM to elute the products. The compound was isolated as a pale, clear yellow oil.

Yield: 8.03g (24.1 mmol, 72.5 %).

$^1\text{H-NMR}$ (CDCl_3): 5.84 (4H, m, $\text{CH}_2=\text{CH}-\text{CH}_2$), 5.16 (4H, m, $\text{CH}_2=\text{CH}-\text{CH}_2$ (overlapping peaks)), 2.97 (8H, m, $\text{CH}-\text{CH}_2-\text{N}$), 2.48 (4H, m, $\text{N}-\text{CH}_2-\text{CH}_2$), 1.80 (4H, m, $\text{CH}_2-\text{C}-\text{H}_2$), 1.55-1.20 (12H, m, $\text{CH}_2-\text{C}-\text{H}_2$) ppm

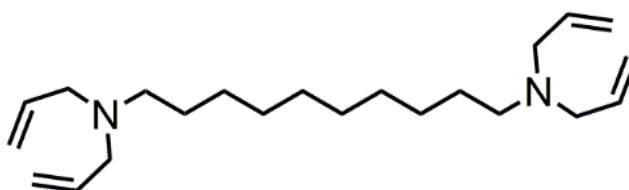


Figure 4.1: Structure of Compound 1 (Bis-1,10-diallylaminodecane).

4.1.2: Compound 2 (Decane-1,10-bis-diallylammonium chloride) (Direct Acidification)

Compound 1 (4.00 g, 12.0 mmol) was further treated with aqueous HCl (37%) in methanol (50ml) to pH 1 under ambient conditions and with stirring. The product was extracted with DCM (2x50 ml), then dried over anhydrous magnesium sulfate, which was subsequently removed by filtration, and the solvent removed under reduced pressure, resulting in a pale, clear yellow oil.

Yield: 4.00 g (9.9 mmol, 82.2 %).

Negative mass spectrometry confirmed the presence of Cl within the compound.

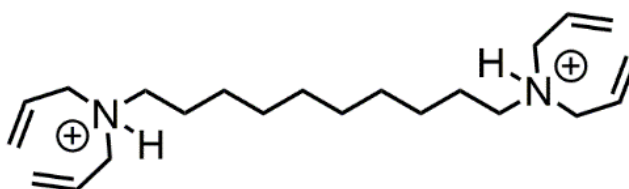


Figure 4.2: Structure of Compound 2 (Decane-1,10-bis-diallylammonium chloride).

4.1.3: Compound 3 (N^1,N^1,N^{12},N^{12} -tetraallyldodecanediamide) (Preparation 2)

1,12-dodecanedioic acid (15.00 g, 65.1 mmol) was added to a solution of oxalyl chloride in DMF (1 M) and DCM (200ml). The mixture was stirred at ambient temperature under nitrogen (10 h). Diallylamine (24 ml, 194.4 mmol) was then added in the presence of trimethylamine (5 ml, 35.9 mmol) before stirring (8 h). The solvents were removed under reduced pressure and the products purified via column chromatography, eluted with DCM, resulting in a clear yellow oil.

Yield: 10.07 g (25.9 mmol, 39.8 %)

$^1\text{H-NMR}$ (CDCl_3): 5.89 (4H, m, $\text{CH}_2=\text{CH}-\text{CH}_2$), 5.20 (4H, m, $\text{CH}_2=\text{CH}-\text{CH}_2$ (overlapping peaks)), 3.70 (8H, m, $\text{CH}-\text{CH}_2-\text{N}$), 2.32 (4H, m, $\text{N}-\text{CH}_2-\text{CH}_2$), 1.76 (4H, m, $\text{CH}_2-\text{C}-\text{H}_2$), 1.55-1.20 (12H, m, $\text{CH}_2-\text{C}-\text{H}_2$) ppm

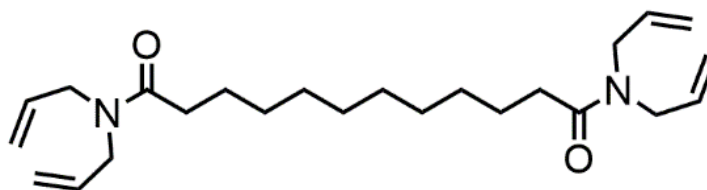


Figure 4.3: Structure of Compound 3 (N^1,N^1,N^{12},N^{12} -tetraallyldodecanediamide).

4.2: Intermediate Bromide Syntheses

4.2.1: Synthesis of Biphenyl Bromide Compounds

4.2.1.1: Compound 4 (4-Cyano-4'-(8-bromooctyloxy)biphenyl)⁷⁵ (Preparation 3)

1,8-dibromooctane (10.00 g, 36.8 mmol) was dissolved in acetone (120 ml) in the presence of potassium carbonate (2.10 g, 15.2 mmol) and 4-hydroxy-4'-cyanobiphenyl (0.50 g, 2.6 mmol). The reaction was heated under reflux (14 h). The mixture was then cooled to ambient temperature before the potassium carbonate was filtered out. The solvent was then removed under reduced pressure and the resultant mixture was separated by column chromatography on silica. Unreacted 1,8-dibromooctane was isolated by elution with hexane, and the product isolated by a gradient elution with hexane and DCM (10% increment of DCM to 50%). The compound was then recrystallized from ethanol, resulting in colourless crystals.

Yield = 0.61 g (1.58 mmol, 60.9 %)

$^1\text{H-NMR}$ (CDCl_3): 7.64 (2H, dd, $J = 6.4 \text{ Hz}$, $J = 2 \text{ Hz}$, $\text{C}_{\text{Ar}}-\text{H}$), 7.62 (2H, dd, $J = 6.4 \text{ Hz}$, $J = 2 \text{ Hz}$, $\text{C}_{\text{Ar}}-\text{H}$), 7.51 (2H, dd, $J = 6.4 \text{ Hz}$, $J = 2 \text{ Hz}$, $\text{NC}-\text{C}-\text{C}_{\text{Ar}}-\text{H}$), 6.97 (2H, dd, $J = 6.4 \text{ Hz}$, $J = 2 \text{ Hz}$, $\text{CO}-\text{C}-\text{C}_{\text{Ar}}-\text{H}$), 3.99 (2H, t, $J = 6.4 \text{ Hz}$, $\text{O}-\text{C}-\text{H}_2$), 3.40 (2H, t, $J = 6.4 \text{ Hz}$, $\text{Br}-\text{C}-\text{H}_2$), 1.82 (4H, m, $\text{CH}_2-\text{C}-\text{H}_2$), 1.53-1.20 (8H, m, $\text{CH}_2-\text{C}-\text{H}_2$) ppm

$^{13}\text{C-NMR}$ (CDCl_3): 159.73 ($\text{O}-\text{C}_{\text{Ar}}$), 145.37 ($\text{Ar}-\text{C}_{\text{Ar}}$ (with cyano-group adjacent to ring)), 132.55 ($\text{C}_{\text{Ar}}-\text{C}_{\text{Ar}}-\text{CN}$), 131.25 ($\text{Ar}-\text{C}_{\text{Ar}}$ (attached to ether)), 128.31 ($\text{C}_{\text{A}}-\text{C}_{\text{Ar}}-\text{Ar}$), 127.06 ($\text{C}_{\text{A}}-\text{C}_{\text{Ar}}-\text{Ar}$), 119.10 ($\text{C}_{\text{Ar}}-\text{C}\equiv\text{N}$),

115.04 ($C_A-C_{Ar}-O$), 109.93 ($C_{Ar}-C\equiv N$), 68.05 (CH_2-CH_2-O), 33.98 (CH_2-CH_2-Br), 32.73 (CH_2-CH_2-Br), 30.93 ($CH_2-CH_2-CH_2$), 29.15 ($CH_2-CH_2-CH_2$), 25.91 ($CH_2-CH_2-CH_2$) ppm

M/z (ESI): 408.0939 (with Na^+)

IR: 3073 (aromatic C-H stretch), 2920 (alkyl C-H stretch), 2849 (alkyl C-H stretch), 2232 (CN stretch), 1738 (aromatic C-H bend), 1601 (Aromatic C=C stretch), 1489 (alkyl C-H bend) 1180 (C-O stretch) cm^{-1}

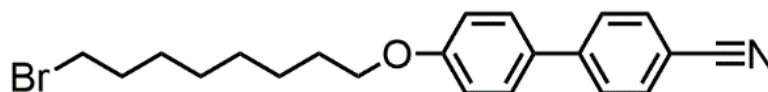


Figure 4.4: Structure of Compound 4 (4-Cyano-4'-(8-bromooctyloxy)biphenyl).

4.2.1.2: Compound 5 (4-Cyano-4'-(9-bromononyloxy)biphenyl)⁷⁵ (Preparation 3)

Compound 5 was prepared using the same methodology as Compound 4. The following quantities were used: 1,9-dibromononane 10.00 g; 35.0 mmol, 4-hydroxy-4'-cyanobiphenyl 0.50 g; 2.6 mmol, potassium carbonate 2.10 g; 15.2 mmol and acetone 120 ml. The product was isolated as colourless crystals.

Yield = 0.60g (1.50 mmol, 57.8 %)

1H -NMR ($CDCl_3$): 7.67 (2H, dd, $J = 6.4$ Hz, $J = 2$ Hz, $C_{Ar}-H$), 7.62 (2H, dd, $J = 6.4$ Hz, $J = 2$ Hz, $C_{Ar}-H$), 7.51 (2H, dd, $J = 6.4$ Hz, $J = 2$ Hz, $NC-C-C_{Ar}-H$), 6.97 (2H, dd, $J = 6.4$ Hz, $J = 2$ Hz, $CO-C-C_{Ar}-H$), 3.99 (2H, t, $J = 6.4$ Hz, $O-C-H_2$), 3.40 (2H, t, $J = 6.4$ Hz, $Br-C-H_2$), 1.81 (4H, m, CH_2-C-H_2), 1.53-1.20 (10H, m, CH_2-C-H_2) ppm

^{13}C -NMR ($CDCl_3$): 159.74 ($O-C_{Ar}$), 145.25 ($Ar-C_{Ar}$ (with cyano-group adjacent to ring)), 132.54 ($C_{Ar}-C_{Ar}-CN$), 131.23 ($Ar-C_{Ar}$ (attached to ether)), 128.29 ($C_A-C_{Ar}-Ar$), 127.04 ($C_A-C_{Ar}-Ar$), 119.11 ($C_{Ar}-C\equiv N$), 115.03 ($C_A-C_{Ar}-O$), 109.98 ($C_{Ar}-C\equiv N$), 68.08 (CH_2-CH_2-O), 34.03 (CH_2-CH_2-Br), 32.75 (CH_2-CH_2-Br), 29.15 ($CH_2-CH_2-CH_2$), 28.65 ($CH_2-CH_2-CH_2$), 25.96 ($CH_2-CH_2-CH_2$) ppm

M/z (ESI): 422.1103 (with Na^+)

IR: 3059 (aromatic C-H stretch), 2920 (alkyl C-H stretch), 2853 (alkyl C-H stretch), 2224 (CN stretch), 1931 (aromatic C-H bend), 1603 (aromatic C=C stretch), 1495 (alkyl C-H bend), 1182 (C-O stretch) cm^{-1}

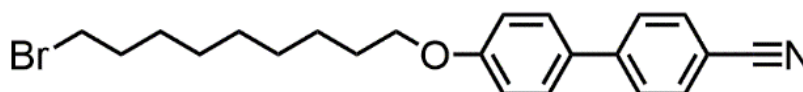


Figure 4.5: Structure of Compound 5 (4-Cyano-4'-(9-bromononyloxy)biphenyl).

4.2.1.3: Compound 6 (4-Cyano-4'-(10-bromodecyloxy)biphenyl)⁷⁵ (Preparation 3)

Compound 6 was prepared using the same methodology as Compound 4. The following quantities were used: 1,10-dibromodecane 10.00 g; 33.3 mmol, 4-hydroxy-4'-cyanobiphenyl 0.50 g; 2.6 mmol, potassium carbonate 2.10 g; 15.2 mmol and acetone 120 ml. The product was isolated as colourless crystals.

Yield = 0.61g (1.48 mmol, 56.8 %)

¹H-NMR (CDCl₃): 7.67 (2H, dd, *J* = 6.4 Hz, *J* = 2 Hz, C_{Ar}-H), 7.62 (2H, dd, *J* = 6.4 Hz, *J* = 2 Hz, C_{Ar}-H), 7.51 (2H, dd, *J* = 6.4 Hz, *J* = 2 Hz, NC-C-C_{Ar}-H), 6.97 (2H, dd, *J* = 6.4 Hz, *J* = 2 Hz, CO-C-C_{Ar}-H), 3.99 (2H, t, *J* = 6.4 Hz, O-C-H₂), 3.39 (2H, t, *J* = 6.4 Hz, Br-C-H₂), 1.82 (4H, m, CH₂-C-H₂), 1.53-1.20 (12H, m, CH₂-C-H₂) ppm

¹³C-NMR (CDCl₃): 159.61 (O-C_{Ar}), 145.17 (Ar-C_{Ar} (with cyano-group adjacent to ring)), 132.55 (C_{Ar}-C_{Ar}-CN), 131.11 (Ar-C_{Ar} (attached to ether)), 128.31 (C_A-C_{Ar}-Ar), 127.05 (C_A-C_{Ar}-Ar), 119.08 (C_{Ar}-C≡N), 115.04 (C_A-C_{Ar}-O), 109.96 (C_{Ar}-C≡N), 68.11 (CH₂-CH₂-O), 34.06 (CH₂-CH₂-Br), 32.78 (CH₂-CH₂-Br), 29.32 (CH₂-CH₂-CH₂), 28.72 (CH₂-CH₂-CH₂), 25.99 (CH₂-CH₂-CH₂) ppm

M/z (ESI): 436.1247 (with Na⁺)

IR: 3075 (aromatic C-H stretch), 2920 (alkyl C-H stretch), 2853 (alkyl C-H stretch), 2236 (CN stretch), 1898 (aromatic C-H bend), 1605 (aromatic C=C stretch), 1462 (alkyl C-H bend), 1182 (C-O stretch) cm⁻¹

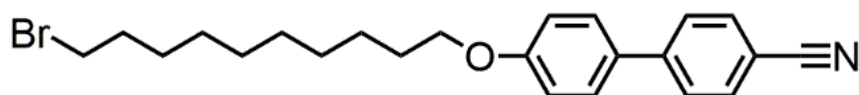


Figure 4.6: Structure of Compound 6 (4-Cyano-4'-(10-bromodecyloxy)biphenyl).

4.2.1.4: Compound 7 (4-Cyano-4'-(11-bromoundecyloxy)biphenyl)⁷⁶ (Preparation 4)

DIAD (0.40 ml, 2.0 mmol) was added dropwise to a solution of 4-hydroxy-4'-cyanobiphenyl (0.37 g, 1.9 mmol), 11-bromoundecanol (0.50 g, 2.0 mmol) and triphenylphosphine (0.51g, 1.9 mmol) in dried THF (150ml) under a nitrogen atmosphere. The reaction was stirred under nitrogen (14 h), and then the solvent was removed under reduced pressure. The product was isolated by column chromatography on silica (eluted with a gradient of petroleum ether (bp 40-60 °C) and DCM as the solvent mixture (10 % increments of DCM from 0 % to 60 %). The product was recrystallized from ethanol, forming colourless crystals.

Yield = 0.70 g (1.64 mmol, 86.3 %)

¹H-NMR (CDCl₃): 7.51 (2H, dd, *J* = 6.4 Hz, *J* = 2 Hz, C_{Ar}-H), 7.45 (2H, dd, *J* = 6.4 Hz, *J* = 2 Hz, C_{Ar}-H), 7.39 (2H, dd, *J* = 6.4 Hz, *J* = 2 Hz, NC-C-C_{Ar}-H), 6.94 (2H, dd, *J* = 6.4 Hz, *J* = 2 Hz, CO-C-C_{Ar}-H), 3.97 (2H,

t, $J = 6.4$ Hz, O-C- H_2), 3.39 (2H, t, $J = 6.4$ Hz, Br-C- H_2), 1.82 (4H, m, CH₂-C- H_2), 1.53-1.20 (14H, m, CH₂-C- H_2) ppm

¹³C-NMR (CDCl₃): 160.12 (O-C_{Ar}), 145.40 (Ar-C_{Ar} (with cyano-group adjacent to ring)), 132.22 (C_{Ar}-C_{Ar}-CN), 131.76 (Ar-C_{Ar} (attached to ether)), 128.26 (C_A-C_{Ar}-Ar), 127.92 (C_A-C_{Ar}-Ar), 120.64 (C_{Ar}-C≡N), 114.86 (C_A-C_{Ar}-O), 109.98 (C_{Ar}-C≡N), 68.10 (CH₂-CH₂-O), 34.04 (CH₂-CH₂-Br), 32.81 (CH₂-CH₂-Br), 29.33 (CH₂-CH₂-CH₂), 28.66 (CH₂-CH₂-CH₂), 26.02 (CH₂-CH₂-CH₂) ppm

M/z (ESI): 450.1999 (with Na⁺)

IR: 3075 (aromatic C-H stretch), 3046 (aromatic C-H stretch), 2918 (alkyl C-H stretch), 2849 (alkyl C-H stretch), 2220 (CN stretch), 1771 (aromatic C-H bend), 1605 (aromatic C=C stretch), 1464 (alkyl C-H bend), 1177 (C-O stretch) cm⁻¹

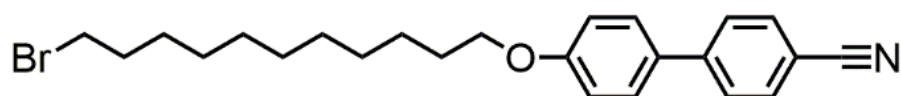


Figure 4.7: Structure of Compound 7 (4-Cyano-4'-(11-bromoundecyloxy)biphenyl).

4.2.1.5: Compound 8 (4-Cyano-4'-(12-bromododecyloxy)biphenyl)⁷⁷ (Preparation 3)

Compound 8 was prepared using the same methodology as Compound 4. The following quantities were used: 1,12-dibromododecane 10.00 g; 30.5 mmol, 4-hydroxy-4'-cyanobiphenyl 0.50 g; 2.6 mmol, potassium carbonate 2.10 g; 15.2 mmol and acetone 120 ml. The product was isolated as colourless crystals.

Yield = 0.62g (1.41 mmol, 54.1 %)

¹H-NMR (CDCl₃): 7.67 (2H, dd, $J = 6.4$ Hz, $J = 2$ Hz, C_{Ar}-H), 7.20 (2H, dd, $J = 6.4$ Hz, $J = 2$ Hz, C_{Ar}-H), 7.51 (2H, dd, $J = 6.4$ Hz, $J = 2$ Hz, NC-C-C_{Ar}-H), 6.97 (2H, dd, $J = 6.4$ Hz, $J = 2$ Hz, CO-C-C_{Ar}-H), 3.99 (2H, t, $J = 6.4$ Hz, O-C- H_2), 3.39 (2H, t, $J = 6.4$ Hz, Br-C- H_2), 1.81 (4H, m, CH₂-C- H_2), 1.55-1.20 (8H, m, CH₂-C- H_2) ppm

¹³C-NMR (CDCl₃): 159.76 (O-C_{Ar}), 145.25 (Ar-C_{Ar} (with cyano-group adjacent to ring)), 132.54 (C_{Ar}-C_{Ar}-CN), 131.20 (Ar-C_{Ar} (attached to ether)), 128.29 (C_A-C_{Ar}-Ar), 127.04 (C_A-C_{Ar}-Ar), 119.11 (C_{Ar}-C≡N), 115.03 (C_A-C_{Ar}-O), 109.98 (C_{Ar}-C≡N), 68.13 (CH₂-CH₂-O), 34.08 (CH₂-CH₂-Br), 32.80 (CH₂-CH₂-Br), 29.50 (CH₂-CH₂-CH₂), 29.19 (CH₂-CH₂-CH₂), 26.00 (CH₂-CH₂-CH₂) ppm

M/z (ESI): 464.1550 (with Na⁺)

IR: 3057 (aromatic C-H stretch), 3034 (aromatic C-H stretch), 2918 (alkyl C-H stretch), 2851 (alkyl C-H stretch), 2236 (CN stretch), 1717 (aromatic C-H bend), 1605 (aromatic C=C stretch), 1474 (alkyl C-H bend), 1182 (C-O stretch) cm⁻¹

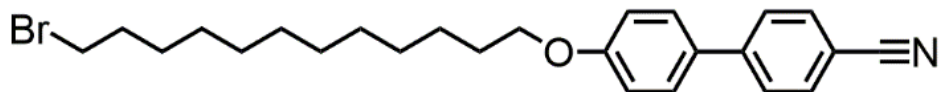


Figure 4.8: Structure of Compound **8** (4-Cyano-4'-(12-bromododecyloxy)biphenyl).

4.2.2: Synthesis of Terphenyl Bromide Compounds

4.2.2.1: Compound **9** (4-Cyano-4''-(8-bromooctyloxy)terphenyl) (Preparation 3)

Compound **9** was prepared using the same methodology as Compound **4**. The following quantities were used: 1,8-dibromooctane 10.00 g; 36.8 mmol, 4-hydroxy-4''-cyanoterphenyl 0.60 g; 2.2 mmol, potassium carbonate 2.00 g; 14.5 mmol and acetone 120 ml. The product was isolated as colourless crystals.

Yield = 0.71 g (1.54 mmol, 70.0 %)

$^1\text{H-NMR}$ (CDCl_3): 7.73 (4H, s, $\text{C}_{\text{Ar}}\text{-H}$), 7.66 (4H, m, $\text{C}_{\text{Ar}}\text{-H}$), 7.57 (2H, dd, $J = 6.4$ Hz, $J = 2$ Hz, $\text{C}_{\text{Ar}}\text{-H}$), 7.00 (2H, dd, $J = 6.4$ Hz, $J = 2$ Hz, $\text{C}_{\text{Ar}}\text{-H}$), 4.01 (2H, t, $J = 6.4$, O- CH_2), 3.42 (2H, t, $J = 6.4$ Hz, Br- CH_2), 1.85 (4H, m, C- CH_2), 1.55-1.20 (8H, m, $\text{CH}_2\text{-CH}_2$) ppm

$^{13}\text{C-NMR}$ (CDCl_3): 159.00 (O- C_{Ar}), 145.19 (Ar- C_{Ar} (with cyano-group adjacent to ring)), 141.22 (Ar- C_{Ar}), 132.63 ($\text{C}_{\text{Ar}}\text{-C}_{\text{Ar}}\text{-CN}$), 132.46 (Ar- C_{Ar} (attached to ether)), 128.07 ($\text{C}_{\text{A}}\text{-C}_{\text{Ar}}\text{-Ar}$), 127.54 ($\text{C}_{\text{A}}\text{-C}_{\text{Ar}}\text{-Ar}$), 127.48 (Ar- $\text{C}_{\text{Ar}}\text{-C}_{\text{Ar}}$), 119.05 ($\text{C}_{\text{Ar}}\text{-C}\equiv\text{N}$), 114.89 ($\text{C}_{\text{A}}\text{-C}_{\text{Ar}}\text{-O}$), 110.61 ($\text{C}_{\text{Ar}}\text{-C}\equiv\text{N}$), 67.98 ($\text{CH}_2\text{-CH}_2\text{-O}$), 34.03 ($\text{CH}_2\text{-CH}_2\text{-Br}$), 32.75 ($\text{CH}_2\text{-CH}_2\text{-Br}$), 29.19 ($\text{CH}_2\text{-CH}_2\text{-CH}_2$), 28.67 ($\text{CH}_2\text{-CH}_2\text{-CH}_2$), 25.95 ($\text{CH}_2\text{-CH}_2\text{-CH}_2$) ppm

M/z (ESI): 484.1257 (with Na^+)

IR: 3030 (aromatic C-H stretch), 2934 (alkyl C-H stretch), 2857 (alkyl C-H stretch), 2234 (CN stretch), 1734 (aromatic C-H bend), 1601 (aromatic C=C stretch), 1462 (alkyl C-H bend), 1180 (C-O stretch) cm^{-1}

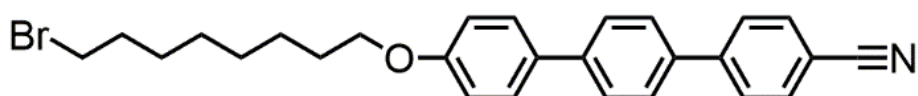


Figure 4.9: Structure of Compound **9** (4-Cyano-4''-(8-bromooctyloxy)terphenyl).

4.2.2.2: Compound **10** (4-Cyano-4''-(9-bromononyloxy)terphenyl) (Preparation 3)

Compound **10** was prepared using the same methodology as Compound **4**. The following quantities were used: 1,9-dibromononane 10.00 g; 35.0 mmol, 4-hydroxy-4''-cyanoterphenyl 0.60 g; 2.2 mmol, potassium carbonate 2.00 g; 14.5 mmol and acetone 120 ml. The product was isolated as colourless crystals.

Yield = 0.65 g (1.37 mmol, 62.2 %)

$^1\text{H-NMR}$ (CDCl_3): 7.72 (4H, s, $\text{C}_{\text{Ar-H}}$), 7.64 (4H, m, $\text{C}_{\text{Ar-H}}$), 7.55 (2H, dd, $J = 6.4 \text{ Hz}$, $J = 2 \text{ Hz}$, $\text{C}_{\text{Ar-H}}$), 6.98 (2H, dd, $J = 6.4 \text{ Hz}$, $J = 2 \text{ Hz}$, $\text{C}_{\text{Ar-H}}$), 3.99 (2H, t, $J = 6.4$, O- CH_2), 3.40 (2H, t, $J = 6.4 \text{ Hz}$, Br- CH_2), 1.83 (4H, m, C- CH_2), 1.55-1.20 (10H, m, $\text{CH}_2\text{-CH}_2$) ppm

$^{13}\text{C-NMR}$ (CDCl_3): 159.07 (O- C_{Ar}), 145.18 (Ar- C_{Ar} (with cyano-group adjacent to ring)), 141.21 (Ar- C_{Ar}), 132.62 ($\text{C}_{\text{Ar}}\text{-C}_{\text{Ar}}\text{-CN}$), 132.28 (Ar- C_{Ar} (attached to ether)), 128.05 ($\text{C}_{\text{A}}\text{-C}_{\text{Ar}}\text{-Ar}$), 127.53 ($\text{C}_{\text{A}}\text{-C}_{\text{Ar}}\text{-Ar}$), 127.53 (Ar- $\text{C}_{\text{Ar}}\text{-C}_{\text{Ar}}$), 119.03 ($\text{C}_{\text{Ar}}\text{-C}\equiv\text{N}$), 114.89 ($\text{C}_{\text{A}}\text{-C}_{\text{Ar}}\text{-O}$), 110.72 ($\text{C}_{\text{Ar}}\text{-C}\equiv\text{N}$), 68.03 ($\text{CH}_2\text{-CH}_2\text{-O}$), 34.06 ($\text{CH}_2\text{-CH}_2\text{-Br}$), 32.78 ($\text{CH}_2\text{-CH}_2\text{-Br}$), 29.34 ($\text{CH}_2\text{-CH}_2\text{-CH}_2$), 28.67 ($\text{CH}_2\text{-CH}_2\text{-CH}_2$), 26.00 ($\text{CH}_2\text{-CH}_2\text{-CH}_2$) ppm

M/z (ESI): 498.1413 (with Na^+)

IR: 3063 (aromatic C-H stretch), 3030 (aromatic C-H stretch), 2920 (alkyl C-H stretch), 2851 (alkyl C-H stretch), 2222 (CN stretch), 1917 (aromatic C-H bend), 1601 (aromatic C=C stretch), 1489 (alkyl C-H bend), 1177 (C-O stretch) cm^{-1}

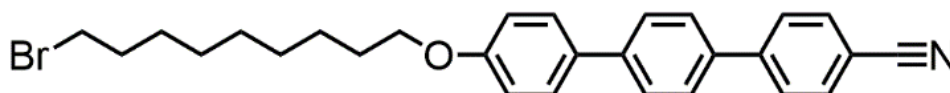


Figure 4.10: Structure of Compound **10** (4-Cyano-4''-(9-bromononyloxy)terphenyl).

4.2.2.3: Compound **11** (4-Cyano-4''-(10-bromodecyloxy)terphenyl) (Preparation 3)

Compound **11** was prepared using the same methodology as Compound **4**. The following quantities were used: 1,10-dibromodecane 10.00 g; 33.3 mmol, 4-hydroxy-4''-cyanoterphenyl 0.60 g; 2.2 mmol, potassium carbonate 2.00 g; 14.5 mmol and acetone 120 ml. The product was isolated as colourless crystals.

Yield = 0.66g (1.35 mmol, 61.3 %)

$^1\text{H-NMR}$ (CDCl_3): 7.73 (4H, s, $\text{C}_{\text{Ar-H}}$), 7.66 (4H, m, $\text{C}_{\text{Ar-H}}$), 7.56 (2H, dd, $J = 6.4 \text{ Hz}$, $J = 2 \text{ Hz}$, $\text{C}_{\text{Ar-H}}$), 6.99 (2H, dd, $J = 6.4 \text{ Hz}$, $J = 2 \text{ Hz}$, $\text{C}_{\text{Ar-H}}$), 3.98 (2H, t, $J = 6.4$, O- CH_2), 3.44 (2H, t, $J = 6.4 \text{ Hz}$, Br- CH_2), 1.84 (4H, m, C- CH_2), 1.54-1.20 (12H, m, $\text{CH}_2\text{-CH}_2$) ppm

$^{13}\text{C-NMR}$ (CDCl_3): 160.22 (O- C_{Ar}), 145.21 (Ar- C_{Ar} (with cyano-group adjacent to ring)), 141.20 (Ar- C_{Ar}), 132.77 ($\text{C}_{\text{Ar}}\text{-C}_{\text{Ar}}\text{-CN}$), 132.02 (Ar- C_{Ar} (attached to ether)), 127.81 ($\text{C}_{\text{A}}\text{-C}_{\text{Ar}}\text{-Ar}$), 125.77 ($\text{C}_{\text{A}}\text{-C}_{\text{Ar}}\text{-Ar}$), 125.10 (Ar- $\text{C}_{\text{Ar}}\text{-C}_{\text{Ar}}$), 120.00 ($\text{C}_{\text{Ar}}\text{-C}\equiv\text{N}$), 115.78 ($\text{C}_{\text{A}}\text{-C}_{\text{Ar}}\text{-O}$), 110.55 ($\text{C}_{\text{Ar}}\text{-C}\equiv\text{N}$), 68.34 ($\text{CH}_2\text{-CH}_2\text{-O}$), 34.22 ($\text{CH}_2\text{-CH}_2\text{-Br}$), 32.70 ($\text{CH}_2\text{-CH}_2\text{-Br}$), 29.47 ($\text{CH}_2\text{-CH}_2\text{-CH}_2$), 28.21 ($\text{CH}_2\text{-CH}_2\text{-CH}_2$), 25.98 ($\text{CH}_2\text{-CH}_2\text{-CH}_2$) ppm

M/z (ESI): 512.1553 (with Na^+)

IR: 3063 (aromatic C-H stretch), 2940 (alkyl C-H stretch), 2857 (alkyl C-H stretch), 2226 (CN stretch), 1740 (aromatic C-H bend), 1599 (aromatic C=C stretch), 1493 (alkyl C-H bend), 1180 (C-O stretch) cm^{-1}

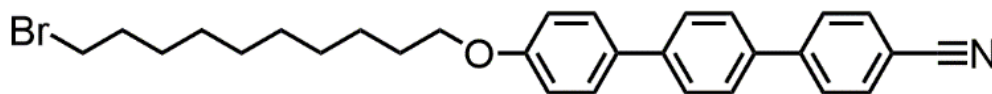


Figure 4.11: Structure of Compound **11** (4-Cyano-4''-(10-bromodecyloxy)terphenyl).

4.2.2.4: Compound **12** (4-Cyano-4''-(11-bromoundecyloxy)terphenyl) (Preparation 4)

Compound **12** was prepared using the same methodology as Compound **7**. The following quantities were used: 11-bromoundecanol 0.49 g; 2.0 mmol, 4-hydroxy-4''-cyanoterphenyl 0.50 g; 1.8 mmol, triphenylphosphine 0.50 g; 1.9 mmol, DIAD 0.39ml; g; 2.0 mmol, and dry THF 150 ml. The product was isolated as colourless crystals.

Yield = 0.63g (1.25 mmol, 69.6 %)

$^1\text{H-NMR}$ (CDCl_3): 7.71 (4H, s, $\text{C}_{\text{Ar-H}}$), 7.64 (4H, m, $\text{C}_{\text{Ar-H}}$), 7.55 (2H, dd, $J = 6.4 \text{ Hz}$, $J = 2 \text{ Hz}$, $\text{C}_{\text{Ar-H}}$), 6.97 (2H, dd, $J = 6.4 \text{ Hz}$, $J = 2 \text{ Hz}$, $\text{C}_{\text{Ar-H}}$), 3.97 (2H, t, $J = 6.4$, O- CH_2), 3.39 (2H, t, $J = 6.4 \text{ Hz}$, Br- CH_2), 1.81 (4H, m, C- CH_2), 1.53-1.20 (14H, m, $\text{CH}_2\text{-CH}_2$) ppm

$^{13}\text{C-NMR}$ (CDCl_3): 159.02 (O- C_{Ar}), 145.24 (Ar-C_{Ar} (with cyano-group adjacent to ring)), 141.22 (Ar-C_{Ar}), 132.63 ($\text{C}_{\text{Ar-C}_{\text{Ar-CN}}}$), 132.59 (Ar-C_{Ar} (attached to ether)), 128.06 ($\text{C}_{\text{A-C}_{\text{Ar-Ar}}}$), 127.54 ($\text{C}_{\text{A-C}_{\text{Ar-Ar}}}$), 127.48 ($\text{Ar-C}_{\text{Ar-C}_{\text{Ar}}}$), 119.01 ($\text{C}_{\text{Ar-C}\equiv\text{N}}$), 114.90 ($\text{C}_{\text{A-C}_{\text{Ar-O}}}$), 110.64 ($\text{C}_{\text{Ar-C}\equiv\text{N}}$), 68.10 ($\text{CH}_2\text{-CH}_2\text{-O}$), 34.06 ($\text{CH}_2\text{-CH}_2\text{-Br}$), 32.80 ($\text{CH}_2\text{-CH}_2\text{-Br}$), 29.52 ($\text{CH}_2\text{-CH}_2\text{-CH}_2$), 28.71 ($\text{CH}_2\text{-CH}_2\text{-CH}_2$), 26.02 ($\text{CH}_2\text{-CH}_2\text{-CH}_2$) ppm

M/z (ESI): 526.1718 (with Na^+)

IR: 3065 (aromatic C-H stretch), 3032 (aromatic C-H stretch), 2918 (alkyl C-H stretch), 2851 (alkyl C-H stretch), 2232 (CN stretch), 1917 (aromatic C-H bend), 1601 (aromatic C=C stretch), 1489 (alkyl C-H bend), 1180 (C-O stretch) cm^{-1}

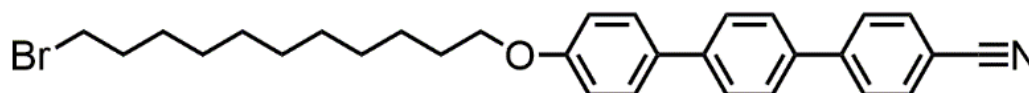


Figure 4.12: Structure of Compound **12** (4-Cyano-4''-(11-bromoundecyloxy)terphenyl).

4.2.2.5: Compound **13** (4-Cyano-4''-(12-bromododecyloxy)terphenyl) (Preparation 3)

Compound **13** was prepared using the same methodology as Compound **4**. The following quantities were used: 1,12-dibromododecane 10.00 g; 30.5 mmol, 4-hydroxy-4''-cyanoterphenyl 0.60 g; 2.2 mmol, potassium carbonate 2.00 g; 14.5 mmol and acetone 120 ml. The product was isolated as colourless crystals.

Yield = 0.71g (1.37 mmol, 62.4 %)

$^1\text{H-NMR}$ (CDCl_3): 7.71 (4H, s, $\text{C}_{\text{Ar}}\text{-H}$), 7.64 (4H, m, $\text{C}_{\text{Ar}}\text{-H}$), 7.54 (2H, dd, $J = 6.4 \text{ Hz}$, $J = 2 \text{ Hz}$, $\text{C}_{\text{Ar}}\text{-H}$), 6.98 (2H, dd, $J = 6.4 \text{ Hz}$, $J = 2 \text{ Hz}$, $\text{C}_{\text{Ar}}\text{-H}$), 3.99 (2H, t, $J = 6.4$, O-CH_2), 3.39 (2H, t, $J = 6.4 \text{ Hz}$, Br-CH_2), 1.82 (4H, m, C-CH_2), 1.54-1.20 (16H, m, $\text{CH}_2\text{-CH}_2$) ppm

$^{13}\text{C-NMR}$ (CDCl_3): 159.11 (O-C_{Ar}), 145.13 (Ar-C_{Ar} (with cyano-group adjacent to ring)), 141.21 (Ar-C_{Ar}), 132.67 (Ar-C_{Ar} (attached to ether)), 132.62 ($\text{C}_{\text{Ar}}\text{-C}_{\text{Ar}}\text{-CN}$), 128.04 ($\text{C}_{\text{A}}\text{-C}_{\text{Ar}}\text{-Ar}$), 127.53 ($\text{C}_{\text{A}}\text{-C}_{\text{Ar}}\text{-Ar}$), 127.47 ($\text{Ar-C}_{\text{Ar}}\text{-C}_{\text{Ar}}$), 119.01 ($\text{C}_{\text{Ar}}\text{-C}\equiv\text{N}$), 114.89 ($\text{C}_{\text{A}}\text{-C}_{\text{Ar}}\text{-O}$), 110.72 ($\text{C}_{\text{Ar}}\text{-C}\equiv\text{N}$), 68.10 ($\text{CH}_2\text{-CH}_2\text{-O}$), 34.09 ($\text{CH}_2\text{-CH}_2\text{-Br}$), 32.81 ($\text{CH}_2\text{-CH}_2\text{-Br}$), 29.53 ($\text{CH}_2\text{-CH}_2\text{-CH}_2$), 28.75 ($\text{CH}_2\text{-CH}_2\text{-CH}_2$), 26.03 ($\text{CH}_2\text{-CH}_2\text{-CH}_2$) ppm

M/z (ESI): 540.1869 (with Na^+)

IR: 3065 (aromatic C-H stretch), 3030 (aromatic C-H stretch), 2918 (alkyl C-H stretch), 2851 (alkyl C-H stretch), 2234 (CN stretch), 1717 (aromatic C-H bend), 1601 (aromatic C=C stretch), 1489 (alkyl C-H bend), 1180 (C-O stretch) cm^{-1}

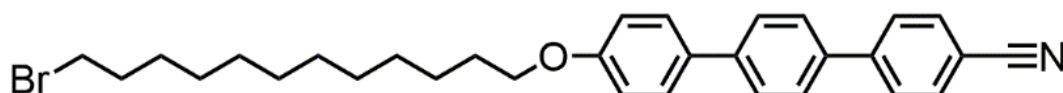


Figure 4.13: Structure of Compound 13 (4-Cyano-4''-(12-bromododecyloxy)terphenyl).

4.3: Diallylamine-Terminated Compound Syntheses

4.3.1: Synthesis of Biphenyl Amine Compounds

4.3.1.1: Compound 14 (4'-cyano-4-(8-*N,N*-diallylaminoctyloxy)biphenyl) (Preparation 1)

Diallylamine (1.50 ml, 12.2 mmol), was added dropwise to a solution of Compound 4 (0.25 g, 0.65 mmol), potassium carbonate (0.70 g, 5.1 mmol) and a catalytic amount of potassium iodide (<0.01 g) in acetone (150 ml). The reaction was heated under reflux (14 h) and then cooled to room temperature, filtered to remove inorganic salts, and the solvent removed under reduced pressure. The product was isolated by column chromatography (on silica) (eluted with DCM to remove impurities and then with methanol and ethyl acetate (40:60) to isolate the product). The product was recrystallized from ethanol to yield colourless crystals.

Yield = 0.22 g (0.55 mmol, 83.9 %)

$^1\text{H-NMR}$ (CDCl_3): 7.67 (2H, dd, $J = 6.4 \text{ Hz}$, $J = 2 \text{ Hz}$, $\text{C}_{\text{Ar}}\text{-H}$), 7.61 (2H, dd, $J = 6.4 \text{ Hz}$, $J = 2 \text{ Hz}$, $\text{C}_{\text{Ar}}\text{-H}$), 7.51 (2H, dd, $J = 6.4 \text{ Hz}$, $J = 2 \text{ Hz}$, $\text{NC-C-C}_{\text{Ar}}\text{-H}$), 6.97 (2H, dd, $J = 6.4 \text{ Hz}$, $J = 2 \text{ Hz}$, $\text{CO-C-C}_{\text{Ar}}\text{-H}$), 5.85 (2H, m, $\text{CH}_2=\text{CH-CH}_2$), 5.15 (8H, m, $\text{CH}_2=\text{CH-CH}_2$ (overlapping peaks)), 3.99 (2H, t, $J = 6.4 \text{ Hz}$, O-C-H_2), 3.70 (2H, m, $\text{N-CH}_2\text{-CH}_2$), 1.80 (4H, m, $\text{CH}_2\text{-C-H}_2$), 1.55-1.20 (8H, m, $\text{CH}_2\text{-C-H}_2$) ppm

$^{13}\text{C-NMR}$ (CDCl_3): 159.68 (O-C_{Ar}), 145.26 (Ar-C_{Ar} (with cyano-group adjacent to ring)), 132.63 ($\text{CH}_2=\text{CH}$), 132.56 ($\text{C}_{\text{Ar}}\text{-C}_{\text{Ar}}\text{-CN}$), 131.12 (Ar-C_{Ar} (attached to ether)), 128.31 ($\text{C}_{\text{A}}\text{-C}_{\text{Ar}}\text{-Ar}$), 127.05 ($\text{C}_{\text{A}}\text{-C}_{\text{Ar}}\text{-Ar}$), 119.18 ($\text{C}_{\text{Ar}}\text{-C}\equiv\text{N}$), 119.07 ($\text{CH}_2=\text{CH}$), 115.03 ($\text{C}_{\text{A}}\text{-C}_{\text{Ar}}\text{-O}$), 110.01 ($\text{C}_{\text{Ar}}\text{-C}\equiv\text{N}$), 68.08 ($\text{CH}_2\text{-CH}_2\text{-O}$), 62.24 ($\text{CH-CH}_2\text{-N}$), 57.29 ($\text{CH}_2\text{-CH}_2\text{-N}$), 30.04 ($\text{CH}_2\text{-CH}_2\text{-CH}_2$), 29.18 ($\text{CH}_2\text{-CH}_2\text{-CH}_2$), 25.97 ($\text{CH}_2\text{-CH}_2\text{-CH}_2$) ppm

M/z (ESI): 403.2746

IR: 3073 (aromatic C-H stretch), 2926 (alkyl C-H stretch), 2855 (alkyl C-H stretch) 2795 (alkyl C-H stretch next to amine), 2224 ($\text{C}\equiv\text{N}$ stretch), 1732 (aromatic C-H bend), 1641 (alkene $\text{C}=\text{C}$ stretch), 1603 (aromatic $\text{C}=\text{C}$ stretch), 1495 (alkyl C-H bend), 1248 (amine C-N stretch), 1179 (C-O stretch) cm^{-1}

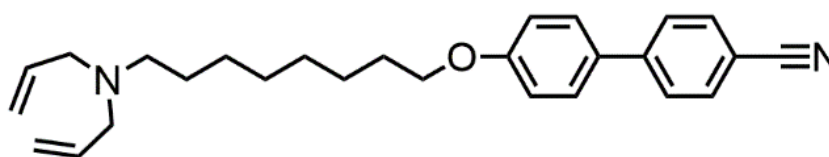


Figure 4.14: Structure of Compound **14** (4'-Cyano-4-(8-N,N-diallylaminoethoxy)biphenyl).

4.3.1.2: Compound 15 (4'-cyano-4-(9-N,N-diallylaminoethoxy)biphenyl) (Preparation 1)

Compound **15** was prepared using the same methodology as Compound **14**. The following quantities were used: Compound **5** (0.25 g; 0.63 mmol), diallylamine (1.5 ml; 12.2 mmol), potassium carbonate (0.70 g; 5.1 mmol), potassium iodide (<0.01 g), and acetone 150 ml. The product was isolated as colourless crystals.

Yield = 0.24g (0.58 mmol, 91.3 %)

$^1\text{H-NMR}$ (CDCl_3): 7.68 (2H, dd, $J = 6.4$ Hz, $J = 2$ Hz, $\text{C}_{\text{Ar}}\text{-H}$), 7.63 (2H, dd, $J = 6.4$ Hz, $J = 2$ Hz, $\text{C}_{\text{Ar}}\text{-H}$), 7.52 (2H, dd, $J = 6.4$ Hz, $J = 2$ Hz, $\text{NC-C-C}_{\text{Ar}}\text{-H}$), 6.99 (2H, dd, $J = 6.4$ Hz, $J = 2$ Hz, $\text{CO-C-C}_{\text{Ar}}\text{-H}$), 5.85 (2H, ddt, $J = 6.4$ Hz, $J = 10.4$ Hz, $J = 18$ Hz $\text{CH}_2=\text{CH-CH}_2$), 5.14 (8H, m, $\text{CH}_2=\text{CH-CH}_2$ (overlapping peaks)), 4.00 (2H, t, $J = 6.4$ Hz, O-C-H_2), 3.08 (2H, m, $\text{N-CH}_2\text{-CH}_2$), 1.80 (4H, m, $\text{CH}_2\text{-C-H}_2$), 1.55-1.20 (10H, m, $\text{CH}_2\text{-C-H}_2$) ppm

$^{13}\text{C-NMR}$ (CDCl_3): 159.74 (O-C_{Ar}), 145.21 (Ar-C_{Ar} (with cyano-group adjacent to ring)), 135.73 ($\text{CH}_2=\text{CH}$), 132.50 ($\text{C}_{\text{Ar}}\text{-C}_{\text{Ar}}\text{-CN}$), 131.16 (Ar-C_{Ar} (attached to ether)), 128.25 ($\text{C}_{\text{A}}\text{-C}_{\text{Ar}}\text{-Ar}$), 127.00 ($\text{C}_{\text{A}}\text{-C}_{\text{Ar}}\text{-Ar}$), 119.08 ($\text{C}_{\text{Ar}}\text{-C}\equiv\text{N}$), 117.27 ($\text{CH}_2=\text{CH}$), 115.01 ($\text{C}_{\text{A}}\text{-C}_{\text{Ar}}\text{-O}$), 110.94 ($\text{C}_{\text{Ar}}\text{-C}\equiv\text{N}$), 68.09 ($\text{CH}_2\text{-CH}_2\text{-O}$), 56.79 ($\text{CH-CH}_2\text{-N}$), 53.31 ($\text{CH}_2\text{-CH}_2\text{-N}$), 29.45 ($\text{CH}_2\text{-CH}_2\text{-CH}_2$), 29.28 ($\text{CH}_2\text{-CH}_2\text{-CH}_2$), 25.96 ($\text{CH}_2\text{-CH}_2\text{-CH}_2$) ppm

M/z (ESI): 417.2915

IR: 3073 (aromatic C-H stretch), 2924 (alkyl C-H stretch), 2853 (alkyl C-H stretch), 2793 (alkyl C-H stretch next to amine), 2224 (C≡N stretch), 1641 (alkene C=C stretch), 1601 (aromatic C=C stretch), 1493 (alkyl C-H bend), 1248 (amine C-N stretch), 1177 (C-O stretch) cm⁻¹

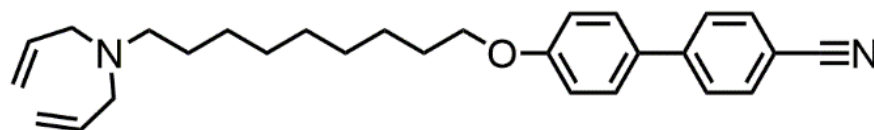


Figure 4.15: Structure of Compound **15** (4'-Cyano-4-(9-*N,N*-diallylaminononyloxy)biphenyl).

4.3.1.3: Compound 16 (4'-cyano-4-(10-*N,N*-diallylaminodecyloxy)biphenyl) (Preparation 1)

Compound **16** was prepared using the same methodology as Compound **14**. The following quantities were used: Compound **6** (0.25 g; 0.61 mmol), diallylamine (1.5 ml; 12.2 mmol), potassium carbonate (0.70 g; 5.1 mmol), potassium iodide (<0.01 g), and acetone 150 ml. The product was isolated as colourless crystals.

Yield = 0.23g (0.53 mmol, 87.4 %)

¹H-NMR (CDCl₃): 7.66 (2H, dd, *J* = 6.4 Hz, *J* = 2 Hz, C_{Ar}-H), 7.61 (2H, dd, *J* = 6.4 Hz, *J* = 2 Hz, C_{Ar}-H), 7.52 (2H, dd, *J* = 6.4 Hz, *J* = 2 Hz, NC-C-C_{Ar}-H), 6.97 (2H, dd, *J* = 6.4 Hz, *J* = 2 Hz, CO-C-C_{Ar}-H), 5.84 (2H, ddt, *J* = 6.4 Hz, *J* = 10.4 Hz, *J* = 17 Hz CH₂=CH-CH₂), 5.14 (8H, m, CH₂=CH-CH₂ (overlapping peaks)), 3.99 (2H, t, *J* = 6.4 Hz, O-C-H₂), 3.68 (2H, m, N-CH₂-CH₂), 1.74 (4H, m, CH₂-C-H₂), 1.50-1.20 (12H, m, CH₂-C-H₂) ppm

¹³C-NMR (CDCl₃): 159.69 (O-C_{Ar}), 145.19 (Ar-C_{Ar} (with cyano-group adjacent to ring)), 135.46 (CH₂=CH), 132.46 (C_{Ar}-C_{Ar}-CN), 131.12 (Ar-C_{Ar} (attached to ether)), 128.22 (C_A-C_{Ar}-Ar), 126.97 (C_A-C_{Ar}-Ar), 119.04 (C_{Ar}-C≡N), 117.44 (CH₂=CH), 114.98 (C_A-C_{Ar}-O), 110.86 (C_{Ar}-C≡N), 68.07 (CH₂-CH₂-O), 58.13 (CH-CH₂-N), 53.26 (CH₂-CH₂-N), 29.44 (CH₂-CH₂-CH₂), 29.28 (CH₂-CH₂-CH₂), 25.93 (CH₂-CH₂-CH₂) ppm

M/z (ESI): 431.3051

IR: 3061 (aromatic C-H stretch), 3030 (aromatic C-H stretch), 2920 (alkyl C-H stretch), 2851 (alkyl C-H stretch), 2222 (C≡N stretch), 1636 (alkene C=C stretch), 1603 (aromatic C=C stretch), 1489 (alkyl C-H bend), 1242 (amine C-N stretch), 1177 (C-O stretch) cm⁻¹

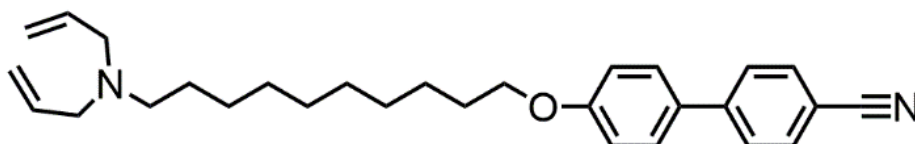


Figure 4.16: Structure of Compound **16** (4'-Cyano-4-(10-*N,N*-diallylaminodecyloxy)biphenyl).

4.3.1.4: Compound 17 (4'-cyano-4-(11-*N,N*-diallylaminoundecyloxy)biphenyl) (Preparation 1)

Compound **17** was prepared using the same methodology as Compound **14**. The following quantities were used: Compound **7** (0.25 g; 0.59 mmol), diallylamine (1.5 ml; 12.2 mmol), potassium carbonate (0.70 g; 5.1 mmol), potassium iodide (<0.01 g), and acetone 150 ml. The product was isolated as colourless crystals.

Yield = 0.26g (0.58 mmol, 98.9 %)

¹H-NMR (CDCl₃): 7.66 (2H, dd, *J* = 6.4 Hz, *J* = 2 Hz, C_{Ar}-H), 7.60 (2H, dd, *J* = 6.4 Hz, *J* = 2 Hz, C_{Ar}-H), 7.49 (2H, dd, *J* = 6.4 Hz, *J* = 2 Hz, NC-C-C_{Ar}-H), 6.96 (2H, dd, *J* = 6.4 Hz, *J* = 2 Hz, CO-C-C_{Ar}-H), 5.83 (2H, ddt, *J* = 6.4 Hz, *J* = 10.4 Hz, *J* = 17 Hz CH₂=CH-CH₂), 5.12 (6H, m, CH₂=CH-CH₂ (overlapping peaks)), 3.97 (2H, t, *J* = 6.4 Hz, O-C-H₂), 3.06 (2H, m, N-CH₂-CH₂), 1.79 (4H, m, CH₂-C-H₂), 1.50-1.20 (14H, m, CH₂-C-H₂) ppm

¹³C-NMR (CDCl₃): 159.71 (O-C_{Ar}), 145.17 (Ar-C_{Ar} (with cyano-group adjacent to ring)), 135.76 (CH₂=CH), 132.46 (C_{Ar}-C_{Ar}-CN), 131.95 (Ar-C_{Ar} (attached to ether)), 128.44 (C_A-C_{Ar}-Ar), 126.96 (C_A-C_{Ar}-Ar), 119.04 (C_{Ar}-C≡N), 117.20 (CH₂=CH), 114.98 (C_A-C_{Ar}-O), 110.89 (C_{Ar}-C≡N), 68.07 (CH₂-CH₂-O), 57.02 (CH-CH₂-N), 53.29 (CH₂-CH₂-N), 29.50 (CH₂-CH₂-CH₂), 29.36 (CH₂-CH₂-CH₂), 25.95 (CH₂-CH₂-CH₂) ppm

M/z (ESI): 445.3209

IR: 3073 (aromatic C-H stretch), 2924 (alkyl C-H stretch), 2853 (alkyl C-H stretch), 2801 (alkyl C-H stretch next to amine), 2226 (C≡N stretch), 1730 (aromatic C-H bend), 1641 (alkene C=C stretch), 1603 (aromatic C=C stretch), 1495 (alkyl C-H bend), 1248 (amine C-N stretch), 1179 (C-O stretch) cm⁻¹

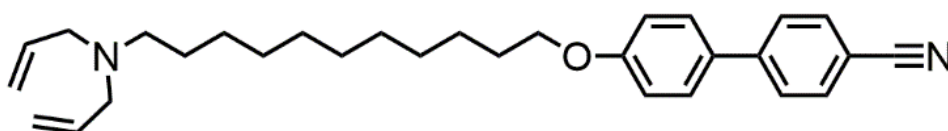


Figure 4.17: Structure of Compound **17** (4'-Cyano-4-(11-*N,N*-diallylaminoundecyloxy)biphenyl).

4.3.1.5: Compound 18 (4'-cyano-4-(12-*N,N*-diallylaminododecyloxy)biphenyl) (Preparation 1)

Compound **18** was prepared using the same methodology as Compound **14**. The following quantities were used: Compound **8** (0.25 g; 0.57 mmol), diallylamine (1.5 ml; 12.2 mmol), potassium carbonate (0.70 g; 5.1 mmol), potassium iodide (<0.01 g), and acetone 150 ml. The product was isolated as colourless crystals.

Yield = 0.25g (0.54 mmol, 95.5 %)

¹H-NMR (CDCl₃): 7.67 (2H, dd, *J* = 6.4 Hz, *J* = 2 Hz, C_{Ar}-H), 7.61 (2H, dd, *J* = 6.4 Hz, *J* = 2 Hz, C_{Ar}-H), 7.50 (2H, dd, *J* = 6.4 Hz, *J* = 2 Hz, NC-C-C_{Ar}-H), 6.97 (2H, dd, *J* = 6.4 Hz, *J* = 2 Hz, CO-C-C_{Ar}-H), 5.84 (2H,

ddt, $J = 6.4$ Hz, $J = 10.4$ Hz, $J = 17$ Hz $\text{CH}_2=\text{CH}-\text{CH}_2$), 5.12 (8H, m, $\text{CH}_2=\text{CH}-\text{CH}_2$ (overlapping peaks)), 3.99 (2H, t, $J = 6.4$ Hz, O-C- H_2), 3.67 (2H, m, N- CH_2-CH_2) 1.78 (4H, m, $\text{CH}_2-\text{C}-H_2$), 1.50-1.20 (16H, m, $\text{CH}_2-\text{C}-H_2$) ppm

^{13}C -NMR (CDCl_3): 159.76 (O- C_{Ar}), 145.25 ($\text{Ar}-C_{Ar}$ (with cyano-group adjacent to ring)), 135.61 ($\text{CH}_2=\text{CH}$), 132.53 ($C_{Ar}-C_{Ar}-\text{CN}$), 131.14 ($\text{Ar}-C_{Ar}$ (attached to ether)), 128.28 ($C_A-C_{Ar}-\text{Ar}$), 127.04 ($C_A-C_{Ar}-\text{Ar}$), 119.12 ($C_{Ar}-\text{C}\equiv\text{N}$), 117.43 ($\text{CH}_2=\text{CH}$), 115.04 ($C_A-C_{Ar}-\text{O}$), 109.93 ($C_{Ar}-\text{C}\equiv\text{N}$), 68.14 ($\text{CH}_2-\text{CH}_2-\text{O}$), 56.77 ($\text{CH}-\text{CH}_2-\text{N}$), 53.34 ($\text{CH}_2-\text{CH}_2-\text{N}$), 29.37 ($\text{CH}_2-\text{CH}_2-\text{CH}_2$), 27.47 ($\text{CH}_2-\text{CH}_2-\text{CH}_2$), 26.00 ($\text{CH}_2-\text{CH}_2-\text{CH}_2$) ppm

M/z (ESI): 459.3379

IR: 3065 (aromatic C-H stretch), 3034 (aromatic C-H stretch), 2918 (alkyl C-H stretch), 2851 (alkyl C-H stretch), 2236 ($\text{C}\equiv\text{N}$ stretch), 1717 (aromatic C-H bend), 1653 (alkene C=C stretch), 1605 (aromatic C=C stretch), 1495 (alkyl C-H bend), 1250 (amine C-N stretch), 1182 (C-O stretch) cm^{-1}

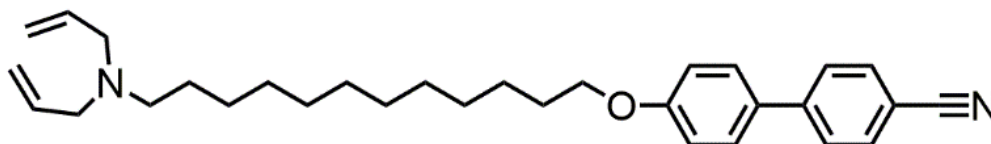


Figure 4.18: Structure of Compound 18 (4'-Cyano-4-(12-*N,N*-diallylaminododecyloxy)biphenyl).

4.3.2: Synthesis of Terphenyl Amine Compounds

4.3.2.1: Compound 19 (4''-cyano-4-(8-*N,N*-diallylamino-octyloxy)terphenyl) (Preparation 1)

Compound 19 was prepared using the same methodology as Compound 14. The following quantities were used: Compound 9 (0.25 g; 0.54 mmol), diallylamine (1.5 ml; 12.2 mmol), potassium carbonate (0.70 g; 5.1 mmol), potassium iodide (<0.01 g), and acetone 150 ml. The product was isolated as colourless crystals.

Yield = 0.24g (0.50 mmol, 92.7 %)

^1H -NMR (CDCl_3): 7.72 (4H, s, $C_{Ar}-H$), 7.64 (4H, m, $C_{Ar}-H$), 7.55 (2H, dd, $J = 6.4$ Hz, $J = 2$ Hz, $C_{Ar}-H$), 6.97 (2H, dd, $J = 6.4$ Hz, $J = 2$ Hz, $C_{Ar}-H$), 5.85 (2H, ddt, $J = 6.4$ Hz, $J = 10.4$ Hz, $J = 17$ Hz $\text{CH}_2=\text{CH}-\text{CH}_2$), 5.13 (8H, m, $\text{CH}_2=\text{CH}-\text{CH}_2$ (overlapping peaks)), 3.99 (2H, t, $J = 6.4$ Hz, O-C- H_2), 3.70 (2H, m, N- CH_2-CH_2) 1.80 (4H, m, $\text{CH}_2-\text{C}-H_2$), 1.54-1.20 (8H, m, $\text{CH}_2-\text{C}-H_2$) ppm

^{13}C -NMR (CDCl_3): 159.00 (O- C_{Ar}), 145.69 ($\text{Ar}-C_{Ar}$ (with cyano-group adjacent to ring)), 141.24 ($\text{Ar}-C_{Ar}$), 135.84 ($\text{CH}_2=\text{CH}$), 132.65 ($\text{Ar}-C_{Ar}$ (attached to ether)), 132.62 ($C_{Ar}-C_{Ar}-\text{CN}$), 128.07 ($C_A-C_{Ar}-\text{Ar}$), 127.54 ($C_A-C_{Ar}-\text{Ar}$), 127.47 ($\text{Ar}-C_{Ar}-C_{Ar}$), 118.84 ($C_{Ar}-\text{C}\equiv\text{N}$), 117.19 ($\text{CH}_2=\text{CH}$), 114.89 ($C_A-C_{Ar}-\text{O}$), 110.74 ($C_{Ar}-\text{C}\equiv\text{N}$), 68.37 ($\text{CH}_2-\text{CH}_2-\text{O}$), 56.30 ($\text{CH}-\text{CH}_2-\text{N}$), 53.35 ($\text{CH}_2-\text{CH}_2-\text{N}$), 29.39 ($\text{CH}_2-\text{CH}_2-\text{CH}_2$), 27.42 ($\text{CH}_2-\text{CH}_2-\text{CH}_2$), 26.09 ($\text{CH}_2-\text{CH}_2-\text{CH}_2$) ppm

M/z (ESI): 479.3063

IR: 3073 (aromatic C-H stretch), 3007 (aromatic C-H stretch), 2924 (alkyl C-H stretch), 2853 (alkyl C-H stretch), 2793 (alkyl C-H stretch next to amine), 2224 (C≡N stretch), 1641 (alkene C=C stretch), 1601 (aromatic C=C stretch), 1493 (alkyl C-H bend), 1248 (amine C-N stretch), 1177 (C-O stretch) cm^{-1}

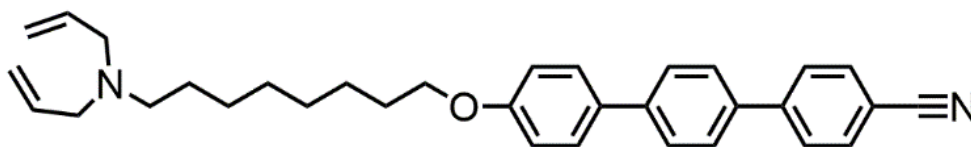


Figure 4.19: Structure of Compound **19** (4''-Cyano-4-(8-*N,N*-diallylaminooctyloxy)terphenyl).

4.3.2.2: Compound **20** (4''-cyano-4-(9-*N,N*-diallylaminononyloxy)terphenyl) (Preparation 1)

Compound **20** was prepared using the same methodology as Compound **14**. The following quantities were used: Compound **10** (0.25 g; 0.53 mmol), diallylamine (1.5 ml; 12.2 mmol), potassium carbonate (0.70 g; 5.1 mmol), potassium iodide (<0.01 g), and acetone 150 ml. The product was isolated as colourless crystals.

Yield = 0.25g (0.51 mmol, 95.6 %)

$^1\text{H-NMR}$ (CDCl_3): 7.71 (4H, s, $\text{C}_{\text{Ar-H}}$), 7.64 (4H, m, $\text{C}_{\text{Ar-H}}$), 7.55 (2H, dd, $J = 6.4 \text{ Hz}$, $J = 2 \text{ Hz}$, $\text{C}_{\text{Ar-H}}$), 6.98 (2H, dd, $J = 6.4 \text{ Hz}$, $J = 2 \text{ Hz}$, $\text{C}_{\text{Ar-H}}$), 5.77 (2H, ddt, $J = 6.4 \text{ Hz}$, $J = 10.4 \text{ Hz}$, $J = 17 \text{ Hz}$ $\text{CH}_2=\text{CH}-\text{CH}_2$), 5.17 (8H, m, $\text{CH}_2=\text{CH}-\text{CH}_2$ (overlapping peaks)), 3.99 (2H, t, $J = 6.4 \text{ Hz}$, $\text{O}-\text{C}-\text{H}_2$), 3.40 (2H, m, $\text{N}-\text{CH}_2-\text{CH}_2$) 1.81 (4H, m, $\text{CH}_2-\text{C}-\text{H}_2$), 1.56-1.20 (10H, m, $\text{CH}_2-\text{C}-\text{H}_2$) ppm

$^{13}\text{C-NMR}$ (CDCl_3): 159.03 ($\text{O}-\text{C}_{\text{Ar}}$), 145.23 ($\text{Ar}-\text{C}_{\text{Ar}}$ (with cyano-group adjacent to ring)), 141.21 ($\text{Ar}-\text{C}_{\text{Ar}}$), 137.24 ($\text{CH}_2=\text{CH}$), 132.63 ($\text{Ar}-\text{C}_{\text{Ar}}$ (attached to ether)), 132.32 ($\text{C}_{\text{Ar}}-\text{C}_{\text{Ar}}-\text{CN}$), 128.05 ($\text{C}_{\text{A}}-\text{C}_{\text{Ar}}-\text{Ar}$), 127.53 ($\text{C}_{\text{A}}-\text{C}_{\text{Ar}}-\text{Ar}$), 127.47 ($\text{Ar}-\text{C}_{\text{Ar}}-\text{C}_{\text{Ar}}$), 118.97 ($\text{C}_{\text{Ar}}-\text{C}\equiv\text{N}$), 117.41 ($\text{CH}_2=\text{CH}$), 114.88 ($\text{C}_{\text{A}}-\text{C}_{\text{Ar}}-\text{O}$), 110.72 ($\text{C}_{\text{Ar}}-\text{C}\equiv\text{N}$), 68.04 ($\text{CH}_2-\text{CH}_2-\text{O}$), 56.44 ($\text{CH}-\text{CH}_2-\text{N}$), 53.77 ($\text{CH}_2-\text{CH}_2-\text{N}$), 29.24 ($\text{CH}_2-\text{CH}_2-\text{CH}_2$), 28.12 ($\text{CH}_2-\text{CH}_2-\text{CH}_2$), 26.00 ($\text{CH}_2-\text{CH}_2-\text{CH}_2$) ppm

M/z (ESI): 493.3238

IR: 3038 (aromatic C-H stretch), 2920 (alkyl C-H stretch), 2851 (alkyl C-H stretch), 2222 (C≡N stretch), 1738 (aromatic C-H bend), 1684 (alkene C=C stretch), 1601 (aromatic C=C stretch), 1489 (alkyl C-H bend), 1242 (amine C-N stretch), 1175 (C-O stretch) cm^{-1}

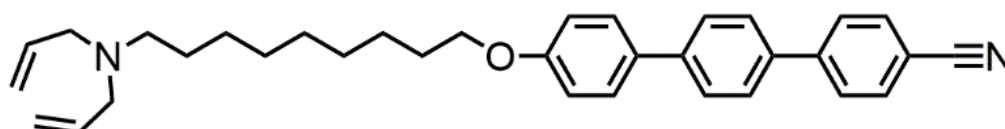


Figure 4.20: Structure of Compound **20** (4''-Cyano-4-(9-*N,N*-diallylaminononyloxy)terphenyl).

4.3.2.3: Compound 21 (4''-cyano-4-(10-*N,N*-diallylaminodecyloxy)terphenyl) (Preparation 1)

Compound **21** was prepared using the same methodology as Compound **14**. The following quantities were used: Compound **11** (0.25 g; 0.51 mol), diallylamine (1.5 ml; 12.2 mmol), potassium carbonate (0.70 g; 5.1 mmol), potassium iodide (<0.01 g), and acetone 150 ml. The product was isolated as colourless crystals.

Yield = 0.23g (0.45 mmol, 88.9 %)

¹H-NMR (CDCl₃): 7.72 (4H, s, C_{Ar}-H), 7.65 (4H, m, C_{Ar}-H), 7.56 (2H, dd, *J* = 6.4 Hz, *J* = 2 Hz, C_{Ar}-H), 6.99 (2H, dd, *J* = 6.4 Hz, *J* = 2 Hz, C_{Ar}-H), 5.85 (2H, ddt, *J* = 6.4 Hz, *J* = 10.4 Hz, *J* = 17 Hz CH₂=CH-CH₂), 5.14 (8H, m, CH₂=CH-CH₂ (overlapping peaks)), 4.00 (2H, t, *J* = 6.4 Hz, O-C-H₂), 3.09 (2H, m, N-CH₂-CH₂) 1.80 (4H, m, CH₂-C-H₂), 1.54-1.20 (12H, m, CH₂-C-H₂) ppm

¹³C-NMR (CDCl₃): 159.09 (O-C_{Ar}), 145.69 (Ar-C_{Ar} (with cyano-group adjacent to ring)), 141.66 (Ar-C_{Ar}), 135.58 (CH₂=CH), 132.63 (Ar-C_{Ar} (attached to ether)), 132.49 (C_{Ar}-C_{Ar}-CN), 128.05 (C_A-C_{Ar}-Ar), 127.54 (C_A-C_{Ar}-Ar), 127.46 (Ar-C_{Ar}-C_{Ar}), 118.64 (C_{Ar}-C≡N), 116.94 (CH₂=CH), 114.90 (C_A-C_{Ar}-O), 110.92 (C_{Ar}-C≡N), 68.10 (CH₂-CH₂-O), 56.67 (CH-CH₂-N), 53.61 (CH₂-CH₂-N), 29.55 (CH₂-CH₂-CH₂), 27.42 (CH₂-CH₂-CH₂), 25.82 (CH₂-CH₂-CH₂) ppm

M/z (ESI): 507.3398

IR: 3073 (aromatic C-H stretch), 2920 (alkyl C-H stretch), 2851 (alkyl C-H stretch), 2797 (alkyl C-H stretch next to amine), 2224 (C≡N stretch), 1915 (aromatic C-H bend), 1643 (alkene C=C stretch), 1601 (aromatic C=C stretch), 1489 (alkyl C-H bend), 1246 (amine C-N stretch), 1177 (C-O stretch) cm⁻¹

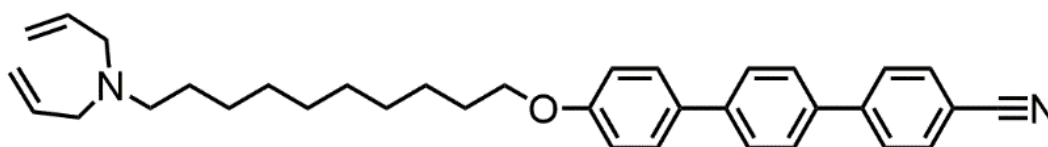


Figure 4.21: Structure of Compound **21** (4''-Cyano-4-(10-*N,N*-diallylaminodecyloxy)terphenyl).

4.3.2.4: Compound 22 (4''-cyano-4-(11-*N,N*-diallylaminoundecyloxy)terphenyl) (Preparation 1)

Compound **22** was prepared using the same methodology as Compound **14**. The following quantities were used: Compound **12** (0.25 g; 0.50 mmol), diallylamine (1.5 ml; 12.2 mmol), potassium carbonate (0.70 g; 5.7 mmol), potassium iodide (<0.01 g), and acetone 150 ml. The product was isolated as colourless crystals.

Yield = 0.25g (0.48 mmol, 95.9 %)

¹H-NMR (CDCl₃): 7.71 (4H, s, C_{Ar}-H), 7.64 (4H, m, C_{Ar}-H), 7.54 (2H, dd, *J* = 6.4 Hz, *J* = 2 Hz, C_{Ar}-H), 6.97 (2H, dd, *J* = 6.4 Hz, *J* = 2 Hz, C_{Ar}-H), 5.85 (2H, ddt, *J* = 6.4 Hz, *J* = 10.4 Hz, *J* = 17 Hz CH₂=CH-CH₂), 5.12

(8H, m, CH₂=CH-CH₂ (overlapping peaks)), 3.99 (2H, t, *J* = 6.4 Hz, O-C-H₂), 3.07 (2H, m, N-CH₂-CH₂) 1.79 (4H, m, CH₂-C-H₂), 1.50-1.20 (14H, m, CH₂-C-H₂) ppm

¹³C-NMR (CDCl₃): 159.08 (O-C_{Ar}), 145.20 (Ar-C_{Ar} (with cyano-group adjacent to ring)), 141.22 (Ar-C_{Ar}), 135.74 (CH₂=CH), 132.61 (Ar-C_{Ar} (attached to ether)), 132.33 (C_{Ar}-C_{Ar}-CN), 128.03 (C_A-C_{Ar}-Ar), 127.52 (C_A-C_{Ar}-Ar), 127.45 (Ar-C_{Ar}-C_{Ar}), 118.93 (C_{Ar}-C≡N), 117.33 (CH₂=CH), 114.88 (C_A-C_{Ar}-O), 110.71 (C_{Ar}-C≡N), 68.10 (CH₂-CH₂-O), 56.80 (CH-CH₂-N), 53.35 (CH₂-CH₂-N), 29.53 (CH₂-CH₂-CH₂), 27.48 (CH₂-CH₂-CH₂), 26.04 (CH₂-CH₂-CH₂) ppm

M/z (ESI): 521.3567

IR: 3071 (aromatic C-H stretch), 3036 (aromatic C-H stretch), 2920 (alkyl C-H stretch), 2849 (alkyl C-H stretch), 2795 (alkyl C-H stretch next to amine), 2224 (C≡N stretch), 1915 (aromatic C-H bend), 1713 (aromatic C-H bend), 1643 (alkene C=C stretch), 1601 (aromatic C=C stretch), 1489 (alkyl C-H bend), 1244 (amine C-N stretch), 1175 (C-O stretch) cm⁻¹

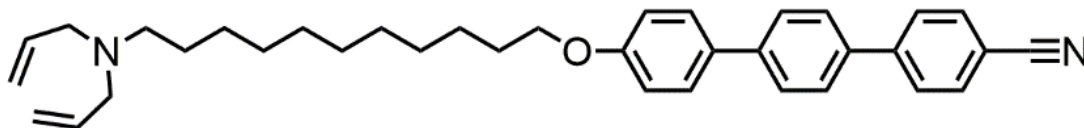


Figure 4.22: Structure of Compound **22** (4''-Cyano-4-(11-*N,N*-diallylaminoundecyloxy)terphenyl).

4.3.2.5: Compound **23** (4''-cyano-4-(12-*N,N*-diallylaminododecyloxy)terphenyl) (Preparation 1)

Compound **23** was prepared using the same methodology as Compound **14**. The following quantities were used: Compound **13** (0.25 g; 0.48 mmol), diallylamine (1.5 ml; 12.2 mmol), potassium carbonate (0.70 g; 5.7 mmol), potassium iodide (<0.01 g), and acetone 150 ml. The product was isolated as colourless crystals.

Yield = 0.24g (0.45 mmol, 93.4 %)

¹H-NMR (CDCl₃): 7.71 (4H, s, C_{Ar}-H), 7.64 (4H, m, C_{Ar}-H), 7.54 (2H, dd, *J* = 6.4 Hz, *J* = 2 Hz, C_{Ar}-H), 6.97 (2H, dd, *J* = 6.4 Hz, *J* = 2 Hz, C_{Ar}-H), 5.84 (2H, ddt, *J* = 6.4 Hz, *J* = 10.4 Hz, *J* = 17 Hz CH₂=CH-CH₂), 5.12 (8H, m, CH₂=CH-CH₂ (overlapping peaks)), 3.99 (2H, t, *J* = 6.4 Hz, O-C-H₂), 3.07 (2H, m, N-CH₂-CH₂) 1.79 (4H, m, CH₂-C-H₂), 1.59-1.20 (16H, m, CH₂-C-H₂) ppm

¹³C-NMR (CDCl₃): 159.08 (O-C_{Ar}), 145.22 (Ar-C_{Ar} (with cyano-group adjacent to ring)), 141.23 (Ar-C_{Ar}), 135.78 (CH₂=CH), 132.62 (Ar-C_{Ar} (attached to ether)), 132.34 (C_{Ar}-C_{Ar}-CN), 128.04 (C_A-C_{Ar}-Ar), 127.53 (C_A-C_{Ar}-Ar), 127.47 (Ar-C_{Ar}-C_{Ar}), 118.93 (C_{Ar}-C≡N), 117.31 (CH₂=CH), 114.89 (C_A-C_{Ar}-O), 110.71 (C_{Ar}-C≡N), 68.12 (CH₂-CH₂-O), 56.82 (CH-CH₂-N), 53.36 (CH₂-CH₂-N), 29.58 (CH₂-CH₂-CH₂), 27.49 (CH₂-CH₂-CH₂), 26.04 (CH₂-CH₂-CH₂) ppm

M/z (ESI): 535.3751

IR: 3075 (aromatic C-H stretch), 2920 (alkyl C-H bend), 2849 (alkyl C-H stretch), 2799 (alkyl C-H stretch next to amine), 2232 (C≡N stretch), 1917 (aromatic C-H bend), 1738 (aromatic C-H bend), 1643 (alkene C=C stretch), 1601 (aromatic C=C stretch), 1489 (alkyl C-H bend), 1258 (amine C-N stretch), 1180 (C-O stretch) cm^{-1}

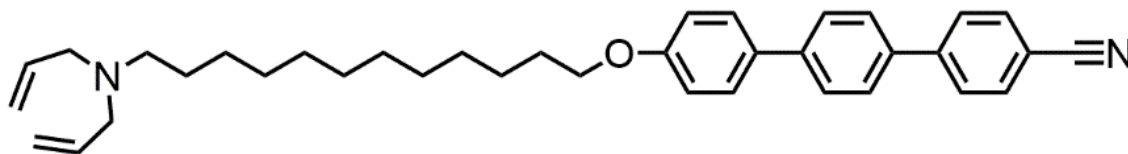


Figure 4.23: Structure of Compound **23** (4''-Cyano-4-(12-*N,N*-diallylaminododecyloxy)terphenyl).

4.4: Synthesis of Ester Compounds

4.4.1: Synthesis of Bromo-terminated Benzoate Ester Compounds

4.4.1.1: Compound 24 (Ethyl 4-((8-bromooctyl)oxy)benzoate) (Preparation 3)

Ethyl-4-hydroxy benzoate (0.50 g, 3.0 mmol), 1,8-dibromooctane (8.00 g, 29.4 mmol) and potassium carbonate (2.00 g, 14.5 mmol) were mixed in acetone (120 ml) and heated under reflux (20 h). The reaction was cooled to room temperature, filtered to remove the inorganic salts, and the solvent was then removed under reduced pressure. The mixture was separated by column chromatography on silica (the unreacted excess 1,8-dibromooctane eluted with hexane, the target compound with hexane:DCM (90:10), and the di-substituted compound with DCM). The product obtained was a white solid.

Yield = 0.63 g (1.76 mmol, 58.8 %)

$^1\text{H-NMR}$ (CDCl_3): 7.92 (2H, d, $J = 8.84$ Hz, $\text{C}_{\text{Ar}}\text{H-C}_{\text{Ar}}\text{-C=O}$), 6.85 (2H, d, $J = 8.84$ Hz, $\text{C}_{\text{Ar}}\text{H-C}_{\text{Ar}}\text{-C-O}$), 4.26 (2H, q, $J = 6.8$ Hz, $\text{C}_{\text{Ar}}\text{-C(O)-O-CH}_2\text{-CH}_3$), 3.94 (2H, t, $J = 6.4$ Hz, $\text{C}_{\text{Ar}}\text{-C-O-CH}_2\text{-CH}_2$), 3.36 (2H, t, $J = 7.2$ Hz, $\text{Br-CH}_2\text{-CH}_2$), 1.82 (4H, m, (O or Br)- $\text{CH}_2\text{-CH}_2\text{-CH}_2$, overlapping peaks), 1.53-1.08 (11H, m, $\text{CH}_2\text{-CH}_2\text{-CH}_2$ and CH_3) ppm

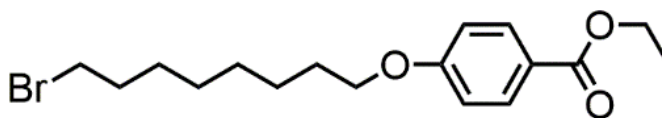


Figure 4.24: Structure of Compound **24** (Ethyl 4-((8-bromooctyl)oxy)benzoate).

4.4.1.2: Compound 25 (Ethyl 4-((9-bromononyl)oxy)benzoate) (Preparation 3)

Compound **25** was prepared using the same methodology as Compound **24**. The following quantities were used: Ethyl 4-hydroxybenzoate (0.50 g; 3.0 mmol), 1,9-dibromononane (8.00 g; 28.0 mmol), potassium carbonate (2.00 g; 14.5 mmol) and acetone 120 ml. The product was isolated as a white powder.

Yield = 0.66g (1.78 mmol, 59.2 %)

$^1\text{H-NMR}$ (CDCl_3): 7.93 (2H, d, $J = 8.84$ Hz, $\text{C}_{\text{Ar}}\text{H-C}_{\text{Ar}}\text{-C=O}$), 6.88 (2H, d, $J = 8.84$ Hz, $\text{C}_{\text{Ar}}\text{H-C}_{\text{Ar}}\text{-C-O}$), 4.33 (2H, q, $J = 6.8$ Hz, $\text{C}_{\text{Ar}}\text{-C(O)-O-CH}_2\text{-CH}_3$), 3.97 (2H, t, $J = 6.4$ Hz, $\text{C}_{\text{Ar}}\text{-C-O-CH}_2\text{-CH}_2$), 3.39 (2H, t, $J = 7.2$ Hz, $\text{Br-CH}_2\text{-CH}_2$), 1.82 (4H, m, (O or Br)- $\text{CH}_2\text{-CH}_2\text{-CH}_2$, overlapping peaks), 1.53-1.08 (13H, m, $\text{CH}_2\text{-CH}_2\text{-CH}_2$ and CH_3) ppm

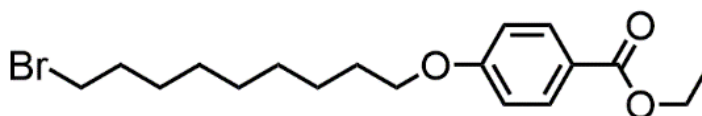


Figure 4.25: Structure of Compound **25** (Ethyl 4-((9-bromononyl)oxy)benzoate).

4.4.1.3: Compound 26 (Ethyl 4-((10-bromodecyl)oxy)benzoate) (Preparation 3)

Compound **26** was prepared using the same methodology as Compound **24**. The following quantities were used: Ethyl 4-hydroxybenzoate (0.50 g; 3.0 mmol), 1,9-dibromodecane (8.00 g; 26.7 mmol), potassium carbonate (2.00 g; 14.5 mmol) and acetone 120 ml. The product was isolated as a white solid.

Yield = 0.61 g (1.58 mmol, 52.8 %)

$^1\text{H-NMR}$ (CDCl_3): 7.96 (2H, d, $J = 8.84$ Hz, $\text{C}_{\text{Ar}}\text{H-C}_{\text{Ar}}\text{-C=O}$), 6.88 (2H, d, $J = 8.84$ Hz, $\text{C}_{\text{Ar}}\text{H-C}_{\text{Ar}}\text{-C-O}$), 4.31 (2H, q, $J = 6.8$ Hz, $\text{C}_{\text{Ar}}\text{-C(O)-O-CH}_2\text{-CH}_3$), 3.80 (2H, t, $J = 6.4$ Hz, $\text{C}_{\text{Ar}}\text{-C-O-CH}_2\text{-CH}_2$), 3.39 (2H, t, $J = 7.2$ Hz, $\text{Br-CH}_2\text{-CH}_2$), 1.81 (4H, m, (O or Br)- $\text{CH}_2\text{-CH}_2\text{-CH}_2$, overlapping peaks), 1.53-1.08 (15H, m, $\text{CH}_2\text{-CH}_2\text{-CH}_2$ and CH_3) ppm

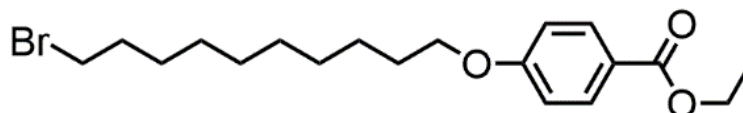


Figure 4.26: Structure of Compound **26** (Ethyl 4-((10-bromodecyl)oxy)benzoate).

4.4.1.4: Compound 27 (Ethyl 4-((11-bromoundecyl)oxy)benzoate) (Preparation 4)

DIAD (0.70 ml, 3.55 mmol) was added dropwise to a stirred solution of 11-bromoundecanol (0.75 g, 3.0 mmol) ethyl-4-hydroxybenzoate (0.52 g, 3.1 mmol) and triphenylphosphine (0.77 g, 2.9 mmol) in dry THF (150 ml) under a nitrogen atmosphere. The reaction was stirred (14 h) until completion and then the solvent was removed under reduced pressure. The product was isolated by column chromatography on silica (eluted with a gradient of petroleum ether (bp 40-60 °C) and DCM, 10% increments of DCM from 0 % to 60 %). The product was isolated as a white powder.

Yield = 0.72 g (1.80 mmol, 60.1 %)

$^1\text{H-NMR}$ (CDCl_3): 7.95 (2H, d, $J = 8.84$ Hz, $\text{C}_{\text{Ar}}\text{H-C}_{\text{Ar}}\text{-C=O}$), 6.87 (2H, d, $J = 8.84$ Hz, $\text{C}_{\text{Ar}}\text{H-C}_{\text{Ar}}\text{-C-O}$), 4.32 (2H, q, $J = 6.8$ Hz, $\text{C}_{\text{Ar}}\text{-C(O)-O-CH}_2\text{-CH}_3$), 3.97 (2H, t, $J = 6.4$ Hz, $\text{C}_{\text{Ar}}\text{-C-O-CH}_2\text{-CH}_2$), 3.38 (2H, t, $J = 7.2$ Hz, $\text{Br-CH}_2\text{-CH}_2$), 1.81 (4H, m, (O or Br)- $\text{CH}_2\text{-CH}_2\text{-CH}_2$, overlapping peaks), 1.53-1.08 (17H, m, $\text{CH}_2\text{-CH}_2\text{-CH}_2$ and CH_3) ppm

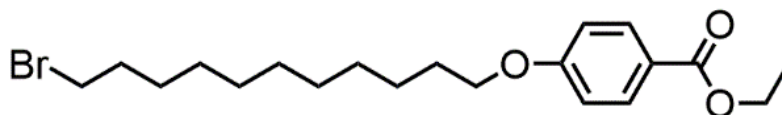


Figure 4.27: Structure of Compound **27** (Ethyl 4-((11-bromoundecyl)oxy)benzoate).

4.4.1.5: Compound 28 (Ethyl 4-((12-bromododecyl)oxy)benzoate) (Preparation 3)

Compound **28** was prepared using the same methodology as Compound **24**. The following quantities were used: Ethyl 4-hydroxybenzoate (0.50 g; 3.0 mmol), 1,9-dibromododecane (8.00 g; 24.4 mmol), potassium carbonate (2.00 g; 14.5 mmol) and acetone 120 ml. The product was isolated as a white solid.

Yield = 0.63g (1.52 mmol, 50.8 %)

$^1\text{H-NMR}$ (CDCl_3): 7.93 (2H, d, $J = 8.84$ Hz, $\text{C}_{\text{Ar}}\text{H-C}_{\text{Ar}}\text{-C=O}$), 6.85 (2H, d, $J = 8.84$ Hz, $\text{C}_{\text{Ar}}\text{H-C}_{\text{Ar}}\text{-C-O}$), 4.28 (2H, q, $J = 6.8$ Hz, $\text{C}_{\text{Ar}}\text{-C(O)-O-CH}_2\text{-CH}_3$), 3.94 (2H, t, $J = 6.4$ Hz, $\text{C}_{\text{Ar}}\text{-C-O-CH}_2\text{-CH}_2$), 3.35 (2H, t, $J = 7.2$ Hz, $\text{Br-CH}_2\text{-CH}_2$), 1.81 (4H, m, $(\text{O or Br})\text{-CH}_2\text{-CH}_2\text{-CH}_2$, overlapping peaks), 1.53-1.08 (19H, m, $\text{CH}_2\text{-CH}_2$ and CH_3) ppm

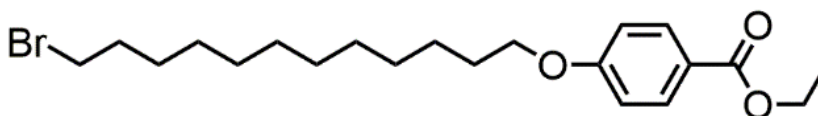


Figure 4.28: Structure of Compound **28** (Ethyl 4-((12-bromododecyl)oxy)benzoate).

4.4.2: Synthesis of Amino-terminated Benzoate Ester Compounds

4.4.2.1: Compound 29 (Ethyl 4-((8-diallylamino)octyl)oxy)benzoate) (Preparation 1)

Compound **29** was prepared using the same methodology as Compound **14**. The following quantities were used: Compound **24** (0.50 g; 1.40 mmol), diallylamine (5 ml; 40.5 mmol), potassium carbonate (2.00 g; 14.5 mmol), potassium iodide (<0.01 g), and acetone 100 ml. The product was isolated as a yellow oil.

Yield = 0.49 g (1.31 mmol, 93.7 %)

$^1\text{H-NMR}$ (CDCl_3): 7.92 (2H, d, $J = 8.84$ Hz, $\text{C}_{\text{Ar}}\text{H-C}_{\text{Ar}}\text{-C=O}$), 6.85 (2H, d, $J = 8.84$ Hz, $\text{C}_{\text{Ar}}\text{H-C}_{\text{Ar}}\text{-C-O}$), 5.89 (2H, ddt, $J = 6.4$ Hz, $J = 10.4$ Hz, $J = 17$ Hz $\text{CH}_2=\text{CH-CH}_2$), 5.23 (8H, m, $\text{CH}_2=\text{CH-CH}_2$ (overlapping peaks)), 4.29 (2H, q, $J = 6.8$ Hz, $\text{C}_{\text{Ar}}\text{-C(O)-O-CH}_2\text{-CH}_3$), 3.93 (2H, t, $J = 6.4$ Hz, $\text{C}_{\text{Ar}}\text{-C-O-CH}_2\text{-CH}_2$), 3.16 (2H, m, $\text{N-CH}_2\text{-CH}_2$), 2.45 (2H, t, $J = 7.2$ Hz, $\text{Br-CH}_2\text{-CH}_2$), 1.83 (4H, m, $\text{O-CH}_2\text{-CH}_2\text{-CH}_2$, overlapping peaks), 1.46-1.08 (13H, m, $\text{CH}_2\text{-CH}_2\text{-CH}_2$ and CH_3) ppm

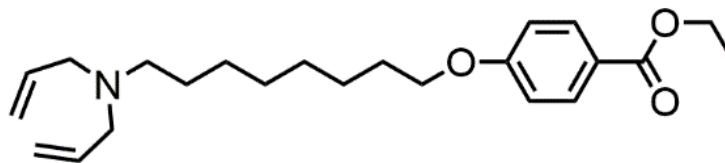


Figure 4.29: Structure of Compound **29** (Ethyl 4-((8-diallylamino)octyl)oxy)benzoate).

4.4.2.2: Compound 30 (Ethyl 4-((9-diallylamino)nonyl)oxy)benzoate) (Preparation 1)

Compound **30** was prepared using the same methodology as Compound **14**. The following quantities were used: Compound **25** (0.50 g; 1.35 mmol), diallylamine (5 ml; 40.5 mmol), potassium carbonate (2.00 g; 14.5 mmol), potassium iodide (<0.01 g), and acetone 100 ml. The product was isolated as a yellow oil.

Yield = 0.51g (1.32 mmol, 97.5 %)

$^1\text{H-NMR}$ (CDCl_3): 7.94 (2H, d, $J = 8.84$ Hz, $\text{C}_{\text{Ar}}\text{H-C}_{\text{Ar}}\text{-C=O}$), 6.84 (2H, d, $J = 8.84$ Hz, $\text{C}_{\text{Ar}}\text{H-C}_{\text{Ar}}\text{-C-O}$), 5.84 (2H, ddt, $J = 6.4$ Hz, $J = 10.4$ Hz, $J = 17$ Hz $\text{CH}_2=\text{CH-CH}_2$), 5.11 (8H, m, $\text{CH}_2=\text{CH-CH}_2$ (overlapping peaks)), 4.28 (2H, q, $J = 6.8$ Hz, $\text{C}_{\text{Ar}}\text{-C(O)-O-CH}_2\text{-CH}_3$), 3.94 (2H, t, $J = 6.4$ Hz, $\text{C}_{\text{Ar}}\text{-C-O-CH}_2\text{-CH}_2$), 3.18 (2H, m, $\text{N-CH}_2\text{-CH}_2$), 2.37 (2H, t, $J = 7.2$ Hz, $\text{N-CH}_2\text{-CH}_2$), 1.73 (4H, m, $\text{O-CH}_2\text{-CH}_2\text{-CH}_2$, overlapping peaks), 1.33-1.08 (15H, m, $\text{CH}_2\text{-CH}_2\text{-CH}_2$ and CH_3) ppm

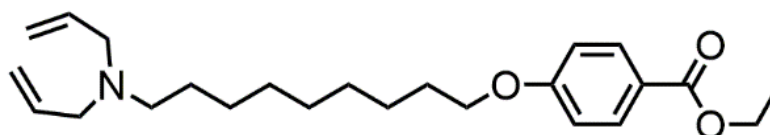


Figure 4.30: Structure of Compound **30** (Ethyl 4-((9-diallylamino)nonyl)oxy)benzoate).

4.4.2.3: Compound 31 (Ethyl 4-((10-diallylamino)decyl)oxy)benzoate) (Preparation 1)

Compound **31** was prepared using the same methodology as Compound **14**. The following quantities were used: Compound **26** (0.50 g; 1.30 mmol), diallylamine (5 ml; 40.5 mmol), potassium carbonate (2.00 g; 14.5 mmol), potassium iodide (<0.01 g), and acetone 100 ml. The product was isolated as a yellow oil.

Yield = 0.49 g (1.22 mmol, 93.9 %)

$^1\text{H-NMR}$ (CDCl_3): 7.98 (2H, d, $J = 8.84$ Hz, $\text{C}_{\text{Ar}}\text{H-C}_{\text{Ar}}\text{-C=O}$), 6.90 (2H, d, $J = 8.84$ Hz, $\text{C}_{\text{Ar}}\text{H-C}_{\text{Ar}}\text{-C-O}$), 5.89 (2H, ddt, $J = 6.4$ Hz, $J = 10.4$ Hz, $J = 17$ Hz $\text{CH}_2=\text{CH-CH}_2$), 5.22 (8H, m, $\text{CH}_2=\text{CH-CH}_2$ (overlapping peaks)), 4.35 (2H, q, $J = 6.8$ Hz, $\text{C}_{\text{Ar}}\text{-C(O)-O-CH}_2\text{-CH}_3$), 3.98 (2H, t, $J = 6.4$ Hz, $\text{C}_{\text{Ar}}\text{-C-O-CH}_2\text{-CH}_2$), 3.38 (2H, m, $\text{N-CH}_2\text{-CH}_2$), 2.45 (2H, t, $J = 7.2$ Hz, $\text{N-CH}_2\text{-CH}_2$), 1.82 (4H, m, $\text{O-CH}_2\text{-CH}_2\text{-CH}_2$, overlapping peaks), 1.53-1.08 (17H, m, $\text{CH}_2\text{-CH}_2\text{-CH}_2$ and CH_3) ppm

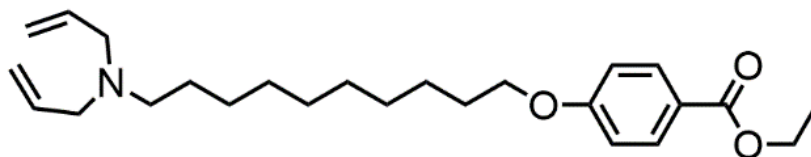


Figure 4.31: Structure of Compound **31** (Ethyl 4-((10-diallylamino)decyl)oxy)benzoate).

4.4.2.4: Compound 32 (Ethyl 4-((11-diallylamino)undecyl)oxy)benzoate) (Preparation 1)

Compound **32** was prepared using the same methodology as Compound **14**. The following quantities were used: Compound **27** (0.50 g; 1.25 mmol), diallylamine (5 ml; mmol), potassium carbonate (2.00 g; mol), potassium iodide (<0.01 g), and acetone 100 ml. The product was isolated as a yellow oil.

Yield = 0.50 g (1.20 mmol, 96.2 %)

¹H-NMR (CDCl₃): 7.95 (2H, d, *J* = 8.84 Hz, C_{Ar}H-C_{Ar}-C=O), 6.88 (2H, d, *J* = 8.84 Hz, C_{Ar}H-C_{Ar}-C-O), 5.89 (2H, ddt, *J* = 6.4 Hz, *J* = 10.4 Hz, *J* = 17 Hz CH₂=CH-CH₂), 5.16 (8H, m, CH₂=CH-CH₂ (overlapping peaks)), 4.31 (2H, q, *J* = 6.8 Hz, C_{Ar}-C(O)-O-CH₂-CH₃), 3.98 (2H, t, *J* = 6.4 Hz, C_{Ar}-C-O-CH₂-CH₂), 3.12 (2H, m, N-CH₂-CH₂), 2.45 (2H, t, *J* = 7.2 Hz, N-CH₂-CH₂), 1.81 (4H, m, O-CH₂-CH₂-CH₂, overlapping peaks), 1.53-1.08 (19H, m, CH₂-CH₂-CH₂ and CH₃) ppm

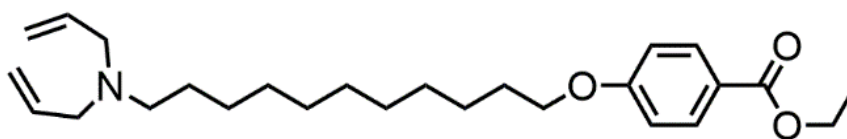


Figure 4.32: Structure of Compound **32** (Ethyl 4-((11-diallylamino)undecyl)oxy)benzoate).

4.4.2.5: Compound 33 (Ethyl 4-((12-diallylamino)dodecyl)oxy)benzoate) (Preparation 1)

Compound **33** was prepared using the same methodology as Compound **14**. The following quantities were used: Compound **28** (0.50 g; 1.21 mmol), diallylamine (5 ml; 40.5 mmol), potassium carbonate (2.00 g; 14.5 mmol), potassium iodide (<0.01 g), and acetone 100 ml. The product was isolated as a yellow oil.

Yield = 0.48 g (1.12 mmol, 92.3 %)

¹H-NMR (CDCl₃): 7.99 (2H, d, *J* = 8.84 Hz, C_{Ar}H-C_{Ar}-C=O), 6.90 (2H, d, *J* = 8.84 Hz, C_{Ar}H-C_{Ar}-C-O), 5.89 (2H, ddt, *J* = 6.4 Hz, *J* = 10.4 Hz, *J* = 17 Hz CH₂=CH-CH₂), 5.22 (8H, m, CH₂=CH-CH₂ (overlapping peaks)), 4.36 (2H, q, *J* = 6.8 Hz, C_{Ar}-C(O)-O-CH₂-CH₃), 3.98 (2H, t, *J* = 6.4 Hz, C_{Ar}-C-O-CH₂-CH₂), 3.12 (2H, m, N-CH₂-CH₂), 2.45 (2H, t, *J* = 7.2 Hz, N-CH₂-CH₂), 1.81 (4H, m, O-CH₂-CH₂-CH₂, overlapping peaks), 1.53-1.08 (21H, m, CH₂-CH₂-CH₂ and CH₃) ppm

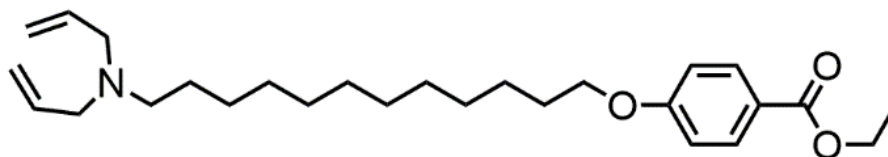


Figure 4.33: Structure of Compound **33** (Ethyl 4-((12-diallylamino)dodecyl)oxy)benzoate).

4.4.3: Deprotection of Benzoate Esters

4.4.3.1: Compound 34 (4-((8-diallylamino)octyl)oxy)benzoic acid) (Preparation 5)

Compound **29** (0.50 g, 1.34 mmol) and potassium hydroxide (0.20 g, 3.6 mmol) were dissolved in a mixture of water, methanol and acetonitrile (1ml:9ml:40ml respectively). The mixture was heated under reflux (20 h) before being slowly cooled to room temperature. The reaction was further cooled to -20°C and acetyl chloride was added dropwise until the mixture reached pH1 and the precipitate had stopped being formed. The precipitate was filtered off and the product extracted into DCM (50 ml), and dried with anhydrous magnesium sulfate, the solvent removed under reduced pressure to yield yellow oil. No further purification was subsequently attempted.

Yield = 0.44 g (1.27 mmol, 94.8 %)

$^1\text{H-NMR}$ (CDCl_3): 11.43 (1H, s, COOH), 7.60 (2H, d, $J = 8.84$ Hz, $\text{C}_{\text{Ar}}\text{H-C}_{\text{Ar}}\text{-C=O}$), 6.93 (2H, d, $J = 8.84$ Hz, $\text{C}_{\text{Ar}}\text{H-C}_{\text{Ar}}\text{-C-O}$), 5.88 (2H, ddt, $J = 6.4$ Hz, $J = 10.4$ Hz, $J = 17$ Hz $\text{CH}_2=\text{CH-CH}_2$), 5.22 (8H, m, $\text{CH}_2=\text{CH-CH}_2$ (overlapping peaks)), 3.93 (2H, t, $J = 6.4$ Hz, $\text{C}_{\text{Ar}}\text{-C-O-CH}_2\text{-CH}_2$), 3.30 (2H, m, $\text{N-CH}_2\text{-CH}_2$), 2.63 (2H, t, $J = 7.2$ Hz, $\text{N-CH}_2\text{-CH}_2$), 1.58 (4H, m, $\text{O-CH}_2\text{-CH}_2\text{-CH}_2$, overlapping peaks), 1.53-1.08 (10H, m, $\text{CH}_2\text{-CH}_2\text{-CH}_2$ and CH_3) (NH not observed) ppm

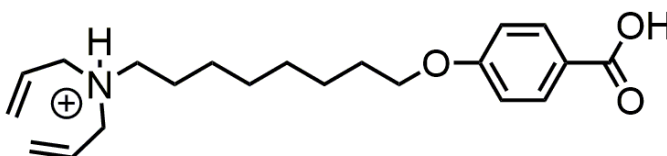


Figure 4.34: Structure of Compound **34** (4-((8-diallylamino)octyl)oxy)benzoic acid).

4.4.3.2: Compound 35 (4-((9-diallylamino)nonyl)oxy)benzoic acid) (Preparation 5)

Compound **35** was prepared using the same methodology as Compound **34**. The following quantities were used: Compound **30** (0.50 g; 1.29 mmol), potassium hydroxide (0.20 g; 3.6 mmol), water (1 ml), methanol (9 ml) and acetonitrile (40 ml). The product was isolated as a yellow oil.

Yield = 0.44 g (1.22 mmol, 94.6 %)

$^1\text{H-NMR}$ (CDCl_3): 7.60 (2H, d, $J = 8.84$ Hz, $\text{C}_{\text{Ar}}\text{H-C}_{\text{Ar}}\text{-C=O}$), 6.92 (2H, d, $J = 8.84$ Hz, $\text{C}_{\text{Ar}}\text{H-C}_{\text{Ar}}\text{-C-O}$), 5.85 (2H, ddt, $J = 6.4$ Hz, $J = 10.4$ Hz, $J = 17$ Hz $\text{CH}_2=\text{CH-CH}_2$), 5.25 (8H, m, $\text{CH}_2=\text{CH-CH}_2$ (overlapping peaks)), 3.93 (2H, t, $J = 6.4$ Hz, $\text{C}_{\text{Ar}}\text{-C-O-CH}_2\text{-CH}_2$), 3.26 (2H, m, $\text{N-CH}_2\text{-CH}_2$), 2.60 (2H, t, $J = 7.2$ Hz, $\text{N-CH}_2\text{-CH}_2$),

1.74 (4H, m, O-CH₂-CH₂-CH₂, overlapping peaks), 1.53-1.08 (12H, m, CH₂-CH₂-CH₂ and CH₃) (acidic Hs not observed) ppm

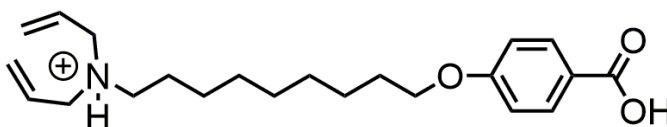


Figure 4.35: Structure of Compound **35** (4-((9-diallylamino)nonyl)oxy)benzoic acid).

4.4.3.3: Compound 36 (4-((10-diallylamino)decyl)oxy)benzoic acid) (Preparation 5)

Compound **36** was prepared using the same methodology as Compound **34**. The following quantities were used: Compound **31** (0.50 g; 1.25 mmol), potassium hydroxide (0.20 g; 3.6 mmol), water (1 ml), methanol (9 ml) and acetonitrile (40 ml). The product was isolated as a yellow oil.

Yield = 0.42g (1.12 mmol, 89.7 %)

¹H-NMR (CDCl₃): 7.63 (2H, d, *J* = 8.84 Hz, C_{Ar}H-C_{Ar}-C=O), 6.94 (2H, d, *J* = 8.84 Hz, C_{Ar}H-C_{Ar}-C-O), 5.83 (2H, ddt, *J* = 6.4 Hz, *J* = 10.4 Hz, *J* = 17 Hz CH₂=CH-CH₂), 5.19 (8H, m, CH₂=CH-CH₂ (overlapping peaks)), 3.93 (2H, t, *J* = 6.4 Hz, C_{Ar}-C-O-CH₂-CH₂), 3.26 (2H, m, N-CH₂-CH₂), 2.69 (2H, t, *J* = 7.2 Hz, N-CH₂-CH₂), 1.74 (4H, m, O-CH₂-CH₂-CH₂, overlapping peaks), 1.53-1.08 (14H, m, CH₂-CH₂-CH₂ and CH₃) (acidic Hs not observed) ppm

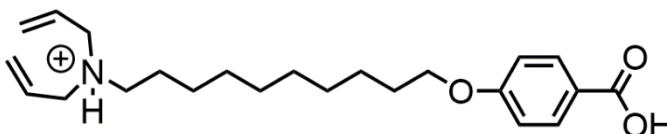


Figure 4.36: Structure of Compound **36** (4-((10-diallylamino)decyl)oxy)benzoic acid).

4.4.3.4: Compound 37 (4-((11-diallylamino)undecyl)oxy)benzoic acid) (Preparation 5)

Compound **37** was prepared using the same methodology as Compound **34**. The following quantities were used: Compound **32** (0.50 g; 1.20 mmol), potassium hydroxide (0.20 g; 3.6 mmol), water (1 ml), methanol (9 ml) and acetonitrile (40 ml). The product was isolated as a yellow oil.

Yield = 0.45g (1.16 mmol, 96.5 %)

¹H-NMR (CDCl₃): 7.86 (2H, d, *J* = 8.84 Hz, C_{Ar}H-C_{Ar}-C=O), 6.88 (2H, d, *J* = 8.84 Hz, C_{Ar}H-C_{Ar}-C-O), 5.80 (2H, ddt, *J* = 6.4 Hz, *J* = 10.4 Hz, *J* = 17 Hz CH₂=CH-CH₂), 5.23 (8H, m, CH₂=CH-CH₂ (overlapping peaks)), 4.06 (2H, t, *J* = 6.4 Hz, C_{Ar}-C-O-CH₂-CH₂), 3.19 (2H, m, N-CH₂-CH₂), 2.61 (2H, t, *J* = 7.2 Hz, N-CH₂-CH₂), 1.82 (4H, m, O-CH₂-CH₂-CH₂, overlapping peaks), 1.53-1.08 (16H, m, CH₂-CH₂-CH₂ and CH₃) (acidic Hs not observed) ppm

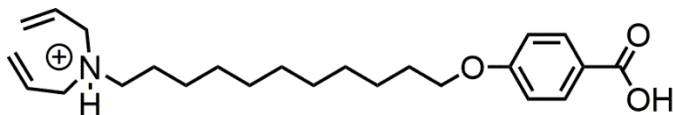


Figure 4.37: Structure of Compound **37** (4-((11-diallylamino)undecyl)oxy)benzoic acid).

4.4.3.5: Compound **38** (4-((12-diallylamino)dodecyl)oxy)benzoic acid) (Preparation 5)

Compound **38** was prepared using the same methodology as Compound **34**. The following quantities were used: Compound **33** (0.50 g; 1.16 mmol), potassium hydroxide (0.20 g; 3.6 mmol), water (1 ml), methanol (9 ml) and acetonitrile (40 ml). The product was isolated as a yellow oil.

Yield = 0.46g (1.14 mmol, 98.5 %)

$^1\text{H-NMR}$ (CDCl_3): 11.19 (1H, s, OH), 7.56 (2H, d, $J = 8.84$ Hz, $\text{C}_{\text{Ar}}\text{H-C}_{\text{Ar}}\text{-C=O}$), 6.92 (2H, d, $J = 8.84$ Hz, $\text{C}_{\text{Ar}}\text{H-C}_{\text{Ar}}\text{-C-O}$), 5.86 (2H, ddt, $J = 6.4$ Hz, $J = 10.4$ Hz, $J = 17$ Hz $\text{CH}_2=\text{CH-CH}_2$), 5.22 (6H, m, $\text{CH}_2=\text{CH-CH}_2$ (overlapping peaks)), 3.93 (2H, t, $J = 6.4$ Hz, $\text{C}_{\text{Ar}}\text{-C-O-CH}_2\text{-CH}_2$), 3.26 (2H, m, $\text{N-CH}_2\text{-CH}_2$), 2.60 (2H, t, $J = 7.2$ Hz, $\text{N-CH}_2\text{-CH}_2$), 1.74 (4H, m, $\text{O-CH}_2\text{-CH}_2\text{-CH}_2$, overlapping peaks), 1.53-1.08 (18H, m, $\text{CH}_2\text{-CH}_2\text{-CH}_2$ and CH_3) (NH not observed) ppm

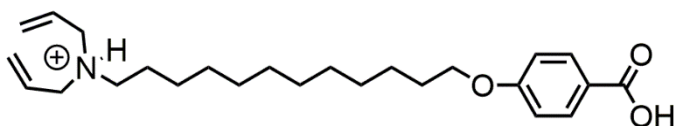


Figure 4.38: Structure of Compound **38** (4-((12-diallylamino)dodecyl)oxy)benzoic acid).

4.4.4: Synthesis of Ester Motifs

4.4.4.1: Compound **39** (4-cyanophenyl 4-((8-(diallylamino)octyl)oxy)benzoate) (Preparation 6)

Compound **34** (0.50 g, 1.44 mmol), EDAC (0.44 g, 2.3 mmol), DMAP (0.01 g, 0.08 mmol) and 4-hydroxybenzotrile (0.28 g, 2.4 mmol) were mixed together in DCM (150ml) and left to stir at room temperature (24 h). The reaction was then treated with sodium carbonate (2M, 20ml) and extracted with DCM (2 x 25 ml). The organic layer was then washed with water (4 x 50ml) and dried over anhydrous magnesium sulfate. The mixture was filtered, and the solvent removed under reduced pressure. The product was isolated by column chromatography on silica, (impurities eluted with DCM, with a gradient to ethyl acetate, increasing 20% per fraction and the product isolated using ethyl acetate:methanol (60:40)). The compound was then filtered through a pad of alumina, washed with ethyl acetate:methanol (60:40) before the solvents were removed under reduced pressure, yielding a colourless oil.

Yield = 0.27 g (0.60 mmol, 41.9 %)

$^1\text{H-NMR}$ (CDCl_3): 7.94 (2H, dd, $J = 6.4$ Hz, $J = 2$ Hz, $\text{C}_{\text{Ar}}\text{-H}$), 7.31 (2H, dd, $J = 6.4$ Hz, $J = 2$ Hz, $\text{C}_{\text{Ar}}\text{-H}$), 6.93 (2H, dd, $J = 6.4$ Hz, $J = 2$ Hz, $\text{NC-C-C}_{\text{Ar}}\text{-H}$), 6.84 (2H, dd, $J = 6.4$ Hz, $J = 2$ Hz, $\text{CO-C-C}_{\text{Ar}}\text{-H}$), 5.82 (2H, ddt, $J = 6.4$ Hz, $J = 10.4$ Hz, $J = 17$ Hz $\text{CH}_2=\text{CH-CH}_2$), 5.11 (8H, m, $\text{CH}_2=\text{CH-CH}_2$ (overlapping peaks)),

3.96 (2H, t, $J = 6.4$ Hz, O-C- H_2), 3.06 (2H, m, N- CH_2 - CH_2) 1.75 (4H, m, CH_2 -C- H_2), 1.58-1.20 (10H, m, CH_2 -C- H_2) ppm

^{13}C -NMR ($CDCl_3$): 166.86 (C_{Ar} -C=O(-O)), 162.88 (CH_2 -O- C_{Ar} - C_{Ar}), 154.40 (O=C-O- C_{Ar}), 135.42 ($CH_2=CH$ - CH_2), 133.61 (C_{Ar} - C_{Ar} -C \equiv N), 131.50 (C_{Ar} - C_{Ar} -COO), 122.95 (C_{Ar} - C_{Ar} -O-C=O), 122.23 (C_{Ar} -COO), 118.33 (C_{Ar} -C \equiv N), 117.53 ($CH_2=CH$ - CH_2), 113.99 (CH_2 -O- C_{Ar} - C_{Ar}), 109.47 (C_{Ar} -C \equiv N), 68.09 (CH_2 -O- C_{Ar}), 56.72 (N- CH_2 -CH), 53.22 (N- CH_2 - CH_2), 29.38 (CH_2 - CH_2 - CH_2), 29.23 (CH_2 - CH_2 - CH_2), 27.33 (CH_2 - CH_2 - CH_2), 25.87 (CH_2 - CH_2 - CH_2) ppm

M/z (ESI): 447.2650

IR: 3076 (aromatic C-H stretch), 2930 (alkyl C-H stretch), 2855 (alkyl C-H stretch), 2801 (alkyl C-H stretch next to amine), 2226 (C \equiv N stretch), 1717 (ester C=O stretch), 1641 (alkene C=C stretch), 1605 (aromatic C=C stretch), 1510 (alkyl C-H bend), 1250 (amine C-N stretch), 1165 (C-O stretch ether), 1103 (C-O stretch ester) cm^{-1}

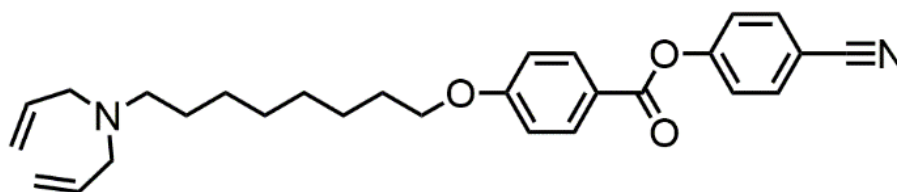


Figure 4.39: Structure of Compound **39** (4-cyanophenyl 4-((8-(diallylamino)octyl)oxy)benzoate).

4.4.4.2: Compound **40** (4-cyanophenyl 4-((9-(diallylamino)nonyl)oxy)benzoate) (Preparation 6)

Compound **40** was prepared using the same methodology as Compound **39**. The following quantities were used: Compound **35** (0.50 g; 1.39 mmol), 4-hydroxybenzonitrile (0.28 g; 2.4 mmol), EDAC (0.44 g; 2.3 mmol), DMAP (0.01 g; 0.08 mmol), and DCM 150 ml. The product was isolated as a clear colourless oil.

Yield = 0.29g (0.63 mmol, 45.2 %)

1H -NMR ($CDCl_3$): 7.94 (2H, dd, $J = 6.4$ Hz, $J = 2$ Hz, C_{Ar} - H), 7.40 (2H, dd, $J = 6.4$ Hz, $J = 2$ Hz, C_{Ar} - H), 6.86 (2H, dd, $J = 6.4$ Hz, $J = 2$ Hz, NC-C- C_{Ar} - H), 6.77 (2H, dd, $J = 6.4$ Hz, $J = 2$ Hz, CO-C- C_{Ar} - H), 5.83 (2H, ddt, $J = 6.4$ Hz, $J = 10.4$ Hz, $J = 17$ Hz $CH_2=CH$ - CH_2), 5.11 (8H, m, $CH_2=CH$ - CH_2 (overlapping peaks)), 3.96 (2H, t, $J = 6.4$ Hz, O-C- H_2), 3.04 (2H, m, N- CH_2 - CH_2) 1.75 (4H, m, CH_2 -C- H_2), 1.46-1.20 (10H, m, CH_2 -C- H_2) ppm

^{13}C -NMR ($CDCl_3$): 166.86 (C_{Ar} -C=O(-O)), 162.89 (CH_2 -O- C_{Ar} - C_{Ar}), 155.04 (O=C-O- C_{Ar}), 135.75 ($CH_2=CH$ - CH_2), 134.00 (C_{Ar} - C_{Ar} -C \equiv N), 131.50 (C_{Ar} - C_{Ar} -COO), 122.23 (C_{Ar} -COO), 122.21 (C_{Ar} - C_{Ar} -O-C=O), 117.26 (C_{Ar} -C \equiv N), 117.16 ($CH_2=CH$ - CH_2), 113.99 (CH_2 -O- C_{Ar} - C_{Ar}), 109.51 (C_{Ar} -C \equiv N), 68.11 (CH_2 -O- C_{Ar}), 56.80 (N- CH_2 -CH), 53.31 (N- CH_2 - CH_2), 29.43 (CH_2 - CH_2 - CH_2), 29.24 (CH_2 - CH_2 - CH_2), 27.41 (CH_2 - CH_2 - CH_2), 25.91 (CH_2 - CH_2 - CH_2) ppm

M/z (ESI): 461.2816

IR: 3075 (aromatic C-H stretch), 2926 (alkyl C-H stretch), 2855 (alkyl C-H stretch), 2789 (alkyl C-H stretch next to amine), 2220 (C≡N stretch), 1717 (ester C=O stretch), 1692 (aromatic C-H bend), 1641 (alkene C=C stretch), 1605 (aromatic C=C stretch), 1510 (alkyl C-H bend), 1277 (C-O stretch ester), 1250 (amine C-N stretch), 1167 (C-O stretch ether) cm⁻¹

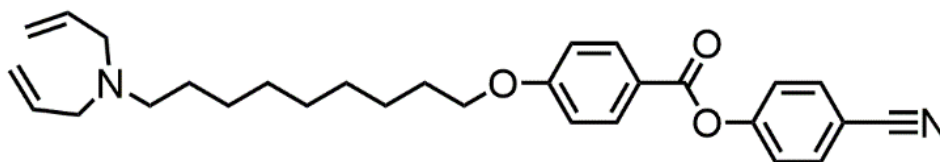


Figure 4.40: Structure of Compound **40** (4-cyanophenyl 4-((9-(diallylamino)nonyl)oxy)benzoate).

4.4.4.3: Compound **41** (4-cyanophenyl 4-((10-(diallylamino)decyl)oxy)benzoate) (Preparation 6)

Compound **41** was prepared using the same methodology as Compound **39**. The following quantities were used: Compound **36** (0.50 g; 1.33 mmol), 4-hydroxybenzonitrile (0.28 g; 2.4 mmol), EDAC (0.44 g; 2.3 mmol), DMAP (0.01 g; 0.08 mmol), and DCM 150 ml. The product was isolated as a clear, colourless oil.

Yield = 0.25g (0.53 mmol, 39.5 %)

¹H-NMR (CDCl₃): 7.95 (2H, dd, *J* = 6.4 Hz, *J* = 2 Hz, C_{Ar}-H), 7.31 (2H, dd, *J* = 6.4 Hz, *J* = 2 Hz, C_{Ar}-H), 6.95 (2H, dd, *J* = 6.4 Hz, *J* = 2 Hz, NC-C-C_{Ar}-H), 6.87 (2H, dd, *J* = 6.4 Hz, *J* = 2 Hz, CO-C-C_{Ar}-H), 5.83 (2H, ddt, *J* = 6.4 Hz, *J* = 10.4 Hz, *J* = 17 Hz CH₂=CH-CH₂), 5.11 (8H, m, CH₂=CH-CH₂ (overlapping peaks)), 3.95 (2H, t, *J* = 6.4 Hz, O-C-H₂), 3.05 (2H, m, N-CH₂-CH₂) 1.77 (4H, m, CH₂-C-H₂), 1.46-1.20 (12H, m, CH₂-C-H₂) ppm

¹³C-NMR (CDCl₃): 166.86 (C_{Ar}-C=O(-O)), 162.90 (CH₂-O-C_{Ar}-C_{Ar}), 155.34 (O=C-O-C_{Ar}), 135.75 (CH₂=CH-CH₂), 133.61 (C_{Ar}-C_{Ar}-C≡N), 131.50 (C_{Ar}-C_{Ar}-COO), 122.96 (C_{Ar}-COO), 122.23 (C_{Ar}-C_{Ar}-O-C=O), 117.27 (C_{Ar}-C≡N), 117.19 (CH₂=CH-CH₂), 113.99 (CH₂-O-C_{Ar}-C_{Ar}), 109.55 (C_{Ar}-C≡N), 68.13 (CH₂-O-C_{Ar}), 56.80 (N-CH₂-CH), 53.33 (N-CH₂-CH₂), 29.50 (CH₂-CH₂-CH₂), 29.29 (CH₂-CH₂-CH₂), 27.43 (CH₂-CH₂-CH₂), 25.92 (CH₂-CH₂-CH₂) ppm

M/z (ESI): 475.2958

IR: 3076 (aromatic C-H stretch), 2924 (alkyl C-H stretch), 2853 (alkyl C-H stretch), 2795 (alkyl C-H stretch next to amine), 2230 (C≡N stretch), 1717 (ester C=O stretch), 1653 (alkene C=C stretch), 1605 (aromatic C=C stretch), 1578 (aromatic C-H bend), 1510 (alkyl C-H bend), 1277 (C-O stretch ester), 1252 (amine C-N stretch), 1165 (C-O stretch ether) cm⁻¹

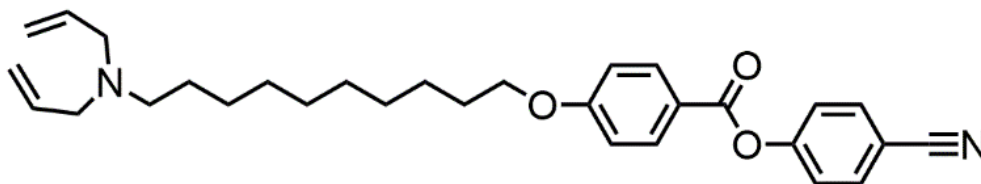


Figure 4.41: Structure of Compound **41** (4-cyanophenyl 4-((10-(diallylamino)decyl)oxy)benzoate).

4.4.4.4: Compound 42 (4-cyanophenyl 4-((11-(diallylamino)undecyl)oxy)benzoate) (Preparation 6)

Compound **42** was prepared using the same methodology as Compound **39**. The following quantities were used: Compound **37** (0.50 g; 1.29 mmol), 4-hydroxybenzonitrile (0.26 g; 2.4 mmol), EDAC (0.44 g; 2.3 mmol), DMAP (0.01 g; 0.08 mmol), and DCM 150 ml. The product was isolated as a clear colourless oil.

Yield = 0.21 g (0.43 mmol, 33.3 %)

$^1\text{H-NMR}$ (CDCl_3): 7.68 (2H, dd, $J = 6.4 \text{ Hz}$, $J = 2 \text{ Hz}$, $\text{C}_{\text{Ar}}\text{-H}$), 7.65 (2H, dd, $J = 6.4 \text{ Hz}$, $J = 2 \text{ Hz}$, $\text{C}_{\text{Ar}}\text{-H}$), 7.53 (2H, dd, $J = 6.4 \text{ Hz}$, $J = 2 \text{ Hz}$, $\text{NC-C-C}_{\text{Ar}}\text{-H}$), 7.47 (2H, dd, $J = 6.4 \text{ Hz}$, $J = 2 \text{ Hz}$, $\text{CO-C-C}_{\text{Ar}}\text{-H}$), 5.76 (2H, ddt, $J = 6.4 \text{ Hz}$, $J = 10.4 \text{ Hz}$, $J = 17 \text{ Hz}$ $\text{CH}_2=\text{CH-CH}_2$), 5.16 (8H, m, $\text{CH}_2=\text{CH-CH}_2$ (overlapping peaks)), 3.99 (2H, t, $J = 6.4 \text{ Hz}$, O-C-H_2), 3.09 (2H, m, $\text{N-CH}_2\text{-CH}_2$) 1.93 (4H, m, $\text{CH}_2\text{-C-H}_2$), 1.49-1.20 (14H, m, $\text{CH}_2\text{-C-H}_2$) ppm

$^{13}\text{C-NMR}$ (CDCl_3): 166.93 ($\text{C}_{\text{Ar}}\text{-C=O(-O)}$), 162.80 ($\text{CH}_2\text{-O-C}_{\text{Ar}}\text{-C}_{\text{Ar}}$), 155.03 ($\text{O=C-O-C}_{\text{Ar}}$), 135.80 ($\text{CH}_2=\text{CH-CH}_2$), 133.02 ($\text{C}_{\text{Ar}}\text{-C}_{\text{Ar}}\text{-C}\equiv\text{N}$), 131.91 ($\text{C}_{\text{Ar}}\text{-C}_{\text{Ar}}\text{-COO}$), 122.36 ($\text{C}_{\text{Ar}}\text{-COO}$), 122.29 ($\text{C}_{\text{Ar}}\text{-C}_{\text{Ar}}\text{-O-C=O}$), 117.21 ($\text{C}_{\text{Ar}}\text{-C}\equiv\text{N}$), 117.05 ($\text{CH}_2=\text{CH-CH}_2$), 113.76 ($\text{CH}_2\text{-O-C}_{\text{Ar}}\text{-C}_{\text{Ar}}$), 109.53 ($\text{C}_{\text{Ar}}\text{-C}\equiv\text{N}$), 68.16 ($\text{CH}_2\text{-O-C}_{\text{Ar}}$), 56.77 ($\text{N-CH}_2\text{-CH}$), 53.63 ($\text{N-CH}_2\text{-CH}_2$), 29.52 ($\text{CH}_2\text{-CH}_2\text{-CH}_2$), 29.26 ($\text{CH}_2\text{-CH}_2\text{-CH}_2$), 27.36 ($\text{CH}_2\text{-CH}_2\text{-CH}_2$), 25.91 ($\text{CH}_2\text{-CH}_2\text{-CH}_2$) ppm

M/z (ESI): 489.3096

IR: 3055 (aromatic C-H stretch), 2980 (alkyl C-H stretch), 2930 (alkyl C-H stretch), 2857 (alkyl C-H stretch next to amine), 2131 ($\text{C}\equiv\text{N}$ stretch), 1989 (aromatic C-H bend), 1740 (ester C=O stretch), 1711 (alkene C=C stretch), 1601 (aromatic C=C stretch), 1437 (C-O stretch ester), 1244 (amine C-N stretch), 1182 (C-O stretch ether) cm^{-1}

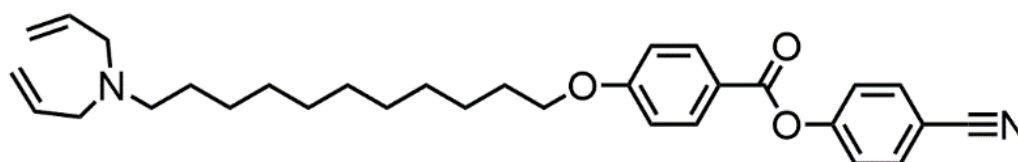


Figure 4.42: Structure of Compound **42** (4-cyanophenyl 4-((11-(diallylamino)undecyl)oxy)benzoate).

4.4.4.5: Compound 43 (4-cyanophenyl 4-((12-(diallylamino)dodecyl)oxy)benzoate) (Preparation 6)

Compound **43** was prepared using the same methodology as Compound **39**. The following quantities were used: Compound **38** (0.50 g; 1.24 mmol), 4-hydroxybenzonitrile (0.26 g; 0.24

mmol), EDAC (0.44 g; 0.23 mmol), DMAP (0.01 g; 0.08 mmol), and DCM 150 ml. The product was isolated as a clear, colourless oil.

Yield = 0.28 g (0.56 mmol, 44.9 %)

$^1\text{H-NMR}$ (CDCl_3): 7.96 (2H, dd, $J = 6.4 \text{ Hz}$, $J = 2 \text{ Hz}$, $\text{C}_{\text{Ar}}\text{-H}$), 7.34 (2H, dd, $J = 6.4 \text{ Hz}$, $J = 2 \text{ Hz}$, $\text{C}_{\text{Ar}}\text{-H}$), 6.96 (2H, dd, $J = 6.4 \text{ Hz}$, $J = 2 \text{ Hz}$, $\text{NC-C-C}_{\text{Ar}}\text{-H}$), 6.87 (2H, dd, $J = 6.4 \text{ Hz}$, $J = 2 \text{ Hz}$, $\text{CO-C-C}_{\text{Ar}}\text{-H}$), 5.85 (2H, ddt, $J = 6.4 \text{ Hz}$, $J = 10.4 \text{ Hz}$, $J = 17 \text{ Hz}$ $\text{CH}_2=\text{CH-CH}_2$), 5.13 (8H, m, $\text{CH}_2=\text{CH-CH}_2$ (overlapping peaks)), 3.99 (2H, t, $J = 6.4 \text{ Hz}$, O-C-H_2), 3.08 (2H, m, $\text{N-CH}_2\text{-CH}_2$) 1.80 (4H, m, $\text{CH}_2\text{-C-H}_2$), 1.56-1.20 (16H, m, $\text{CH}_2\text{-C-H}_2$) ppm

$^{13}\text{C-NMR}$ (CDCl_3): 166.88 ($\text{C}_{\text{Ar}}\text{-C=O(-O)}$), 162.91 ($\text{CH}_2\text{-O-C}_{\text{Ar}}\text{-C}_{\text{Ar}}$), 154.35 ($\text{O=C-O-C}_{\text{Ar}}$), 135.69 ($\text{CH}_2=\text{CH-CH}_2$), 133.64 ($\text{C}_{\text{Ar}}\text{-C}_{\text{Ar}}\text{-C}\equiv\text{N}$), 131.52 ($\text{C}_{\text{Ar}}\text{-C}_{\text{Ar}}\text{-COO}$), 122.96 ($\text{C}_{\text{Ar}}\text{-COO}$), 122.24 ($\text{C}_{\text{Ar}}\text{-C}_{\text{Ar}}\text{-O-C=O}$), 117.35 ($\text{C}_{\text{Ar}}\text{-C}\equiv\text{N}$), 117.20 ($\text{CH}_2=\text{CH-CH}_2$), 114.00 ($\text{CH}_2\text{-O-C}_{\text{Ar}}\text{-C}_{\text{Ar}}$), 109.51 ($\text{C}_{\text{Ar}}\text{-C}\equiv\text{N}$), 68.15 ($\text{CH}_2\text{-O-C}_{\text{Ar}}$), 56.79 ($\text{N-CH}_2\text{-CH}$), 53.34 ($\text{N-CH}_2\text{-CH}_2$), 29.55 ($\text{CH}_2\text{-CH}_2\text{-CH}_2$), 29.33 ($\text{CH}_2\text{-CH}_2\text{-CH}_2$), 27.46 ($\text{CH}_2\text{-CH}_2\text{-CH}_2$), 25.94 ($\text{CH}_2\text{-CH}_2\text{-CH}_2$) ppm

M/z (ESI): 503.3254

IR: 3076 (aromatic C-H stretch), 2924 (alkyl C-H stretch), 2853 (alkyl C-H stretch), 2795 (alkyl C-H stretch next to amine), 2230 ($\text{C}\equiv\text{N}$ stretch), 1717 (ester C=O stretch), 1643 (alkene C=C stretch), 1605 (aromatic C=C stretch), 1578 (aromatic C-H bend), 1510 (alkyl C-H bend), 1277 (C-O stretch ester), 1252 (amine C-N stretch), 1165 (C-O stretch ether) cm^{-1}

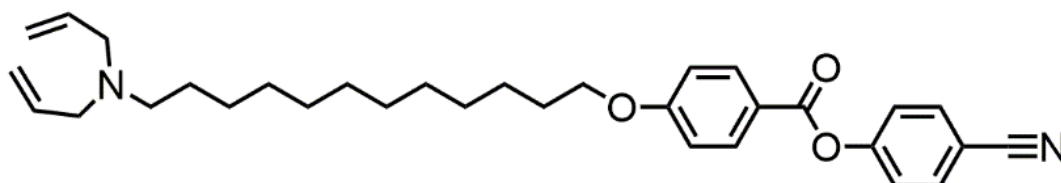


Figure 4.43: Structure of Compound **43** (4-cyanophenyl 4-((12-(diallylamino)dodecyl)oxy)benzoate).

5: Thermal Studies of Compounds

Compounds **4-8** (bromoalkoxybiphenyls), **9-13** (bromoalkoxyterphenyls), **14-18** (diallylaminoalkoxybiphenyls), **19-23** (diallylaminoalkoxyterphenyls) and **39-43** (esters) were all investigated by polarised optical microscopy, differential scanning calorimetry and x-ray diffraction to characterise their liquid crystal behaviour.

One potentially interesting aspect of the compounds studied is whether there is a well-defined odd/even effect through each of the homologous series where alkyl chain lengths of 8 to 12 have been prepared. Each series was examined to determine if there were any structure-property correlations that could be elucidated particularly with mesophase behaviour and x-ray structure.

5.1: Analysis of Bromo-terminated Biphenyl Intermediates (Compounds 4-8)

Bromo-terminated compounds were prepared as intermediates in the synthesis of the target diallylamine compounds. However, these compounds all exhibited liquid crystalline behaviour. The major difference between the terminal bromides and the diallylamine terminated compounds is the volume of the terminal group. Since the bromo terminal substituent is a single atom and does not exhibit conformational freedom that may be seen in the amines then it was expected to exhibit phase behaviour at higher temperature. Indeed, these compounds are similar to the alkoxycyanobiphenyls that were first reported by Gray et al.⁸¹

The transition temperatures for Compounds **4-8** are reported in Table 5.1 and the DSC thermograms are shown in Figures 5.1-5.5. The phase identification was carried out using polarised optical microscopy and the transition temperatures determined using DSC. A graph showing the transition temperatures is given in Figure 5.6.

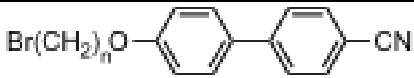
							
		Transition Temperature / °C					
Cpd No	n	Recryst	K		N		Iso
4	8	58.6 [30.8]	•	80.1 [41.5]	(•)	67.5 [0.5]	•
5	9	43.7 [21.7]	•	71.1 [28.4]	(•)	70.3 [0.6]	•
6	10	44.6 [29.3]	•	72.5 [45.9]	(•)	68.3 [1.0]	•
7	11	62.3 [7.1]	•	91.4 [35.0]	•	95.9 [10.6]	•
8	12	35.2 [33.9]	•	75.9 [50.9]	•	79.2 [2.2]	•

Table 5.1: Transition temperatures (°C) for Compounds **4-8**.

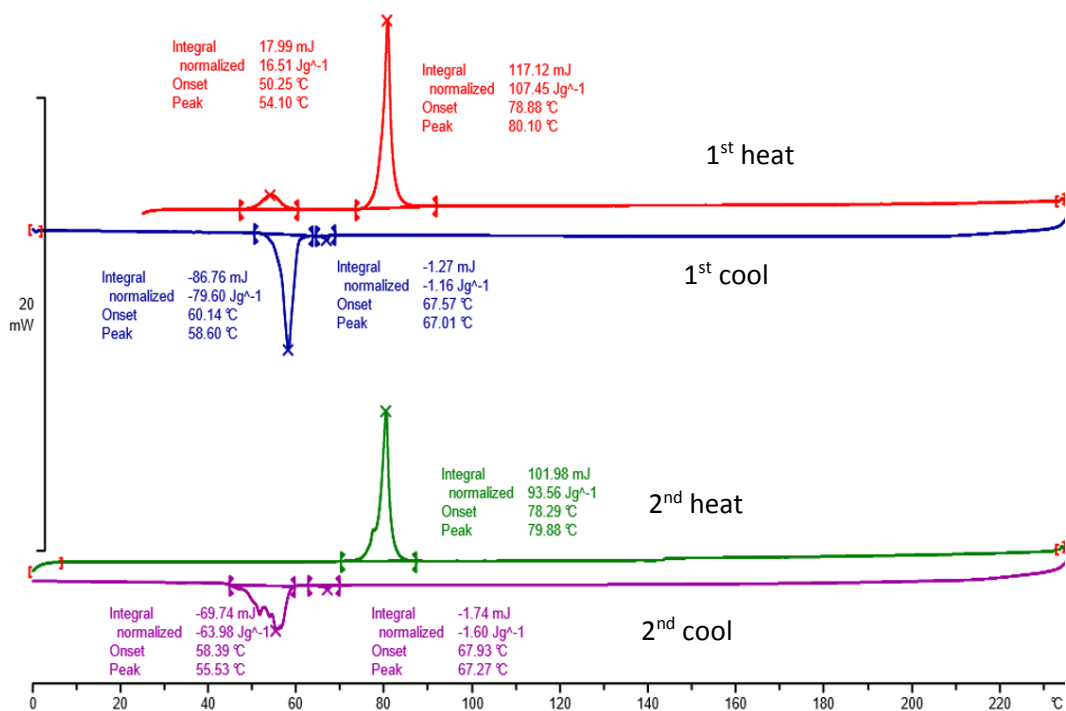


Figure 5.1: DSC thermogram (10 °C min⁻¹) showing the melting behaviour of Compound 4.

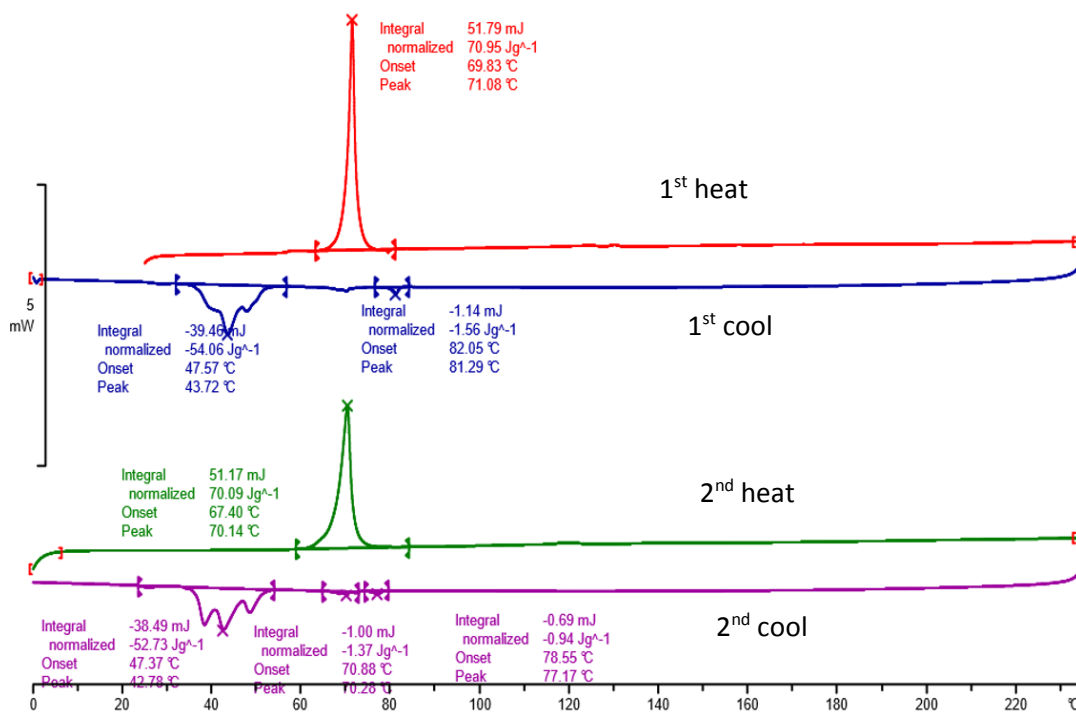


Figure 5.2: DSC thermogram (10 °C min⁻¹) showing the melting behaviour of Compound 5.

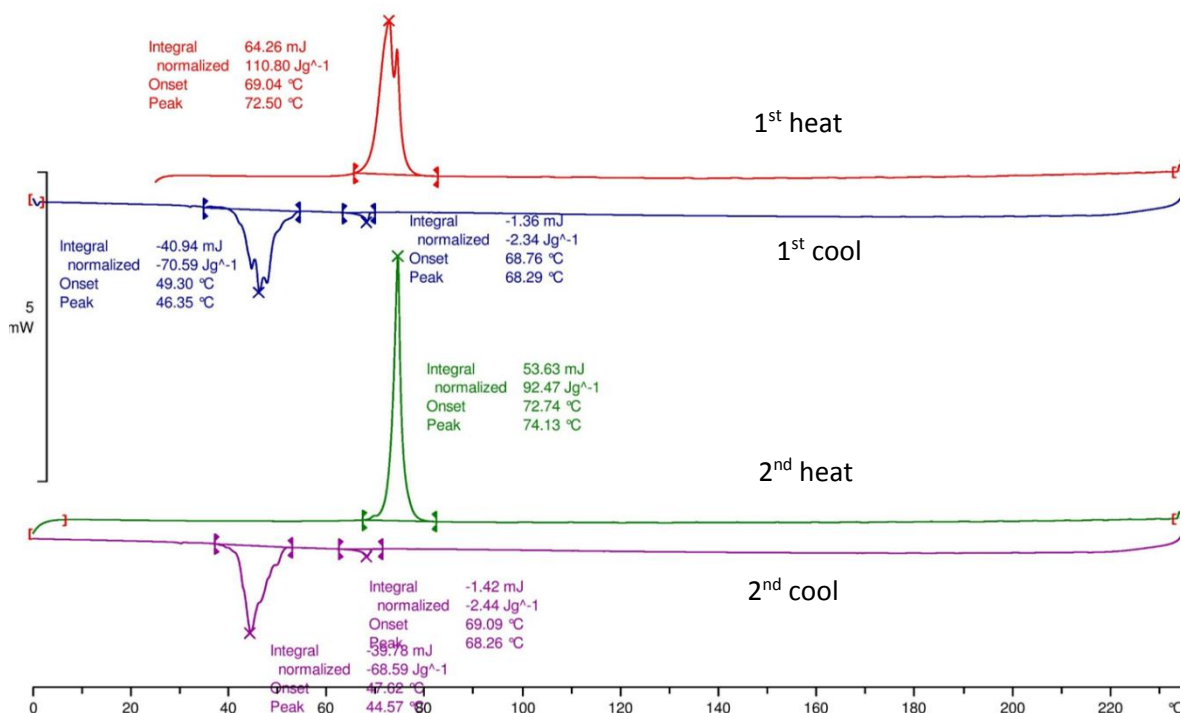


Figure 5.3: DSC thermogram (10 °C min⁻¹) showing the melting behaviour of Compound 6.

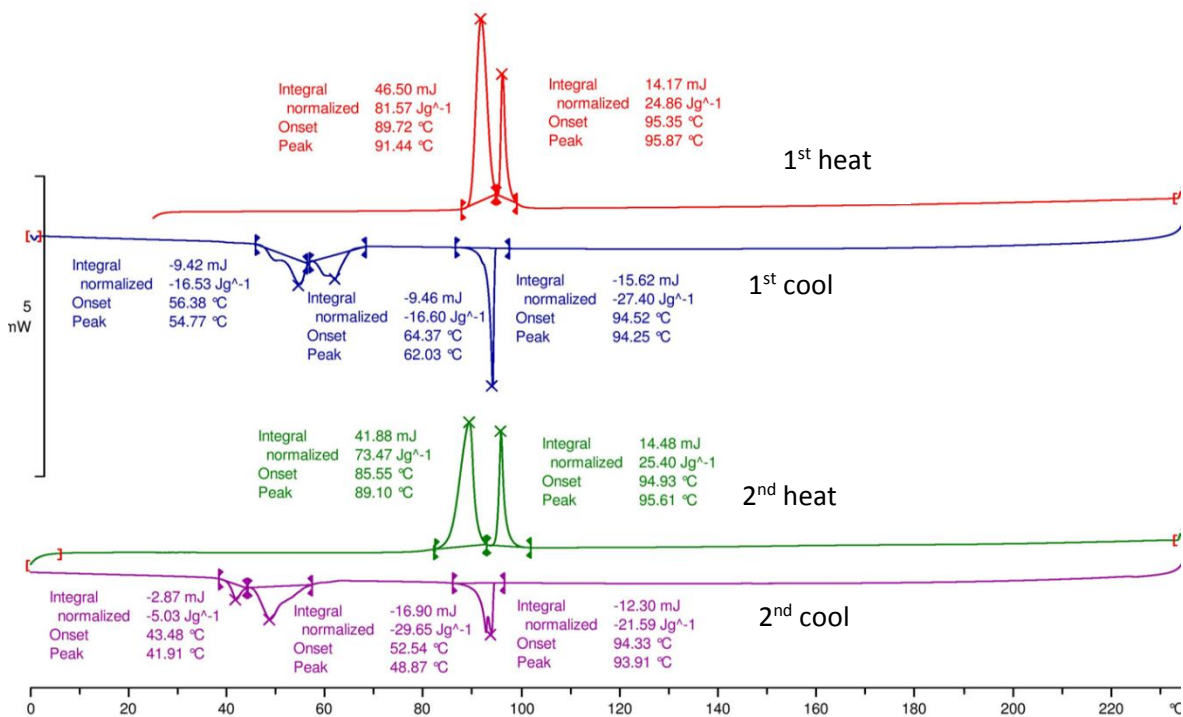


Figure 5.4: DSC thermogram (10 °C min⁻¹) showing the melting behaviour of Compound 7.

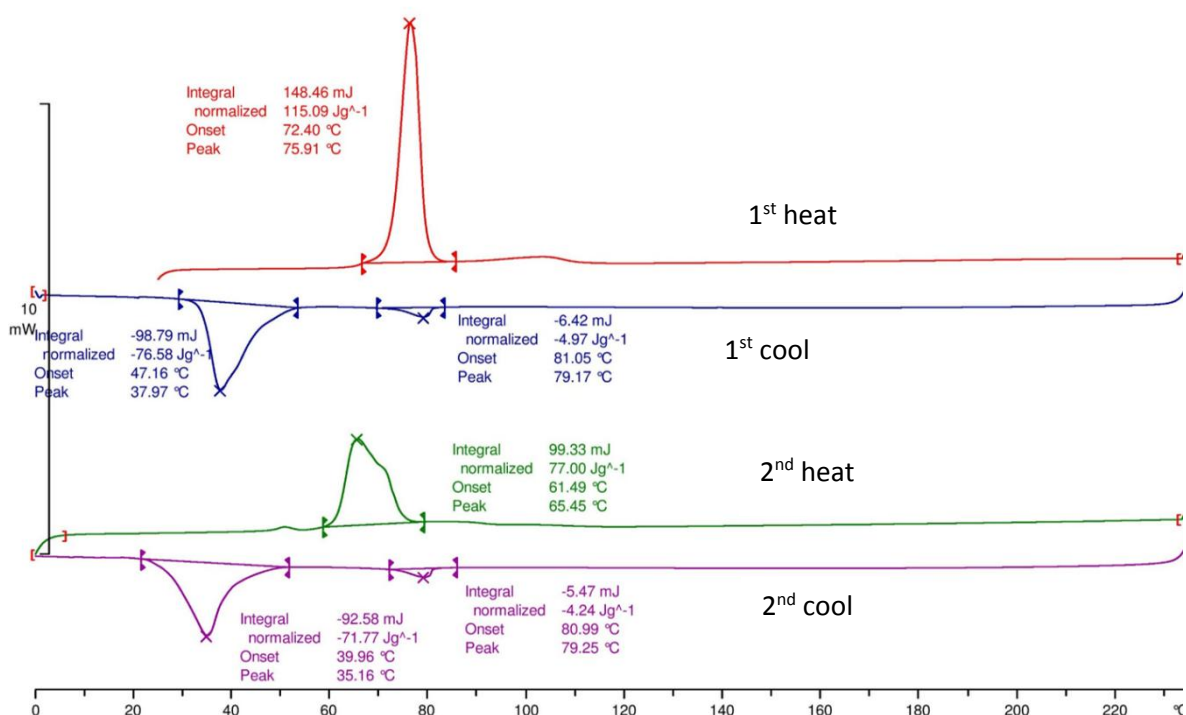


Figure 5.5: DSC thermogram (10 °C min⁻¹) showing the melting behaviour of Compound 8.

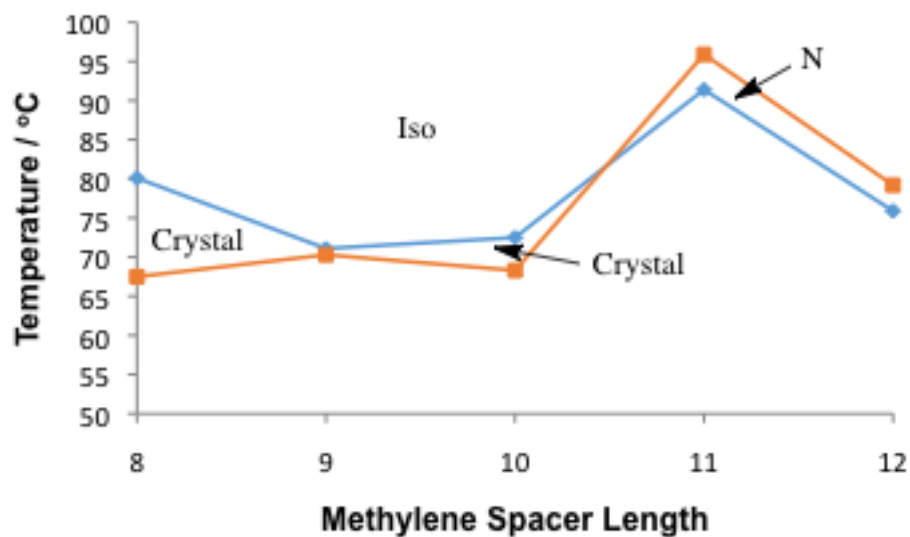


Figure 5.6: Graph showing the transition temperatures as a function of methylene spacer length for Compounds 4-8.

Figure 5.6 shows that the bromo substituent has the effect of reducing the stability of the nematic phase relative to the crystal to the extent that the nematic phase is monotropic until the chain

length reaches 11 methylene units. This behaviour is in stark contrast to the alkoxycyanobiphenyl series reported by Gray *et al*⁸¹ where clearing points were much higher and phase behaviour was enantiotropic. It is also interesting to note at this point that all of the compounds in this series exhibit a nematic phase only whereas the alkoxycyanobiphenyls at similar chain lengths all exhibited smectic A phases. This disordering of the mesophase behaviour is attributed to the bulky nature of the bromide at the terminus of the molecule in comparison to a terminal methyl group.

As shown in Table 5.1, there is a visible trend in the enthalpies of the crystal to nematic phase transition, which is subdivided into two separate trends between the compounds with odd and even length spacer chains. The even length spacer chains (Compounds **4**, **6** and **8** with $n = 8, 10$ and 12 respectively) generally showed higher enthalpies of transition when compared to their odd length counterparts, showing a suppression of the transition enthalpies for these odd length compounds. Within each series there is a general upward trend in the enthalpy with chain length, which correlates with the increased molecular mass, and greater intermolecular attractions (such as van der Waals forces). The suppression of these enthalpies for Compounds **5** and **7** are due to the different shape of the molecules as the odd and even chain lengths have a different angular alignment between the terminal groups, affecting how the molecules pack together. It is worth noting that the general trend of the crystal to nematic transition is echoed in the enthalpies of recrystallization, with clear suppressions being noted for Compounds **5** and **7**, as well as a very slight decrease for Compound **6** when compared to Compound **4** which is contrary to expectations. For the clearing of the compounds to the isotropic phase there is less of a clear trend. This can be attributed to the lower enthalpy of the transition, with any error making more of an impact to the trend.

Microscopy confirmed the presence of nematic phases in this series of compounds through the observation of a nematic schlieren texture where singularity defects containing both 2- and 4-brush defects were observed. Examples of the nematic schlieren texture for Compounds **5**, **6** and **8** are given in Figure 5.7.

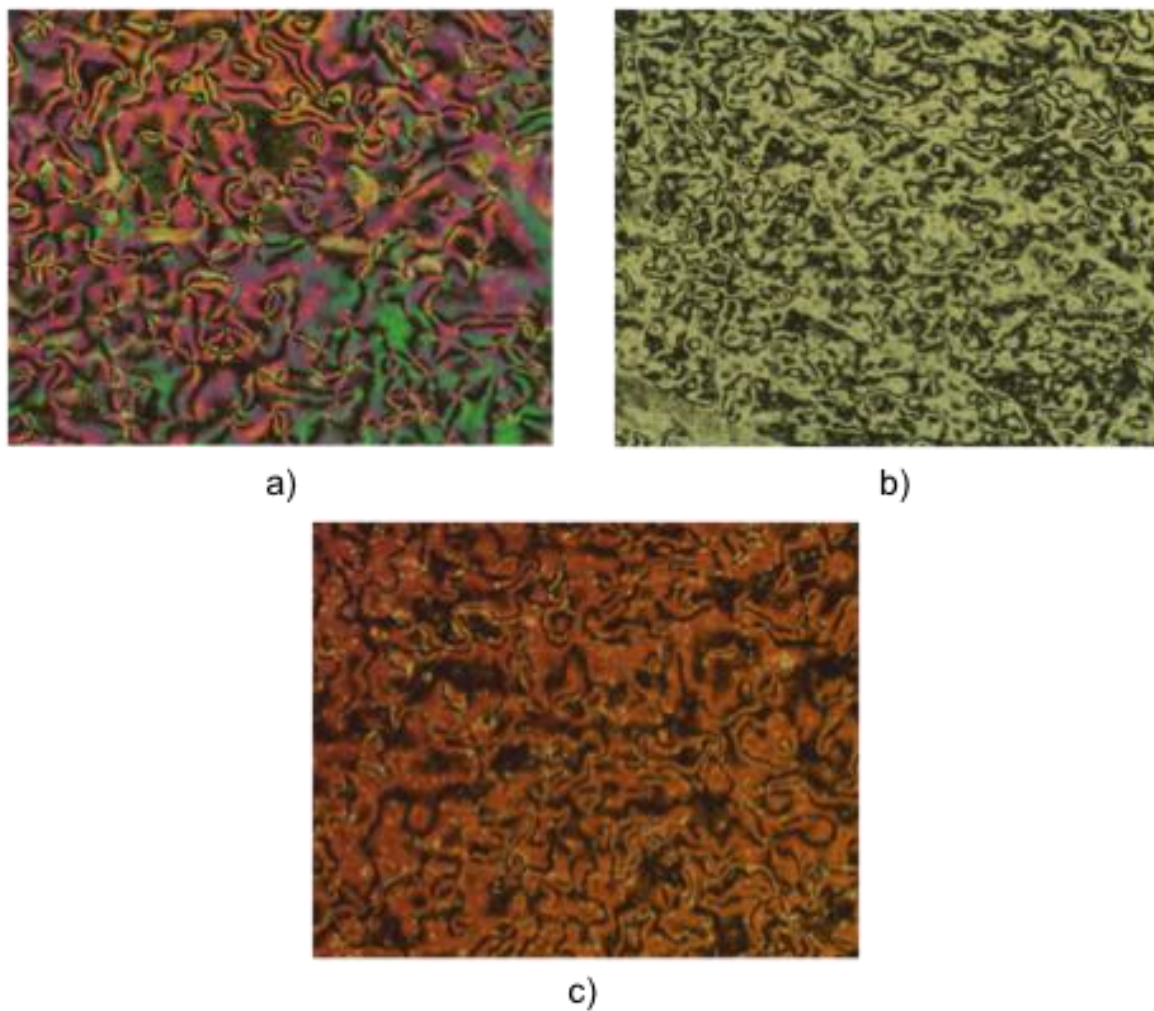


Figure 5.7: Photomicrographs (x100) showing examples of the nematic schlieren texture observed for a) **5** at 61.4 °C b) **6** at 62.2 °C and c) **8** at 65.1 °C view through crossed polarisers.

X-ray diffraction was used to confirm the presence of the nematic phase. Figure 5.8 shows a typical diffraction pattern observed for the nematic phase for Compound **5**. Due to the monotropic nature of the majority of this series of compounds it was not possible to collect sufficient data points in the nematic phase to be able to plot the small angle (relating to the long axis of the molecule) and wide angle peaks (relating to the lateral packing of the molecules) as a function of temperature. These diffraction patterns are typical representations of those observed for nematic phases aligned by magnetic fields in the diffractometer. The peaks are diffuse which represents the weak ordering of the molecules within this phase.

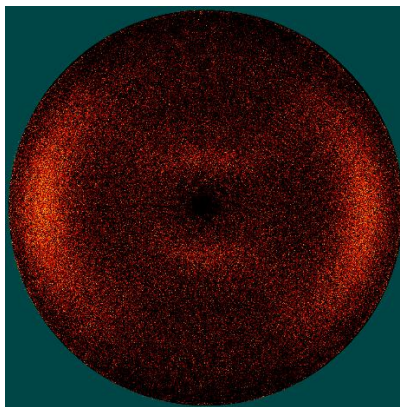


Figure 5.8: X-ray diffraction showing the diffraction pattern for the nematic phase of Compound 5.

5.2: Analysis of Bromo-terminated Terphenyl Intermediates (Compounds 9 to 13)

One of the issues with the biphenyl compounds was the low clearing points and as a result it was decided that the core should be increased to terphenyl. Changing the motif from a biphenyl group to a terphenyl group should result in an increase in the aspect ratio, i.e., the length is increasing but the width of the molecule remains constant. This increase in length of the core of the molecule will increase the possible π - π -interactions between the molecules. In theory, this should lead to greater interactions between the molecules, leading to an increase in mesophase stability and hence, the clearing point should increase. At the same time it would also mean that physical properties such as birefringence would increase due to the increased number of π -electrons within the core.

The mesophase behaviour was examined by polarised optical microscopy and the transition temperatures confirmed by DSC. The results are summarised in Table 5.2, the DSC thermograms are shown in Figures 5.9-5.14 and the transition temperatures are plotted as a function of methylene spacer in Figure 5.15.

<chem>Br(CH2)nO-C6H4-C6H4-C6H4-CN</chem>											
Cpd		Transition Temperature / °C									
No	n	Recryst	K		B		SmA		N		Iso
9	8	41.1 [11.7]	•	87.0 [25.7]	•	138.6 [4.6]	•	146.9 [0.3]	•	227.2 [0.6]	•
10	9	<0 [N/A]	•	73.9 [21.4]	•	140.2 [4.4]	•	146.5 [0.5]	•	217.8 [0.9]	•
11	10	54.9 [20.6]	•	91.6 [30.4]	•	140.3 [4.6]	•	151.5 [0.4]	•	215.8 [1.0]	•
12	11	47.2 [22.6]	•	85.7 [33.6]	•	140.8 [5.9]	•	191.0 [0.3]	•	207.8 [0.8]	•
13	12	71.4 [38.3]	•	107.2 [54.5]	•	137.9 [3.9]	•	194.5 [0.5]	•	205.1 [1.0]	•

Table 5.2: Transition temperatures (°C) for Compounds 9-13.

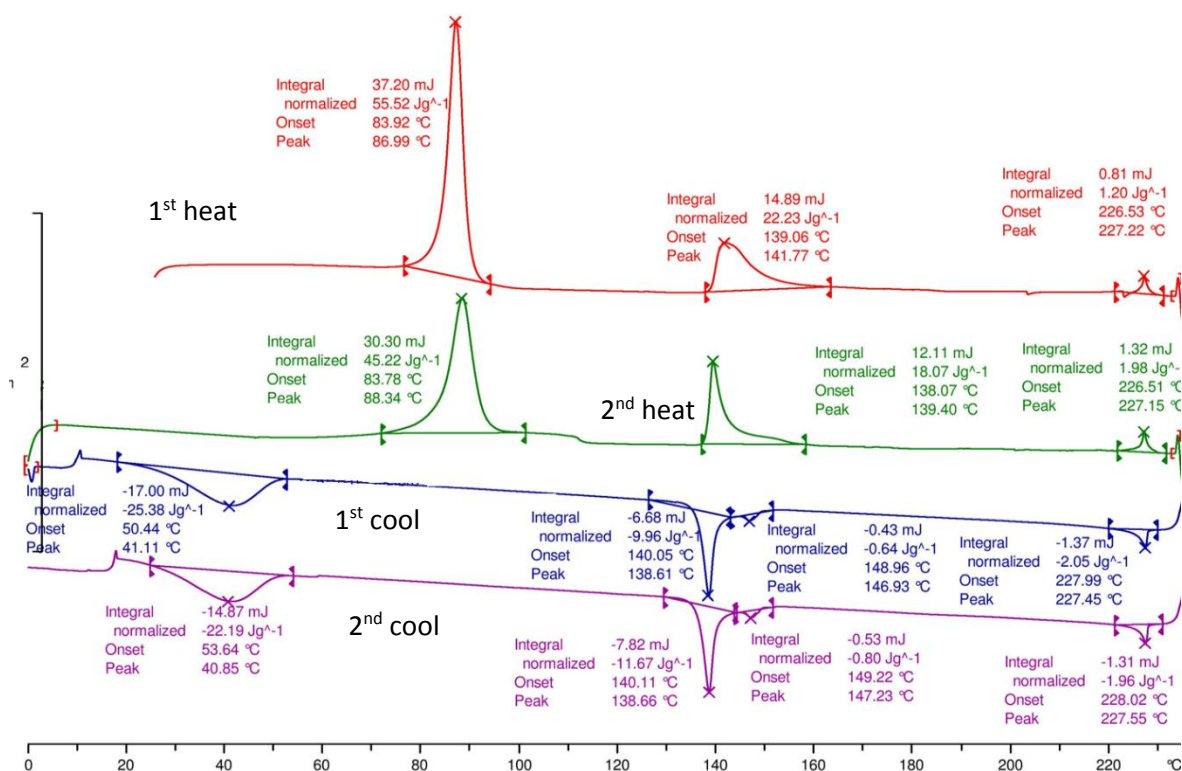
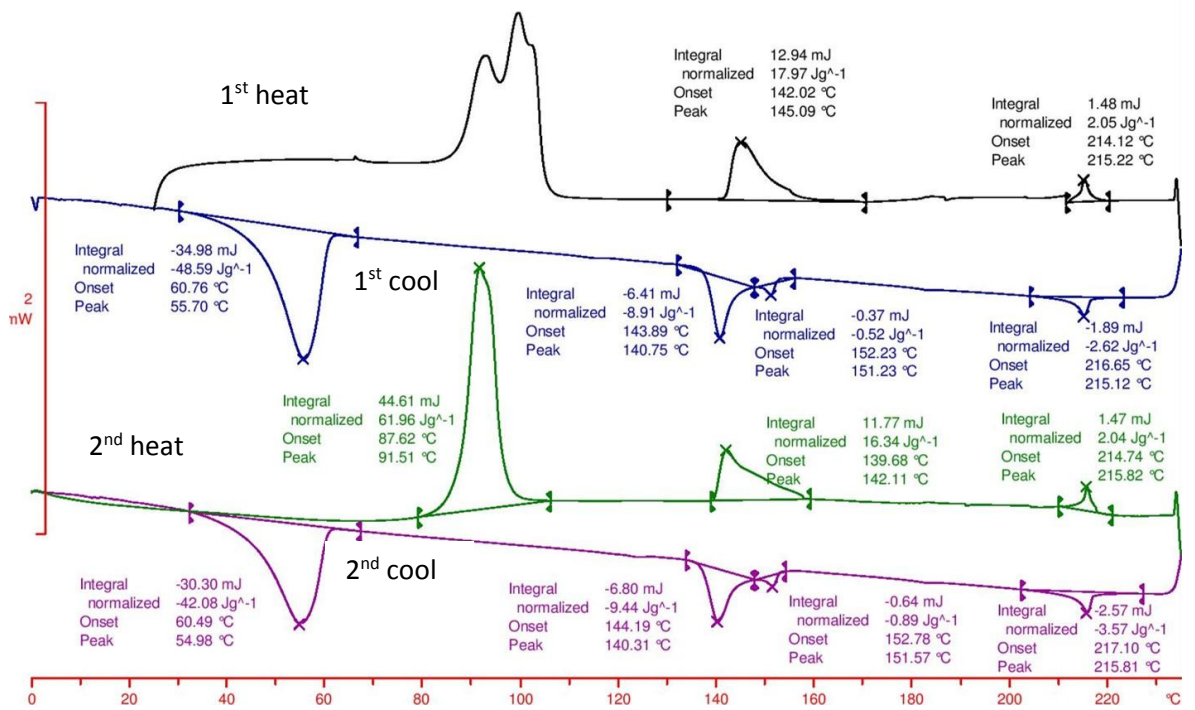
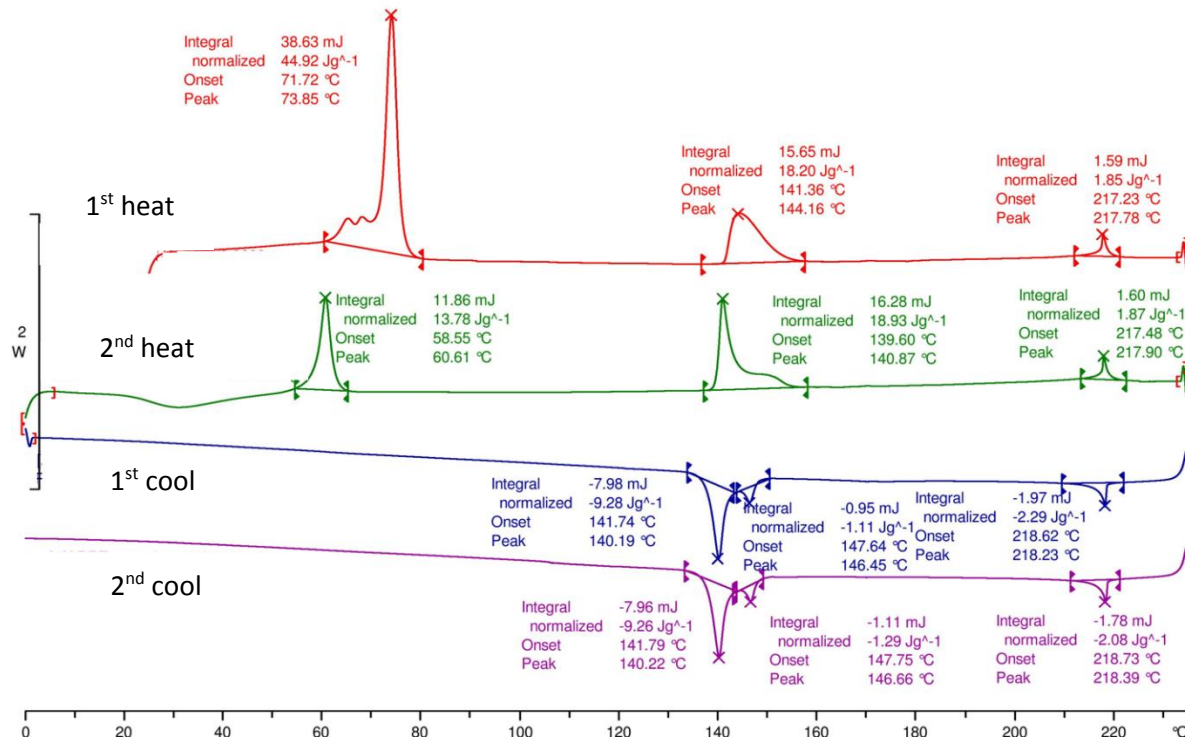


Figure 5.9: DSC thermogram (10 °C min⁻¹) showing the melting behaviour of Compound 9.



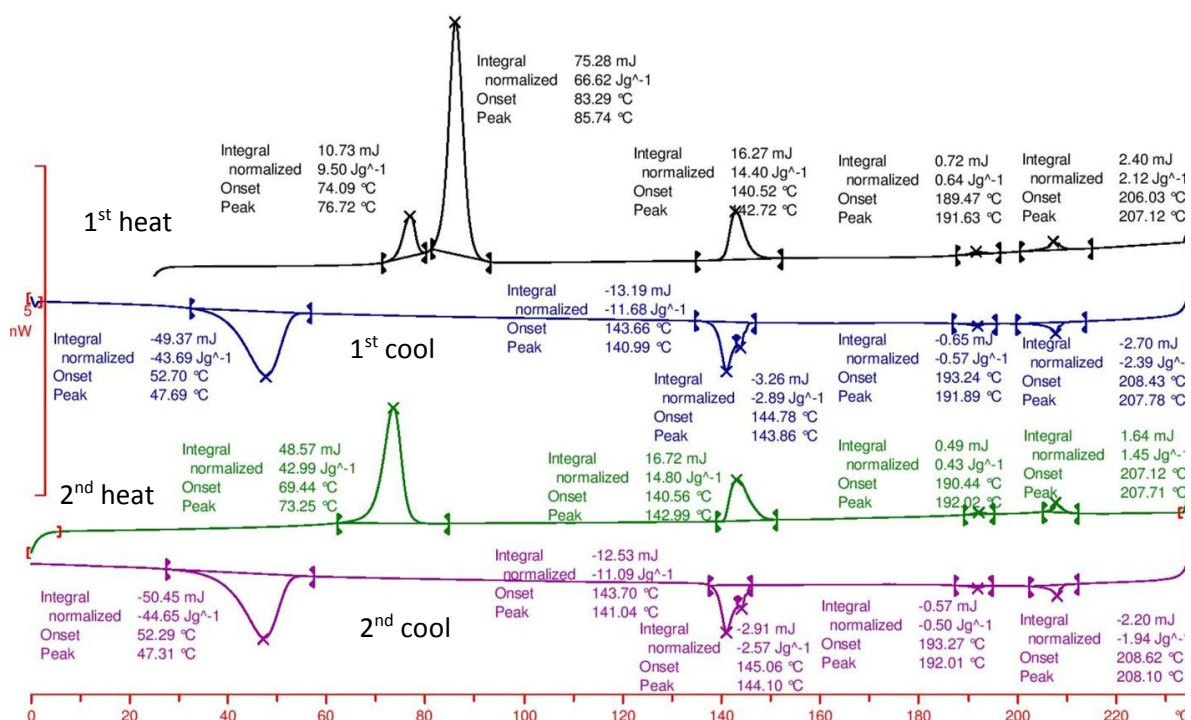


Figure 5.12: DSC thermogram (10 °C min⁻¹) showing the melting behaviour of Compound 12.

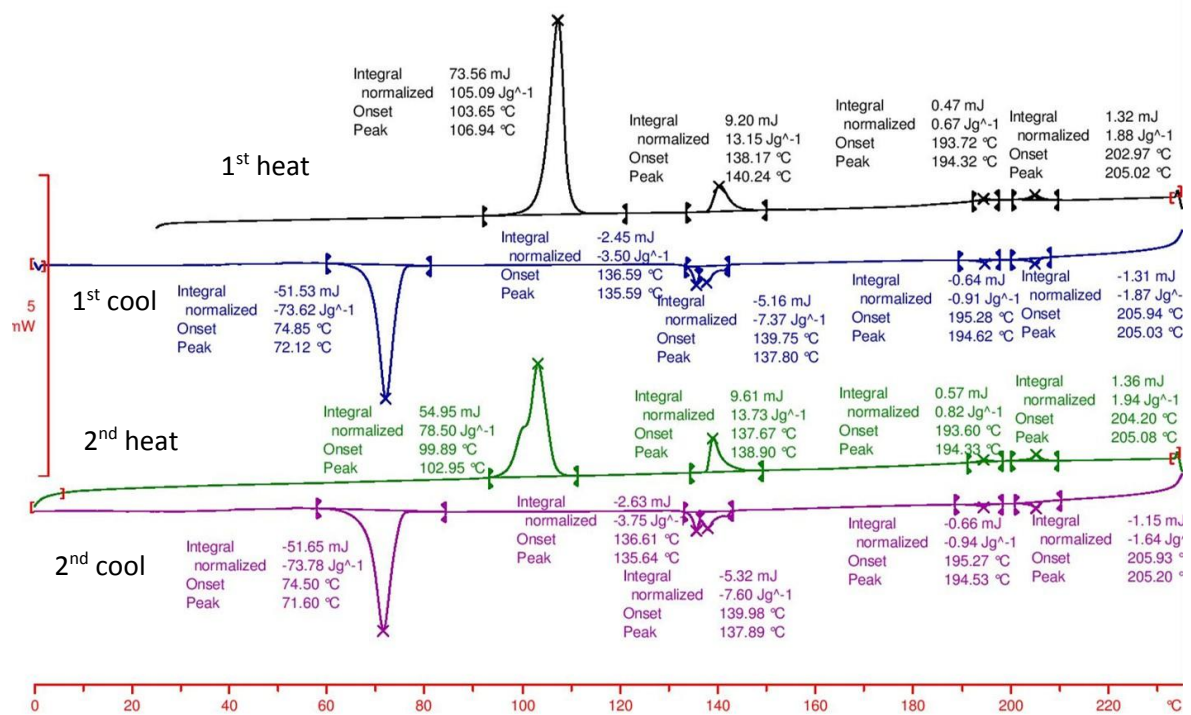


Figure 5.13: DSC thermogram (10 °C min⁻¹) showing the melting behaviour of Compound 13.

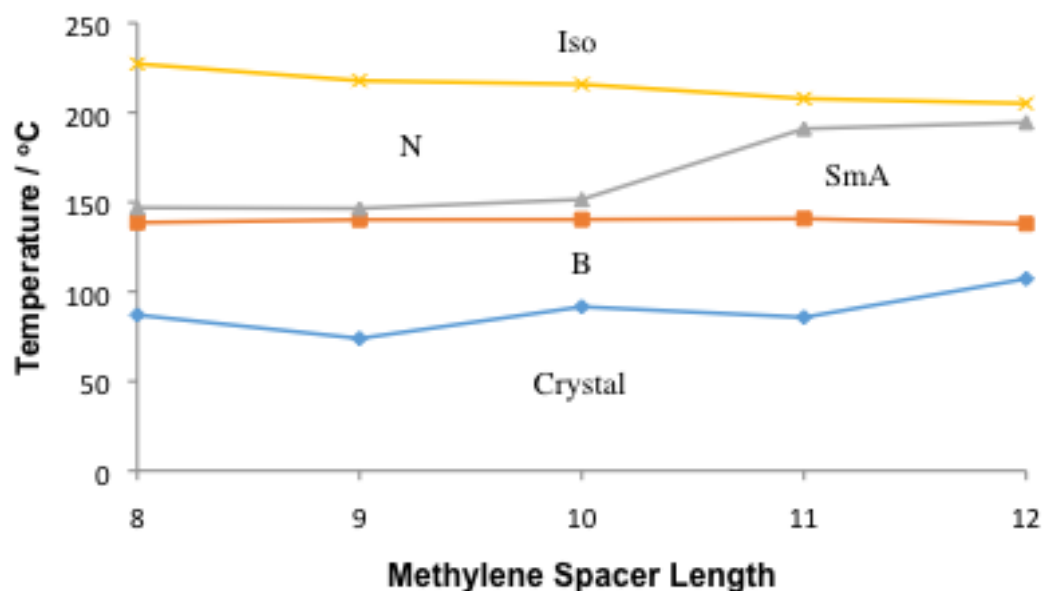


Figure 5.14: Graph showing the transition temperatures (°C) for Compounds **9-13**.

The increase in core from biphenyl to terphenyl has seen the transition temperature increase significantly and the clearing point has increased to 205-225 °C. Interestingly there is a small decrease in the clearing point with increase in the methylene spacer. This effect, although unexpected may be accounted for by the increased flexibility of the chain accompanied by the steric bulk of the terminal bromide affecting packing of the molecules. The increase in core has also seen an increase in the mesomorphic behaviour where smectic A and crystal B phases are now observed across the series in addition to the nematic phase. This confirms that the increased number of aromatic units in the core has augmented the molecular interactions and driven the organisation of the molecules to form layered structures. This increase in mesomorphic behaviour mirrors that seen for alkoxy cyanoterphenyls where clearing points exceed 240 °C for the heptyloxy terminal chain, and where nematic, crystal B and a higher ordered smectic phase are observed. In comparison the bromide Compounds **9-13** exhibit nematic, smectic A and crystal B phases. The crystal B phase remains at constant temperature across the phase diagram whereas the smectic A phase increases in stability as the methylene content increases showing that the alkoxy chain is contributing to driving the smectic organisation in these molecules.

Similar to the trends witnessed for Compounds **4** to **8**, the data presented in Table 5.2 shows again a split in the trends for the odd and even spaced compounds. The enthalpy of the transition from crystal to crystal B phase is the most energetic, with the trends also being clearer for this transition. The even length Compounds **9**, **11** and **13** show a clear increase in the enthalpy of the transition, with the intermediate odd length Compounds **10** and **12** not fitting linearly within this trend. Compound **10** shows a lower enthalpy of transition than either Compound **9** (which possesses a shorter chain) and Compound **11** (which is slightly longer), whereas Compound **12** does show a

greater enthalpy than the shorter spaced compounds, but which is significantly reduced when compared to the longer spaced Compound **13**, with the increase being a clearly non-linear progression between the analogous compounds, suggesting a degree of suppression compared to expectations for compounds of a similar shape. This odd/even effect, as well as the general trends witnessed for both series are witnessed in the enthalpies of recrystallization, yet here the enthalpy of the recrystallization of Compound **10** was not determined. The higher temperature transitions show less of a clear trend due to the lower enthalpies witnessed, as well as the reduced ordering of the compounds in the more energetic phases. The clearing transition of the compounds as well is unclear due to the degradation of the compound near to the temperature of the clearing points.

Microscopy was used to identify the specific phase types for each of the compounds. Nematic phases were identified by the schlieren texture showing singularity defects with 2- and 4- brushes. The nematic phase also shown marbled textures such as the one in Figure 5.15a although some preparations tended to predominantly form homeotropic texture where the phase could only be determined using shearing of the sample, which caused a temporary realignment of the molecules. The smectic A phase did not easily give rise to focal conic defects that are diagnostic of the smectic A phase. Unfortunately there was a strong tendency for the sample to form a homeotropic texture and as such the paramorphic texture for the subsequent higher ordered phases lacked focal conic or fan-like domains to aid characterisation. Figure 5.15b show domains within the nematic phase that are at the N-SmA phase boundary. These domains are gaining a fingerprint or striped appearance as the edge dislocations of a layered structure appear.

It was unclear if the lower temperature smectic phase was in fact a B phase or an E phase. A mosaic texture appears in the regions that were predominantly homeotropic, see Figure 5.15c-e. The mosaic texture has well defined boundaries and there is a range of different birefringent colours observed. The edges of the mosaic textures appear to show ghosting like effects that are common in E phases but the presence of black regions rule out this possibility because the E phase is a biaxial phase and as such the domains should show birefringence at all orientations. This would indicate that the higher ordered smectic phase is a crystal B phase. Additionally, the phase transition from a smectic A phase to E phase would be accompanied by transition bars across the focal conic domains. These are not evident at the transition for Compound **11** shown in Figure 5.15d.

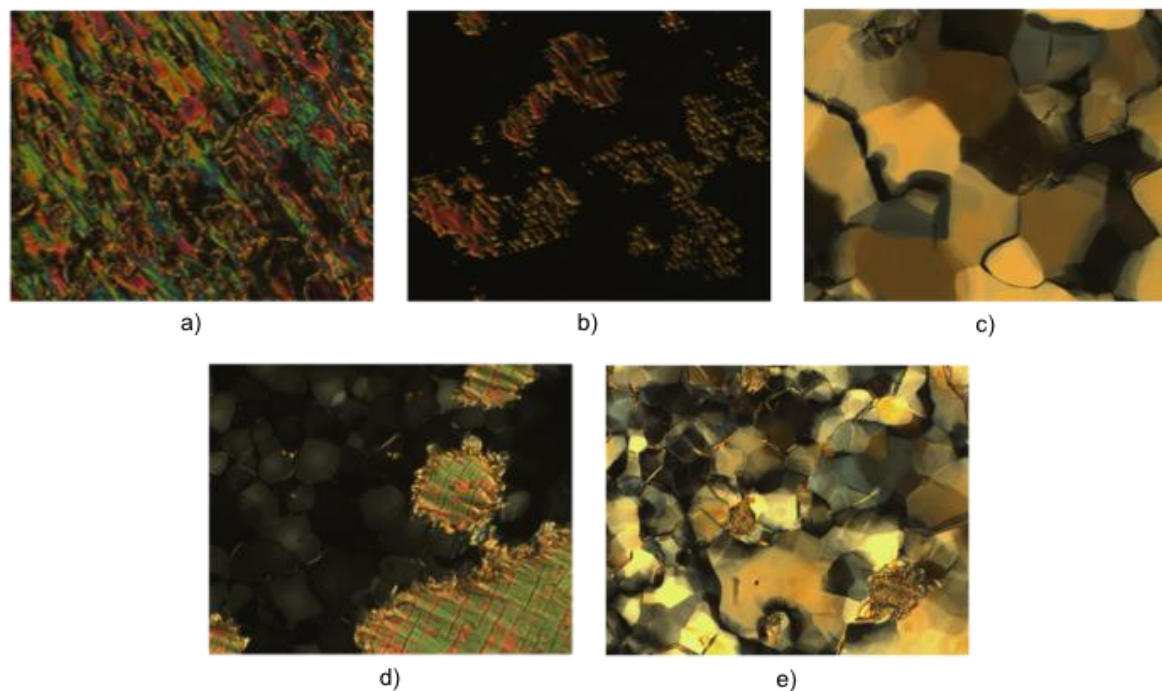


Figure 5.15: Photomicrographs (x100) showing a) Compound **9** in a nematic phase at 165 °C, b) Compound **10** at the N-SmA phase transition, c) mosaic texture of the B phase of Compound **10** at 137.4 °C, d) SmA-B phase transition for Compound **11** and e) B phase of Compound **11** at 142.3°C.

All of the compounds in this series were examined by x-ray diffraction to confirm the phase identification but also to see how the packing of the molecules varies as a function of increasing methylene chain length. In general the behaviour was consistent across the series although there were some slight differences in the layer spacing of the nematic phase and also some additional peaks in the higher ordered smectic phase. The layer spacings for Compound **9** are shown in Figure 5.16 and show that the principal layer spacing is consistent across all phases and once the phase transition to the B phase occurs there is addition 200 and 300 peaks representing $\sqrt{4}$ and $\sqrt{9}$ respectively. In addition there are two peaks in the wide angle (within the detector limits although a third is evident with rotation of the detector) which is typical for a B phase.⁷⁹ The diffraction peaks are shown in figure 5.17 and associated diffraction patterns are presented in Figure 5.18.

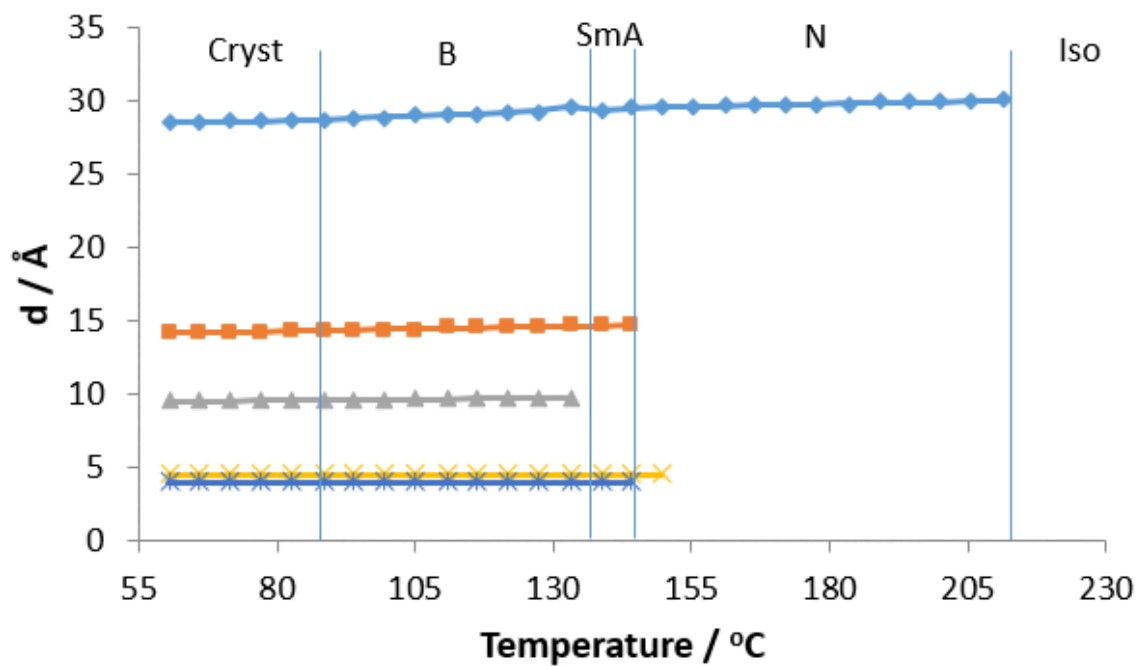


Figure 5.16: Graph showing the layer spacing (\AA) as a function of temperature ($^{\circ}\text{C}$) for Compound 9.

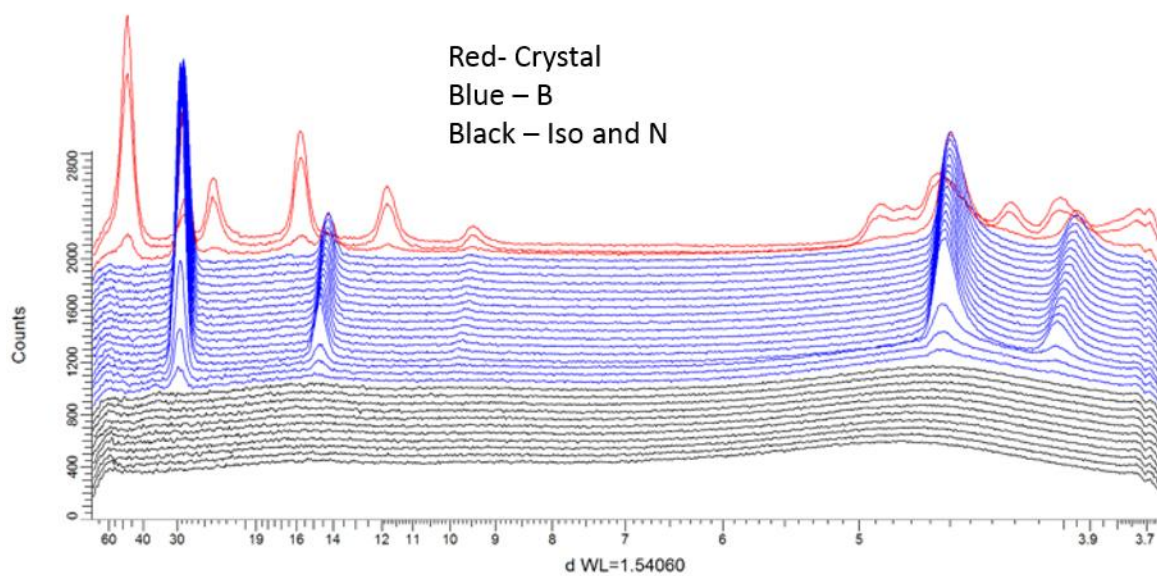


Figure 5.17: Plot showing the diffraction peaks as a function of temperature for Compound 9.

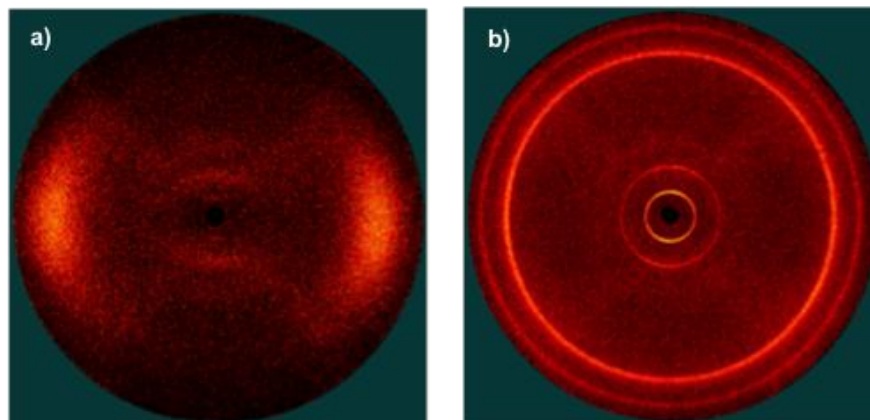


Figure 5.18: Diffraction patterns for Compound **9** showing a) aligned nematic phase with diffuse diffraction peaks and b) B phase showing sharp diffraction peaks.

Compound **10** behaves in a similar manner to Compound **9** although the layer spacing shows a small decrease upon transition in the B phase from the nematic and smectic A phases. The layer spacing as a function of temperature is shown in Figure 5.19. Interestingly the B phase reveals an additional layer spacing that is consistent with 111 relating to the hexagonal packing within the smectic phase. There is very little shrinkage in this system and the layer spacing remain almost constant with decrease in temperature. The diffraction peaks are shown in Figure 5.20 and the associated diffraction patterns are shown in Figure 5.21.

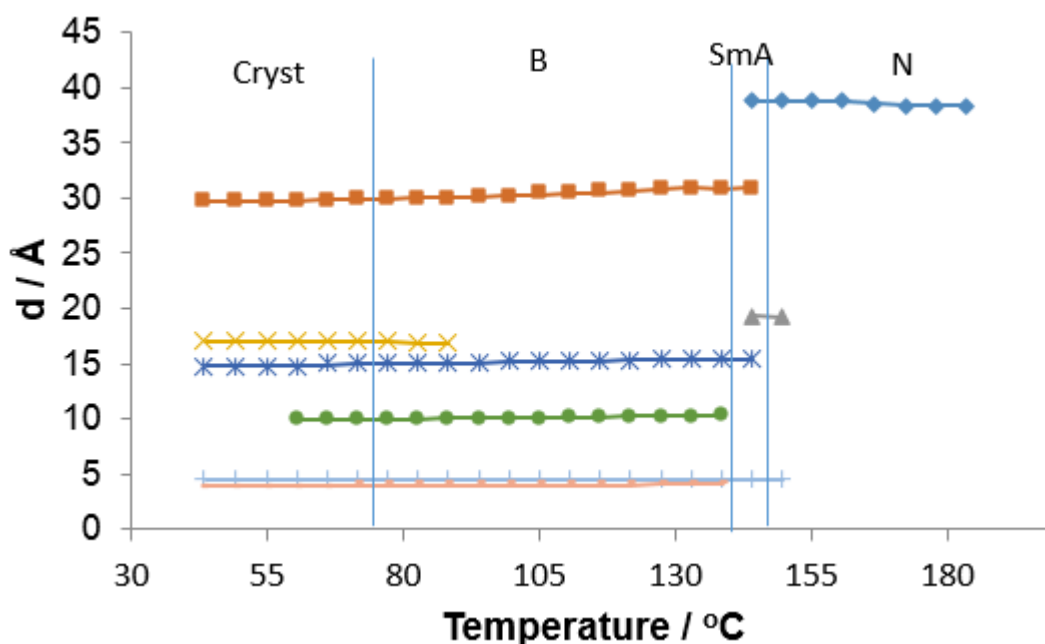


Figure 5.19: Plot showing the layer spacing (Å) as a function of temperature for Compound **10**.

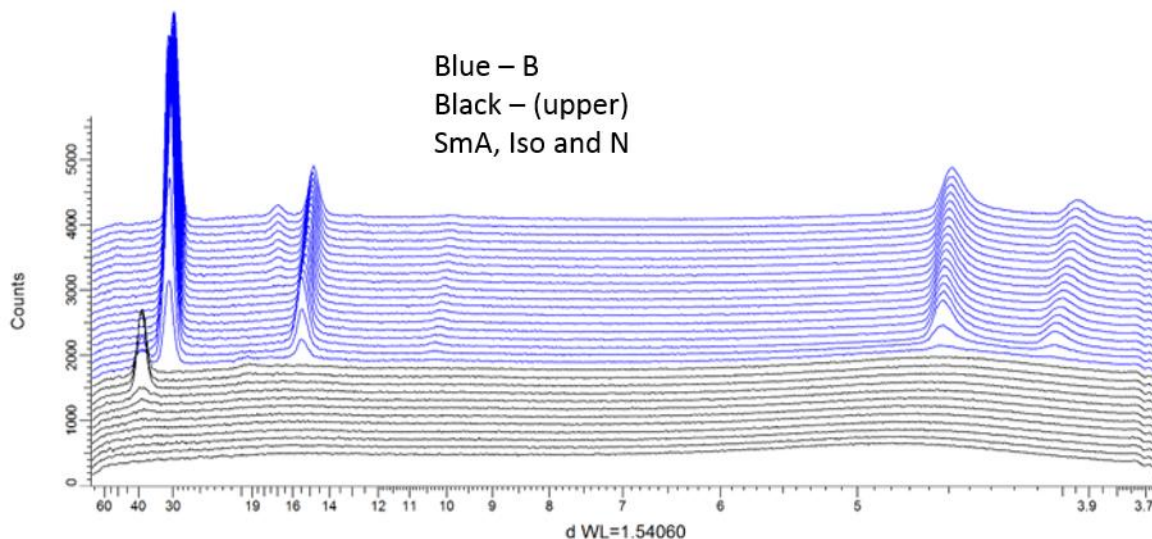


Figure 5.20: Plot showing the diffraction peaks as a function of temperature for Compound **10**.

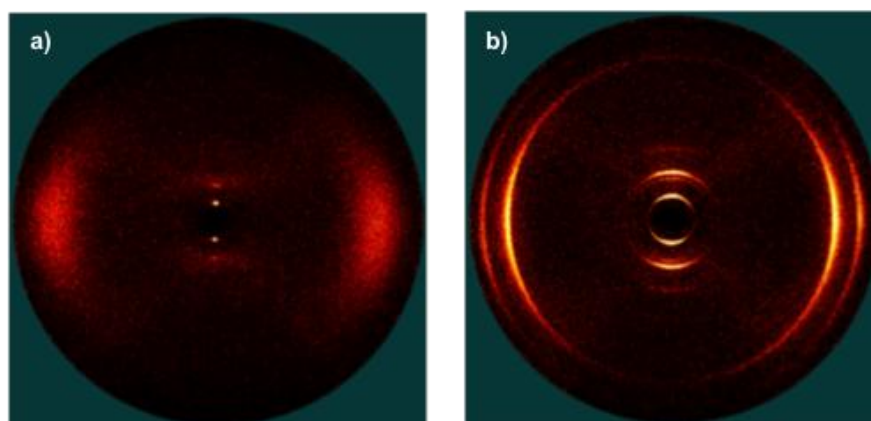


Figure 5.21: Diffraction patterns for Compound **10** showing a) aligned smectic A phase with 100 and 200 peaks and b) B phase showing sharp diffraction peaks including 100, 111, 200 and 300 peaks.

Compound **11** proved to be little unusual in the transition from the smectic A phase into the B phase compared to Compounds **9** and **10** because an additional peak was observed at smaller angle in the x-ray representing a layer spacing at approximately 52 Å. All the other peaks in the x-ray are consistent with both Compounds **9** and **10**. The layer spacing as a function of temperature is shown in Figure 5.22. The B phase shows good alignment in this experiment and the alignment is retained upon crystallisation, see Figures 5.23 and 5.24.

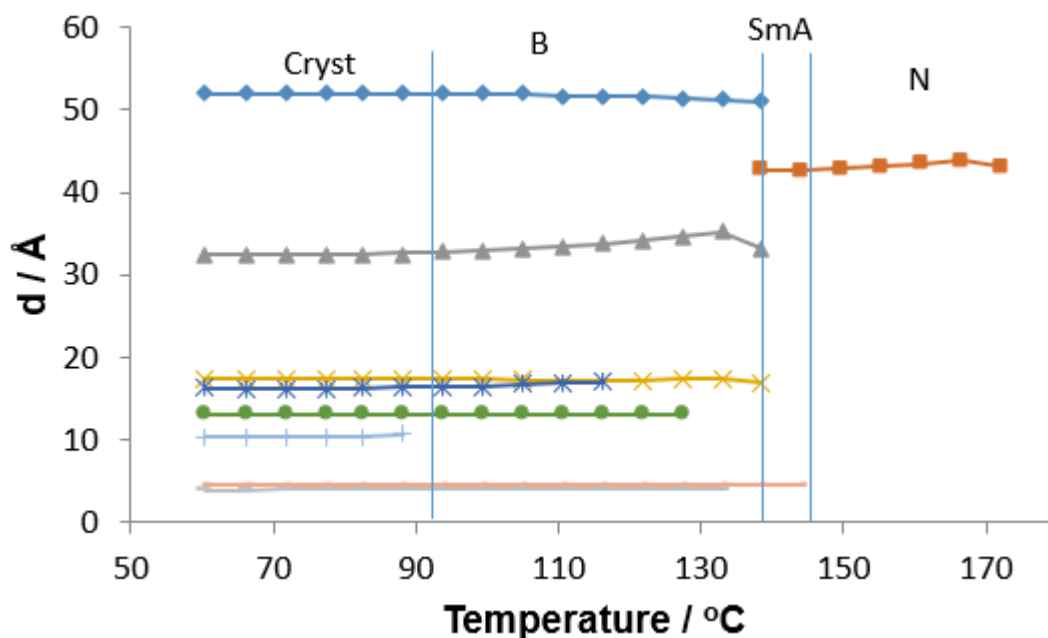


Figure 5.22: Plot showing the layer spacing (Å) as a function of temperature for Compound 11.

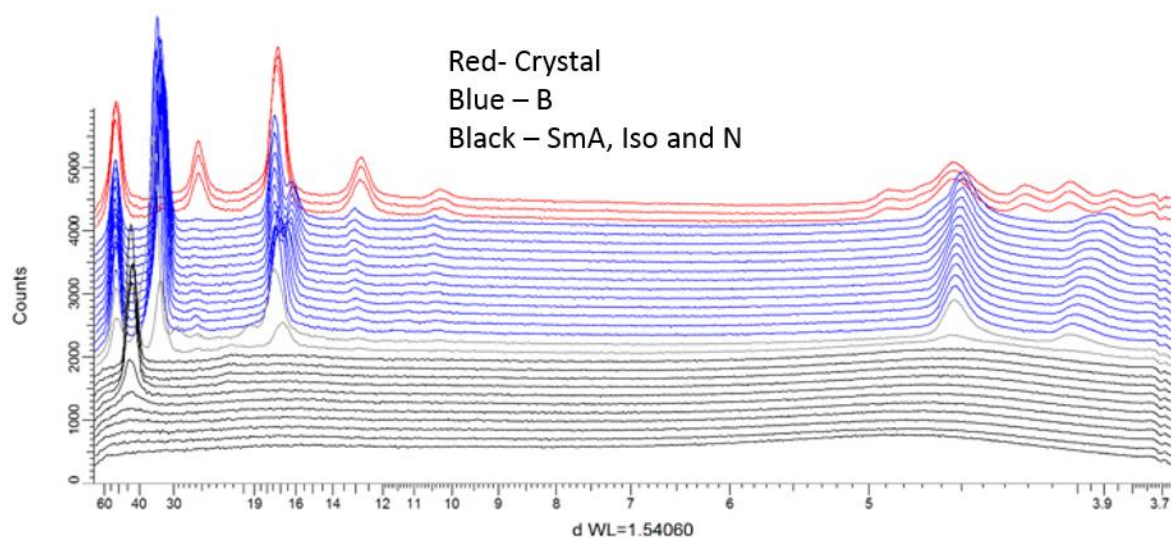


Figure 5.23: Plot showing the diffraction peaks as a function of temperature for Compound 11.

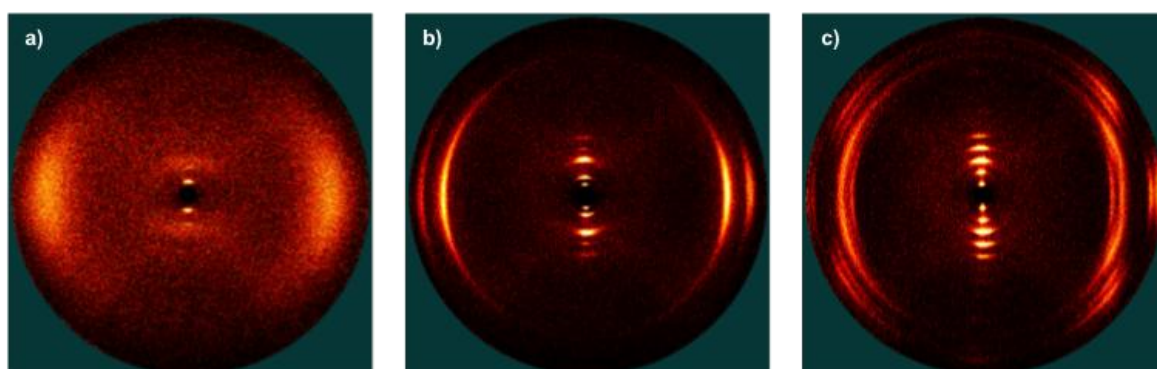


Figure 5.24: Diffraction patterns for Compound 11 showing a) aligned smectic A phase with 100 and 200 peaks and b) B phase showing good alignment and c) crystalline state at low temperature showing strong correlation of the layered structure.

Compound **12** behaves consistently with the rest of the series of compounds. The broader smectic A phase is evident in the diffraction experiments and the phase shows increased coherence and both 100 and 200 peaks are evident. Once again there is very little change in the layer spacing with changes in temperature. The layer spacing as a function of temperature is given in Figure 5.25. The diffraction peaks are shown in Figure 5.26 showing clearly the 100, 200 and 300 peaks observed in the B phase.

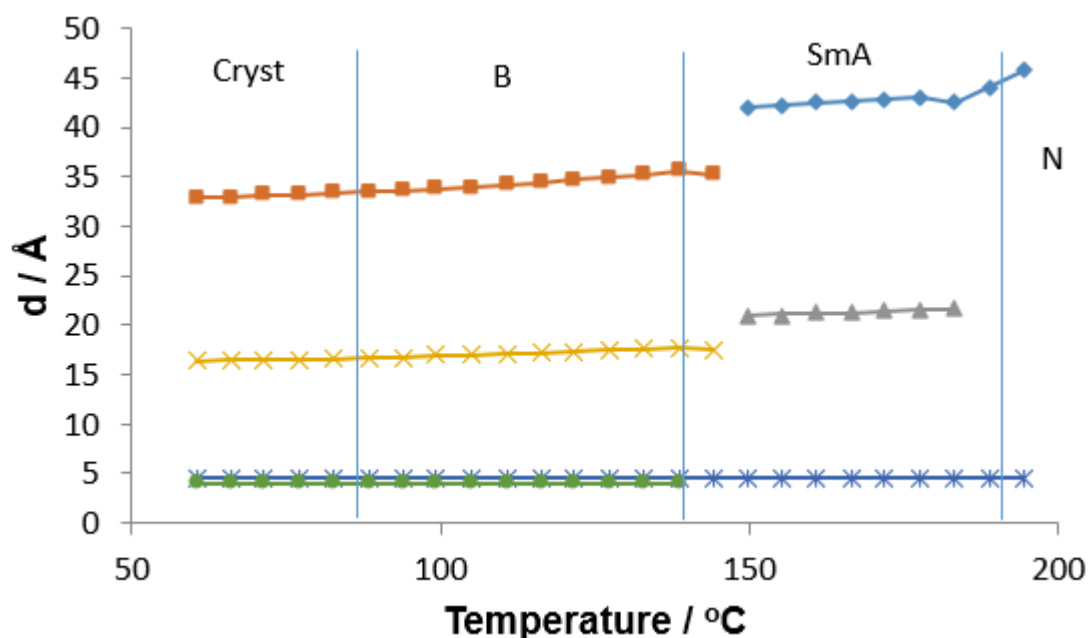


Figure 5.25: Plot showing the layer spacing (\AA) as a function of temperature for Compound **12**.

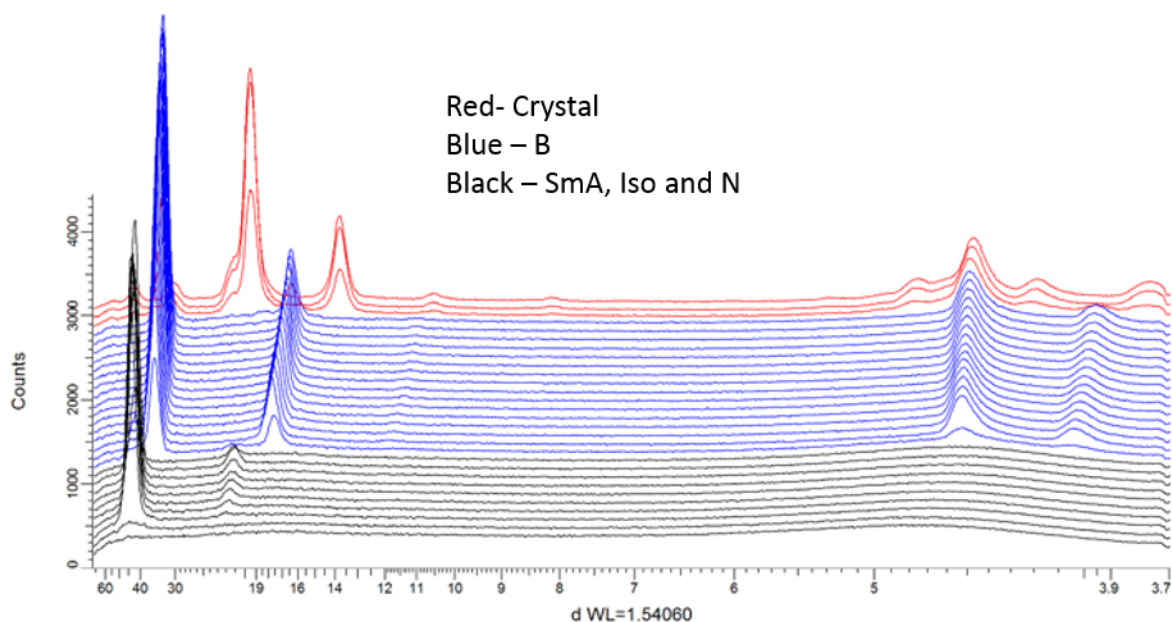


Figure 5.26: Plot showing the diffraction peaks as a function of temperature for Compound **12**.

The final compound in the series, Compound **13**, proved to be difficult to align and as a result only powder patterns were obtained. This meant that it was difficult to draw any conclusions about the orientation of the molecules within the phase. Instead, inference must be made based on the

previous compounds in the series. Interestingly this compound, which has the longest chain length, shows signs of layer compression with decreasing temperature. This behaviour was not observed in previous compounds and may be due to the freedom of motion associated with the increased chain length at higher temperature. As the temperature is decreased the chains begin to interpenetrate at the interface and hence are forced to pack together and fill space more efficiently. The layer spacing as a function of temperature is shown in Figure 5.27. It is possible in this compound that there is another higher order phase observed at lower temperature. Figure 5.28 shows the diffraction peaks observed for this sample as a function of temperature and clearly there are additional peaks appearing in the blue region that relate to possible 110 and 210 diffractions where the peaks exhibit a $\sqrt{2}$ and $\sqrt{5}$ relationship to the 100 peak.

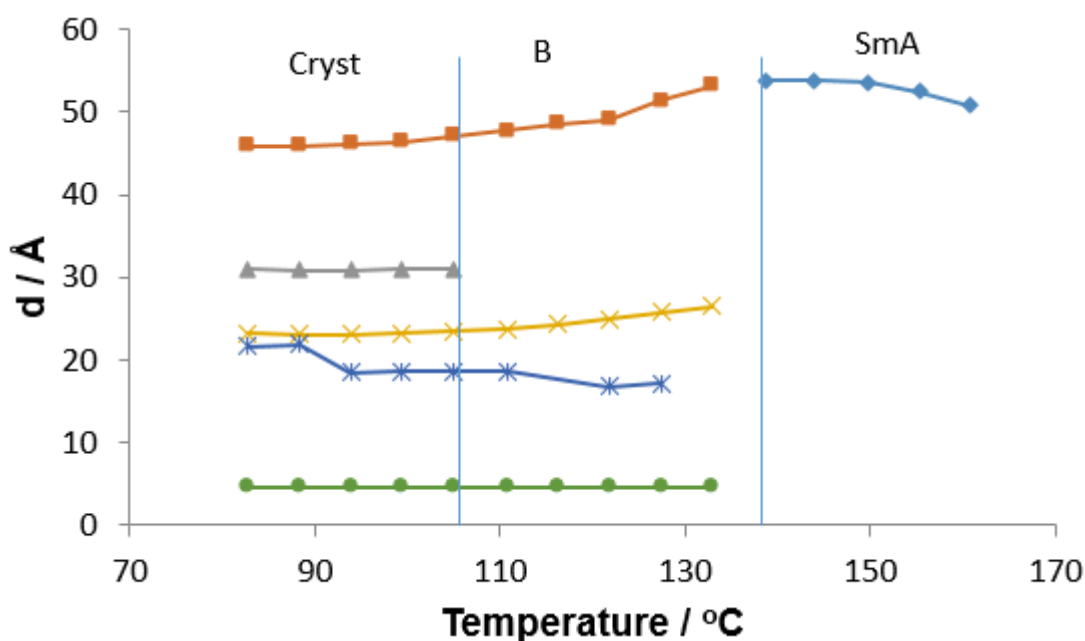


Figure 5.27: Plot showing the layer spacing (Å) as a function of temperature for Compound 13.

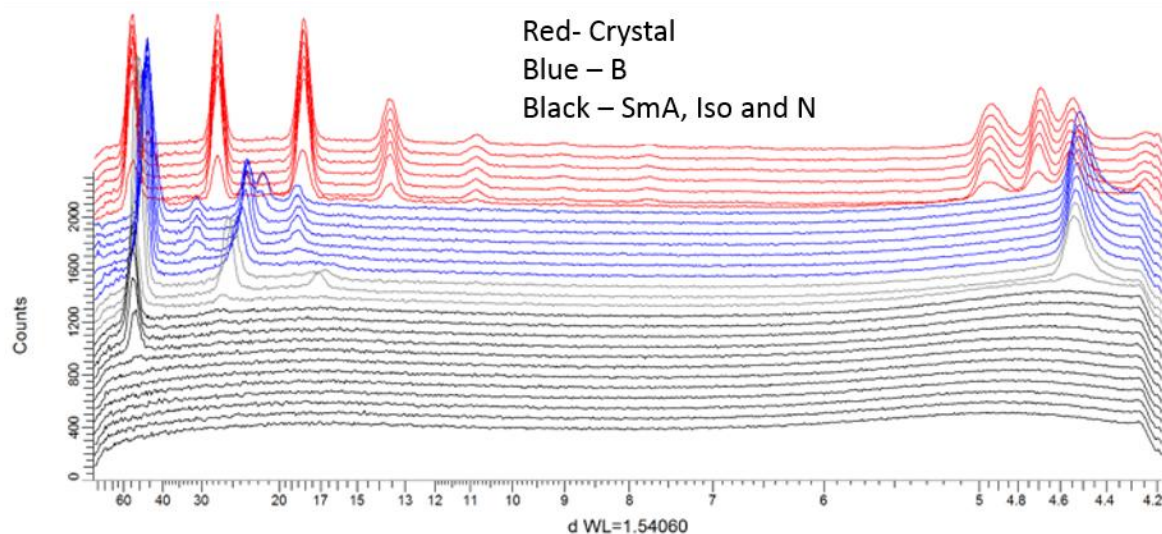


Figure 5.28: Plot showing the diffraction peaks as a function of temperature for Compound 13.

5.3: Analysis of Diallylamino-Terminated Biphenyl Compounds (Compounds 14-18)

Changing the terminal group from bromide to diallylamino was expected to have a considerable effect on the bulk behaviours of the compounds. More specifically, the diallylamino group represents a larger steric bulk than the bromide and as a result it was expected that transition temperatures would decrease due to the increased volume hindering the packing of the molecules. It was also assumed that the bulkiness of the diallyl groups may suppress higher ordered smectic phases which would be amplified by the electronic effects of π electron rich double bonds within the alkyl regions.

The mesophase behaviour was examined by polarised optical microscopy and the transition temperatures confirmed by DSC. The results are summarised in Table 5.3, the DSC thermograms are shown in Figures 5.29-5.31. Unfortunately there were insufficient quantities of Compounds **14** and **17** to be able to carry out complete characterisation. This was partly due to the difficulties in purifying the compounds with such low melting points.

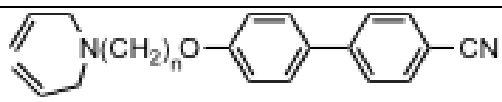
							
		Transition Temperature / °C					
Cpd No	n	Recryst	K		SmA		Iso
14	8		•		•		•
15	9	-0.9 [8.4]	•	17.9 [11.1]	•	42.0 [3.3]	•
16	10	<0 [N/A]	•	<0 [N/A]	•	47.1 [3.1]	•
17	11		•		•		•
18	12	<0 [N/A]	•	32.3 [26.8]	•	52.0 [4.7]	•

Table 5.3: Transition temperature (°C) for Compounds **14-18**.

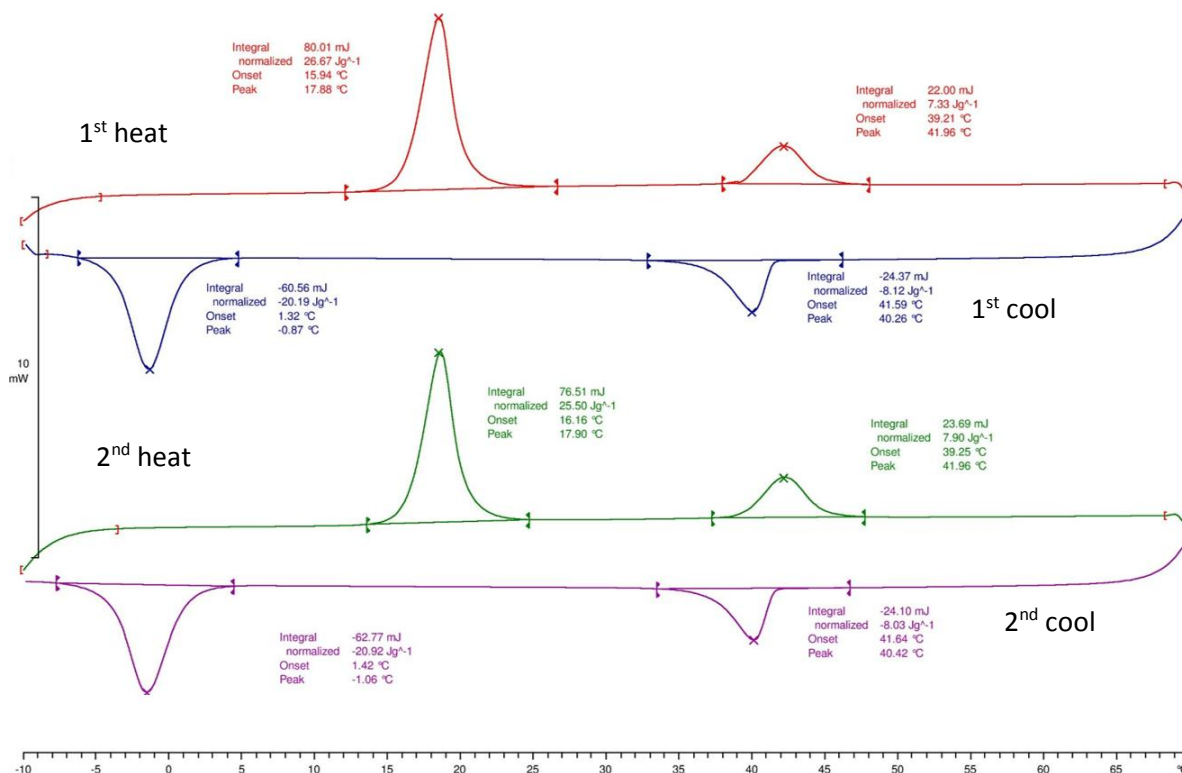


Figure 5.29: DSC thermogram (10 °C min⁻¹) showing the melting behaviour of Compound 15.

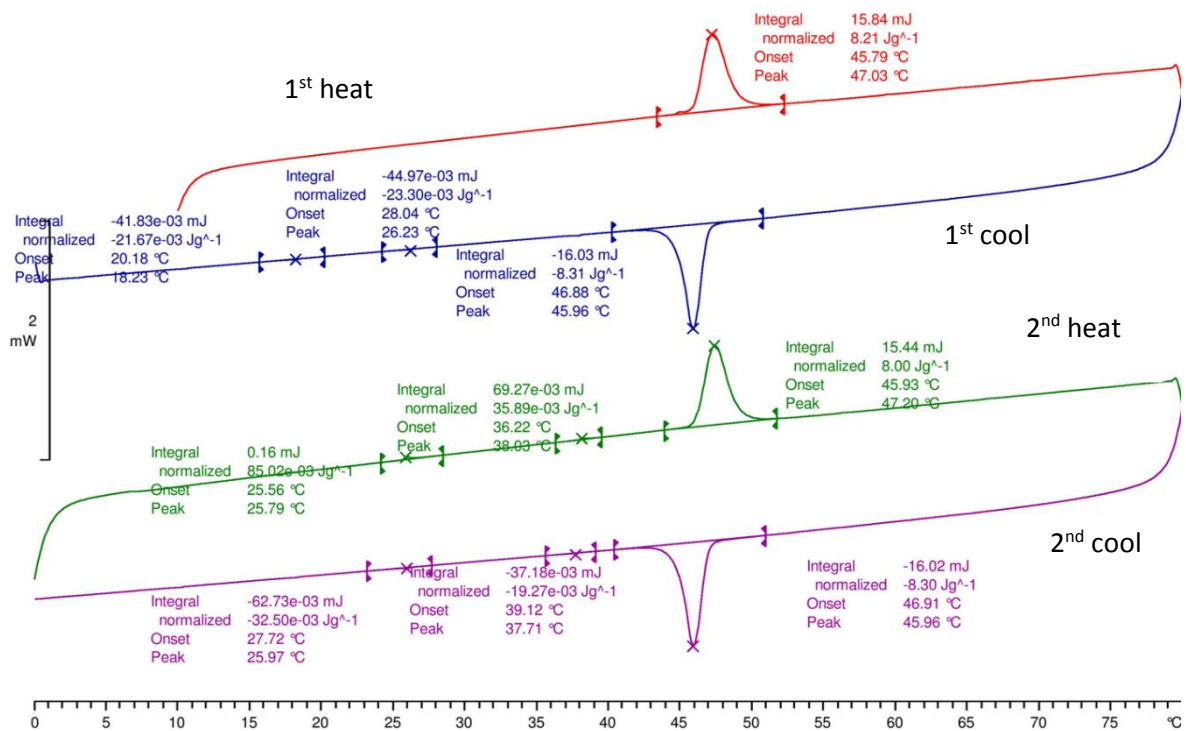


Figure 5.30: DSC thermogram ($10\text{ }^{\circ}\text{C min}^{-1}$) showing the melting behaviour of Compound **16**.

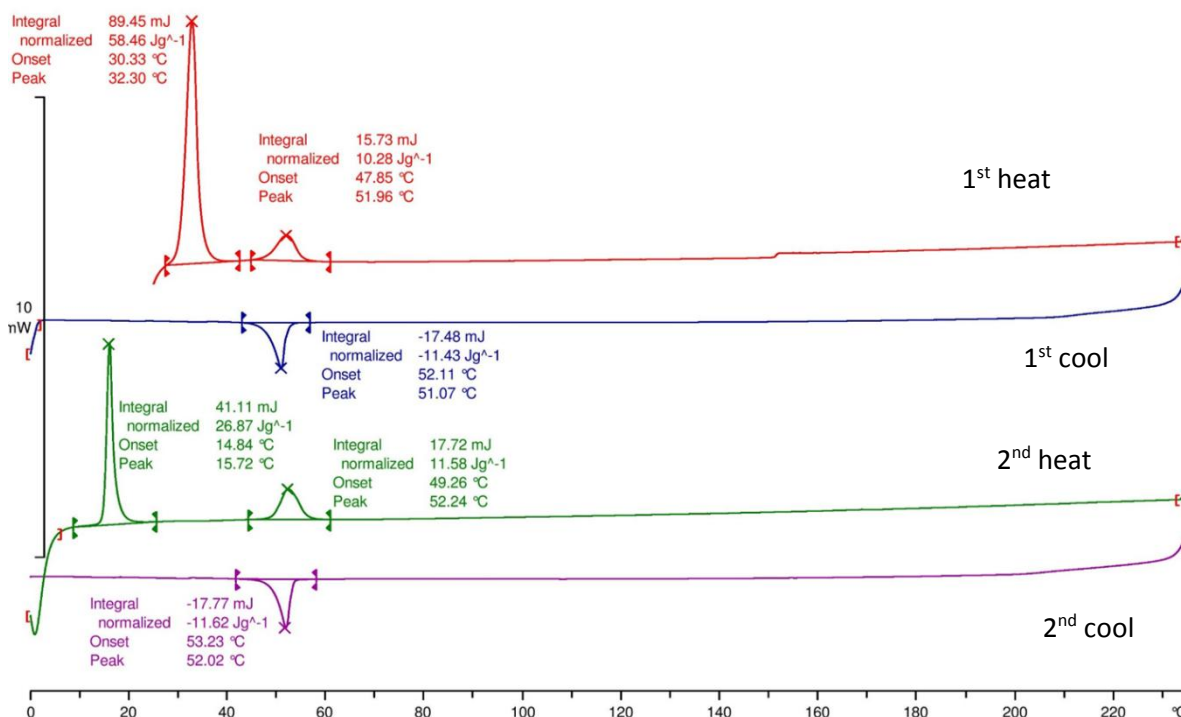


Figure 5.31: DSC thermogram ($10\text{ }^{\circ}\text{C min}^{-1}$) showing the melting behaviour of Compound **18**.

One of the most important features of this series of compounds is the low melting point. Theoretically it was predicted that the increased bulk of the diallylamine at the terminus of the molecule would hinder close packing of the molecules and lead to a disordering and potentially the loss of higher order phase behaviour. It was also predicted that the clearing points would decrease compared to the bromide Compounds **4-9** for similar reasons. Indeed, the melting points have dropped to such an extent that the mesophase behaviour is no longer monotropic and now are enantiotropic.

With the limited data available for transitions for Compounds **14** and **17** (presented in Table 5.3 above), it is not possible to draw a full conclusions over the energetic trends and odd/even effects for these compounds. However, it is possible to see that there is an increase in the enthalpies of transitions may continue to show general increases with increased chain length with the clear elevation of the enthalpy of the crystal to smectic A phase transition seen between Compounds **15** and **18** ($n=9$ and 12 respectively). The enthalpies of this transition are of a comparable magnitude to comparable transitions witnessed in the previous series (for example the crystal to nematic transitions of Compounds **4** to **8**), yet the enthalpies are clearly lower. This is most likely due to the change in the terminal group from the bromide to a larger diallylamino-group, which will have a

greater degree of hindrance in the alignment and packing of compounds, reducing the attractions between the molecules that must be overcome.

Microscopy on this series of compounds reveals that smectic A phases are observed. This phase was classified by observation of focal conic defects showing both hyperbolic and elliptical lines of optical discontinuity accompanied by homeotropic domains where the molecules are aligned perpendicular to the slide surface. It was unexpected that the bulkier group would lead to a phase that is more organised than the nematic phase observed in the bromide series. This behaviour is driven by the polar nature of the amine group which exhibits increased interaction at the interface between molecules which encourages the formation of a layered organisation of the molecules. Examples of the textures of the smectic A phase for Compounds **16** and **18** are given in Figure 5.32.

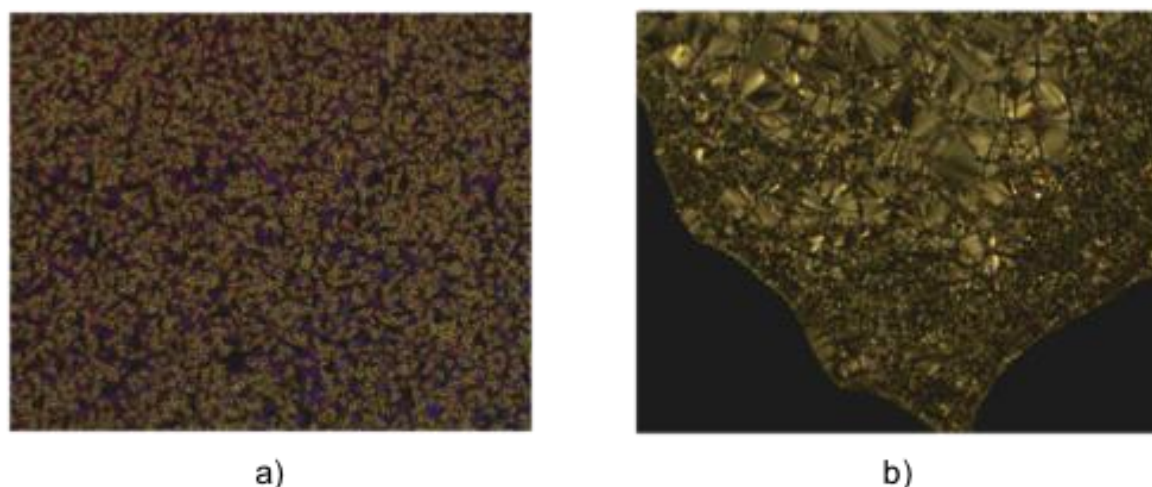


Figure 5.32: Photomicrographs (x100) showing the smectic A focal conic textures of a) Compound **16** and b) Compound **18**.

Compounds **15**, **16** and **18** were examined by x-ray diffraction to show the smectic layer spacing. Due to limitations in the diffractometer furnace it was not possible to cool below room temperature so the temperature range investigated was limited. The layer spacing as a function of temperature is shown in Figure 5.33. This graph shows that the layer spacing increases with decreasing temperature, which is consistent with the bulky amine group being forced out of the smectic interface as it begins to stiffen at lower temperatures in order to maximise the packing of the molecules and effectively fill space at the interface. If the amine remained in the interface then there would be more void volume, which is not permitted energetically. The difference in the layer spacing between compounds is consistent with an addition methylene unit in the spacer. Assuming a fully extended model for each structure, the layer spacing represents approximately 1.6 times the molecular length. This swollen layer spacing is much larger than the 1.4 times the molecular length that is quoted for standard alkylcyanobiphenyls [ref] and this suggests that the diallyamine group at the end of the chain has forced the molecules to be pushed apart due to the packing constraints

of the bulky group. For each compound the number of diffraction peaks was limited to the 100 and 001 peaks representing the layer spacing in the smectic A phase and the lateral packing of the molecules respectively. The wide angle peak was a broad diffuse peak which shows that the lateral packing of the molecules is short range and typical of a smectic A phase. Diffraction plots are for Compounds **15**, **16** and **18** are shown in Figures 5.34-5.37. Due to the absence of a nematic phase it was not possible to induce alignment in these samples and hence only powder patterns could be obtained, see Figure 5.37.

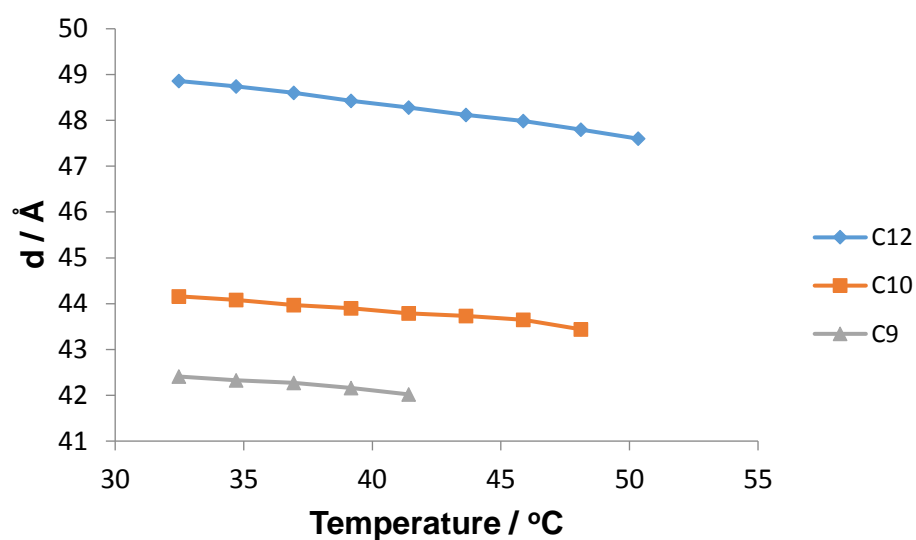


Figure 5.33: Layer spacing (Å) as a function of temperature (°C) for Compounds **15**, **16** and **18**.

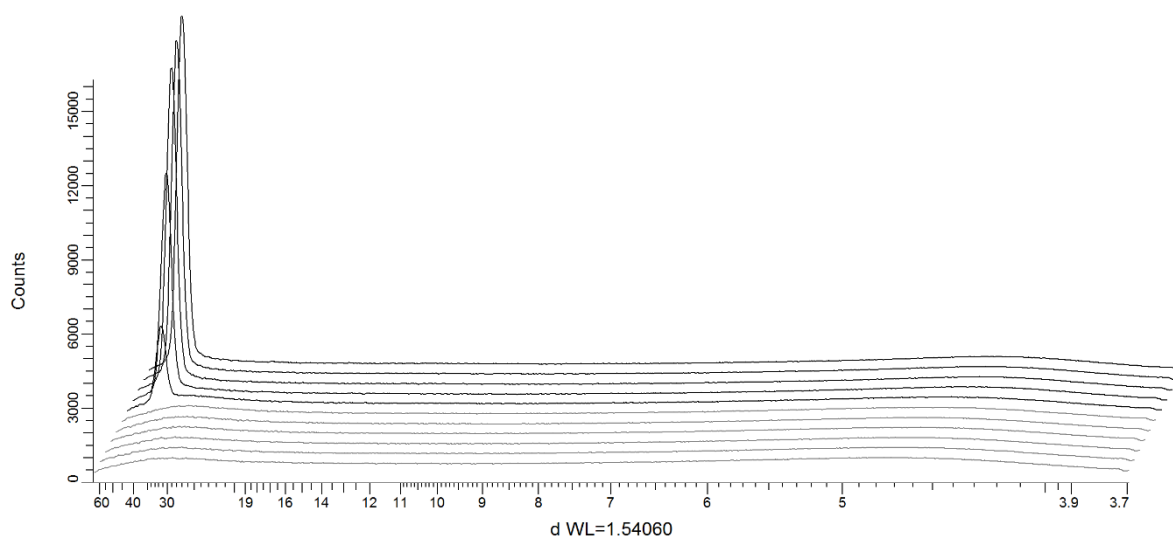


Figure 5.34: Plot showing the diffraction peaks as a function of temperature for Compound **15**.

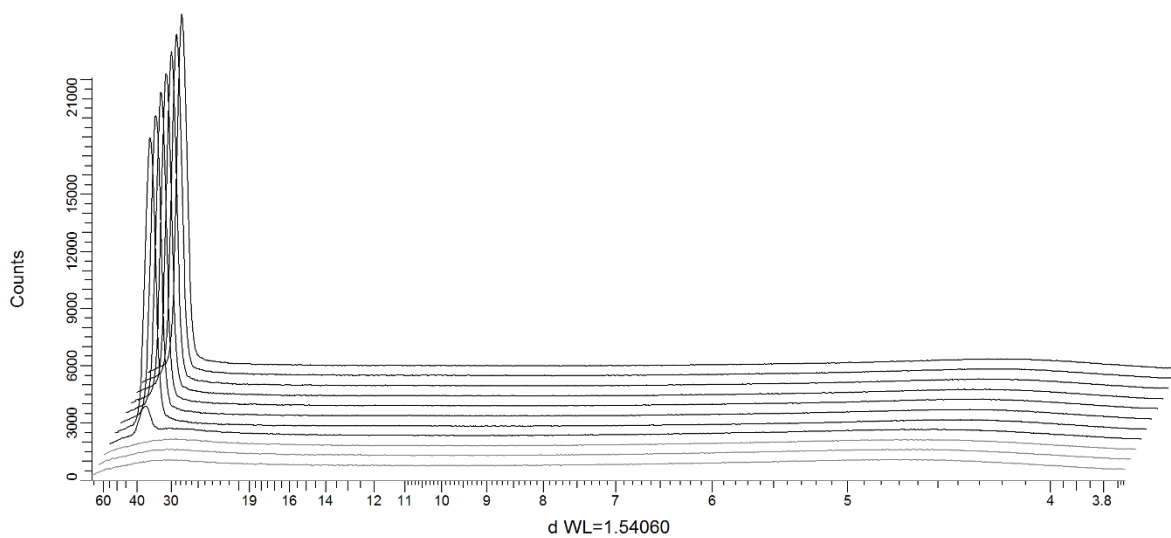


Figure 5.35: Plot showing the diffraction peaks as a function of temperature for Compound **16**.

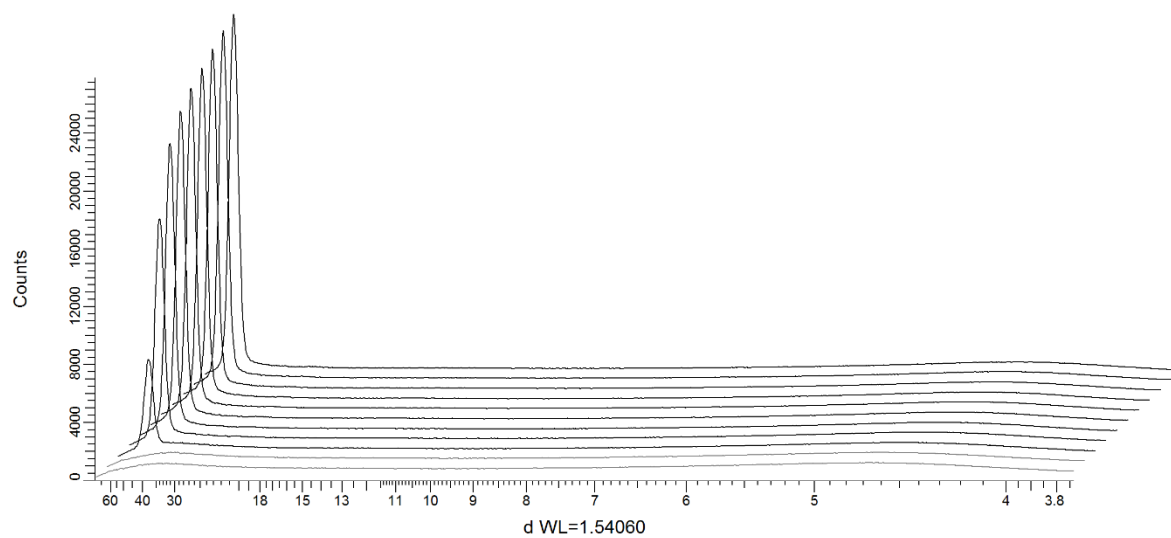


Figure 5.36: Plot showing the diffraction peaks as a function of temperature for Compound **18**.

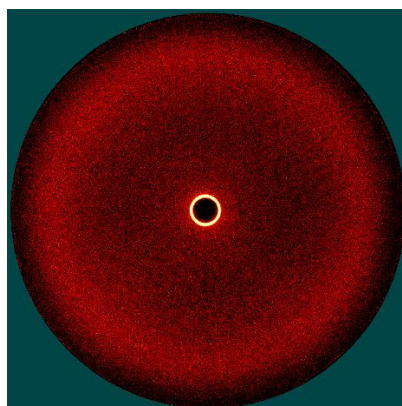


Figure 5.37: Diffraction pattern of the smectic A phase for Compound **18**.

5.4: Analysis of Diallylamine-terminated Terphenyl Compounds (Compounds 19 to 23)

It has been shown for the biphenyl series that the diallylamine moiety has the effect of lowering melting point and clearing point but increasing the stability of higher ordered phases, i.e., a smectic A phase was observed in preference to a nematic phase. The terphenyl bromides had shown that an increase in the core by one aromatic unit had increased clearing points considerably and also increased the variety of mesophases that were observed. Using these pieces of information it would be fair to predict that the terphenyl compounds containing a diallylamine terminal group would exhibit low melting points and enhance the smectic mesomorphism but it was not clear whether the bulkiness of the diallylamine unit would favour a smectic A phase or the B phase that was evident in the terphenyl bromides (9-13).

The mesophase behaviour was examined by polarised optical microscopy and the transition temperatures confirmed by DSC. The results are summarised in Table 5.4, the DSC thermograms are shown in Figures 5.38-5.42 and the transitions are plotted as a function of methylene spacer in Figure 5.43.

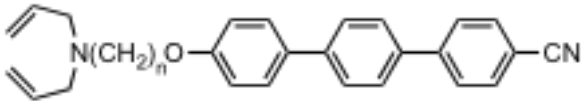
									
		Transition Temperature / °C							
Cpd No	n	Recryst	K		B		SmA		Iso
19	8		•	91.2 [0.07]	•	166.0 [0.7]	•	196.0 [0.3]	•
20	9	<0 [N/A]	•	59.0 [N/A]	•	143.7 [1.2]	•	180.4 [2.5]	•
21	10	23.3 [0.8]	•	62.9 [17.8]	•	151.4 [8.1]	•	189.1 [5.8]	•
22	11	22.2 [0.3]	•	56.7 [15.2]	•	154.4 [7.4]	•	191.3 [5.9]	•
23	12	44.5 [55.1]	•	69.1 [62.1]	•	151.2 [22.5]	•	189.0 [20.6]	•

Table 5.4: Transition temperatures (°C) for Compounds 19-23.

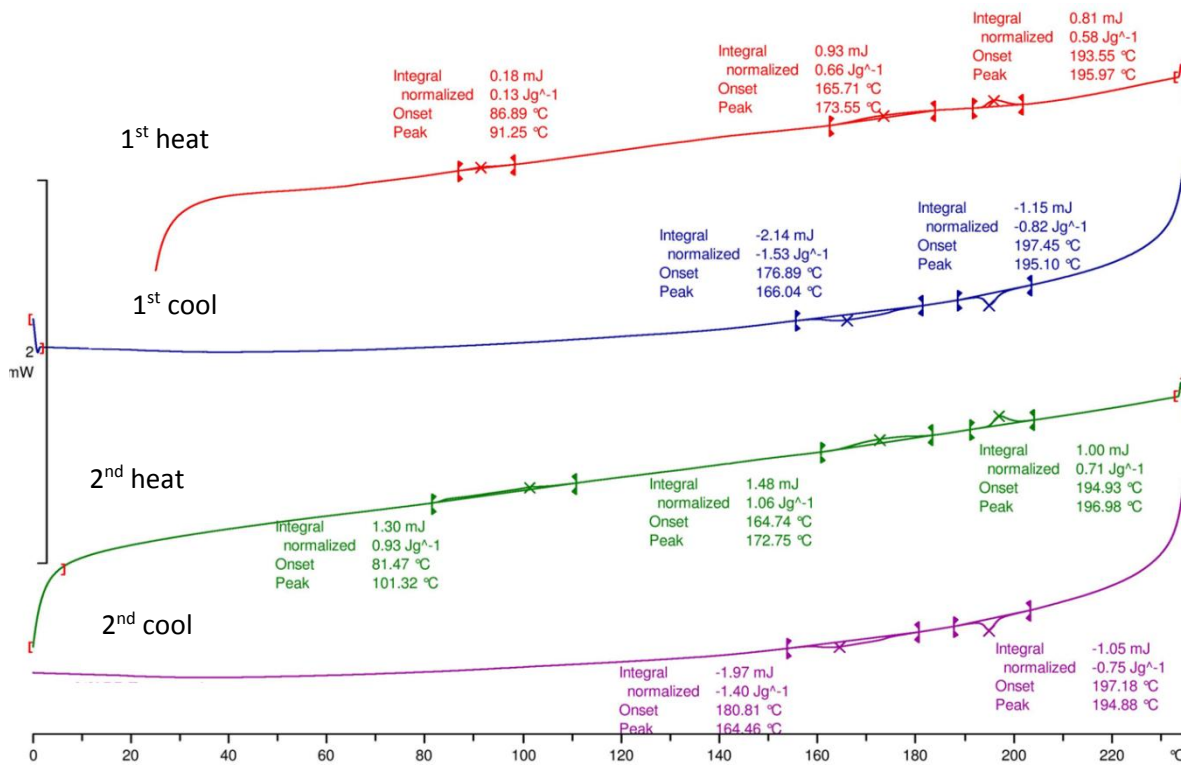


Figure 5.38: DSC thermogram (10 °C min⁻¹) showing the melting behaviour of Compound 19.

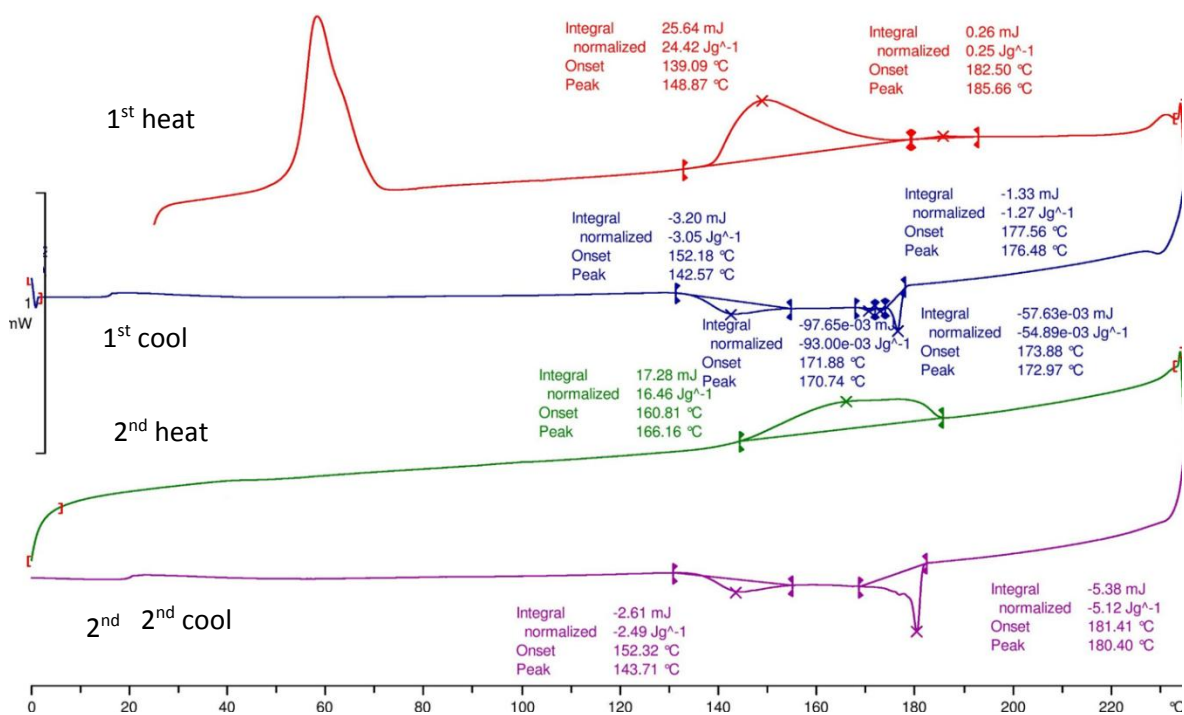


Figure 5.39: DSC thermogram (10 °C min⁻¹) showing the melting behaviour of Compound 20.

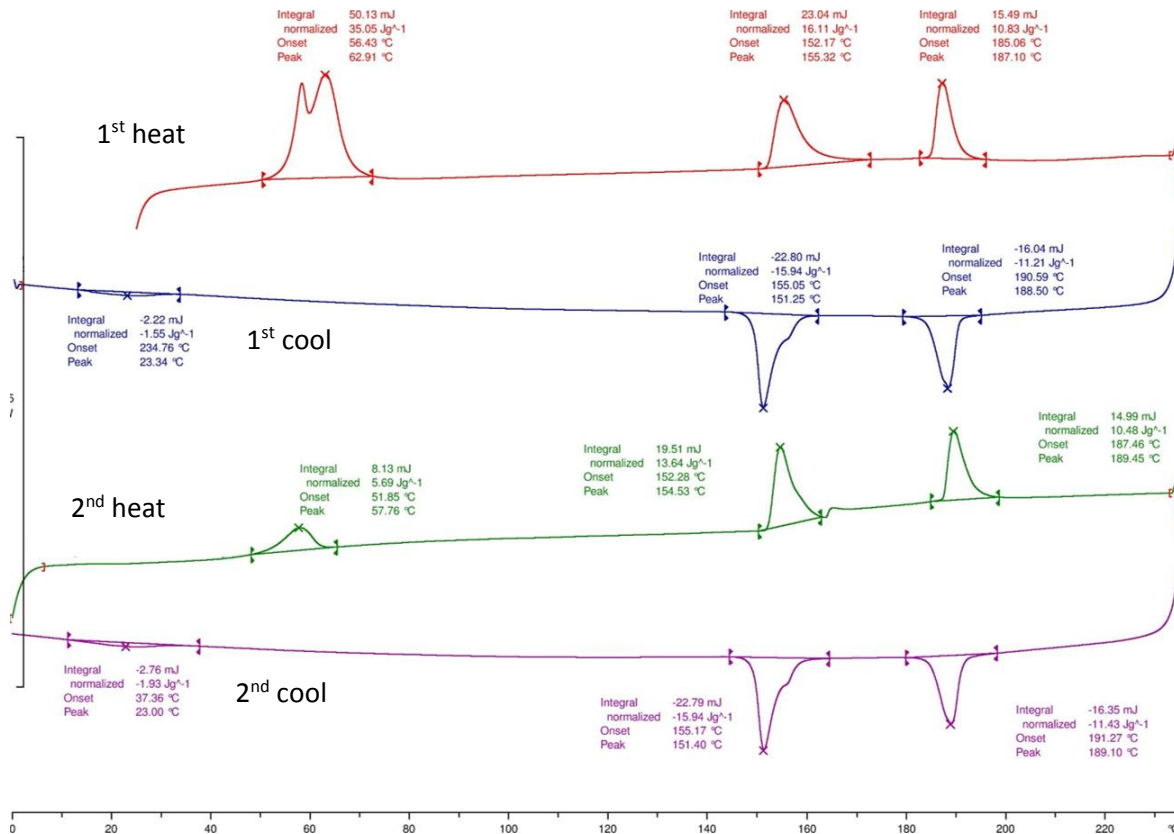


Figure 5.40: DSC thermogram (10 °C min⁻¹) showing the melting behaviour of Compound 21.

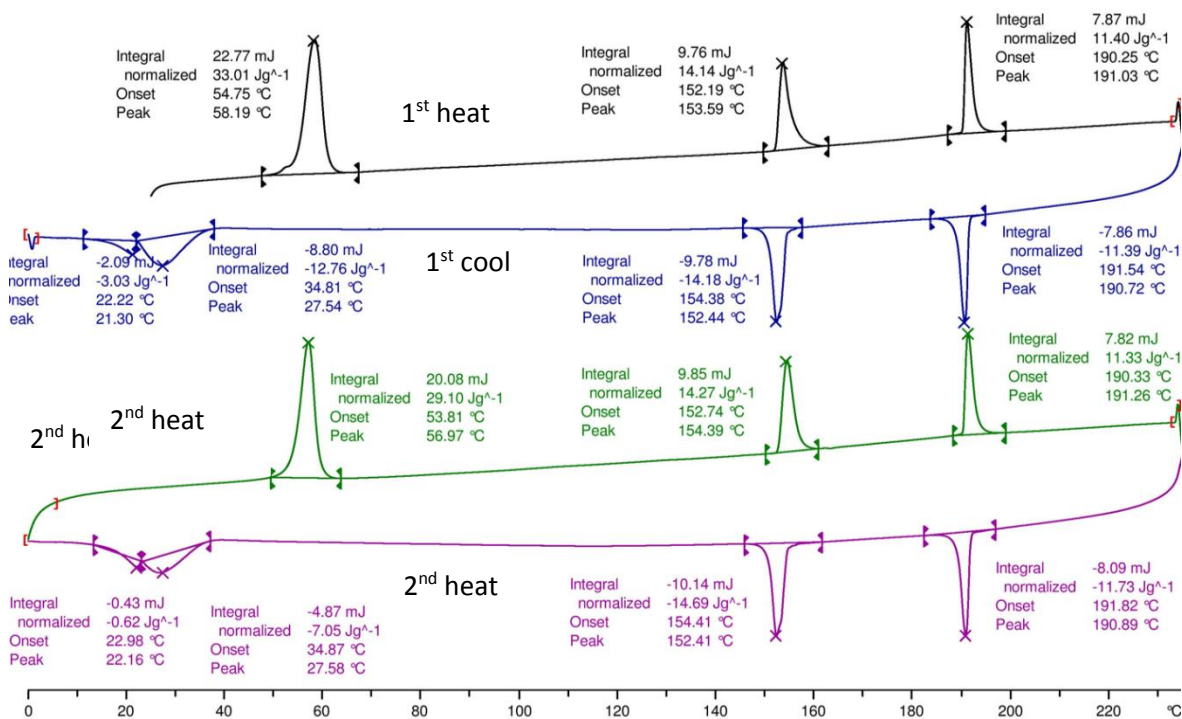


Figure 5.41: DSC thermogram (10 °C min⁻¹) showing the melting behaviour of Compound 22.

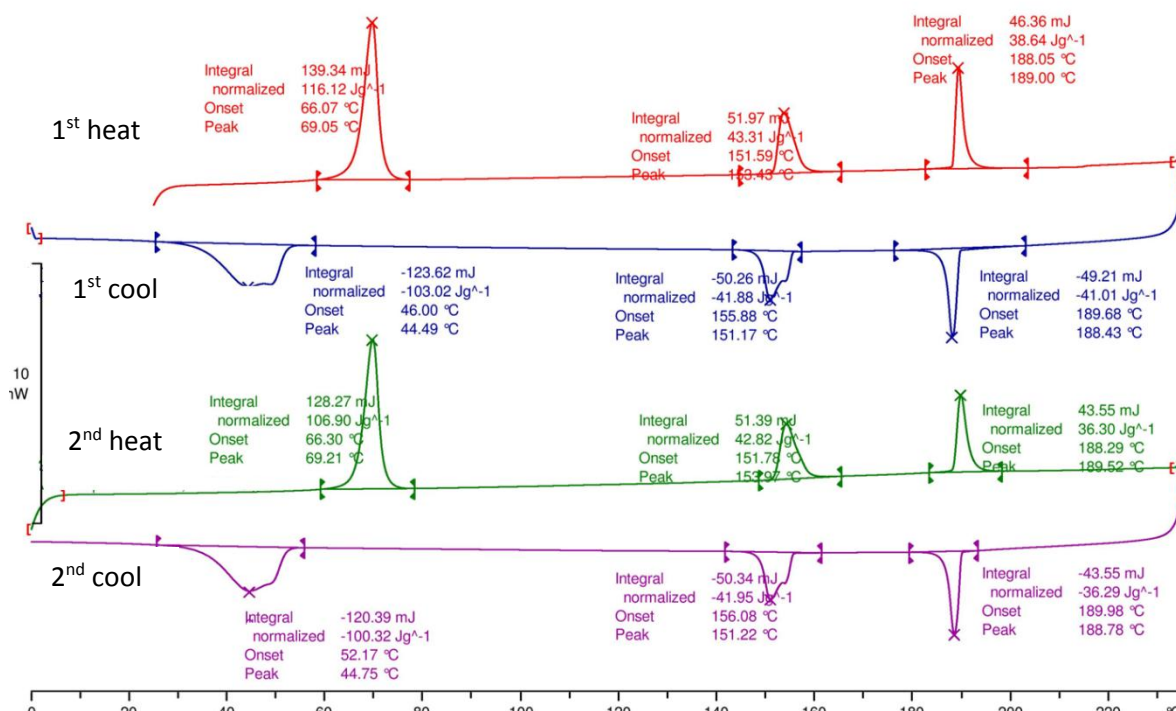


Figure 5.42: DSC thermogram (10 °C min⁻¹) showing the melting behaviour of Compound 23.

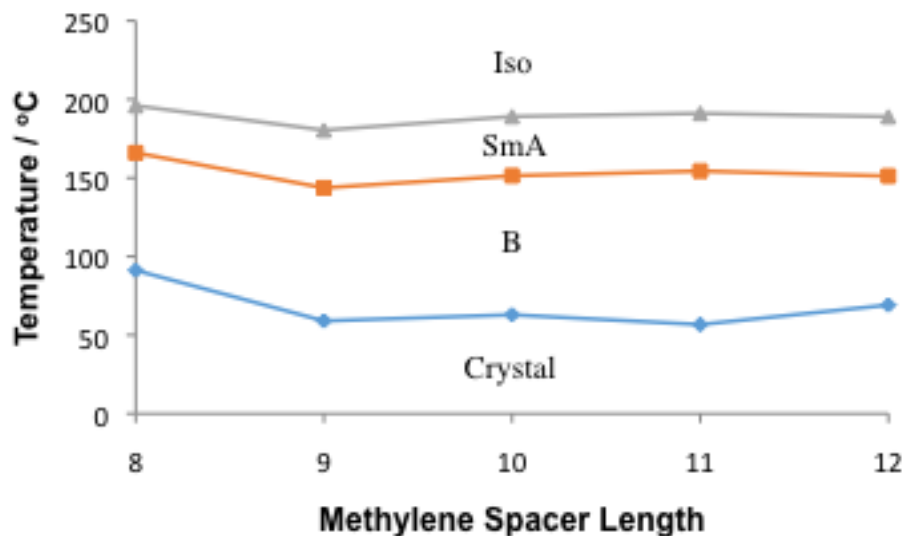


Figure 5.43: Graph showing the transition temperatures (°C) for Compounds 19-23.

The phase diagram shown in Figure 5.43 shows that there is very little variation in the transition temperatures as the methylene chain is increased from 8 to 12 units. The conversion of the bromide to the diallylamine has suppressed the formation of a nematic phase which is consistent with the results observed for the biphenyl series (14 to 18). The diallylamine group has lowered the clearing point by up to 50 °C for the octamethylene spacer compound but for longer chain lengths there is very little difference in temperature suggesting that the effect of the bulky group is diluted the

further it becomes from the core of the molecule with respect to the driving forces for mesophase formation. However, the melting point has been lowered by 20-30 °C for each compound showing that the bulky group has contributed towards destabilisation of a crystal lattice. One of the most interesting observations is that the temperature at which a crystal B phase occurs has not been strongly affected by the incorporation of the diallylamine unit, in fact there has been up to 20 °C increase in the B-SmA phase transition temperature across the whole series. This would indicate that the polar diallylamine unit is not the dominant feature in phase formation, rather it is the terphenyl core unit.

For the compounds presented in Table 5.4, it is clear to see that the enthalpies noted for Compound **19** are incongruous with the data presented for Compounds **20** to **23**, which was due to the nature of the preparation of the DSC pan, and so these enthalpies will not be considered when discussing the energetic trends of these compounds. However, it is also clear that the crystal to crystal B and the recrystallization transitions for Compound **20** were not observed by DSC and were only witnessed by microscopy. However, this is in keeping with the general trend suggested by the other compounds within the series, with a significant difference in the enthalpies for these transitions in the even-chain Compounds **21** and **23**, with a suppression expected for the same transitions in the analogous odd-chain Compounds **20** and **22**. This suppression is witnessed in Compound **22**, and so it would be expected that the enthalpies of these transitions for Compound **20** to be reduced and possibly not visible by DSC. The odd/even effect and general increase in enthalpy is again witnessed in the crystal B to smectic A transitions for these compounds, as well as for the smectic A to isotropic liquid transitions. The general magnitudes of these transitions compared to their parent Compounds **9** to **13** show a reduction in the enthalpies of the more energetic transitions in keeping with what was witnessed for the conversion of the bromide-terminated Compounds **4** to **8** into the diallylamino-terminated Compounds **14** to **18**, with the change of the terminal group from a smaller bromide group to the more voluminous diallylamino-group.

Polarised optical microscopy of these compounds revealed similar results to the terphenyl bromides **14-18** whereby focal conic textures associated with the smectic A phase were observed at high temperatures where the focal conics nucleated from the isotropic liquid as bâtonet. The B phase was characterised through the formation of a well-defined mosaic texture that evolved at the transition from the homeotropic domains in the smectic A phase and there was very little change observed in the focal conic domains. Examples of mesophase textures for the smectic A phase and B phase are shown in Figure 5.44 along with a photo of the phase transition taking place for Compound **22**.

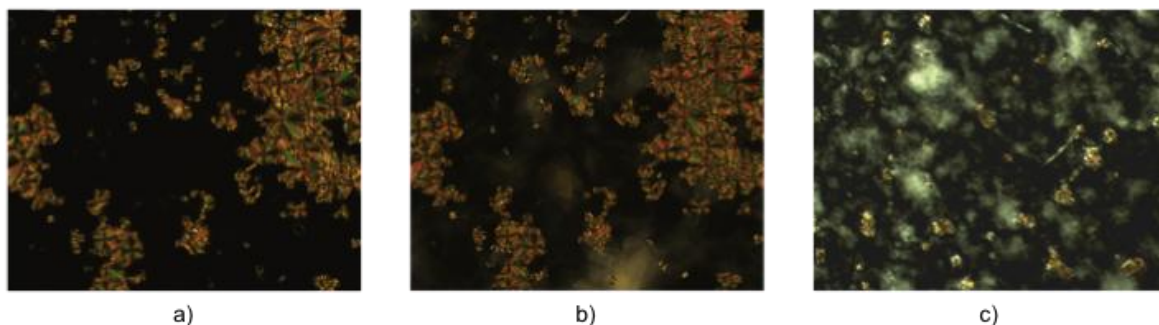


Figure 5.44: Photomicrographs (x100) showing a) smectic A phase b) smectic A – crystal B phase transition and c) crystal B phase mosaic texture for Compound **22**.

Each of these compounds was investigated by x-ray diffraction to provide further evidence of the phase classification although there was insufficient quantity of Compound **23** to be able to investigate further. Overall, the results are consistent with those observed for the terphenyl bromide series except that it proved difficult to align the samples owing to the absence of a nematic phase. There was very little variation in the layer spacing for Compound **19** as a function of temperature, see Figure 5.45. However, the layer spacing was only slightly larger (4\AA) than that observed for the analogous bromide, **10** which can be attributed to the diallylamine moiety. The B phase shows only 200 peaks in addition to the 100 although these are very weak suggesting that the ordering in the B phase is not strong, see figure 5.46. Figure 5.47 shows the diffraction patterns where the intense ring in the centre of the diffraction pattern represents part of the primary beam that has not been obscured by the beamstop.

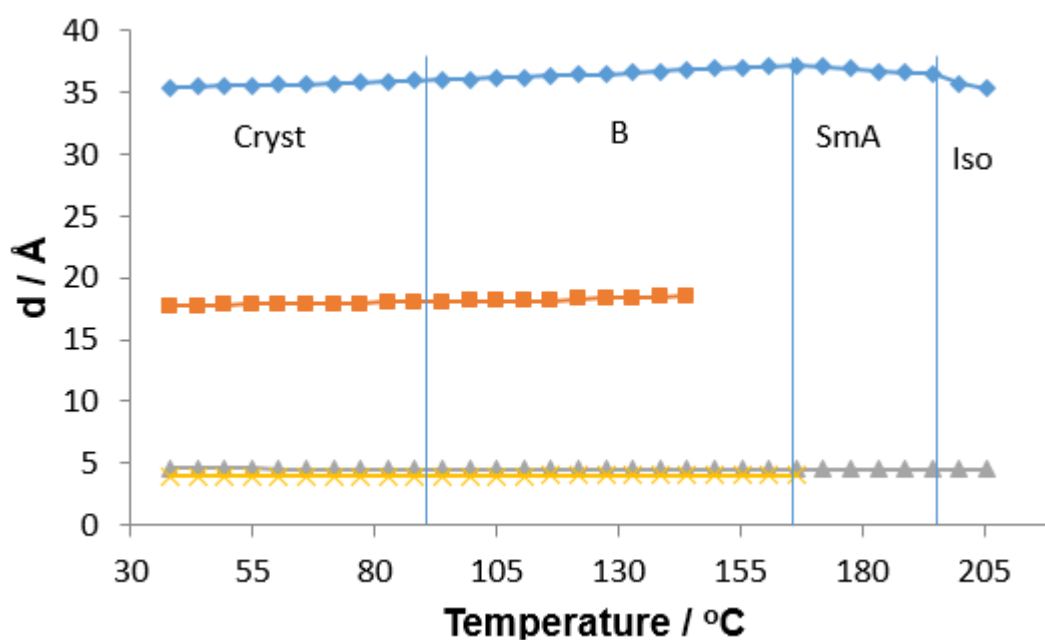


Figure 5.45: Plot showing the layer spacing (\AA) as a function of temperature ($^{\circ}\text{C}$) for Compound **19**.

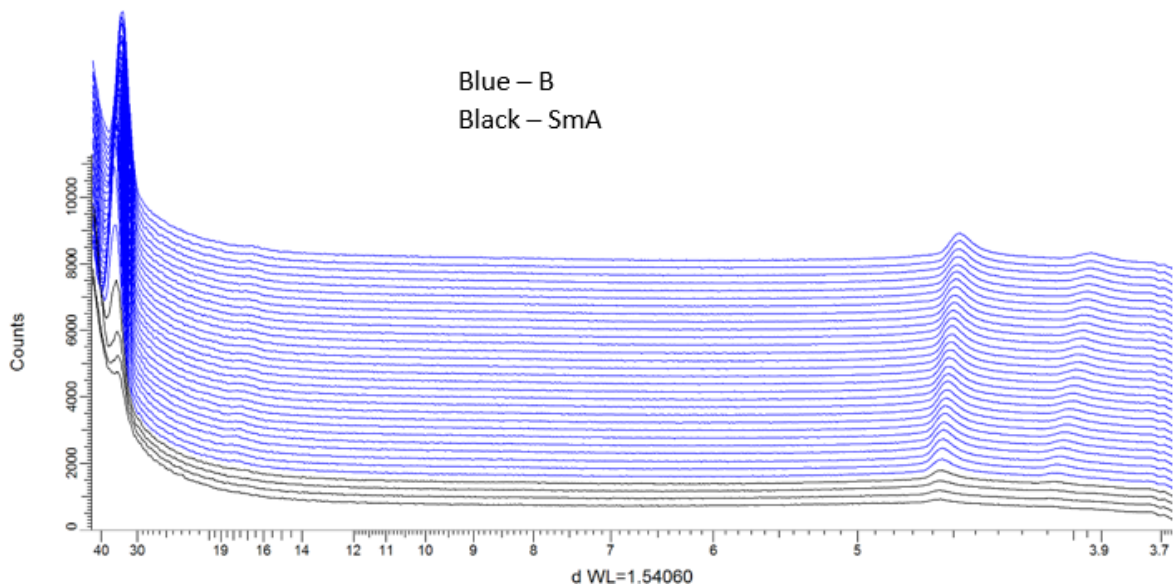


Figure 5.46: Plot showing the diffraction peaks as a function of temperature for Compound **19**.

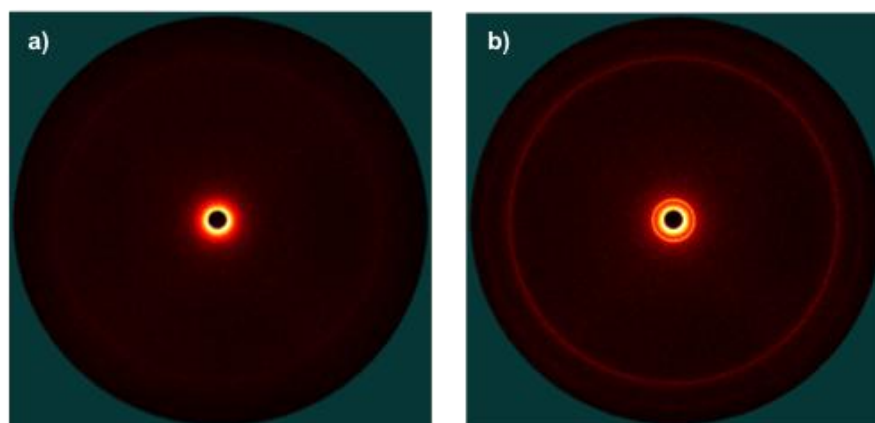


Figure 5.47: Diffraction patterns showing a) smectic A phase and b) crystal B phase for Compound **19**.

Although Compound **20** displayed the same mesophase behaviour as for Compound **19** it was interesting to find that the layer spacing had decreased to approximately 31 Å even though an additional methylene unit was included in the spacer group. It is possible that this is an example of an odd-even effect where the amine group is either projected directly into the interface or along the interface. The B phase shows an increase in coherence compared to Compound **19** where first, second and third order peaks relating to 100, 200 and 300 are observed. The layer spacing is presented in Figure 5.48 and the diffraction peaks are presented in Figure 5.49. The diffraction peaks show that the organisation in the wide angle is consistent with a higher ordered smectic phase where multiple sharp peaks are observed as opposed to the broad, liquid like peaks that are observed for smectic A and nematic phases.

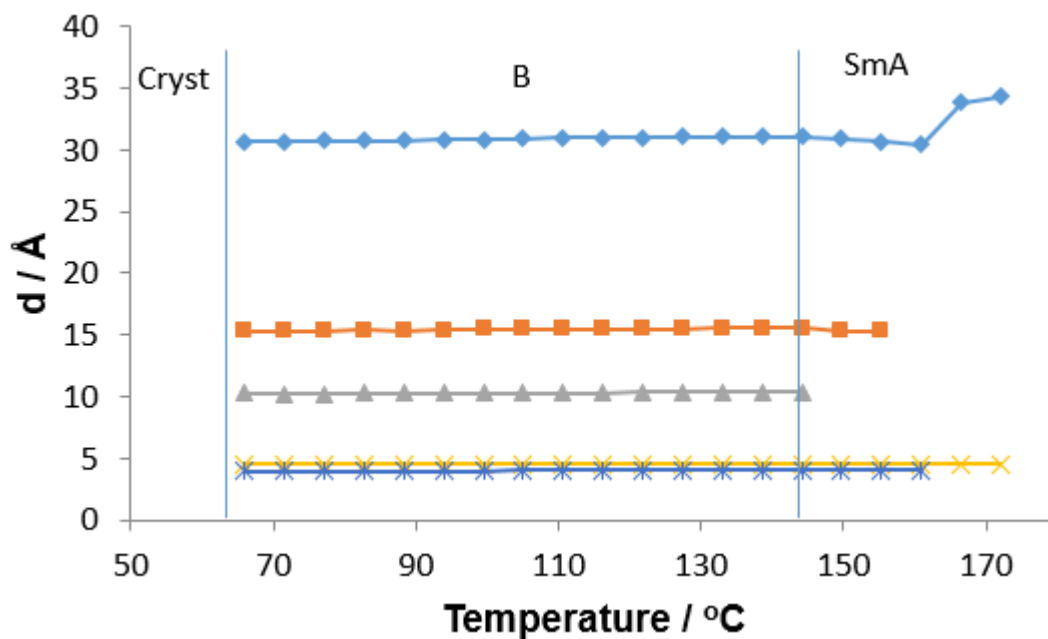


Figure 5.48: Graph showing the layer spacing (\AA) as a function of temperature ($^{\circ}\text{C}$) for Compound **20**.

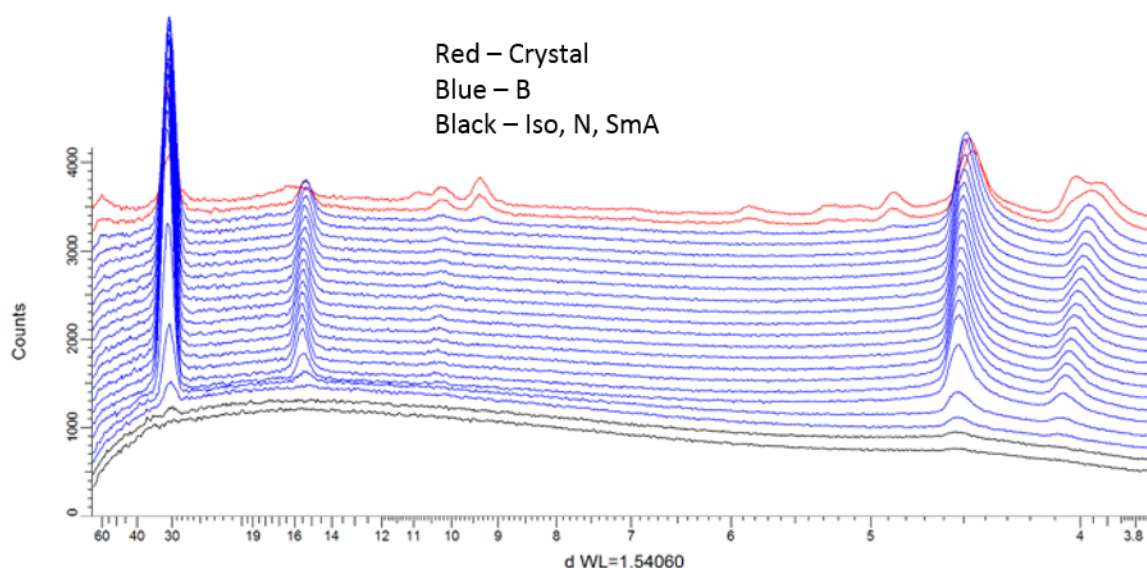


Figure 5.49: Plot showing the diffraction peaks as a function of temperature for Compound **20**.

Compound **21** exhibited consisted diffraction results compared to Compound **19** and **20** but it was interesting to observed that the layer spacing was considerably higher. This result adds to the idea that there is an odd-even effect that needs to be considered for the projection of the diallyamine unit into the smectic interface. The average layer spacing for this Compound is 40 \AA (see Figure 5.50) compared to 35 \AA for Compound **19** (Figure 5.45). The difference here can be attributed to the extra two methylene units in the methylene spacer. There is a small decrease in layer spacing as the sample progresses from the smectic A phase into the B phase. An additional consistency between Compound **21** and **19** is the observation of only two principle peaks in the small angle region of the x-ray diffraction, relating to the 100 and 200 peaks (Figure 5.51) compared to the

three peaks shown in Compound **20**. Diffraction patterns for the smectic A phase and for the crystal B phase are shown in Figure 5.52.

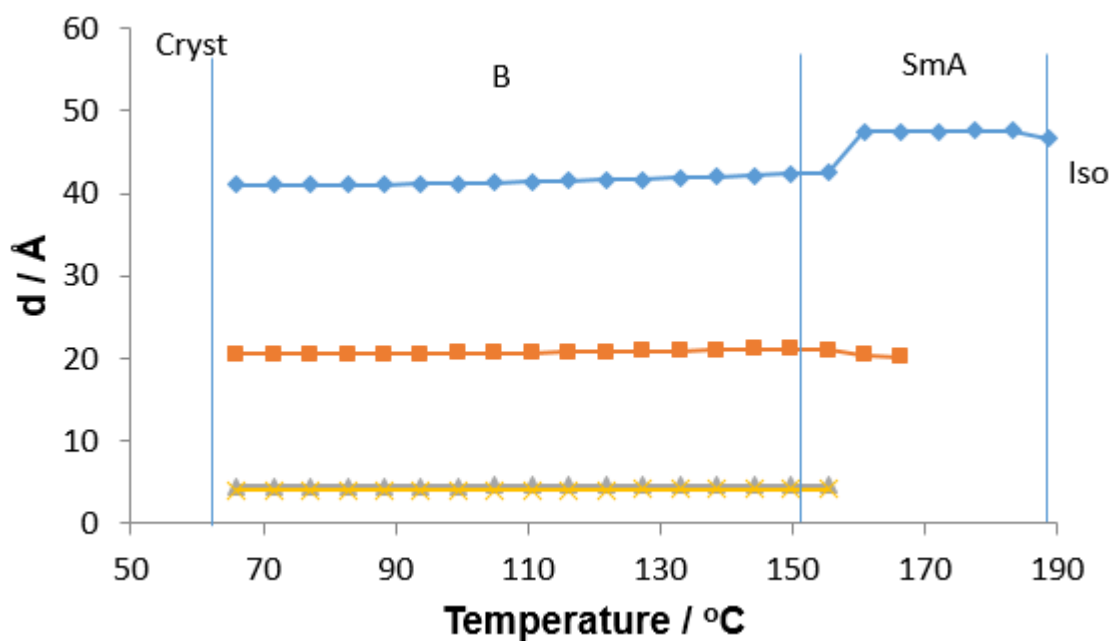


Figure 5.50: Graph showing the layer spacing (Å) as a function of temperature (°C) for Compound **21**.

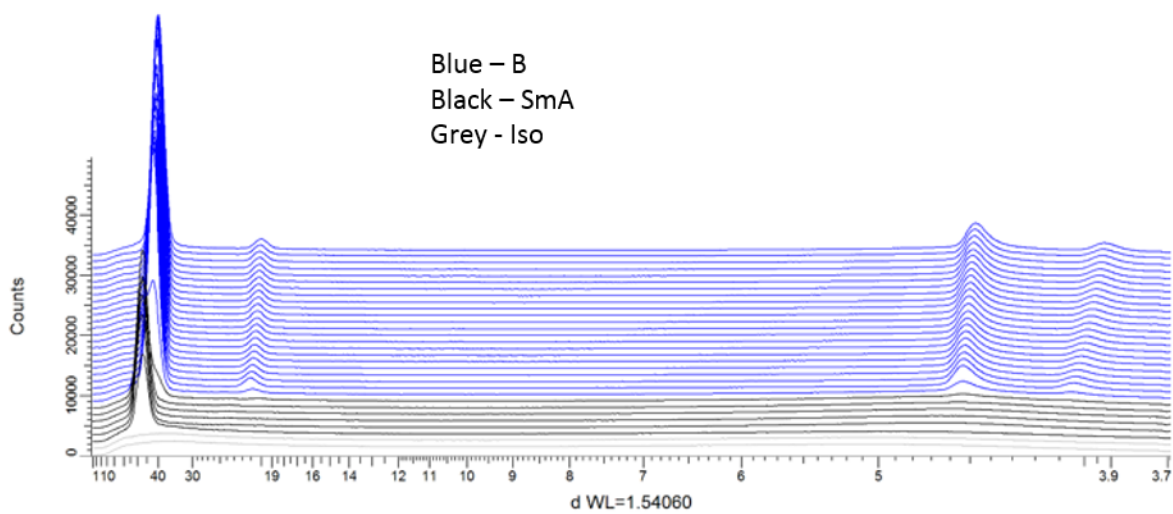


Figure 5.51: Plot showing the diffraction peaks as a function of temperature for Compound **21**.

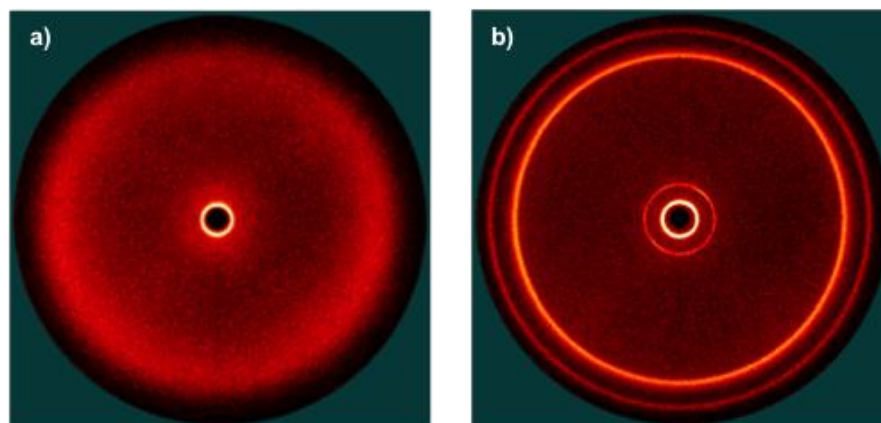


Figure 5.52: Diffraction patterns showing a) Smectic A phase and b) B phase for Compound **21**.

Compound **22** exhibited very similar behaviour to Compound **21** where there was no difference in layer spacing. This may infer that the undecamethylene spacer is long enough that the odd-even effects are diluted by the flexibility of the spacer leading to an overall average layer spacing for this type of compound. The layer spacing decreased at the the SmA-B phase transition and only 100 and 200 peaks were observed in the small angle area of the x-ray diffraction. The layer spacings are summarised in Figure 5.53 and the diffraction peaks are shown in Figure 5.54.

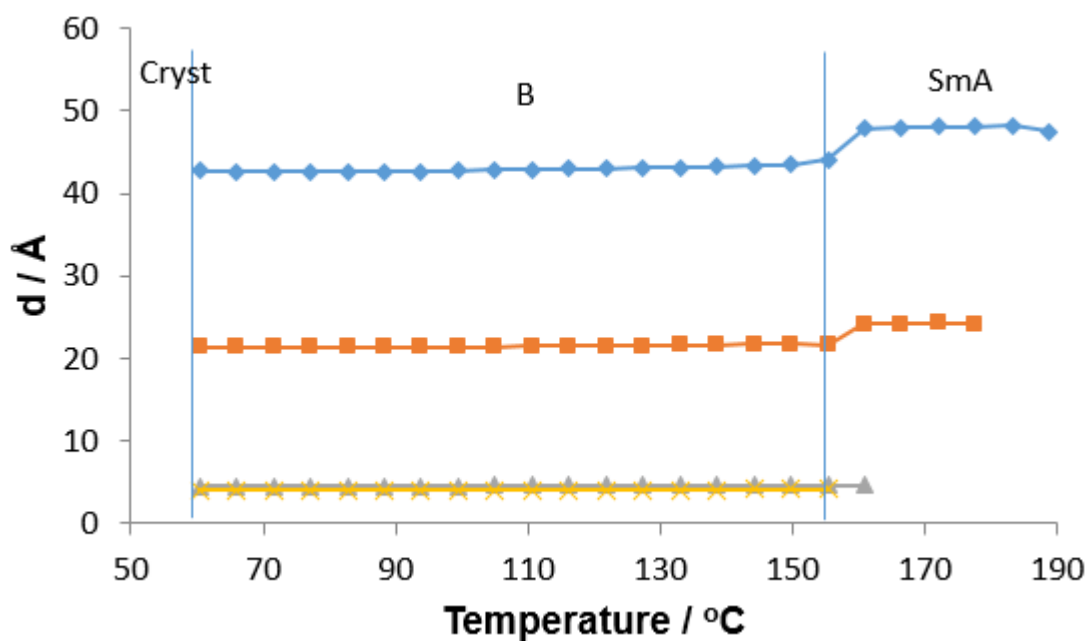


Figure 5.53: Graph showing the layer spacing (Å) as a function of temperature (°C) for Compound **22**.

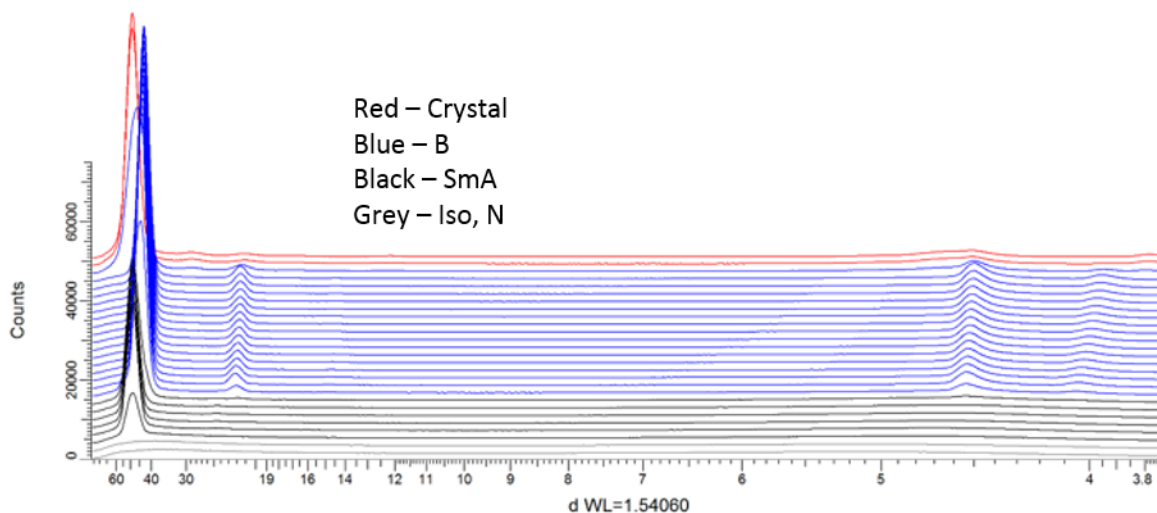


Figure 5.54: Plot showing the diffraction peaks as a function of temperature for Compound **22**.

5.5: Analysis of Ester-based Compounds (39 to 43)

Having studied the thermal behaviours of the alkoxybiphenyl Compounds (**14-18**), it was decided that equivalent compounds should be studied that include an ester linkage in the core of the molecule. This has the effect of disrupting the aromatic core by extending it thereby increasing the length to breadth ratio. For the purpose of this study compounds based on 4-cyano 4-alkoxyphenylbenzoate were investigated.

Unfortunately the incorporation of the ester linkage within the core of the molecule had the effect of disrupting the organisation of the molecules and led to a strong reduction in mesophase stability and melting point. Attempts were made to try to observe phase transitions using a low temperature microscope but unfortunately this was not successful. It must therefore be concluded that in order to obtain liquid crystal phase behaviour the molecule would need to be increased in length such that a minimum of three aromatic rings are included in the core. The phenyl benzoates (**39-43**) showed poor stability such that any behaviour observed on the microscope could not be reproduced in subsequent runs and there were no peaks associated with phase transitions that could be observed by DSC beyond initial melting points. An example of this behaviour is shown for Compound **40** in Figure 5.55.

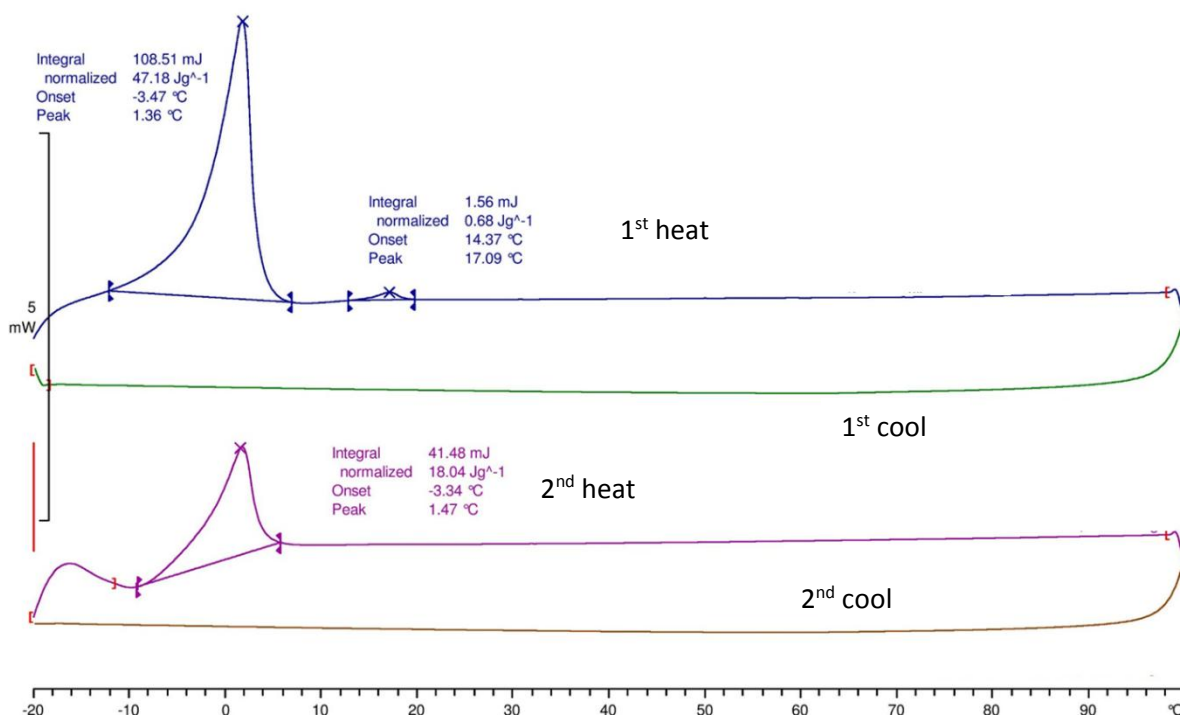


Figure 5.55: DSC thermogram ($10\text{ }^{\circ}\text{C min}^{-1}$) showing the melting behaviour of Compound **40**.

5.6: Comparison of the Impact of Motifs on Thermal Behaviours

It is clearly evident that there is a significant impact on the thermal behaviours of comparable compounds through the nature of the terminal unit. Terphenyl compounds, due to the increased size of the core and more potential for π - π -interactions also have an increase length to breadth ratio. As such the terphenyl compounds exhibit richer mesomorphism than related biphenyls and also show higher ordered phase behaviour, i.e., smectic A and crystal B compared to N for those with terminal bromides and smectic A and crystal B compared to just smectic A for those with terminal diallylamine units. Increase the separation between the rings in the core of the molecule has a detrimental effect on liquid crystallinity whereby all phase behaviour is suppressed.

6: Salt syntheses and Analyses

Having studied the behaviours of the diallylamino-terminated compounds and their bromide intermediates, it was appropriate to analyse the behaviours of the associated quaternary ammonium salt derivatives. The salts made from the amino compounds were targeted as the ultimate compounds in this research because of their potential behaviours after photopolymerisation.

It was expected that the quaternary diallylammonium salt terminated compounds would polymerise more rapidly than the diallylamide and diallylamino-terminated analogues also synthesised. The other significant advantage of the quaternary ammonium salt is in the nature of the counter-ion present, which can affect the behaviours of the product, including their potential for electrical conductivity.

6.1: Selection of Compounds to Be Acidified

Having studied the thermal properties of the diallylamino-terminated compounds, it was decided that Compounds **16** and **17** would be acidified with a range of acids to consider the impacts of each acid on thermal behaviour. These two compounds were chosen as they address the odd/even effect, as well as possessing transition temperatures that are close to operating temperatures for devices. This would allow for the salts to be investigated in the idealised conditions of the operational environment. It should be expected, however, that the transference of the amino group into the quaternary salt will affect the transitions observed.

6.2: Salt Syntheses

The synthesis of the quaternary diallylammonium salts was conducted *via* three generic pathways dependent upon the nature of the anion desired within the system. In order to confirm the uptake of any anion, the compound was analysed by mass spectrometry, with positive and negative ionisation procedures applied, which identified the base cation and the added anion respectively.

6.2.1: Direct Acidification Procedure

The introduction of the chloride anion was conducted *via* a direct acidification of the compound using a one molar etherific solution of the acid. 250mg of each of Compounds **16** and **17** were dissolved in DCM before being treated with the acid solution. The volume of acid added was determined as a stoichiometric ratio of HCl to the corresponding compound. The volumes of acid added are presented below in Table 6.1. Subsequent to the addition of the acid, the mixtures were then stirred for two hours before the removal of solvent under reduced pressure at ambient temperatures. This method was also applied to the addition of acrylic, methacrylic and acetic acid.

Acid	Volume added Compound 16 (ml)	Volume added Compound 17 (ml)
HCl (1M solution)	0.49	0.48
Acrylic acid	0.03	0.03
Methacrylic acid	0.04	0.04
Acetic acid	0.03	0.03

Table 6.1: Volumes of acids added to Compounds **16** and **17**.

6.2.2: Solution Addition Procedure

The addition of organic anions was attempted using a similar reaction procedure, yet the acids observed were, in most cases, in the solid form at ambient temperature, and were not previously in solution. A significant change to the procedure was in the addition of the compounds to the reacting system, with the acids being added in their non-dissolved form to a more dilute solution of Compounds **16** and **17** dissolved in DCM. Further to this, the starting masses of the compounds were significantly reduced in comparison to the chloride salt syntheses. This was due to the demands of excess chloride salt in order to synthesise alternative salts from metatheses.

The natures of the acids reacted, as well as the masses involved are presented below in Tables 6.2, 6.3, 6.4 and 6.5, with the reaction being stirred in DCM for four hours before the removal of the solvent under reduced pressure at ambient temperature. The mass of Compounds **16** and **17** used were 50mg (0.116 mmol and 0.112 mmol respectively).

Acid	Mass used (mg (mmol))	Acid	Mass used (mg (mmol))
Formic acid	5 (0.109)	Pentadecanoic acid	24 (0.101)
Acetic acid	6 (0.100)	Pentyl Bicyclohexanoic acid	28 (0.100)
Propanoic acid	7 (0.094)	Ethyl Cyclohexanoic acid	15 (0.096)
Butanoic acid	9 (0.102)	Propyl Cyclohexanoic acid	17 (0.100)
Pentanoic acid	10 (0.098)	Butyl Cyclohexanoic acid	18 (0.098)
Hexanoic acid	11 (0.095)	Pentyl Cyclohexanoic acid	20 (0.101)
Heptanoic acid	13 (0.100)	4-((10-bromodecyl)oxy)benzoic acid	35 (0.098)
Octanoic acid	14 (0.097)	4-hydroxybenzoic acid	14 (0.101)
Nonanoic acid	16 (0.101)	Propyl Cyclohexyl Benzoic acid	24 (0.097)
Decanoic acid	17 (0.099)	Butyl Cyclohexyl Benzoic acid	26 (0.100)
Undecanoic acid	18 (0.097)	Pentyl Cyclohexyl Benzoic acid	27 (0.099)
Dodecanoic acid	20 (0.100)	Ethyl Bicyclohexanoic acid	24 (0.101)
Tridecanoic acid	21 (0.098)	Propyl Bicyclohexanoic acid	25 (0.099)
Tetradecanoic acid	23 (0.100)	Butyl Bicyclohexanoic acid	26 (0.098)

Table 6.2: Masses of organic acids reacted with Compound **16**.

A small variety of organic di-acids were also reacted with Compound **16**. These were reacted in different manners, with a 1:1 ratio for mono-substitution (labelled as 'mono' in Table 6.3 below) and with a 2:1 ratio for a di-substitution (labelled as 'di' in Table 6.3 below).

Acid	Mass used (mono) (mg(mmol))	Mass used (di) (mg(mmol))
Oxalic acid (Ethanedioic acid)	9 (0.100)	4 (0.044)
Malonic acid (Propanedioic acid)	10 (0.096)	5 (0.048)
Adipic acid (Hexanedioic acid)	14 (0.096)	7 (0.048)
Glutaric acid (Pentanedioic acid)	13 (0.098)	7 (0.053)
Succinic acid (Butanedioic acid)	12 (0.102)	6 (0.051)
Pimelic acid (Heptanedioic acid)	16 (0.100)	8 (0.050)
Suberic acid (Octanedioic acid)	17 (0.098)	9 (0.052)
Azelaic acid (Nonanedioic acid)	19 (0.101)	9 (0.048)
Sebacic acid (Decanedioic acid)	20 (0.099)	10 (0.049)

Table 6.3: Masses of organic di-acids reacted in different ratios with Compound **16**.

The same approach was used for Compound **17**, with slightly different masses used to accommodate the different molecular masses of the compounds.

Acid	Mass used (mg (mmol))	Acid	Mass used (mg (mmol))
Formic acid	4 (0.087)	Pentadecanoic acid	23 (0.095)
Acetic acid	6 (0.100)	Pentyl Bicyclohexanoic acid	27 (0.096)
Propanoic acid	7 (0.094)	Ethyl Cyclohexanoic acid	15 (0.096)
Butanoic acid	8 (0.091)	Propyl Cyclohexanoic acid	16 (0.094)
Pentanoic acid	10 (0.098)	Butyl Cyclohexanoic acid	18 (0.098)
Hexanoic acid	11 (0.095)	Pentyl Cyclohexanoic acid	19 (0.096)
Heptanoic acid	13 (0.100)	4-((10-bromodecyl)oxy)benzoic acid	34 (0.095)
Octanoic acid	14 (0.097)	4-hydroxybenzoic acid	13 (0.094)
Nonanoic acid	15 (0.095)	Propyl Cyclohexyl Benzoic acid	24 (0.097)
Decanoic acid	17 (0.099)	Butyl Cyclohexyl Benzoic acid	25 (0.096)
Undecanoic acid	18 (0.097)	Pentyl Cyclohexyl Benzoic acid	26 (0.095)
Dodecanoic acid	19 (0.095)	Ethy Bicyclohexanoic acid	23 (0.096)
Tridecanoic acid	21 (0.098)	Propyl Bicyclohexanoic acid	24 (0.095)
Tetradecanoic acid	22 (0.096)	Butyl Bicyclohexanoic acid	26 (0.098)

Table 6.4: Masses of organic acids reacted with Compound **17**.

Further to these acids, the same array of organic di-acids were used.

Acid	Mass used (mono) (mg (mmol))	Mass used (di) (mg (mmol))
Oxalic acid (Ethanedioic acid)	9 (0.100)	4 (0.044)
Malonic acid (Propanedioic acid)	10 (0.096)	5 (0.048)
Adipic acid (Hexanedioic acid)	14 (0.096)	7 (0.048)
Glutaric acid (Pentanedioic acid)	13 (0.098)	6 (0.045)
Succinic acid (Butanedioic acid)	11 (0.093)	6 (0.051)
Pimelic acid (Heptanedioic acid)	15 (0.094)	8 (0.050)
Suberic acid (Octanedioic acid)	17 (0.098)	8 (0.046)
Azelaic acid (Nonanedioic acid)	18 (0.096)	9 (0.048)
Sebacic acid (Decanedioic acid)	19 (0.093)	10 (0.049)

Table 6.5: Masses of organic di-acids reacted with Compound **17** in different ratios.

6.2.3: Metathesis/Salt Replacement Procedure

The metathesis approach to salt synthesis requires the initial chloride salt, with the reaction displacing this anion with an alternative, such as the hexafluorophosphate salt, which was the chief consideration in the formation of this procedure.

In order to undertake this process, the chloride salt (50 mg) was dissolved in DCM, with aqueous ammonium hexafluorophosphate solution (1 M) added. The system was then stirred for 15 minutes; then the products were separated, with retention of the organic layer. The organic layer was then dried in the presence of anhydrous magnesium sulfate and filtered. The solvent was then removed under reduced pressure at ambient temperature. The presence of the hexafluorophosphate salt was then verified by phosphorous and fluorine NMR analysis.

6.3: Thermal Analysis of Biphenyl Salts

With the introduction of the salt, it was observed that the liquid-crystalline phases previously observed were no longer exhibited by the salts in question.

Typically, the compounds incorporating the salts were liquid at room temperature, with the exception of the chloride salts of Compounds **16** (Figure 6.1) and **17** (Figure 6.2), which maintained crystallinity at above ambient temperatures.

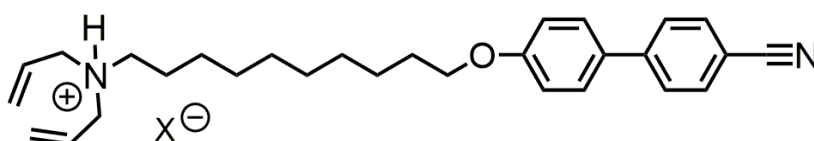


Figure 6.1: Structure of the salt of Compound **16**, where X represents the anion.

In order to observe whether the reactions of the organic acids with the target compounds allowed for liquid-crystalline transitions to be exhibited at reduced temperatures, the liquid compounds were cooled to $-40\text{ }^{\circ}\text{C}$ and held at this temperature for 20 minutes before heating to $40\text{ }^{\circ}\text{C}$, before being cooled back to $-40\text{ }^{\circ}\text{C}$. Of the samples which were liquid at room temperature, the majority showed no phase transitions, remaining liquid at $-40\text{ }^{\circ}\text{C}$, whereas others possessed melting points to the isotropic liquid phase at temperatures $5\text{ }^{\circ}\text{C}$ and $-35\text{ }^{\circ}\text{C}$ respectively.

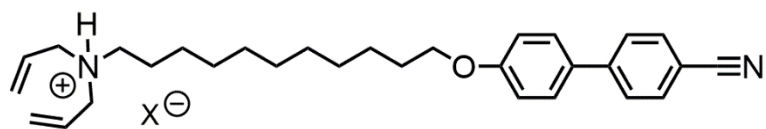


Figure 6.2: Structure of the salt of Compound 17, where X represents the anion.

The only compounds which did not fit these criteria were the chloride salts, which were observed to retain crystallinity to temperatures greater than $30\text{ }^{\circ}\text{C}$. Despite the higher melting points exhibited by these samples, they were determined not to possess any mesophases.

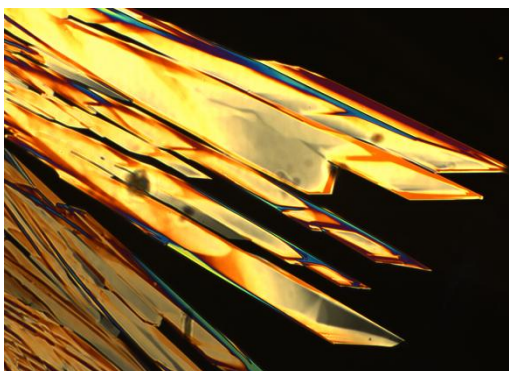


Figure 6.3: An example of the crystal textures observed from studies of biphenyl salt compounds.

6.3.1: Observations of the Effects of Salt Introduction to Biphenyl-Terminated Compounds

The loss of liquid-crystalline behaviour in these compounds can be ascribed to the impact of the change in the terminal group. The nature of the diallylammonium salt leads to a change in the electronic structure of the compound, as well as the shape of the end-group.

The incorporation of the charge at nitrogen leads to repulsive nature between the terminal groups between molecules. The presence of this repulsion leads to a reduction in the ability of the molecules to self-organise, which is required for the formation of smectic liquid crystal phases.

The shape of the diallylamine group is also changed by the introduction of the cation, effectively adding another chain to the pre-existing allyl chains. Smaller anions such as the chloride will have a less severe impact on the size and shape of the terminal group, whereas larger groups such as the decanoate anion will dramatically increase the apparent size of the group, affecting the ratio within the compound between the terminal group size and shape relative to the biphenyl motif. The change in shape of the molecule will lead to it being less cylindrical and rod-like, making it more

tapered and cone-shaped. This change to a cone as opposed to the cylinder is a hindrance to even packing of the molecules, which again hinders the formation of the desired organised phases of matter.

6.3.2: Conclusion of Biphenyl Salt Studies and Further Study

In response to the lack of liquid-crystalline phases exhibited by the biphenyl quaternary diallylammonium-salts, it was decided that the equivalent terphenyl compounds should be investigated because of their greater length to breadth (aspect) ratio. Further to this, the nature of the salts was considered more deeply, with the organic long chain anions being deemed less interesting than the chloride, hexafluorophosphate and acrylate salts.

The selection of the chloride salt was due to the lower impact this exhibited on the overall properties of the system, and, along with the hexafluorophosphate salt, due to the previous work conducted in the area by Hall et al. The behaviours of the chloride and the hexafluorophosphate systems previously studied were in stark contrast, with the chloride salt leading to porosity and shrinkage from exposure to moisture, whereas the hexafluorophosphate salts lead to less shrinkage and no porosity, making an interesting comparison in terms of solvent impacts.

The selection of the acrylate was made due to the nature and action of the acrylates in polymerisation. Significant work has been conducted into the study of acrylate polymer chemistry, particularly in the areas of ultraviolet initiated polymerisations. With the additional polymerizable group being the diallylammonium group, it was expected that it would be interesting to also incorporate another polymerizable component into the mixture. Possible outcomes would include the co-polymerisation of the acrylate into the amine-based backbone, as well as the co-polymerisation of both groups into associated chains. There is also the possibility of the polymerisation processes occurring at different rates, both in terms of the initiation and propagation.

Lastly, each of the counter-ions chosen are relatively small compared to others that have been studied as well as compared to the motif of the compounds.

6.4: Syntheses of Terphenyl Salt Compounds

The terphenyl salts were synthesised from the direct acidification and metathesis reactions outlined for the biphenyl equivalents (Section 6.2), based on the “undecamethylene-spacer/terphenyl” as shown in Compound **22** (Figure 6.4).

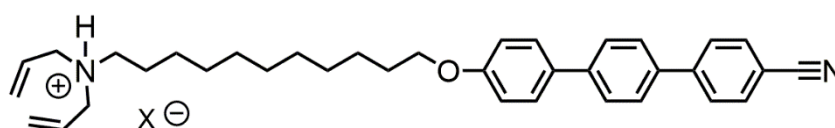


Figure 6.4: Structure of the salt of Compound **22**, where X represents the anion.

The synthesis of the chloride salt was conducted reacting Compound **22** (300 mg) in DCM with etherific HCl (1 M) added dropwise until the mixture reached pH 1, at which point the system was stirred for 20 min before the solvent was removed at ambient temperature under reduced pressure.

The above procedure was also used in the synthesis of the acrylate salt, using Compound **22** (100 mg), adding neat acrylic acid dropwise to the solution until pH 1 was attained before stirring (20 min) and the removal of the DCM by evaporation under reduced pressure at ambient temperature.

The synthesis of the hexafluorophosphate analogue was undertaken by mixing the chloride salt of Compound **22** (100 mg) with an aqueous solution of ammonium hexafluorophosphate, and stirred for 20 min. The mixture was then separated with the organic fraction retained and washed with water (3 x 20 ml). The organic layer was then dried over anhydrous magnesium sulfate, which was subsequently removed by filtration. The presence of the hexafluorophosphate anion was then confirmed through fluorine and phosphorous NMR.

6.5: Thermal Analysis of Terphenyl Quaternary Diallylammonium Salts

The different quaternary diallylammonium salts were studied by DSC and polarising optical microscopy in order to observe the different thermal behaviours that they exhibit, thereby allowing for comparison with the parent Compound **22**.

6.5.1: Analysis of the Chloride Salt

Initial observation of the chloride salt revealed very similar transitions to that of the parent amine, with a slight suppression of the phase transitions due to the presence of ionic character. It was important to note, however, that the smectic A phase was prevalent at temperatures in the region of 190 °C (190.7 °C in Compound **22**, and 190.3 °C in the corresponding salt) on cooling, yet on the heating, the transition for Compound **22** was similar to that on cooling (191.3 °C), with this similar for the chloride salt (190.3 °C).

The other notable transition for Compound **22** was that between the smectic A and smectic B phases at 152.4 °C on cooling and 154.4 °C on heating. This transition was again visible for the salt, with minimal suppression seen on the heating curve at 148 °C and on the cooling curve at 151.3 °C.

The final transition to be noted is that of the crystal to smectic B, with Compound **22** exhibiting the transition at 34.8 °C and 54 °C on cooling and heating respectively. In the chloride salt, this transition was not seen by DSC, but was observed by microscopy, with an adjustment of the melt into the smectic B phase on heating to 49 °C and on cooling to 36 °C.

6.5.2: Analysis of the Acrylate Salt

Similar to the chloride salt, the acrylate salt also showed some slight variations from the parent compound due to the introduction of the cationic properties within the functional group as well as the adherence of the associated anion.

The major impact on the transitions observed for the acrylate salt sample was that certain transitions were harder to observe both on heating and cooling. It was possible to observe the transitions, however, with the clearing point being again comparable to the parent compound **22** at 189.9 °C observed by microscopy on cooling. It was, however, remarkably difficult to observe the lower ordered phases if heated excessively because the compound tended towards autopolymerisation at temperatures close to the clearing point owing to the presence of the acrylate unit.

The smectic A to smectic B transition was also difficult to observe on cooling due to autopolymerisation that occurred when initially clearing the compound, yet this transition was determined at 151.2 °C when polymerisation had been avoided. This compares favourably with the transitions witnessed in both the contemporary salt systems as well as the parent compound.

6.5.3: Analysis of the Hexafluorophosphate Salt

The impact of the hexafluorophosphate on the properties of the parent is most immediately noticed due to the difficulty in observing the smectic B to crystal transition on cooling, yet the thermal discrepancies at more temperate phases are also noticeable.

Similar to the effects noticed in the case of the chloride salt, the clearing point on heating was slightly suppressed to approximately 190.1 °C. Corresponding to this was the similarity observed when analysing the sample on cooling, where the transition was noted at 189.9 °C.

The other easily analysed transition was that between the smectic A and smectic B phases. The transition in the hexafluorophosphate sample was considerably broader on cooling than on heating, or for the parent amine derivative Compound **22**. Aside from the broader range of the transition, the temperature for the onset on heating was slightly higher at 153 °C rather than 152 °C. When considering cooling, the onset of the transition from smectic A to smectic B was elevated to 170 °C, yet the peak determined from DSC studies was observed at 154.2 °C, far closer to that of the onset of Compound **22**. The broadening of the transition suggests that there is an impact from the related anion, yet the thermal behaviour is not completely dissimilar to that of the untreated parent compound.

6.6: Effects of Salt Introduction

The salt compounds observed showed clear differences from the parent compound, similar to those found for the biphenyl compounds. However, the degree of variation was noted to be considerably

less, with slight suppressions in clearing and crystallisation points, as well as a shortening of the range over which the smectic A was present.

The introduction of the acrylate anion lead to complications with exposure of the salt mixture to high temperatures, with thermal polymerisation of the acrylate being initiated. This issue was not seen in the other salt samples.

6.7: Investigation of Salt Mixtures

Having studied the bulk impact of the introduction of “salt” character into Compound **22**, the degree of variation in thermal effects with respect to the parent compound can be studied by varying the degree of acidification of the sample.

The preparation of these samples was conducted by mixing of the fully acidified samples with the parent compound in predetermined ratios by weight. The ratios to be analysed were initially determined to be 3:1 (Compound **22**: salt), 2:1, 1:1, 1:2 and 1:3, allowing a reasonable range over which the effects of incorporation of ionic character could be observed. These ratios were determined by weight between the two samples mixed, with an error of 0.01 mg noted.

The samples were weighed and added together, before dissolving in DCM and stirring, before the solvent was removed under reduced pressure and at ambient temperature to avoid polymerisation.

6.7.1: Chloride Salt Mixtures

The chloride salt of Compound **22** was mixed in the above ratios with the parent previously stated in section 6.7.

6.7.1.1: A 3:1 Mixture of Compound 22: Chloride Salt

The 3:1 mixture gave the least representative approximation to the pure “salt” compound already studied in section 6.5.1, and closest to that of the pure Compound **22** studied in section 5.2.2.4.

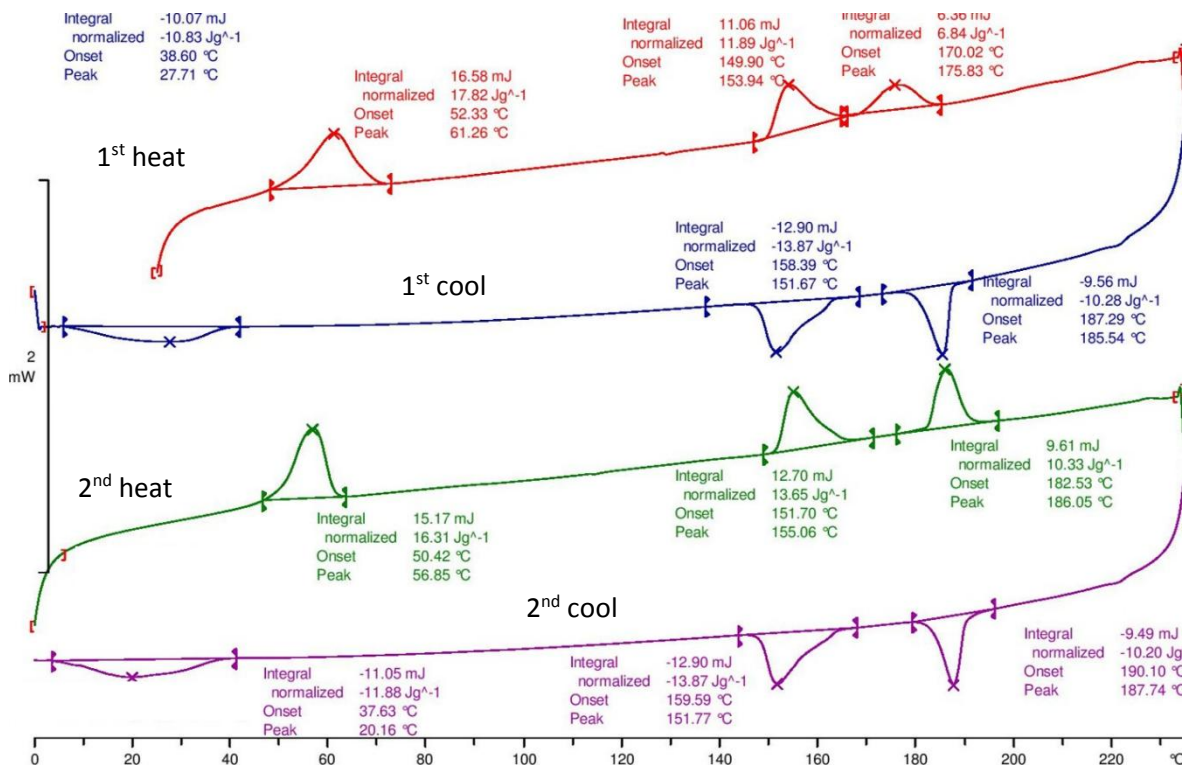


Figure 6.5: DSC thermogram of heat flow (mW^{-1}) as a function of temperature ($^{\circ}\text{C}$) for a 3:1 mixture of Compound **22** : chloride salt.

As can be seen from the DSC thermogram (Figure 6.5), that the 3:1 mixture behaved largely in a similar way to that exhibited by Compound **22**. One obvious difference between the two was the suppression of the clearing point to 187.7°C (189°C by microscopy) on cooling and 186.1°C on heating (the first heat giving an abnormally low value of 175.8°C partially due to the pan settling of the mixture). The smectic A phase observed displayed a typical defect texture for the phase, with clearly defined ‘maltese cross’ point defects.

Apart from the deviation between the clearing points on heating, the transition between smectic A and smectic B was observed to be comparable temperatures in both heating cycles (153.9°C and 155.1°C , the latter being considered more accurate as it was produced subsequent to settling of the mixture) as well as between both cooling cycles (151.7°C).

The most significant discrepancy was observed in the crystallisation, with the melting of the crystal phase into the smectic B phase occurring at approximately 56.9°C (confirmed by microscopy), and the crystallisation occurring at a much reduced temperature of 27.7°C .

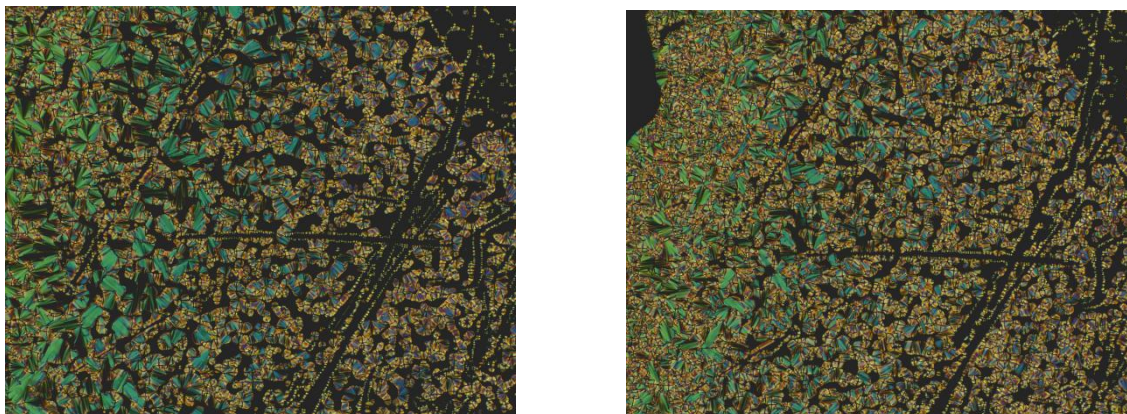


Figure 6.6: Photomicrographs of the 3:1 mixture showing the textures of the smectic A phase close to the transition at 180 °C (left) and the smectic A phase further into the phase at 170 °C (right) (x100 optical zoom).

6.7.1.2: A 2:1 Mixture of Compound 22 : Chloride Salt

A 2:1 mixture was prepared in the manner previously described.

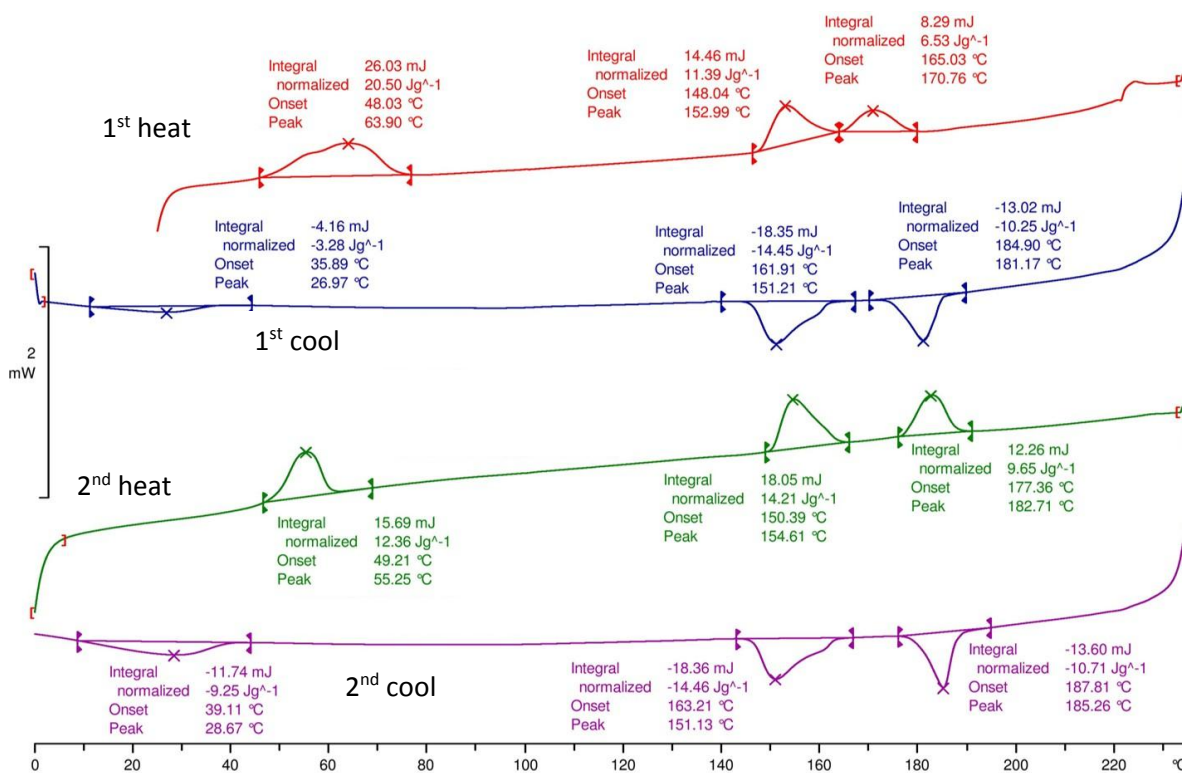


Figure 6.7: DSC thermogram of heat flow (mW^{-1}) as a function of temperature ($^{\circ}\text{C}$) for a 2:1 mixture of Compound 22 : chloride salt.

The transitions observed for the mixture were comparable with the 3:1 mixture, because the percentage concentration of the non-acidified amine was not significantly changed.

The transition point from the liquid on cooling, as shown by the DSC in Figure 6.7, experienced a small suppression in temperature to a value of 181.2 °C (confirmed by microscopy), with the heating curves resulting in a comparable temperature of 182.7 °C, as well as a further discrepancy between each run due to further mixing of the sample after first melting.

The transition between the smectic A and smectic B phases remained constant between each cycle of heating and cooling, with minimal differences being observed. On heating, the transition was observed at 154.6 °C, with the cooling equivalent viewed at 151.2 °C, the discrepancy being slightly larger than in the 3:1 mixture.

Finally, there is again a significant supercooling between the melting from the crystal to the smectic B phase on heating (55 °C) and the crystallisation process back to the crystal phase on cooling (28.7 °C).

The defect textures for the phases are shown in Figure 6.8. In both cases focal-conic and homeotropic textures were observed, which is consistent with the presences of mesophases that are orthogonalsmectic in the structure (smectic A and smectic B).

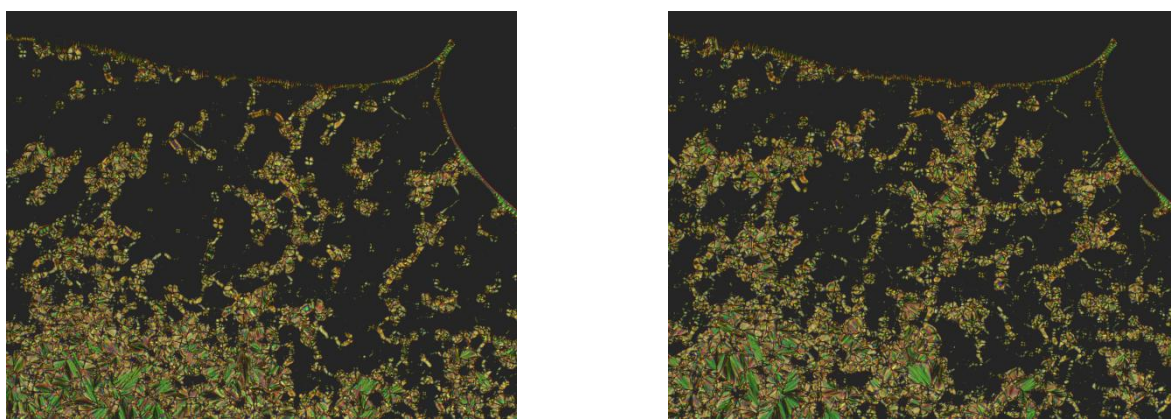


Figure 6.8: Photomicrographs showing the smectic A texture of the 2:1 mixture of Compound **22** and its chloride salt at close to the clearing point at 180 °C (left) and further into the phase at 170 °C (right) (x100 optical zoom).

6.7.1.3: A 1:1 Mixture of Compound 22 : Chloride Salt

The 1:1 mixture was made in the same fashion as previously described.

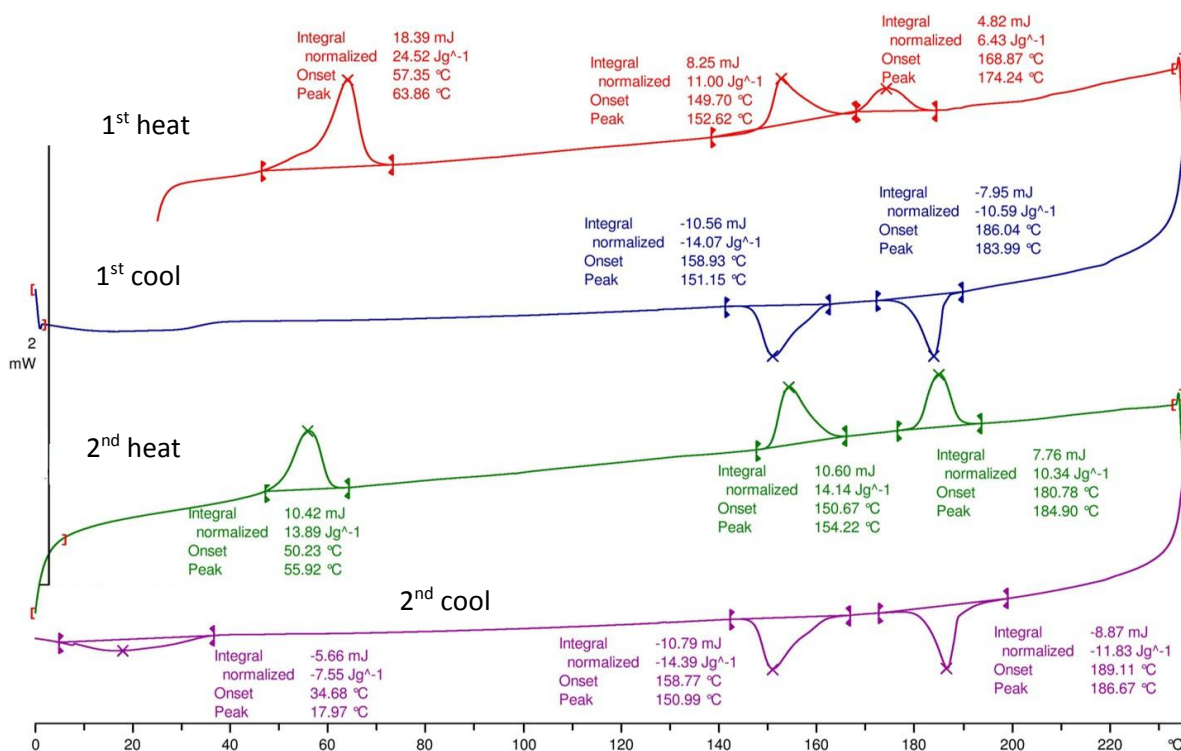


Figure 6.9: DSC thermogram of heat flow (mW^{-1}) as a function of temperature ($^{\circ}\text{C}$) for a 1:1 mixture of Compound 22 : chloride salt.

It can be seen in the DSC presented above, the clearing point on first heating is once again different from that on second heating. As the 1:1 mixture, the clearing point on cooling was seen to be suppressed to 184.0°C (confirmed through the use of microscopy), with the second cooling appearing anomalously high at 186.7°C . The second heating curve of the compound presented a clearing point closer to that of the cooling curve at 184.9°C . The texture of the smectic A phase observed was fairly typical, with clear focal-conic defects shown in Figure 6.10.

As in the preceding mixtures, there is minimal discrepancy between the transitions experienced from the smectic A to the smectic B (on cooling) and from the smectic B to the smectic A (on heating). The former transition was observed at 151.0°C , with the latter at 154.2°C , showing a slighter variation between heating and cooling than seen in the other mixtures.

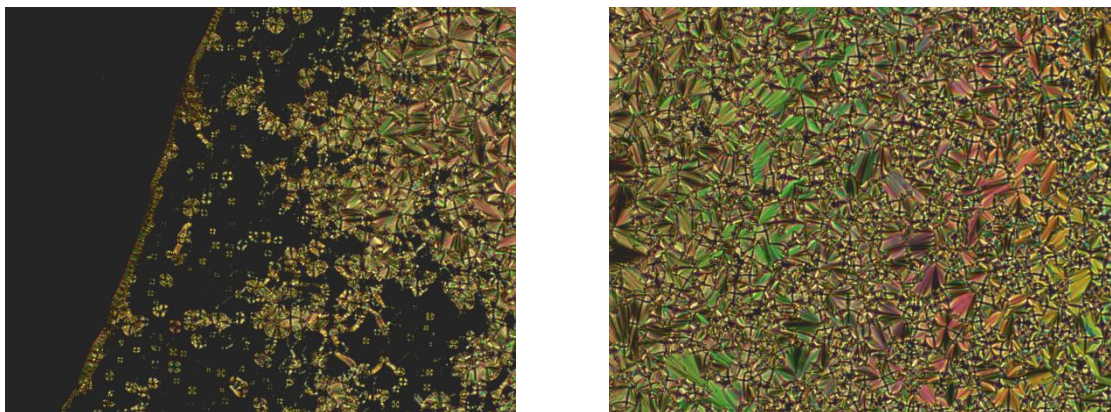


Figure 6.10: Photomicrographs showing the smectic A texture of the 1:1 mixture of Compound **22** and its chloride salt 185 °C showing different regions of the slide between left and right (x100 optical zoom).

As has been seen in the other salt mixtures for the chloride salts, the peak profile of the crystallisation is very small, with it being barely visible in this case. The melting from the crystal phase, however, remains clearly visible in both cases in the DSC study, as well as through microscopy, with the melt occurring in the fully mixed sample at 55.9 °C

6.7.1.4: A 1:2 Mixture of Compound **22** : Chloride Salt

The 1:2 mixture was prepared in the same manner as previously described.

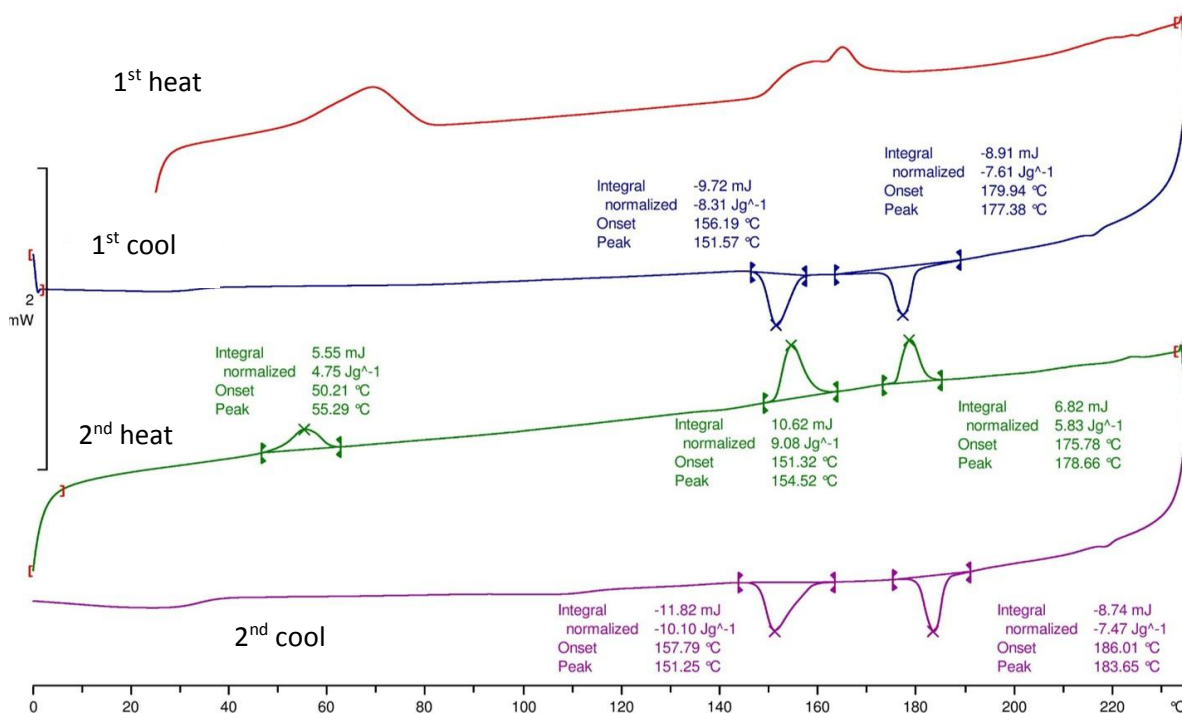


Figure 6.11: DSC thermogram of heat flow (mW^{-1}) as a function of temperature ($^{\circ}\text{C}$) for a 1:2 mixture of Compound **22** : chloride salt.

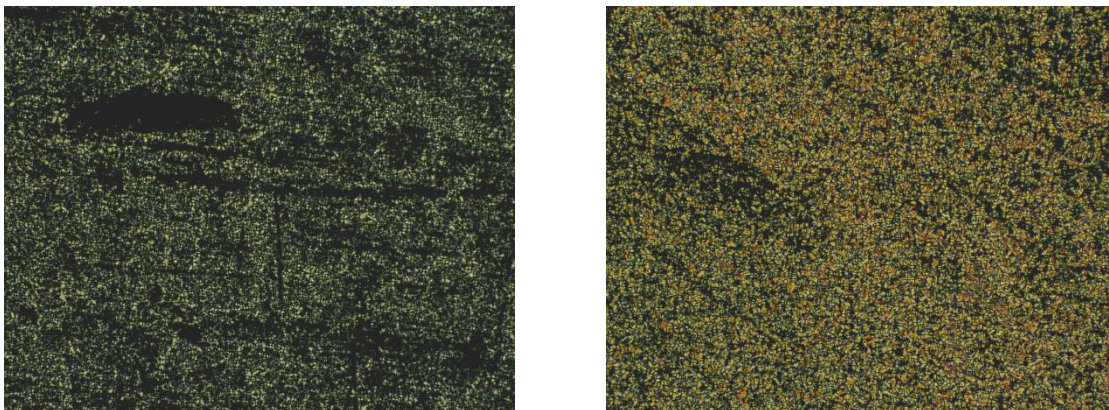


Figure 6.12: Photomicrographs showing the smectic A texture of the 1:2 mixture of Compound **22** and its chloride salt at close to the clearing point at 185 °C (left) and further into the phase at 180 °C (right) (x100 optical zoom).

It can be seen from the DSC thermogram (Figure 6.11), the clearing point on first heating is very different from that on second heating. This time there is a significant overlap with the transition from the smectic B phase to the smectic A phase. As well as this, the second cooling shows poor coordination with the first in terms of the transition, being reported at 177.4 °C on the first cool and 183.7 °C on the second, the latter being confirmed as more accurate by microscopy, revealing it to be 185.5 °C. The smectic A phase observed lead to a fairly atypical texture with it being difficult to resolve the focal conic texture.

The secondary transition between the smectic A and smectic B phases again showed consistency between the cooling curves as well as with the microscopy, with a transition being recorded at 154.5 °C. However, it was impossible to draw comparison between the two heating curves in this example, as shown in the DSC thermogram. Moreover, in this case the texture of the smectic B phase formed very small defects (Figure 6.13) making it difficult to observe phase transitions.

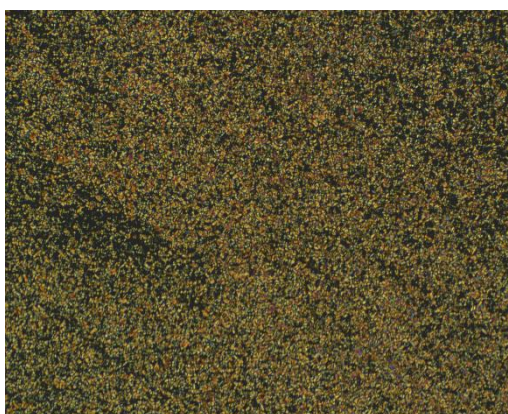


Figure 6.13: Photomicrograph of the smectic B phase of the 1:2 mixture of Compound **22** and its chloride salt at 128 °C.

Following the trend previously outlined from the other mixtures, the crystallisation again was reduced in status, being unnoticeable on both cooling cycles by DSC.

6.7.1.5: A 1:3 Mixture of Compound 22 : Chloride Salt

The 1:3 mixture of Compound **22** and the chloride salt was made in the same fashion as previously described.

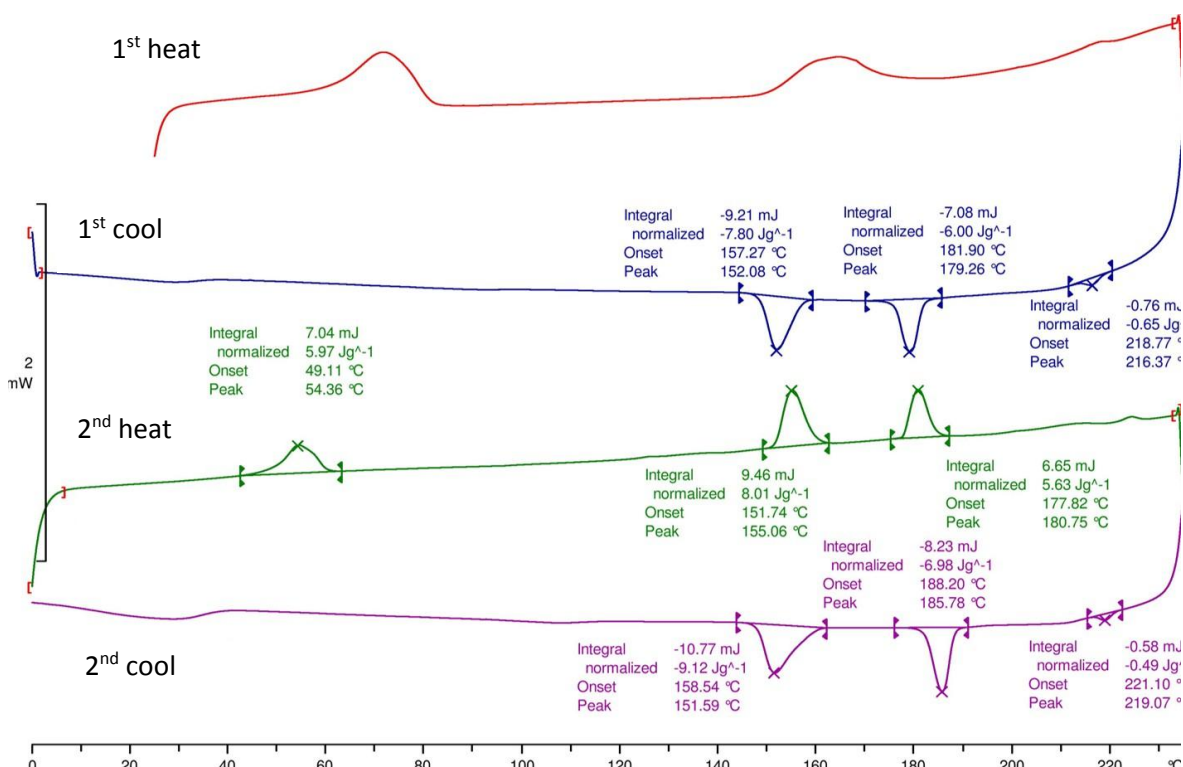


Figure 6.14: DSC thermogram of heat flow (mW^{-1}) as a function of temperature ($^{\circ}\text{C}$) for a 1:3 mixture of Compound **22** : chloride salt.

It can be seen from the DSC thermogram (Figure 6.14) that the trend of the clearing point on first heating approaching the smectic B to smectic A phase changes the transitions have become continuous, with a near perfect overlap. In similarity to the previously noted example of the 1:2 mixture, there is also a discrepancy between the clearing point on first cooling (179.3°C) and on second cooling (185.8°C), with the latter result being supported by optical microscopy (186.5°C) as a more accurate representation. The photomicrograph presented (Figure 6.15, left) of the smectic A texture is typical of the phase, showing both homeotropic and focal conic defects. The homeotropic defect area indicates that the mesophase is uniaxial with its optic axis perpendicular to the substrates, and therefore the rod-like molecules are also perpendicular to the glass substrate. This conforms that the phase can only be smectic A or smectic B (Figure 6.15, right).

The smectic A to smectic B transition (on cooling) was again consistent in both cycles at 152.1°C and 151.6°C . Again, it is impossible to compare the DSC heating curves to one another, yet the discrepancy between second heating and second cooling is far smaller than that for the clearing transition.

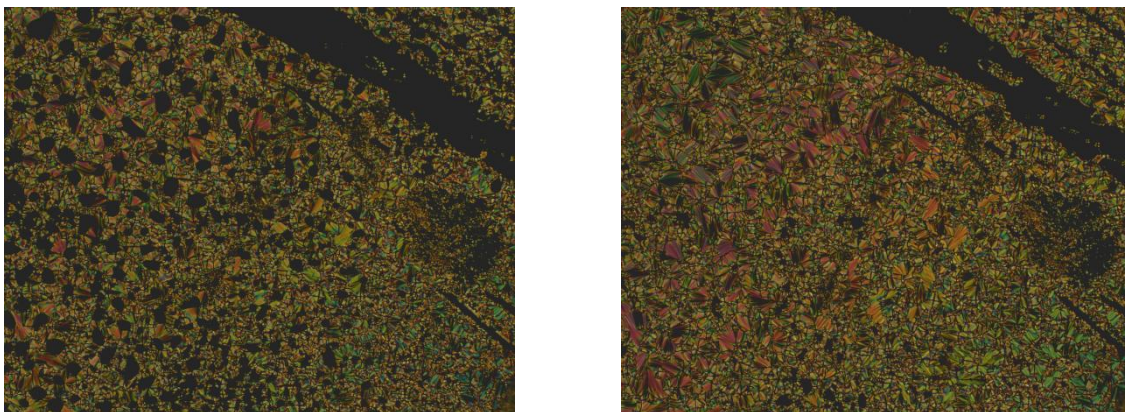


Figure 6.15: Photomicrographs showing the smectic A texture of the 1:3 mixture of Compound **22** and its chloride salt at close to the clearing point at 185 °C (left) and further into the phase at 170 °C (right) (x100 optical zoom).

6.7.1.6: Determination of Effects of Chloride Salt Introduction into Mixtures

In order to investigate the impacts of the chloride salt prevalence in the mixture with the parent, it would be of interest to compare and analyse the clearing points as a function of the percentage of chloride salt present in the mixture.

Thus, by plotting the transition temperatures of both the clearing point and the smectic A to smectic B transition in relation to the percentage composition of the chloride salt within the mixture, it is possible to analyse the impacts of the acidification process.

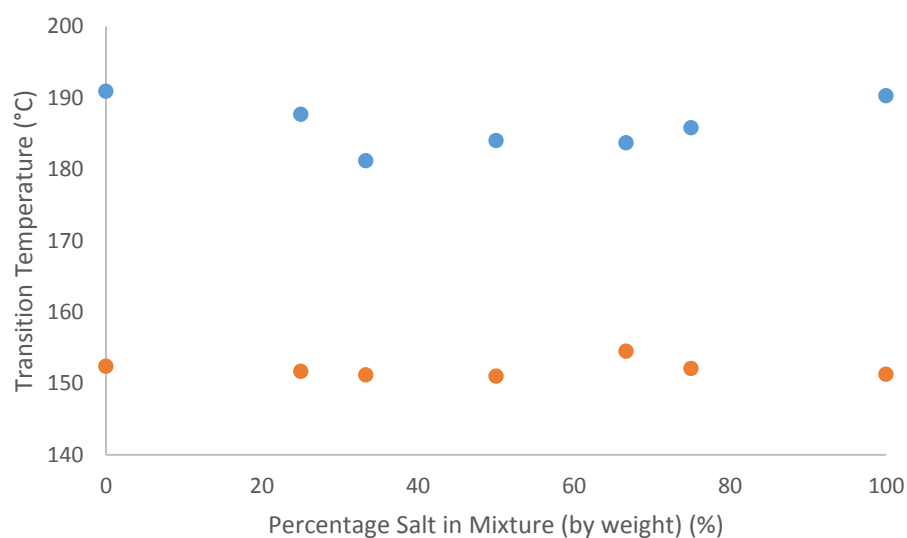


Figure 6.16: Transition temperatures (●- clearing point, ●-smectic A to smectic B) as a function of concentration (wt %) of the chloride salt of Compound **22** with the parent Compound **22**.

As it can be seen from Figure 6.16, there is a general narrowing between the transitions between the clearing point and the smectic A to smectic B transitions around the central point of the phase diagram. It is also apparent that there is a eutectic mixture that can be reached using this binary system, which is in the region of 40% salt mixture.

The general trend from 0% to the theorized eutectic point is that of a shallow curve to lower clearing point temperatures, with the reverse generally being true the other side of this mixture despite a seemingly anomalous point at the 1:2 ratio mixture, which shows a decrease in clearing temperature between the 50% and 75% mixtures.

6.7.2: Acrylate Salt Mixtures

The acrylate salt mixtures were prepared in the same manner and ratios as previously outlined in Section 6.7.

6.7.2.1: A 3:1 Mixture of Compound 22 : Acrylate Salt

The 3:1 ratio for the mixture of Compound **22** to its acrylate salt was prepared in the same manner as for the corresponding chloride mixture (as described in Section 6.7.1.1). The cyclic heating and cooling thermograms for the mixture are shown below in Figure 6.17.

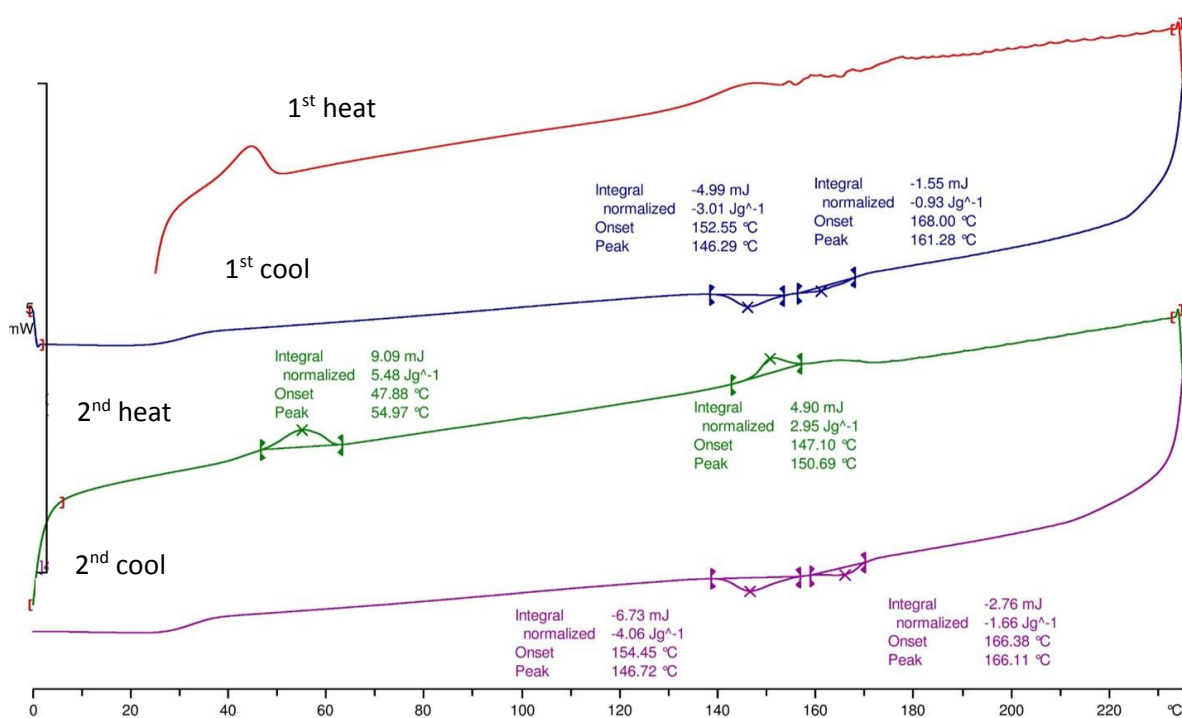


Figure 6.17: DSC thermogram of heat flow (mW^{-1}) as a function of temperature ($^{\circ}\text{C}$) for a 3:1 mixture of Compound **22** : acrylate salt.

It can be seen from the thermogram (Figure 6.17) that the clearing point and smectic B to smectic A transition on the first heating were unable to be detected, with the clearing point being masked on second heating. Despite this, the clearing point was easily visualised on the cooling traces at 166.1 °C, confirmed by microscopy at 172 °C. The defect textures visualised in Figure 6.18, show a moderately atypical representation of the phase with a minimal presence of focal-conic defects owing to the nature of the acrylate salt content, as well as due to being taken at a temperature close to the transition on cooling. The phase is also shown as a more typical example in the right of Figure 6.18.

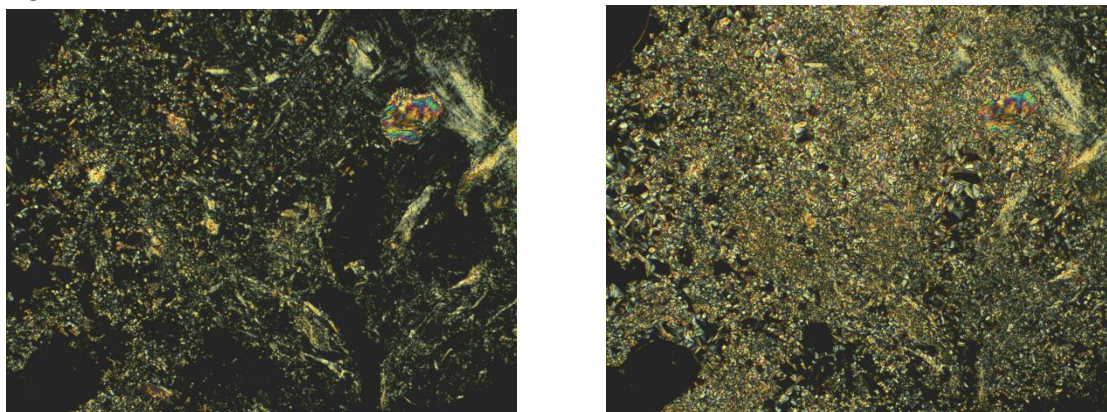


Figure 6.18: Photomicrographs showing the smectic A texture of the 3:1 mixture of Compound **22** and its acrylate salt at close to the clearing point at 170 °C (left) and further into the phase at 160 °C (right) (x100 optical zoom).

The smectic A to smectic B transition on cooling (146.3 and 146.7 for the first and second scans respectively) were also supported by the transition observed by microscopy at 154.9 °C. The smectic B phase was fairly typical in texture, and was more easily observed when allowed more time to form as the sample was cooled on the slide. This indicates that the process is most likely to be kinetically driven than thermodynamically. This is presented with the differences between the left (initial) and right (kinetically formed) textures presented in Figure 6.19.

The crystallisation process on cooling was not observed by DSC, but was apparent at 38 °C by microscopy.

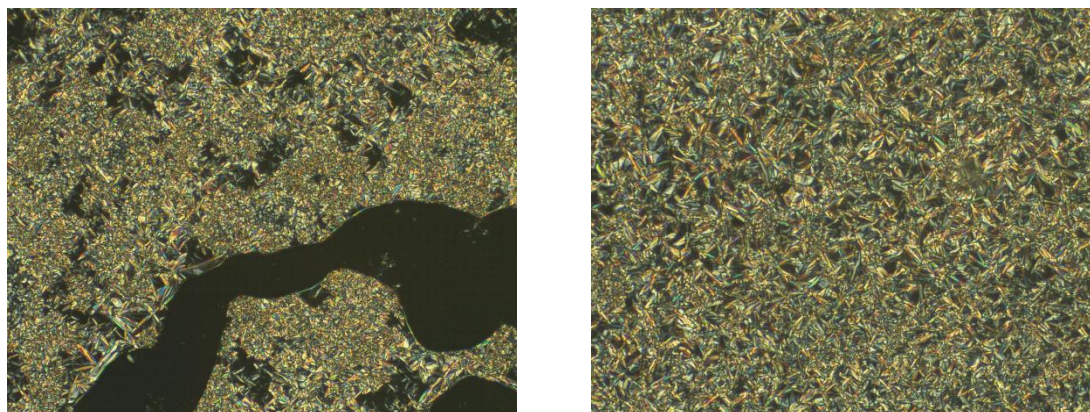


Figure 6.19: Photomicrographs showing the smectic B texture of the 3:1 mixture of Compound **22** and its acrylate salt at close to the clearing point at 125 °C (left) and further into the phase at 101 °C (right) (x100 optical zoom).

6.7.2.2: A 2:1 Mixture of Compound **22** : Acrylate Salt

A 2:1 mixture of Compound **22** and the acrylate salt was prepared in the same manner as previously described. It was then studied by DSC as shown in Figure 6.20 below.

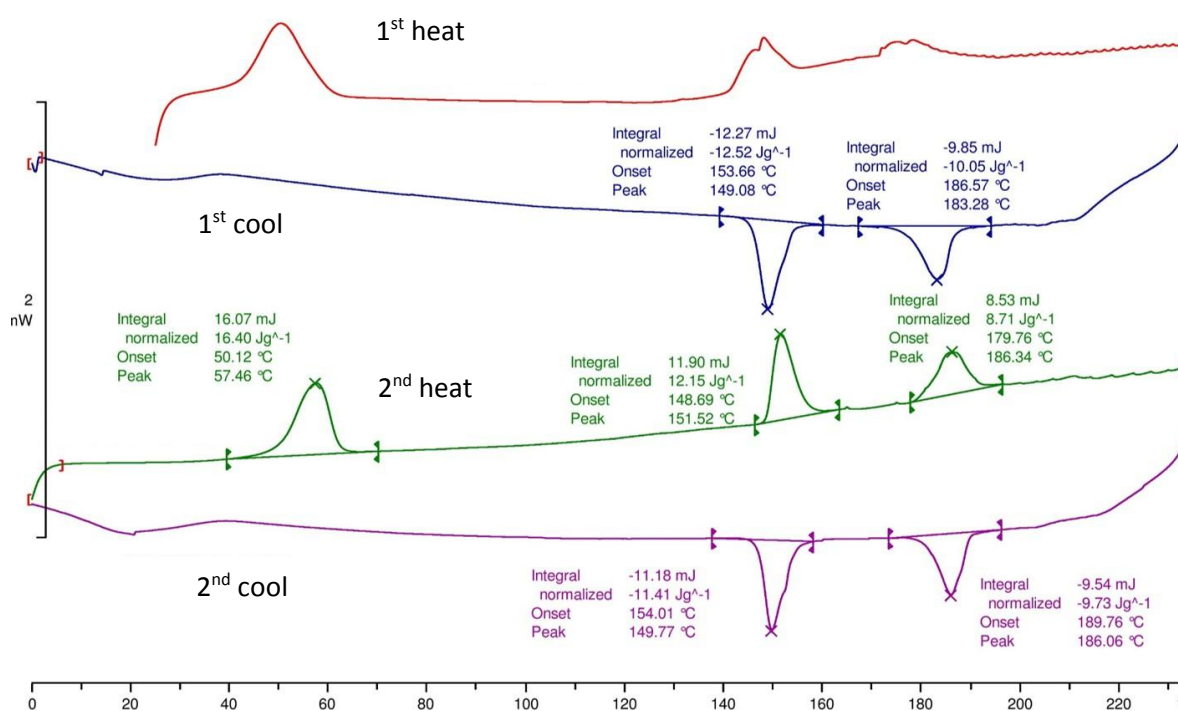


Figure 6.20: DSC thermogram of heat flow (mW^{-1}) as a function of temperature ($^{\circ}\text{C}$) for a 2:1 mixture of Compound **22** : acrylate salt.

For this sample, the first heating scan did not show well defined peaks due to pan and sample settling. However, it was possible to see clearer defined transitions on the second heating, with the clearing point seen at 186.3 °C, which was noted as comparable that seen on the corresponding cooling curve (186.1 °C). The first cooling was slightly different from this with a value of 183.3 °C.

The temperature observed by microscopy was more comparable to that of the second curve with the temperature of 190.4 °C being recorded.

Once again it was difficult to observe clearly identifiable peaks for the smectic B to smectic A transition by DSC in the first scan, yet this transition was clearly visible in the second heating, with the transition noted at 151.5 °C. The corresponding response on cooling was observed at 149.8 °C by DSC and by microscopy.

The crystallisation was found at 38°C by microscopy despite the lack of evidence for this by DSC. This observation was thought to be related to the formation of a glassy state in the solid.

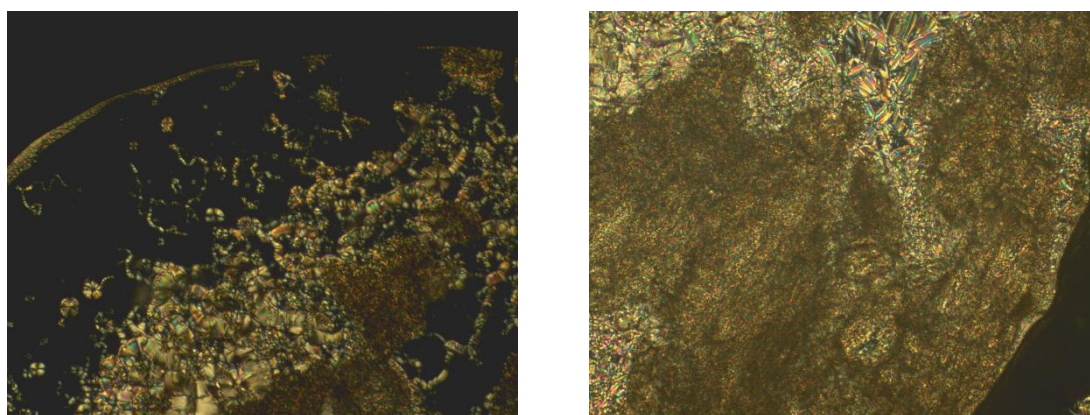


Figure 6.21: Photomicrographs showing the smectic A texture of the 2:1 mixture of Compound **22** and its acrylate salt at close to the clearing point at 170 °C (left) and the smectic B phase at 125 °C (right) (x100 optical zoom).

6.7.2.3: A 1:1 Mixture of Compound **22** : Acrylate Salt

A 1:1 mixture of Compound **22** and the acrylate salt was prepared in the same way as described previously. It can be seen from the DSC thermogram (presented below in Figure 6.22) produced somewhat diffuse results, again due to the materials settling in the pan and becoming fully mixed.

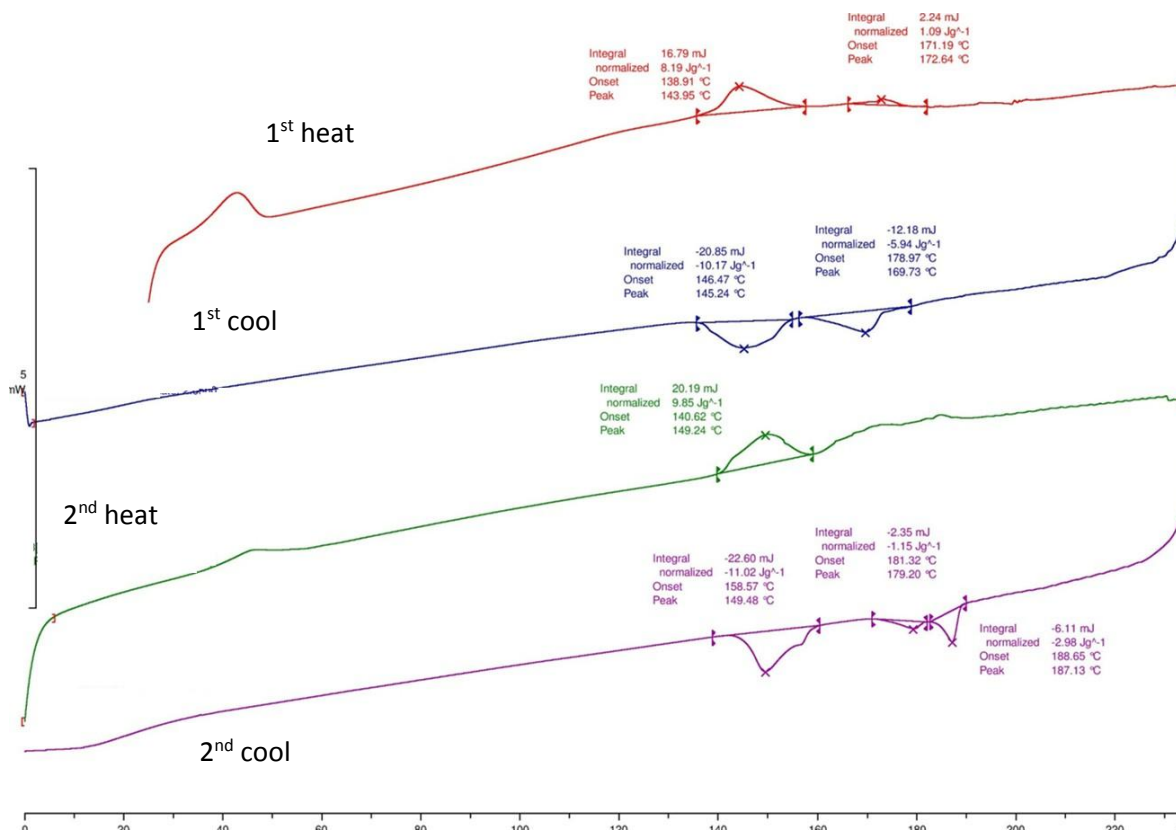


Figure 6.22: DSC thermogram of heat flow (mW^{-1}) as a function of temperature ($^{\circ}\text{C}$) for a 1:1 mixture of Compound **22** : acrylate salt.

The first cooling and the second heating/cooling cycles produced better results with sharper peaks and reproducible data. Again, all of the peaks were broad. Thus, the clearing point on cooling was observed at 188°C by microscopy, which is similar to the temperature observed by DSC on the second cooling (187.1°C). The transition on heating was reduced in comparison, which may have been due to autopolymerization or decomposition.

The transition between the smectic A and smectic B phase on cooling was observed in the region of 155°C by microscopy, which correlates with the results obtained for the second cooling (149.5°C). The shape of the peak on the second cooling appears distorted, along with an extra peak also found, which may suggest that during the second heating, the compound may have undergone thermal polymerisation to some degree due to the presence of the acrylate salt, which can undergo spontaneous thermal initiation.

6.7.2.4: A 1:2 Mixture of Compound 22 : Acrylate Salt

A 1:2 mixture of Compound **22** and its acrylate salt was prepared in the same way as previously described.

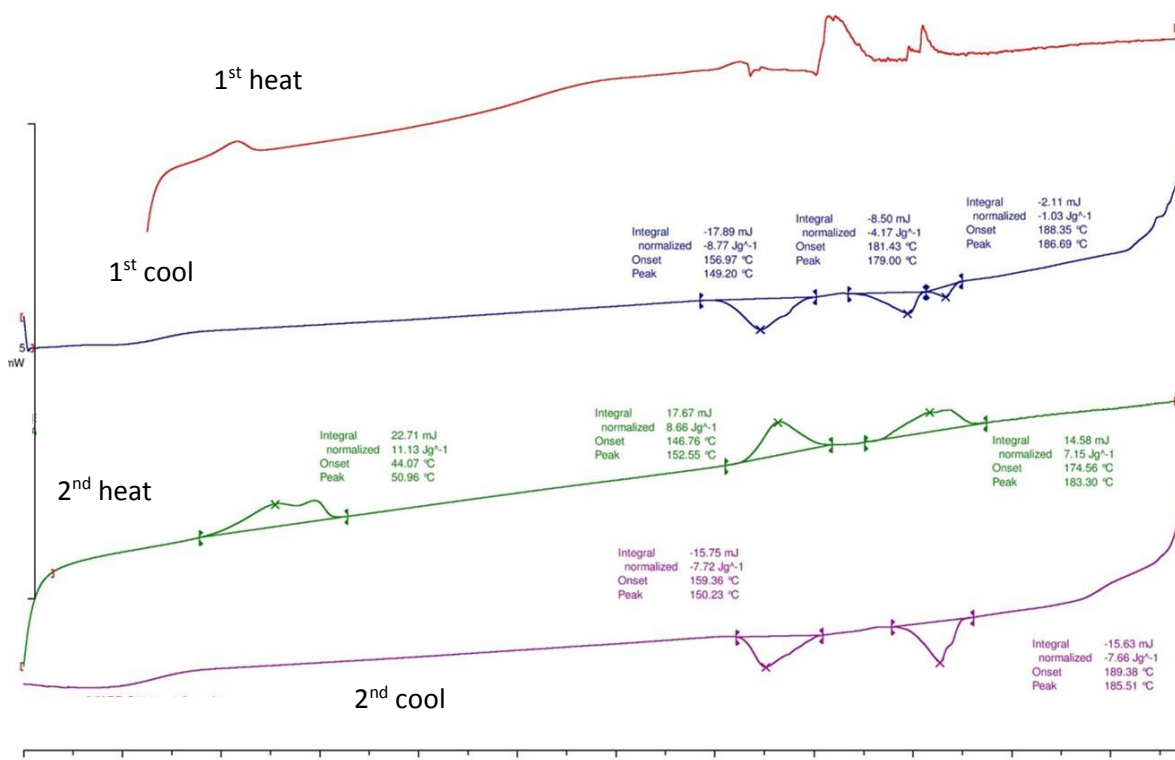


Figure 6.23: DSC thermogram of heat flow (mW^{-1}) as a function of temperature ($^{\circ}\text{C}$) for a 1:2 mixture of Compound **22** : acrylate salt.

It can be seen from the above DSC thermogram (Figure 6.23) that the transitions on first heating were again difficult to analyse due to pan settling, yet were clear on second heating, with the clearing point observed at 183.3 $^{\circ}\text{C}$, which is below that of the 185.5 $^{\circ}\text{C}$ witnessed on cooling, confirmed by microscopy as well as both cooling curves.

The smectic A to smectic B transition observed on cooling remained consistent (149.2 $^{\circ}\text{C}$ on first cooling and 150.2 $^{\circ}\text{C}$ on second cooling). The second heating curve also witnessed the onset of this transition 152.6 $^{\circ}\text{C}$, which corresponds well with the cooling data.

6.7.2.5: A 1:3 Mixture of Compound 22 : Acrylate Salt

A 1:2 mixture of Compound **22** and its acrylate salt was prepared in the same fashion as previously described.

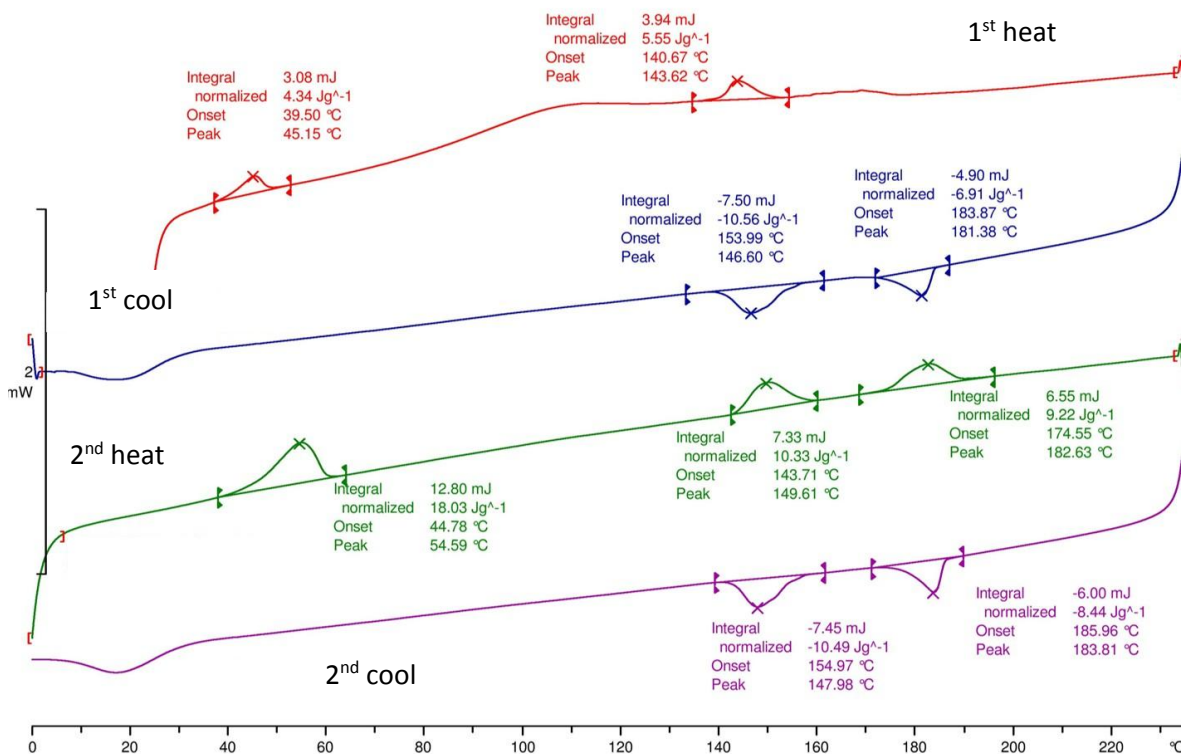


Figure 6.24: DSC thermogram of heat flow (mW^{-1}) as a function of temperature ($^{\circ}\text{C}$) for a 1:3 mixture of Compound **22** : acrylate salt.

It can be seen from the DSC thermogram presented above in Figure 6.24 that the transitions on first heating were difficult to analyse due to pan settling, yet were clearer on second heating, thus the mixture displayed a sharp smectic B to smectic A transition on first heating, yet the clearing point was not observed by DSC, however on second heating, both were found. On the other hand, both transitions were clearly noticed on both cooling cycles, with temperatures corresponding to those seen by microscopy.

The clearing point determined on cooling by microscopy was found to be 186.1°C , with the temperature determined on second cooling was at 183.8°C . The first cooling saw a small discrepancy at 181.4°C . These temperatures correspond well with the second heating which shows an onset for this transition at 182.6°C .

The smectic B to smectic A transition on both heating cycles shows at 143.6°C and 149.6°C on first and second heatings respectively, with the lower temperatures of 146.6°C and 148.0°C on the corresponding cooling cycles.

Similar to other acidified samples, as described previously, the crystallisation process from Smectic B to crystal was not clearly observed by DSC.

6.7.2.6: Impact of the Addition of the Acrylate Salt

In the same manner as for the chloride salt, it is advisable to plot the transition temperatures of the mixture against the percentage composition (wt %) with respect to the acrylate salt introduced.

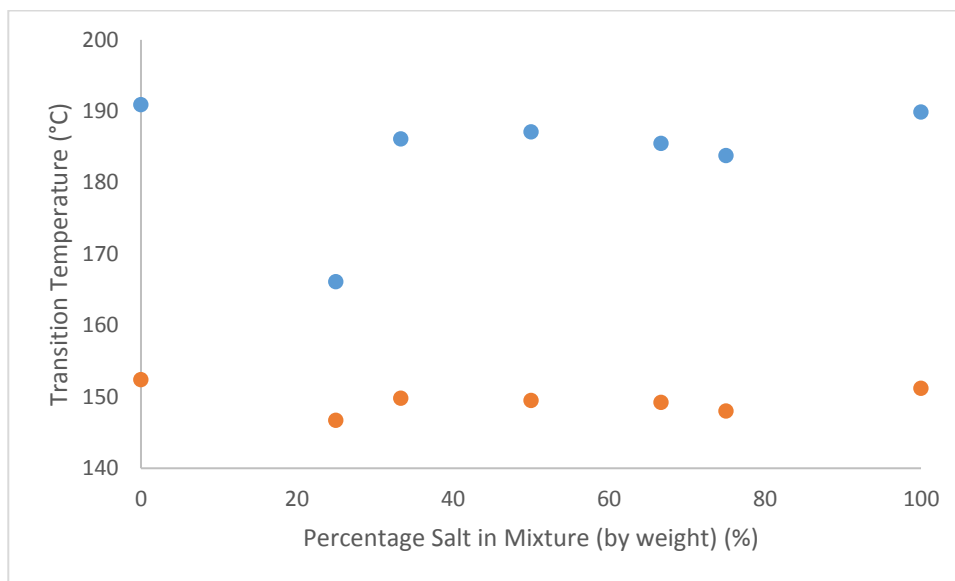


Figure 6.25: Transition temperatures (●- clearing point, ●-smectic A to smectic B) as a function of concentration (wt %) of the chloride salt of Compound **22** with the parent Compound **22**.

It is clearly noticeable that there is a less obvious trend than in the chloride equivalent. The issues noted for this mixture system are largely centred on the thermal issues, resulting in autopolymerisation of the mixture due to the acrylate content and the lack of stabilisers. The decision to not include a stabiliser was made to allow for more accurate determination of the ratio of salt to parent, as well as the purity impact of the acrylate salt on the system with respect to the phase transitions and transition temperatures. The addition of an inhibitor would deter the autopolymerisation of the acrylate salt, yet it would also lead to impurity that would skew the ratio and make it a non-binary mixture of compounds.

It is possible to see a slight trend in the transitions, ignoring the 3:1 mixture clearing point (just above 170 °C compared to the greater than 190 °C for the transitions either side at 0% and 33% acrylate introduction. With this point declared as anomalous, there is a slight downward trend towards the 50:50 mixture with an increase thereafter. However, with the loss of data from 25% acrylate salt presence, it is not correct to draw conclusions from only two data points below this.

6.7.3: Hexafluorophosphate Salt Mixtures

The hexafluorophosphate salt and parent Compound **22** mixtures were prepared in a similar way to the acrylate and chloride salts despite the initial salt compound being synthesised differently. The same ratios for the mixtures were also made, with the range from 3:1 unacidified to acidified, to the 1:3 corresponding mixture.

6.7.3.1: A 3:1 Mixture of Compound 22 : Hexafluorophosphate Salt

A 3:1 mixture of Compound **22** with the hexafluorophosphate salt was prepared in the manner as previously described. The cyclic heating and cooling thermograms for the mixture are shown together in Figure 6.26 (below).

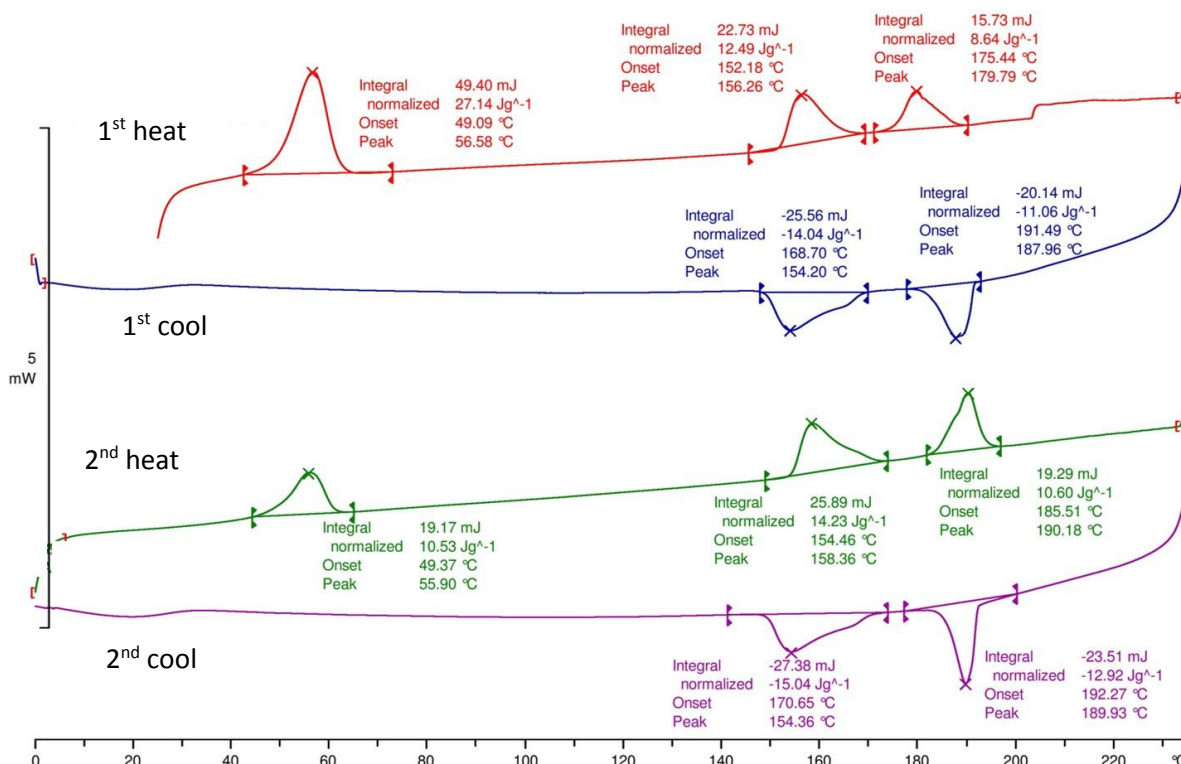


Figure 6.26: DSC thermogram of heat flow (mW^{-1}) as a function of temperature ($^{\circ}\text{C}$) for a 3:1 mixture of Compound **22** : hexafluorophosphate salt.

The major difference between the hexafluorophosphate salt and acrylate salt mixtures is that there appears to be minimal or no pan settling of the sample and no kinetic process, i.e. the hexafluorophosphate salt mixture thus exhibited properties more in keeping with those of a single pure compound. In terms of peak maxima, the salt exhibited a melting at 56.6°C to a smectic B phase, with a second transition to a smectic A phase at 152.2°C before the clearing point was observed at 179.8°C . The peaks obtained for the first heating were a little broader than for the second heating and subsequent cooling, which gave little variance with the overall results.

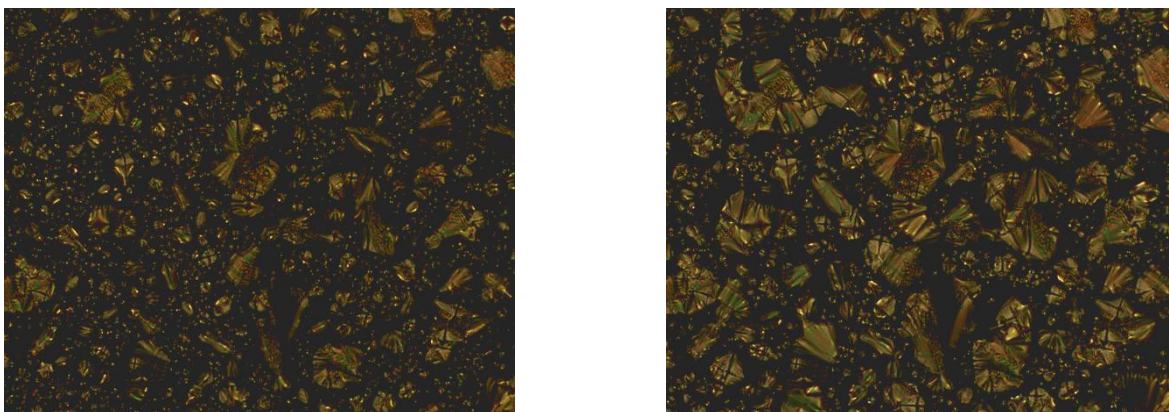


Figure 6.27: Photomicrographs showing the smectic A texture of the 3:1 mixture of Compound **22** and its hexafluorophosphate salt at close to the clearing point at 191 °C (left) and further into the phase at 191 °C (right) (x100 optical zoom).

In comparison, the clearing point observed by thermal optical microscopy was observed to be 192.4 °C, which agreed well with the onset temperatures determined by DSC from the first and second cooling cycles (191.5 °C and 192.3 °C respectively). However, the corresponding onset temperature for the second heating curve gave a value of 185.1 °C, due to the offset values being determined from the tangent of the maximum heat-flow of the enthalpy peak. Classification of the mesophases formed by the 3:1 mixture used polarised light microscopy shows that the higher temperature mesophases is smectic A (shown in Figure 6.27). This heating and cooling cycle with respect to the isotropic liquid indicates that there was no presence of paramorphism, and that the texture was the ‘natural texture’ of the mesophase, which thereby confirms the mesophase as being of smectic A in type (see Figure 6.28 left).

The smectic A to smectic B transition was observed at 170.5 °C by microscopy on cooling (the onset values by DSC were 168.7 °C and 170.7 °C on the first and second coolings respectively). Microscopy showed that there was little change in the defect patterns at the phase transition (Figure 6.28 right), indicating that the texture exhibited by the lower temperature phase was paramorphic of the smectic A phase, thereby indicating that the second phase was more likely to be a smectic B phase than any other smectic phase.

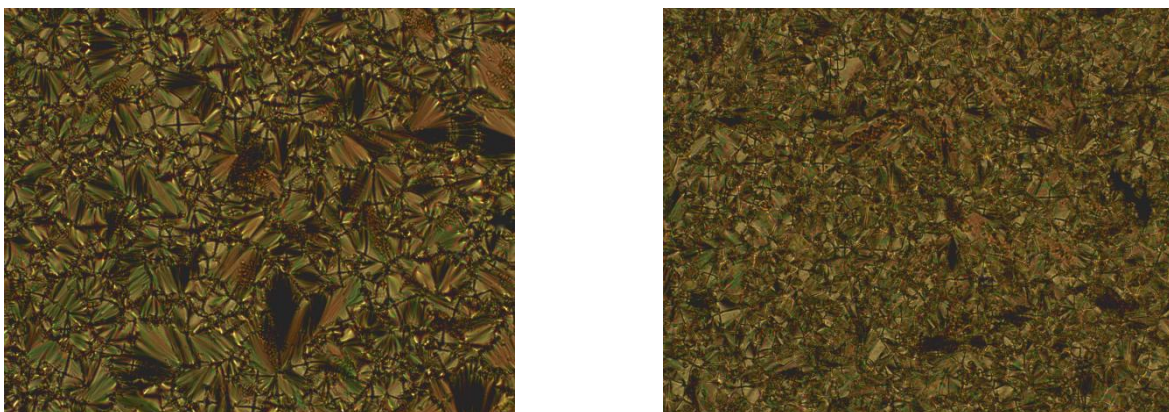


Figure 6.28: Photomicrographs showing the smectic A texture of the 3:1 mixture of Compound **22** and its hexafluorophosphate salt at 185 °C (left) in the smectic B phase at 165 °C (right) (x100 optical zoom).

Crystallisation on cooling was not observed clearly by DSC and the change in the baseline indicates that solidification occurred *via* a process of glassification. This is confirmed by reheating where a large enthalpy for melting was observed. Microscopy revealed that recrystallization probably occurred at approximately 25 °C.

6.7.3.2: A 2:1 Mixture of Compound 22 : Hexafluorophosphate Salt

The 2:1 mixture of Compound **22** : hexafluorophosphate salt was prepared in the fashion previously described, and its melting behaviour was observed by microscopy and DSC (Figure 6.29).

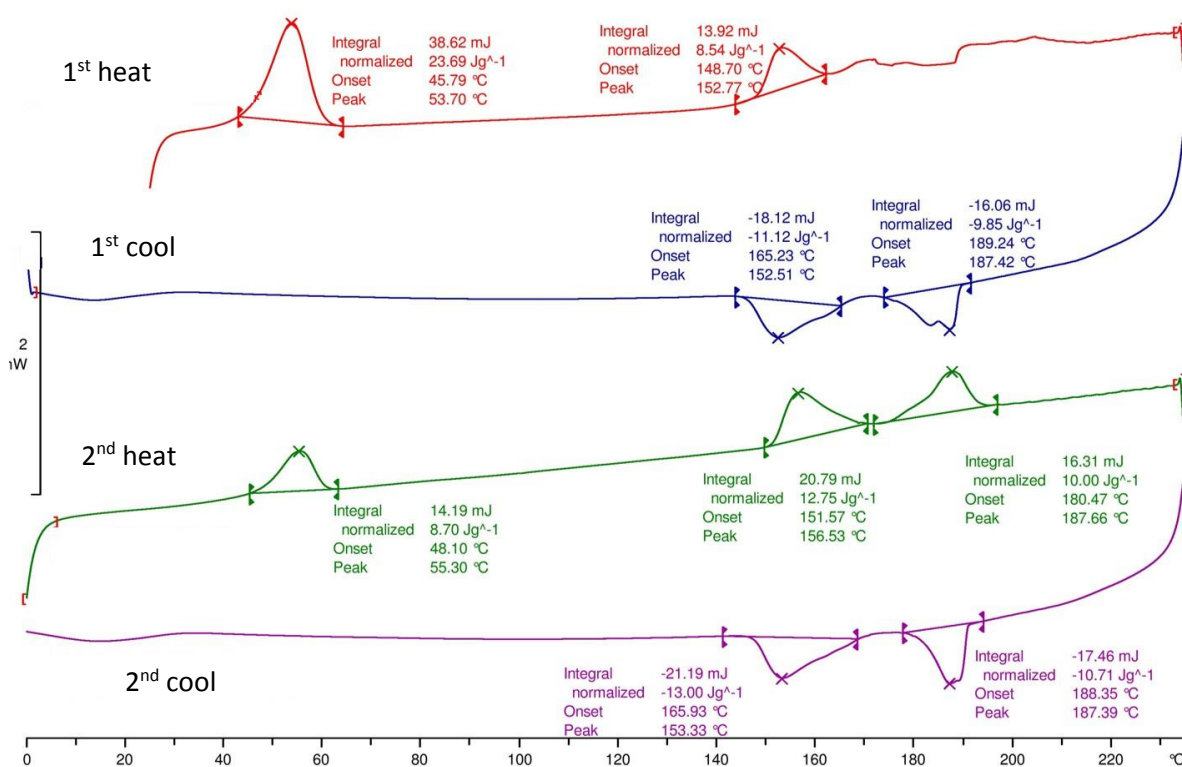


Figure 6.29: DSC thermogram of heat flow (mW^{-1}) as a function of temperature ($^{\circ}\text{C}$) for a 2:1 mixture of Compound **22** : hexafluorophosphate salt.

Unlike the DSC thermogram exhibited by the 3:1 mixture (section 6.7.3.1, Figure 6.27), the results for the 2:1 mixture are similar to those observed for the acrylate and chloride salts with the first heating cycle showing poor definition for the peaks associated with transitions, in particular the clearing transition where no defined peak was observed. Further to this, the clearing point transition peaks on cooling appeared oddly shaped, hinting at the potential for other transitions in the same region, but these were not observed by microscopy. Again, the peaks were typically broad, thereby giving large differences between the onset and maximum peak temperatures. Moreover, the evidence for recrystallization was poor with a broad diffuse peak being the only evidence suggesting the presence of the formation of a glassy state. On the reheat cycle, a melting peak became evident, indicating recrystallization from the glassy state to crystalline variation.

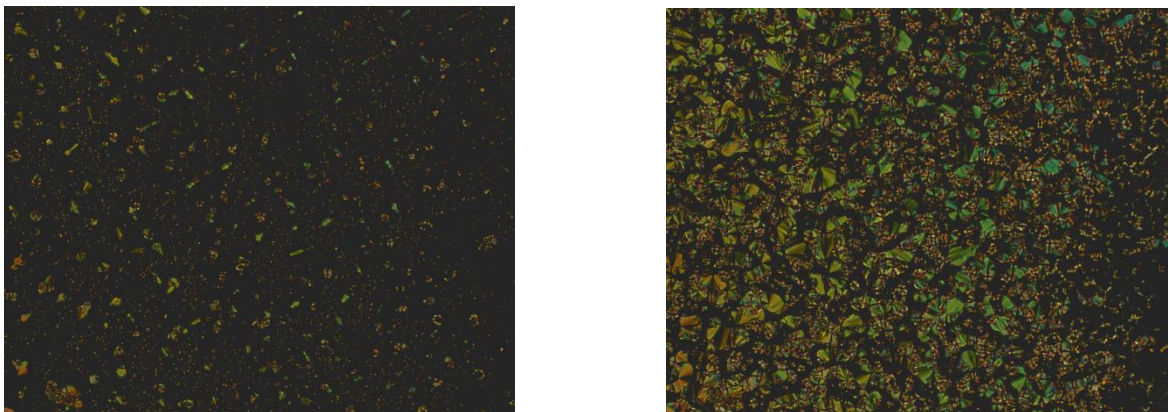


Figure 6.30: Photomicrographs showing the smectic A texture of the 2:1 mixture of Compound **22** and its hexafluorophosphate salt at close to the clearing point at 190 °C (left) and further into the phase at 185 °C (right) (x100 optical zoom).

In comparison, the isotropic to smectic A transition was observed at 189.1 °C (at onset) by microscopy (Figure 6.30), with the onset data from DSC corroborating this at 189.4 °C (first cooling) and 188.4 °C (second cooling) with maxima observed at 187.4 °C on both the first and second cooling cycles. The defect texture of the smectic A phase was observed as described for the 3:1 mixture.

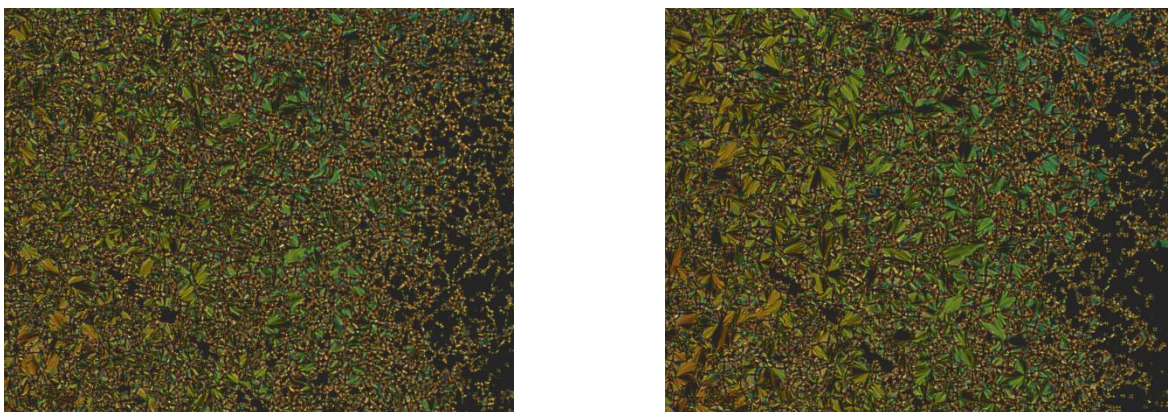


Figure 6.31: Photomicrographs showing the smectic A texture of the 2:1 mixture of Compound **22** and its hexafluorophosphate salt at 180 °C (left) and the smectic B phase at 150 °C (right) (x100 optical zoom).

The smectic A to smectic B transition was observed at 156.1 °C by microscopy on cooling, as well as being backed by the DSC data, with the transition showing at 152.5 °C on first cooling and 153.3 °C on second cooling as maxima, the corresponding onsets observed at 165.2 °C and 165.9 °C respectively.

The defect patterns of both the smectic A and smectic B exhibit both focal-conic and homeotropic textures (Figure 6.30 and Figure 6.31). The presence of both textures confirm absolutely that the upper temperature phase is smectic A, and the paramorphic texture of the lower phase confirms it as smectic B.

6.7.3.3: A 1:1 Mixture of Compound **22** : Hexafluorophosphate Salt

The 1:1 mixture of Compound **22** : hexafluorophosphate salt was prepared as previously described, and its melting behaviour was observed by DSC (Figure 6.32) and microscopy.

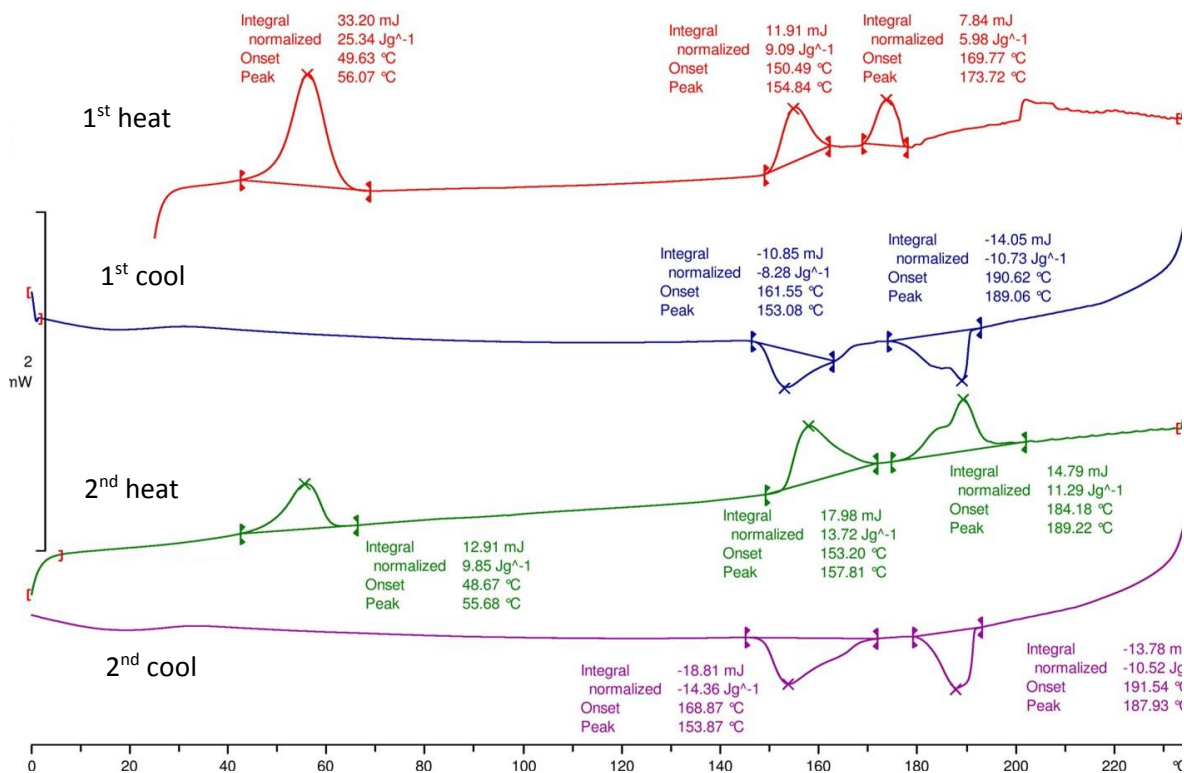


Figure 6.32: DSC thermogram of heat flow (mW^{-1}) as a function of temperature ($^{\circ}\text{C}$) for a 1:1 mixture of Compound **22** : hexafluorophosphate salt.

From the DSC thermogram it is worthwhile noting that the clearing point transition for the 1:1 mixture was visible on the first heating, yet at a reduced temperature compared to that of the second heating, which was possibly due to the settling of the material in the pan, which appeared to persevere to higher temperatures in the isotropic phase, as evidenced by the deviations seen in the baseline at approximately 200°C . It was proposed that this was not due to decomposition due to the reproducible nature of the peaks observed on the subsequent cycles. The texture of the smectic A phase observed displayed focal-conic domains characterised by the elliptical and hyperbolic lines of optical discontinuity (Figure 6.33 right). In some areas there were significant areas of homeotropic alignment, confirming the phase was uniaxial, with the constituents perpendicular to the layers, as in the smectic A phase. The transition from the isotropic into the smectic A phase was witnessed at 191.4°C by microscopy (Figure 6.33 left), with corroborating data from DSC at 190.6°C and 191.5°C (onset temperatures) from successive DSC cooling cycles. The peak maxima were observed at 189.1°C and 187.9°C from the respective cycles, noted due to the broad nature of the peaks.

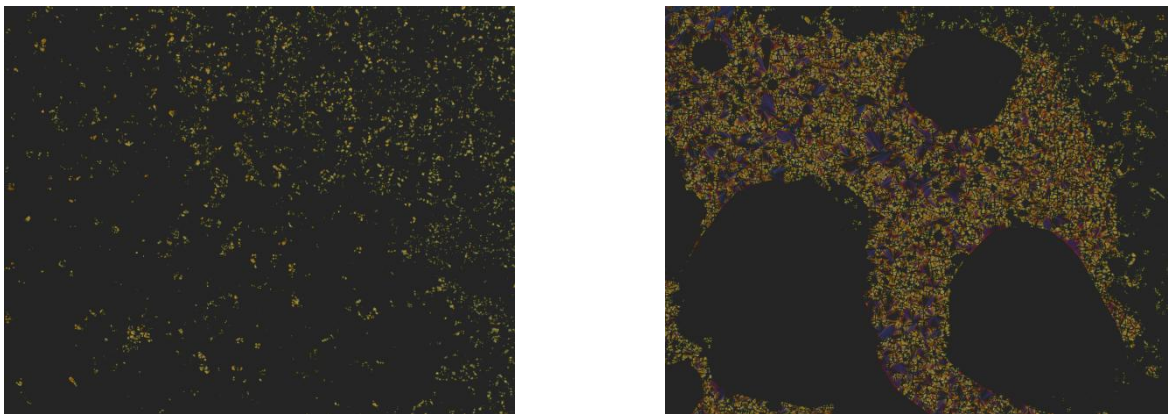


Figure 6.33: Photomicrographs showing the smectic A texture of the 1:1 mixture of Compound **22** and its hexafluorophosphate salt at close to the clearing point at 190 °C (left) and further into the phase at 180 °C (right) (x100 optical zoom).

The transition between the Smectic A and Smectic B phase was found at 170.1°C (at onset) by microscopy, with the DSC confirming this transition at 168.9 °C on the second cooling, with a maximum observed at 153.9 °C due to the broadness of the peak..

As with the other mixtures, the transition into the crystal phase was not found by DSC, but was observed by microscopy at 28.1°C.

6.7.3.4: A 1:2 Mixture of Compound **22** : Hexafluorophosphate Salt

A 1:2 mixture of Compound **22** : hexafluorophosphate salt was prepared as described previously. The cyclic heating and cooling thermograms for the mixture are shown together in Figure 6.34. Again, the difference between the hexafluorophosphate salt and the acrylate and chloride salts is that the hexafluorophosphate salt exhibited properties more in keeping with those of a pure compound, without pan settling and decomposition.

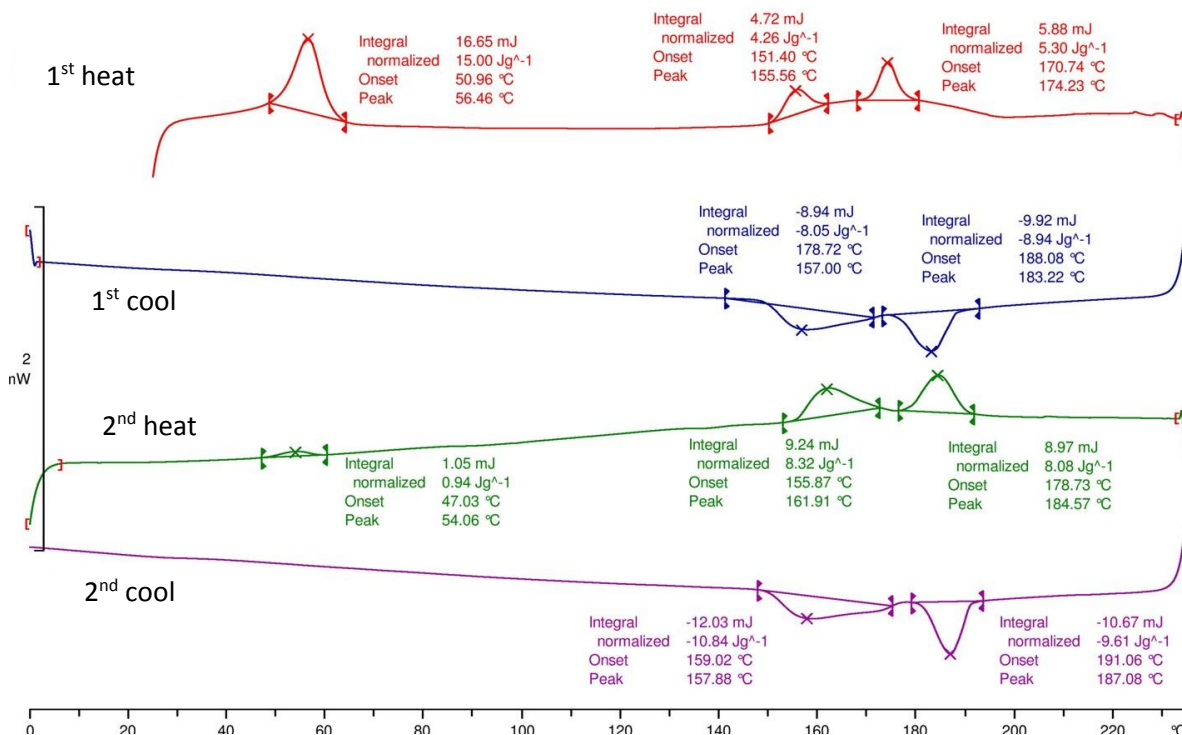


Figure 6.34: DSC thermogram of heat flow (mW^{-1}) as a function of temperature ($^{\circ}\text{C}$) for a 1:2 mixture of Compound **22** : hexafluorophosphate salt.

It is immediately apparent from DSC that there is a significant discrepancy between the clearing points from the first and second heating cycles, with a slight discrepancy witnessed on the cooling cycles.

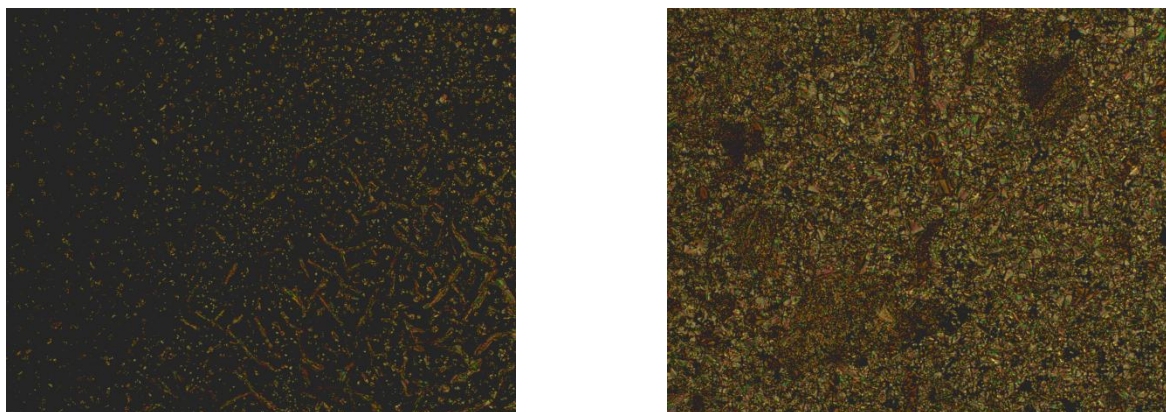


Figure 6.35: Photomicrographs showing the smectic A texture of the 1:2 mixture of Compound **22** and its hexafluorophosphate salt at close to the clearing point at 190°C (left) and further into the phase at 180°C (right) ($\times 100$ optical zoom).

The transition from the isotropic liquid to the smectic A (Figure 6.35) was found by microscopy to be 191.2°C , with the second cooling curve supporting this closely with an onset of 191.1°C and a maximum at 187.1°C , the first heating showing a slightly lower temperature maximum at 174.2°C due to the settling of the mixture. The second heating curve displays the transition maximum at 184.6°C , which supports the transition on cooling by microscopy and DSC.

The onset of transition from the smectic A phase to the more organised smectic B phase was observed at 175.4 °C by microscopy, yet this is not fully supported by DSC evidence because there is a large difference between the transition temperatures from DSC and microscopy. However, better agreement on the first cooling's onset temperature agrees with the microscopy observations at 178.7 °C. DSC maxima for the second cooling at 157.9 °C and the second heating at 161.9 °C differ significantly, partially due to the broad nature of the peaks.

Lastly, crystallisation of the mixture was not clearly identified by microscopy, with only a tentative result at 30.1 °C being indicated by a subtle change in texture. Further to this, there was no obvious transition visible in the cooling curves obtained by DSC. Conversely, the heating cycles exhibited a strong transition at 56.5 °C (first heat) and a weak transition at 54.0 °C (second heat), and with no enthalpies apparent in the same temperature range on cooling, indicates that these two transitions were associated with melting phenomena. Conversion from what could be a glassy state formed in cooling cycles was probably a slow kinetic process, hence the difference in enthalpies.

6.7.3.5: A 1:3 Mixture of Compound 22 : Hexafluorophosphate Salt

A 1:3 mixture of Compound **22** : hexafluorophosphate salt was prepared as previously described. The cyclic heating and cooling thermograms obtained by DSC for the mixture are shown together in Figure 6.36)

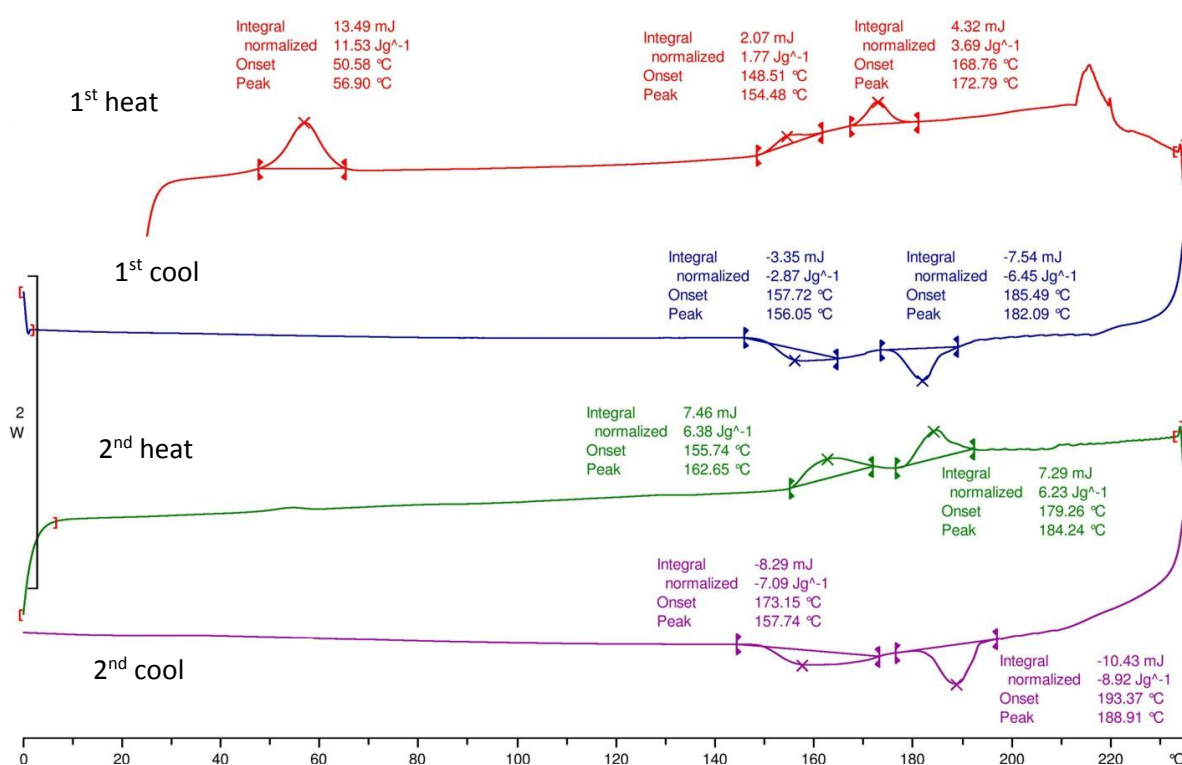


Figure 6.36: DSC thermogram of heat flow (mW^{-1}) as a function of temperature ($^{\circ}\text{C}$) for a 1:3 mixture of Compound **22** : hexafluorophosphate salt.

The heating and cooling cycles of the mixture showed significant discrepancies with respect to transition temperatures. For the first heating cycle there was clearly a change in the baseline at higher temperatures, and a thermal event occurring well above the clearing point of the mixture (approximately 220 °C). A relatively weak melting point was observed (onset 50.6 °C and maximum 56.9 °C) followed by a transition from one mesophase to another (onset 148.5 °C and peak maximum 154.5 °C), and a clearing point from the second mesophase to the liquid (onset 168.8 °C, peak maximum 172.8 °C). The change in baseline and broadness of the peaks demonstrated by the difference between the onset and peak maximum temperatures indicates that there is substantial movement in the pan loading, potential decomposition or thermal polymerization, or kinetic process involved in the phase transitions. However, although the phase transitions may be deemed to be inaccurate and therefore should not be considered, the point is that the melting point is the melting point of the solid isolated from the preparative process and not from the melt which occurs for the first cyclization DSC process.

The transition to the high temperature mesophase from the liquid was first observed at 194.1 °C by microscopy. The mesophase was identified from its defect textures as smectic A. This transition was also observed at an onset of 193.4 °C (peak maximum of 188.9 °C) on the second cooling, but at 185.5 °C (onset, maximum at 182.1 °C) on the first cooling which could be related to the behaviours described above. However, observation by microscopy also shows temperatures near to the clearing point the mesophase formed slowly *via* the formation of small focal-conic defects. Further cooling resulted in the formation of a defect pattern composed mostly of small focal-conic domains plus areas of homeotropic texture (Figure 6.37 left). These results confirm the identity of the mesophase as smectic A. A transition to the smectic B phase was found at 174.1 °C by microscopy with the same transition observed *via* DSC at 173.2 °C. The texture presented in Figure 6.37 (right) was captured at 100 °C showing only a small difference from the bulk texture of the smectic A phase (Figure 6.37 left) at 185 °C. However, on closer inspection, it is worth noting that the cross defects associated with hyperbolic and elliptical lines of discontinuity are no longer clearly visible. However, the presence of a homeotropic texture indicates the presence of a smectic B phase.

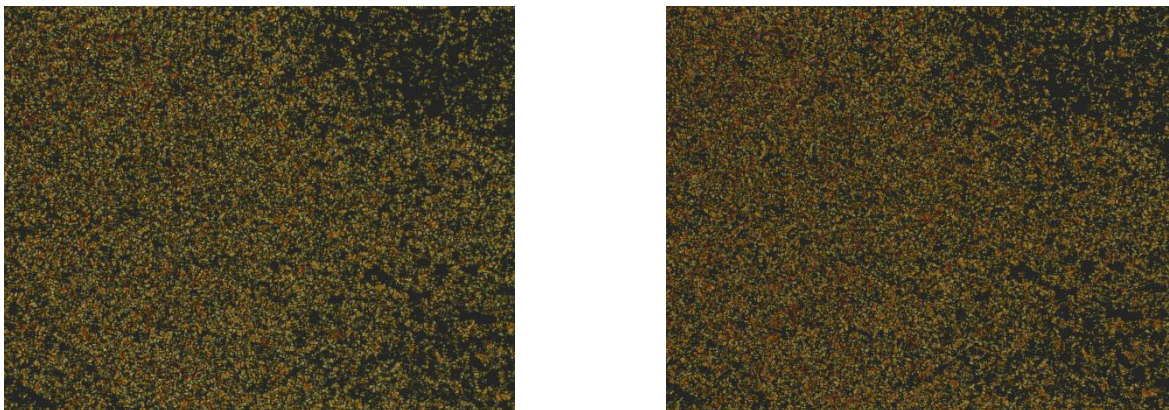


Figure 6.37: Photomicrographs showing the smectic A texture of the 1:3 mixture of Compound **22** and its hexafluorophosphate salt at 180 °C (left) and the smectic B phase at 100 °C (right) (x100 optical zoom).

The Smectic B phase is approached at 174.1 °C, as seen through microscopy, with the same transition observed *via* DSC at 157.4 °C. The texture presented in figure y was captured at 100 °C, showing only a small difference from the bulk texture of the presented Smectic A phase at 185 °C. However, on closer inspection, it is worth noting that the cross defects are no longer visible.

6.7.3.6: Impact of the Addition of the Hexafluorophosphate Salt

Having explored the individual results for the individual mixtures of Compound **22** with its hexafluorophosphate salts, as well as the overall trends for the acrylate and chloride mixtures, it is therefore important to consider any trends that arise from the hexafluorophosphate mixtures as a series. Thus, the transition temperatures were plotted against the percentage composition in relation to the proportion of the hexafluorophosphate salt, as shown in Figure 6.38.

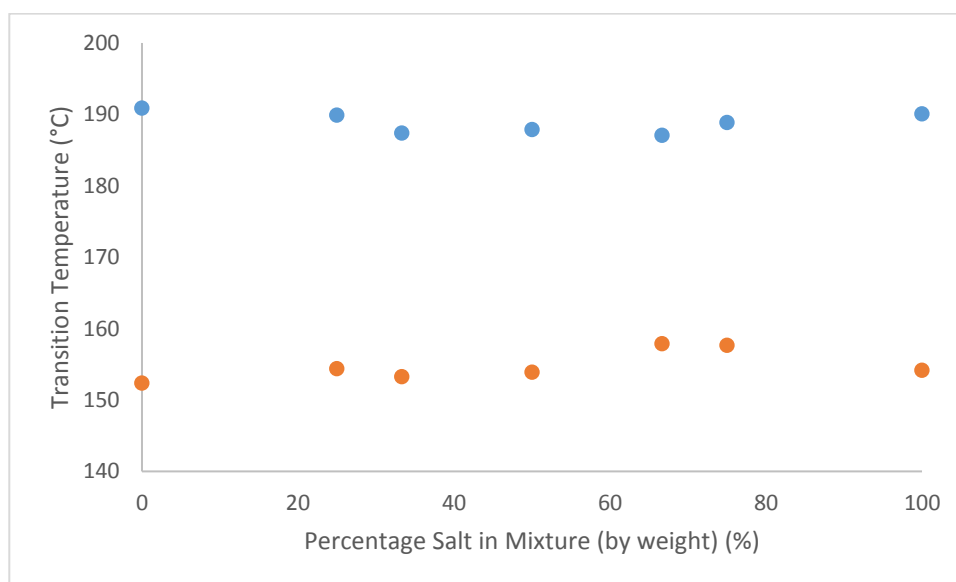


Figure 6.38: Transition temperatures (●- clearing point, ●-smectic A to smectic B) as a function of concentration (wt %) of the hexafluorophosphate salt of Compound **22** with the parent Compound **22**.

The trend presented is similar to that observed from the chloride salt analogue previously reported in Figure 6.16. However, for this example temperature range for the smectic A to smectic B

transition is larger for the 0 % and 100 % compositions in comparison with the mixtures. Additionally, it is clear that there is a decrease in the clearing temperatures towards the 40 % salt composition point.

Contrary to the data presented in the chloride salt equivalent, there is a similar trend presented in both transitions under consideration, rather than a standard level behaviour previously investigated. In this example, the discrepancy between the clearing point and the smectic A to smectic B transition remains consistent for each sample rather than narrowing.

6.8: Overall Observations from the Impact of Salt Introduction

The introduction of 'salts' into mixtures with the parent compounds has a marked effect on the biphenyl compounds, with a suppression and elimination of liquid-crystalline properties when compared with the parents. The parent amine compounds displayed Smectic A phases in the region of 40 °C, yet when acidified to give the quaternary diallylammonium salts it was noted that the phase was eradicated, with only a crystal state being present. In many cases, the transition to the crystal was also suppressed to lower temperatures than the original parent Compounds **16** and **17**.

When the undecamethylene spacer in the terphenyl-terminated Compound **22** was considered, it was found that the introduction of salt characteristics through use of the chloride, acrylate and hexafluorophosphate anion lead to small changes with respect to the determined transition temperatures. The difference between the responses from the biphenyl and terphenyl compounds was thought to be through the nature of the terminal group, with the increased size and electronic interactions of the terphenyl group outweighing the impact of the conversion of the amino-group to the quaternary salt, and for the terphenyl systems the increased aspect ratio caused by the addition of the extra phenyl ring.

Having observed the changes for the terphenyl Compound **22** when introducing salt characteristics, it was then decided to investigate mixtures of these compounds considering the variation of the salt content with a view to potential applications. Through these studies it was clear to see that a eutectic point would be reached in the region of 40% salt content for the chloride and hexafluorophosphate samples. The acrylate salt system was more difficult to investigate due to the autopolymerisation of the compound at higher temperatures which were necessary to investigate due to the high transition temperatures of both the parent compound as well as for the fully converted salt and all mixture compositions between.

Having investigated the nature of the salt mixtures of these compounds, it was then decided to investigate the polymerisations of these compounds by UV-DSC. The introduction of the quaternary ammonium salt functionality would, in theory, allow for rapid polymerisations considering the work previously conducted by Butler.^{20,50,51}

7: UV-Polymerization Studies

7.1: Photoinitiator Studies

One of the most important aspects of the photopolymerization process is the identity of the initiator used within the monomer mixture. It is important to have a different value for λ_{max} of the initiator to the monomer. This means that each initiator will have different compatibility with the different monomers due to the overlaps in absorption seen in the UV-Vis spectra. If there is significant overlap between initiator and monomer, there will be a reduced rate of radicalisation of the initiator, and therefore a reduced rate of polymerisation.

Selection of the initiator must also take into account the output of the UV lamp to be used. Generally, wide spectrum lamps will be able to cause the homolytic cleavage of most UV-radicalised initiators, but there is likely a variation in the intensity across the range of wavelengths output. Though it is possible to change the lamp, operating costs and safety have to be considered when used in any environment, with costs being especially important in an industrial setting. The relative low costs of UV-polymerization in the formation of films is one of the key factors that makes this an attractive option for this project.

Other issues that need to be considered in the selection of an initiator would include the structural impacts on the polymer formed. Using a small quantity of initiator will lead to a lesser extent the impurity incorporated into the synthesised polymer, and so the effects will be relatively minor. Use of smaller quantities of initiator, however, leads to lower rates of polymerization as there are fewer polymer chains initiated, so in order to establish a rapid polymerization, an appreciable proportion of the initiator should be used. This leads to a fine balancing act between the amount of photoinitiator and rate of polymerisation, the degree of polymerization and the overall conversion.

7.1.1: Initial Polymerization Studies

Compounds **1**, **2** and **3** were synthesised for the comparison of the terminal groups that could be used in the synthesis of monomers for film synthesis.

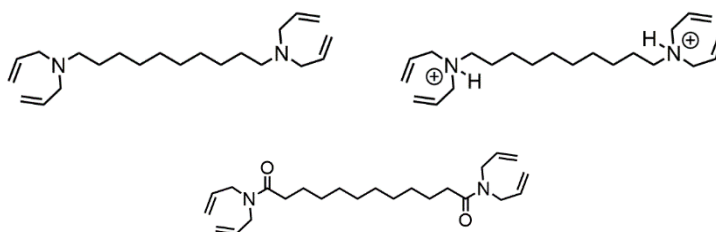


Figure 7.1: Structures of Compound **1** (top left), Compound **2** (top right) and Compound **3** (bottom).

Hall et. al.⁵³ have previously shown that electronic effects within the diallyl terminated end of the molecule has a strong influence on the ability of the functional group to polymerise. Diallylamine

compounds *cf.* Compound **1** donate electrons from the nitrogen atom and polymerise slowly whereas the diallylamines (Compound **3**) exert an electron withdrawing effect thus enhancing the degree and rate of polymerisation. The diallylamine salts (Compound **2**) exerted a greater electron withdrawing effect than the amides and were able to polymerise efficiently and at a faster rate than the amides. These simple compounds polymerise in a more complex fashion compared to mono-functionalised equivalents due to the potential for network growth. The formation of a network is due to the possible reaction at both ends of the molecule, which may react into different backbones, causing a greater order in the system through cross-linking of the polymer chains together. The rate of polymerisation will also be affected by the multiple polymerisable units, partly due to there being more reactive groups to react with, but also because when one unit has polymerised, it holds the molecules closer together and allows for more rapid polymerisation at the other end of the molecule by locating the units closer together.

In order to compare directly to the work of Hall et. al.⁵³ the polymerisation of Compounds **1**, **2** and **3** using 1 wt % photoinitiator (Irgacure 184) between microscope slides under a solarium lamp was conducted. At 20 min intervals, the slides were assessed for freedom of movement or displacement. If no movement was readily possible across the two slides, it suggested that the polymerization process had been completed. Observations of the compounds was purely qualitative.

After the initial 20 min exposure, the slides treated with Compound **2** were very rigidly held and showed virtually no movement. After an hour, the slides treated with Compound **3** were found to be rigidly held, whereas the slides treated with Compound **1** required in excess of two hours, (seen after the 7th inspection). In all cases, it was noted that the polymer formed between the slides had developed a significantly yellow colouration having previously been a clear, colourless solution, suggesting some UV photo-decomposition may have occurred (Figure 7.2).



Figure 7.2: Slide showing the discolouration of photopolymerised Compound **2**.

Following on from this rudimentary study, Compound **2** was studied further using UV-DSC polymerization to obtain a quantitative analysis. Compound **2** was mixed with varying quantities (2, 4, 6 and 8 wt %) of two significantly different photoinitiators, Irgacures 184 and 369. The structures of Irgacures 184 and 369 are presented in Figure 7.3. The samples were dissolved in

DCM to enable thorough mixing before the solvent was removed under reduced pressure at ambient temperature. After the mixtures were thoroughly dried, they were then analysed by UV-DSC to observe the rate of the reaction involved. The target mass polymerised was 10 mg.

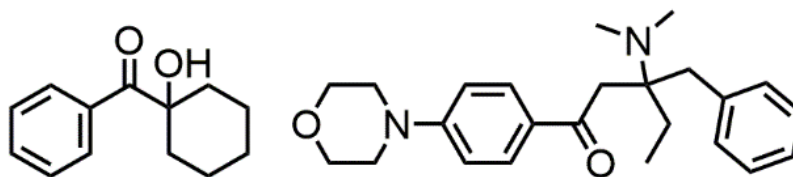


Figure 7.3: Structures of Irgacure 184 (left) and Irgacure 369 (right).

Analysis of the UV-DSC traces observed allows for conclusions to be made for the rate and extent of reaction, as well as the profile. It is therefore possible to compare and contrast the influences of the initiator on the overall system in the polymerisation process. A typical example is given in Figure 7.4 for the polymerisation of Compound 2.

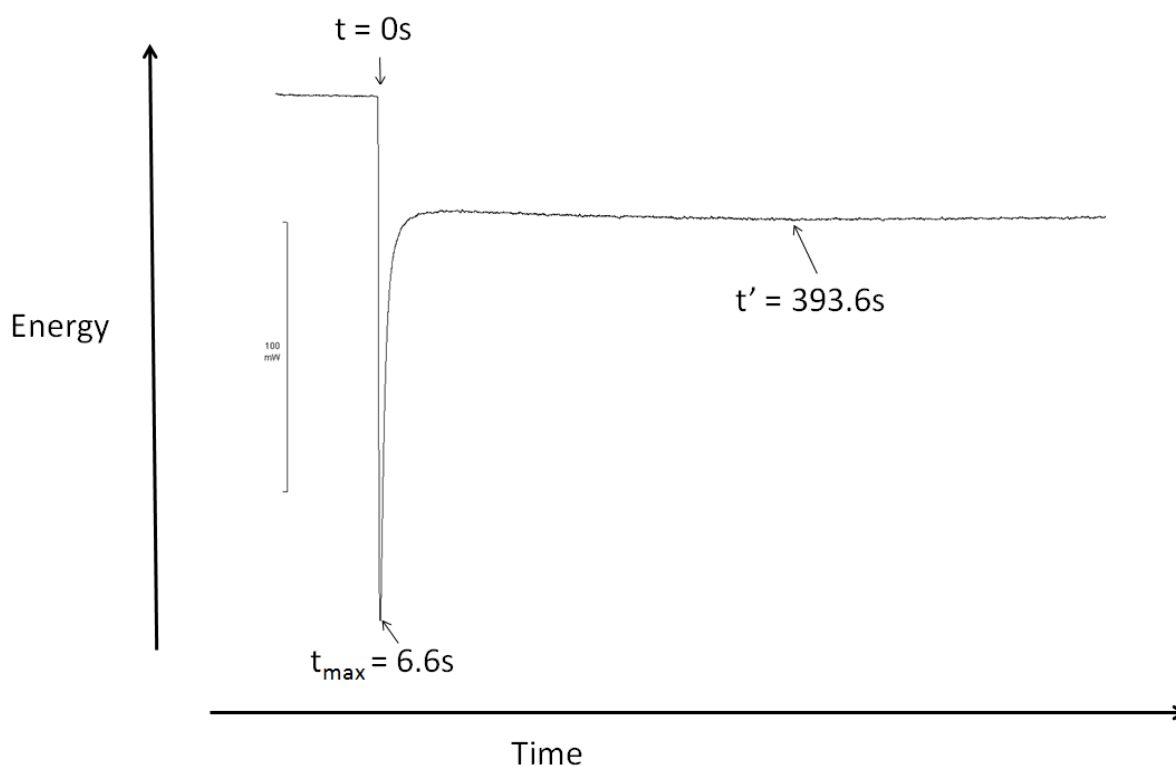


Figure 7.4: UV-DSC trace for the photopolymerisation of Compound 2 using 6 wt % Irgacure 184.

In Figure 7.4 the UV lamp is turned on at $t = 0\text{ s}$ and reaches a maximum initiation at t_{max}^{72} (6.6 s). The reaction has completed by t' (393.6s) where the gradient is zero. There is a slight negative gradient after this point as the polymer begins to experience the 'yellowing' common from ultraviolet exposure. The point where the reaction is started (where $t = 0\text{ s}$) comes after the initiation of the probe.

The polymerisation is carried out with a positive nitrogen gas flow to remove oxygen from the reaction, as oxygen radicals can cause premature termination of the polymerization. The discrepancy between the energy recorded at $t = 0$ s and t' is due to the influence of the UV light source. When the light is turned off, the line returns to the level experienced at $t = 0$ s. The light was left on for prolonged durations to investigate the overall profile of the reaction.

Irgacure Identity	Wt% Irgacure	Enthalpy (J/g)	H_{\max} (mJ)	T_{\max} (s)	t' (s)
184	2	-308.3	-150.49	7.8	453.0
184	4	-507.8	-225.26	4.8	486.0
184	6	-404.6	-224.62	6.6	393.6
184	8	-390.7	-226.54	5.4	292.8
369	2	-599.3	-262.27	6.0	1323
369	4	-479.5	-64.47	6.0	1041
369	6	-258.5	-96.41	4.2	544.2
369	8	-184.7	-74.53	6.0	465.1

Table 7.1: Kinetic analysis of the polymerization of Compound **2** in relation to the identity and concentration of photoinitiator used.

As seen in Table 7.1, the rates of reaction were generally rapid, with t' (the time taken to reach a plateau in the profile of the reaction, suggesting maximum completion) taking a few minutes, and differing between the initiators. T_{\max} signifies the initiation time for the samples, which remained fairly consistent throughout. The initiation time is how long it takes for the rate of polymerization to be greater than the rate of homolytic cleavage of the initiator. This suggests how long it takes for the majority of the initiator to radicalise and promote the growth of polymer chains or networks.

From these studies, it was seen that the different initiators have different impacts on the reaction profile of Compound **2** as a 'blank' standard. Irgacure 184 leads to a faster overall rate of reaction when compared to Irgacure 369, largely due to the nature of the lamp involved. Irgacure 184 has a greater absorbance in the regions of 220 nm to 280 nm, as opposed to Irgacure 369, which absorbs more strongly at longer wavelengths of 325 nm. The lamp outputs UV-irradiation in the range of 200-400 nm, meaning that both will be irradiated at their peak absorbances, yet the relative intensities of the output light at different wavelengths is unknown due to the broad spectrum nature of the lamp. Each of the potential photoinitiators and their relative UV absorbancies are discussed in Section 7.1.2.

The quantity of the initiator used had surprisingly little impact on the rate of photoinitiation but there was a small decrease in the overall time for the polymerisation to progress to completion. Different quantities of initiator should have different advantages and disadvantages when used. A

higher quantity of photoinitiator will lead to a polymer comprised of many short chains due to the high number of initiations but there will also be a larger quantity of residual photoinitiator fragments in the final polymer. Smaller quantities of photoinitiator give rise to longer overall reaction times, where longer polymer chains are formed. There is a compromise between rate of polymerisation and how much residual photoinitiator remains in the polymer. For this reason, a concentration of 4 wt % would be an almost ideal concentration as it allows for a reasonably low concentration of residual photoinitiator while giving reasonable polymerisation times.

7.1.2: Initiator compatibility

In order to polymerize the liquid-crystalline monomer systems pertinent to this thesis, the initiator must be able to photolyse. If the monomer has a similar λ_{\max} to the photoinitiator then there will be a conflict between the absorption of photons. Using a relatively low concentration of photoinitiator means that there is a strong possibility that the photoinitiator will not be activated by UV irradiation due to absorption by the monomers at the same wavelengths required for photolysis to occur. Additionally, when the photons are absorbed by the monomer, the energy is re-radiated at different wavelengths, which will, in most cases, be of a significantly lower energy required to affect the initiators. A typical example of this is the emission of heat, which is readily dissipated to the surroundings.

The monomers investigated in this thesis contain aromatic groups which exhibit a greater absorbance of UV compared to Compounds **1** to **3**. The presence of a cyanoterphenyl motif for Compounds **19** to **23** will induce a significant value for the molar absorption coefficient, which makes an appropriate choice of the initiator even more of an important issue. In order allow for more correct identification of initiators which may be used, it is important to obtain an absorbance spectrum.

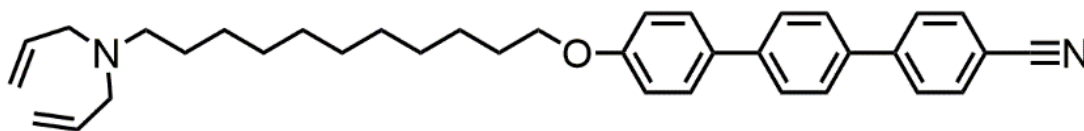


Figure 7.5: Structure of Compound 22.

Compound **22** (Figure 7.5) was selected for these studies particularly due to the number of different mesophases observed allowing an investigation at many different temperatures. This compound has significant absorbances at 286 nm and 228 nm in particular, but generally absorbs across a wide range below 300nm (Figure 7.6). This would suggest that a desirable initiator would need to have stronger absorbances at wavelengths greater than 300 nm. For this reason a range of photoinitiators were examined by UV-Vis spectroscopy.

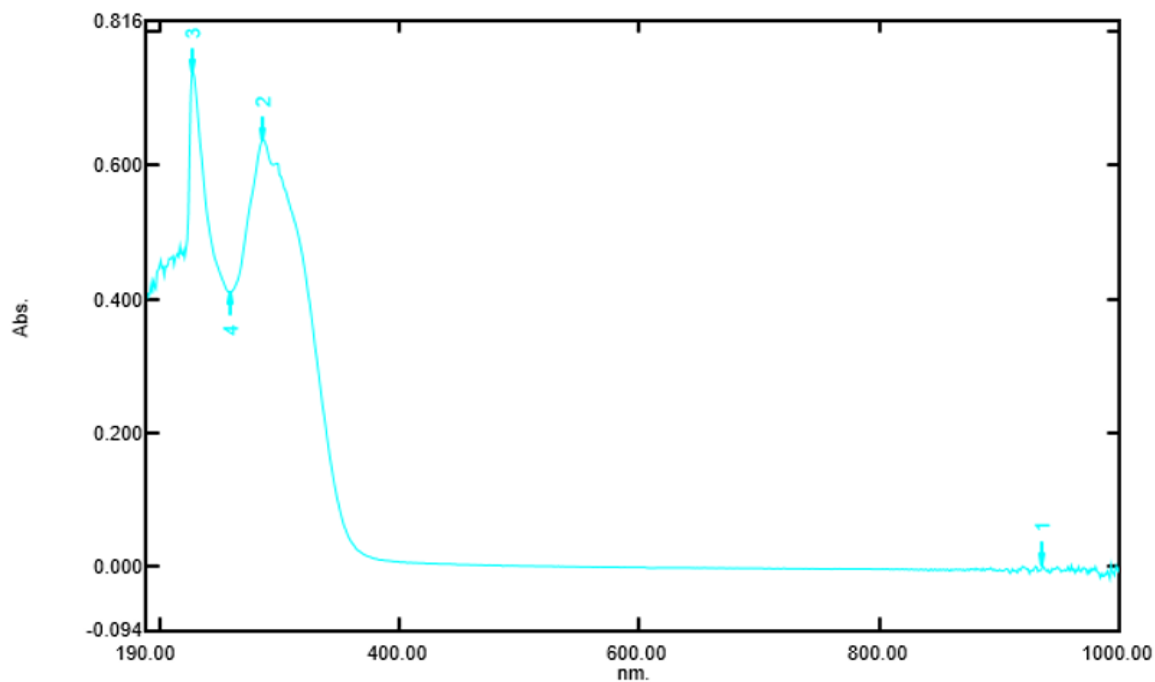


Figure 7.6: UV-Vis absorption spectrum of Compound **22**.

7.1.2.1: UV-Analysis of Irgacure 184

The UV-vis spectrum of Irgacure 184 (Figure 7.7) reveals significant absorbances between 245 nm and 222 nm, with very little at longer wavelengths. Although Irgacure 184 proved to be effective in the polymerisation of Compound **2**, the degree of absorption it exhibits at the shorter wavelengths coincides with those observed in Compound **22**. This means that there will be significant overlap between the monomer and photoinitiator, and thus significant conflict.

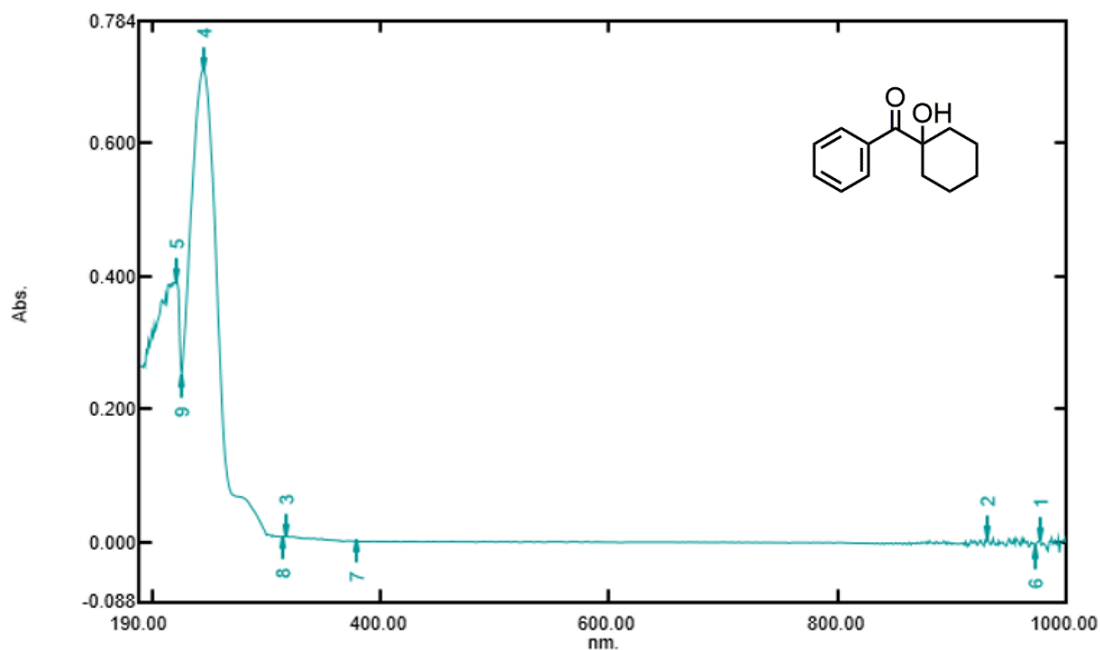


Figure 7.7: UV-Vis absorption spectrum and structure of Irgacure 184.

7.1.3.2: UV-Analysis of Irgacure 369

Irgacure 369 was used in the polymerisation of Compound **2** and had been shown to initiate the polymerisation albeit at a slower rate than Irgacure 184, UV-Vis absorption of Irgacure 369 has two main absorptions at 320 nm and 234 nm, see Figure 7.8. Although there is overlap between the photoinitiator and monomer at 234 nm, the presence of significant absorption at 320 nm suggests that Irgacure 369 is potentially a good candidate for use in the polymerization of Compound **22**.

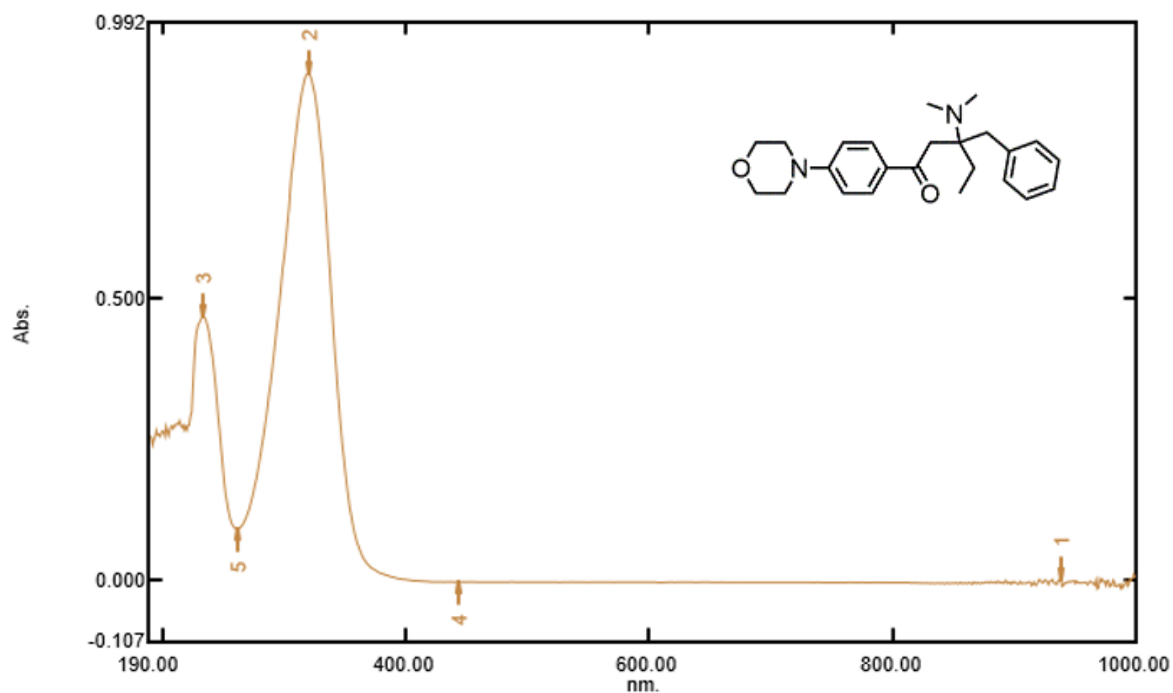


Figure 7.8: UV-Vis absorption spectrum and structure of Irgacure 369.

7.1.3.3: UV-Analysis of Irgacure 651

Another alternative considered was Irgacure 651. The UV-Vis absorption spectrum for this showed strong absorbances at 251 nm and 220 nm (see Figure 7.9), which again conflict with the λ_{max} of Compound **22**. Unlike Irgacure 369, this initiator lacks the longer wavelength absorbance and hence it is not a viable option for use as the chosen photoinitiator.

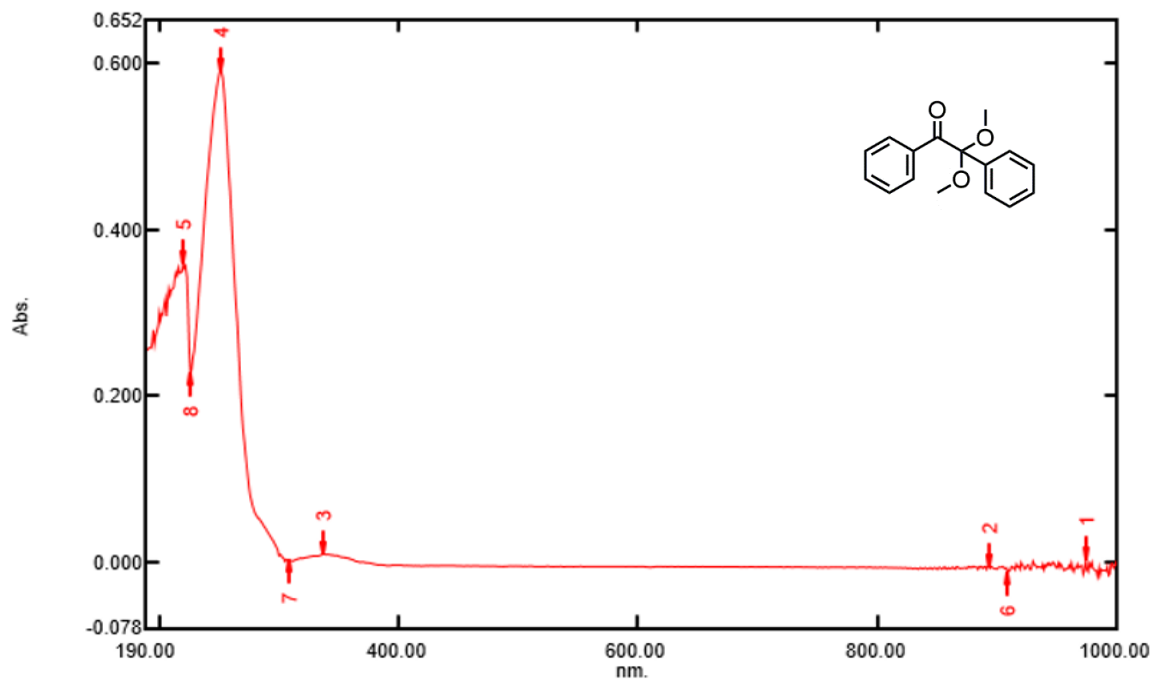


Figure 7.9: UV-Vis absorption spectrum and structure of Irgacure 651.

7.1.3.4: UV-Analysis of Irgacure 819

Despite absorption for Irgacure 819 at 369 nm the major absorption occurs at 294 nm and 234 nm (see Figure 7.10). This indicates that there would be too great a degree of overlap with the absorption in Compound **22** for this to be a particularly successful initiator.

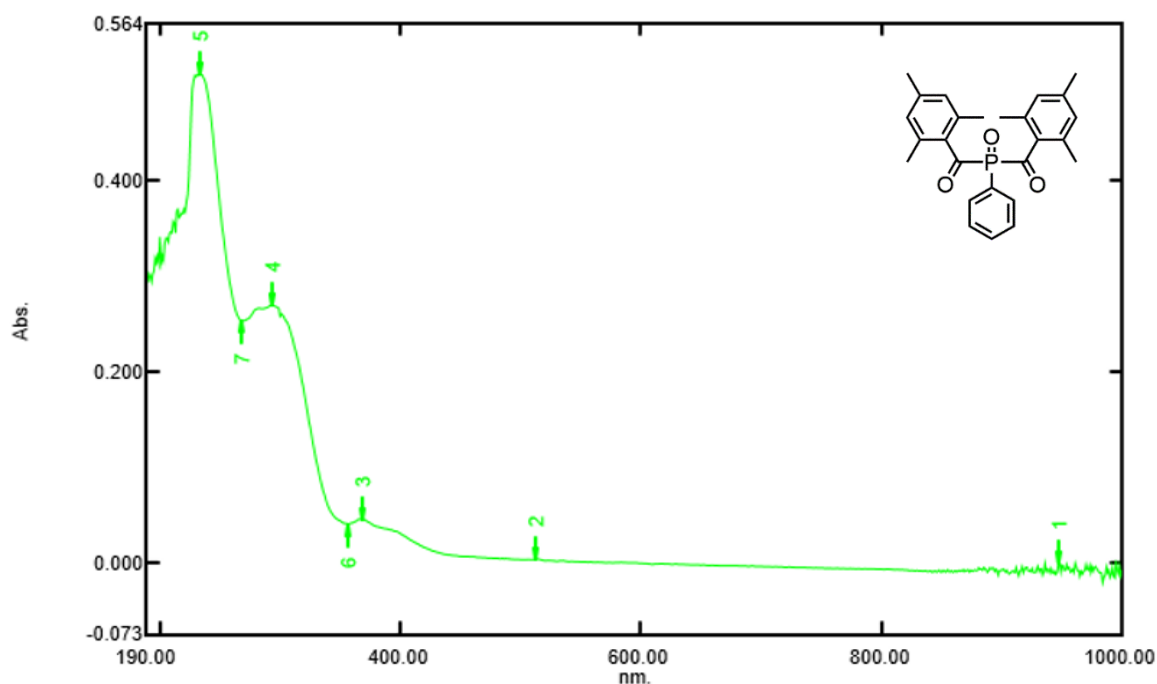


Figure 7.10: UV-Vis absorption spectrum and structure of Irgacure 819.

7.1.3.5: UV-Analysis of Irgacure 907

Another initiator considered was Irgacure 907. This photoinitiator shows a strong absorbance at 306 nm, which is encouraging, with a weaker absorbance at 232 nm (see Figure 7.11). The peak at

306 nm does not coincide with the λ_{max} of Compound **22**, however, it still resides within an area where there is a degree of overlap. For this reason, Irgacure 907 may not necessarily rapidly photolyse in the presence of the monomer which would limit its functionality.

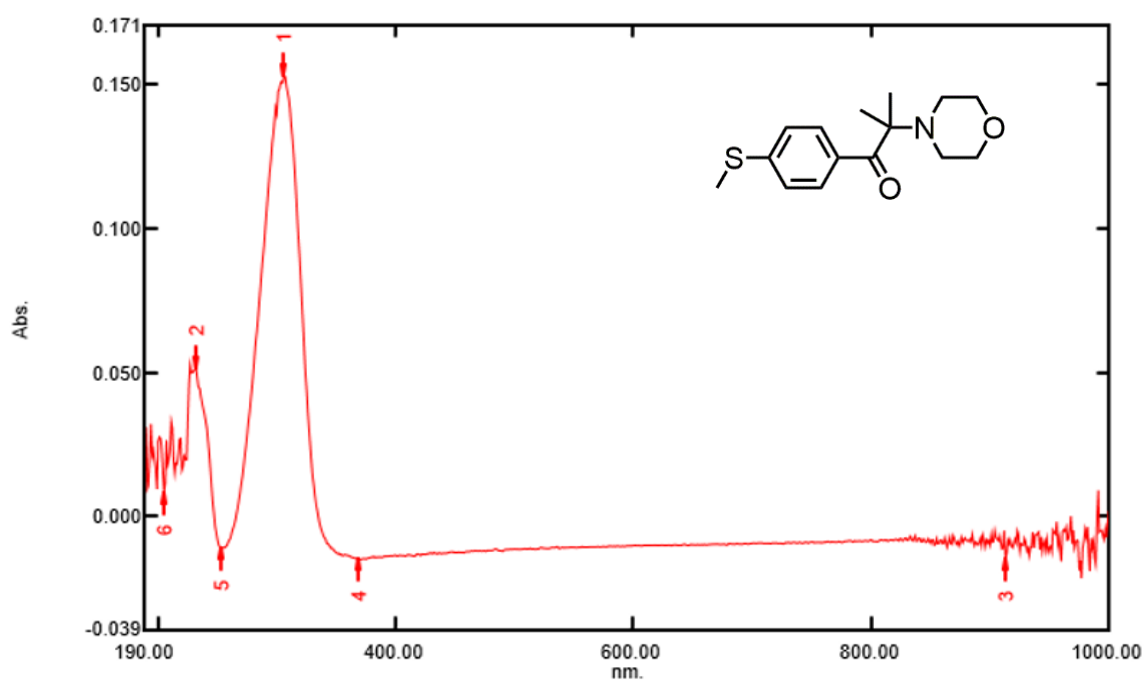


Figure 7.11: UV-Vis absorption spectrum and structure of Irgacure 907.

7.1.3.6: UV-Analysis of Irgacure 1700

The spectrum of Irgacure 1700 predominantly shows absorbance data in high energy, low wavelength regions of the UV-spectrum, thus coinciding with those of the monomer substrate. Significant overlaps will be present with the chief λ_{max} values seen at 281 nm, 245 nm and 219 nm, with these values being well within the absorbance regions of Compound **22**.

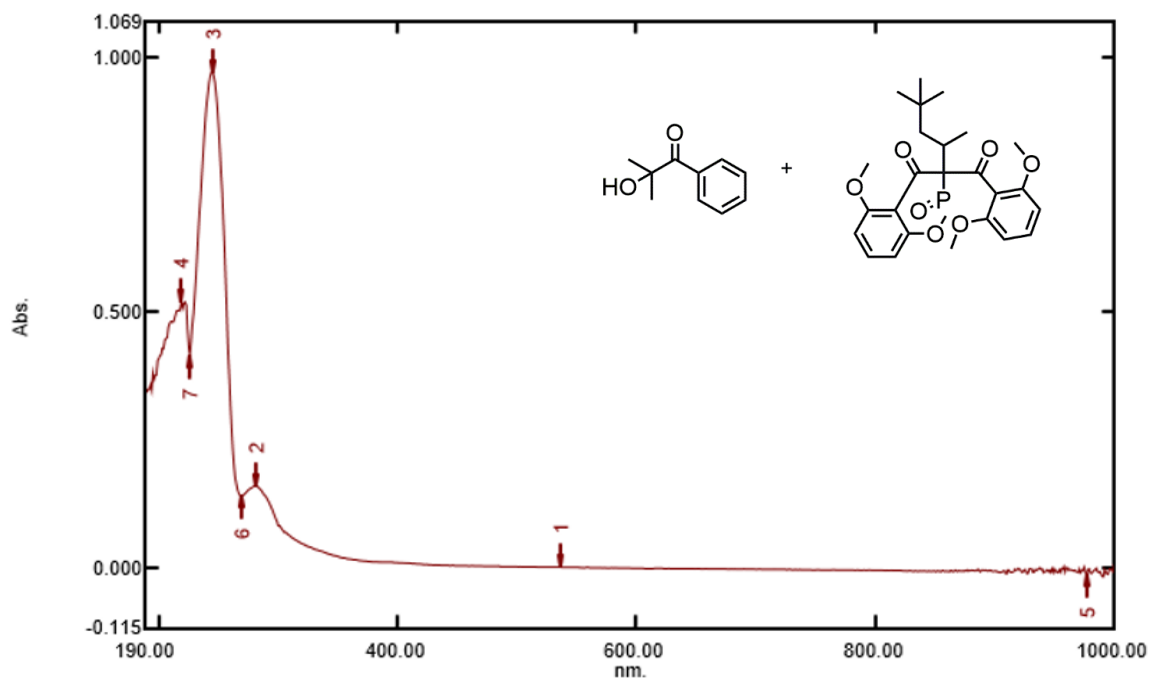


Figure 7.12: UV-Vis absorption spectrum and structure of Irgacure 1700.

7.1.3.7: UV-Analysis of Irgacure 1800

The only difference between Irgacure 1700 and Irgacure 1800 is the proportion of each component and it comes as no surprise that the UV absorption spectra are almost identical, see Figure 7.12 and Figure 7.13. For these reasons this photoinitiator is not considered suitable for the polymerisation of Compound **22**.

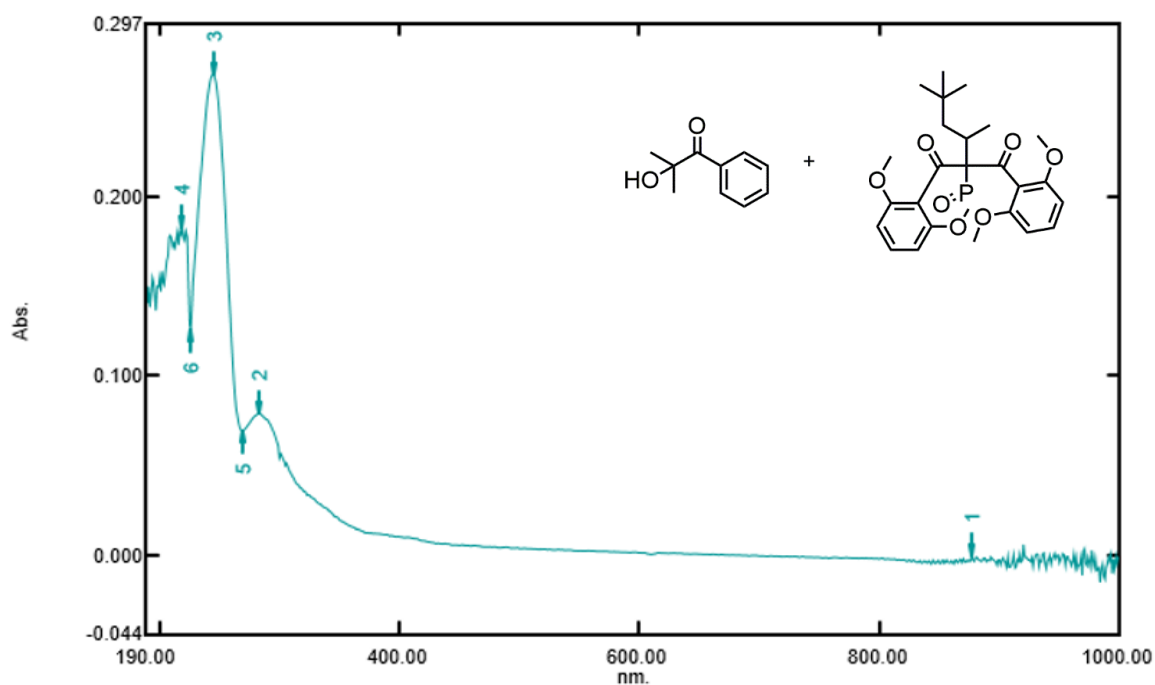


Figure 7.13: UV-Vis absorption spectrum and structure of Irgacure 1800.

7.1.3.8: UV-Analysis of Irgacure 2959

The final Irgacure examined, Irgacure 2959 features a very intense absorption at 275 nm, and a weaker absorption at 226 nm, see Figure 7.14. These overlap considerably with the absorbances shown for Compound **22** and hence this is also not a suitable candidate for photoinitiation.

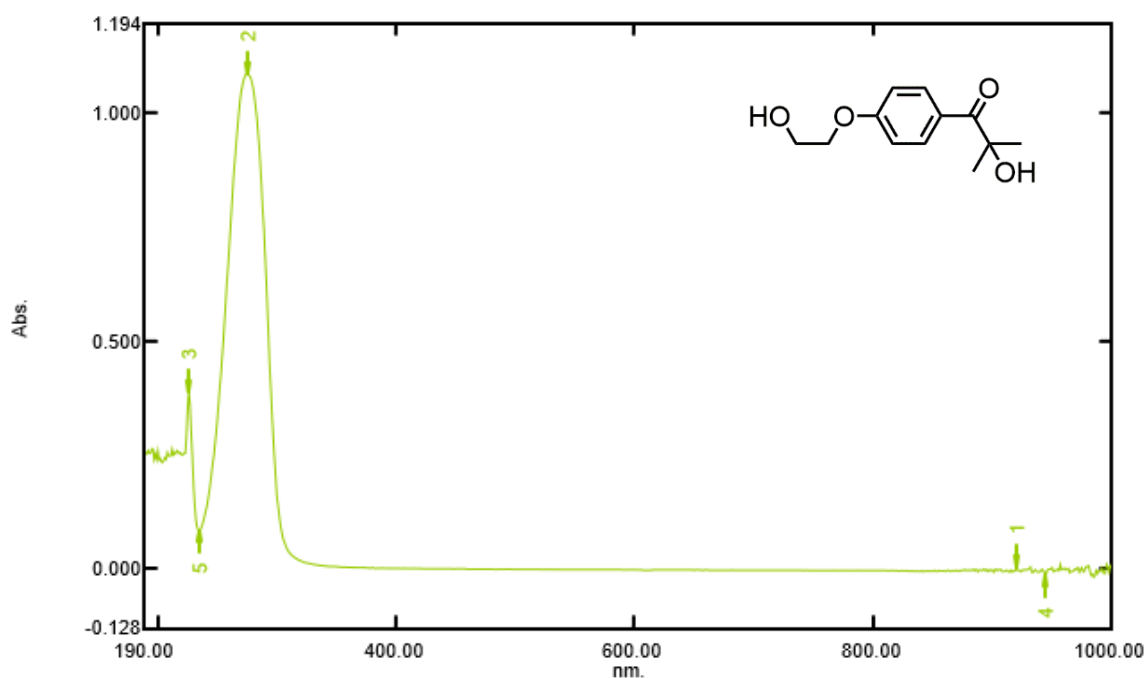


Figure 7.14: UV-Vis absorption spectrum and structure of Irgacure 2959.

7.1.3.9: UV-Analysis of Darocure 4265

Darocure initiators tend to have different purposes than those of the Irgacure families, and thus it would be expected that there would be significant differences in structure and UV absorption. However, the structure of the photoinitiator and the UV absorption are similar and there is significant overlap between UV absorption of the Darocure 4265 initiator (λ_{max} 241 nm, see Figure 7.15) and the monomer, Compound **22**. Again, this indicates that the effectiveness of Darocure 4265 would be minimal for this particular system.

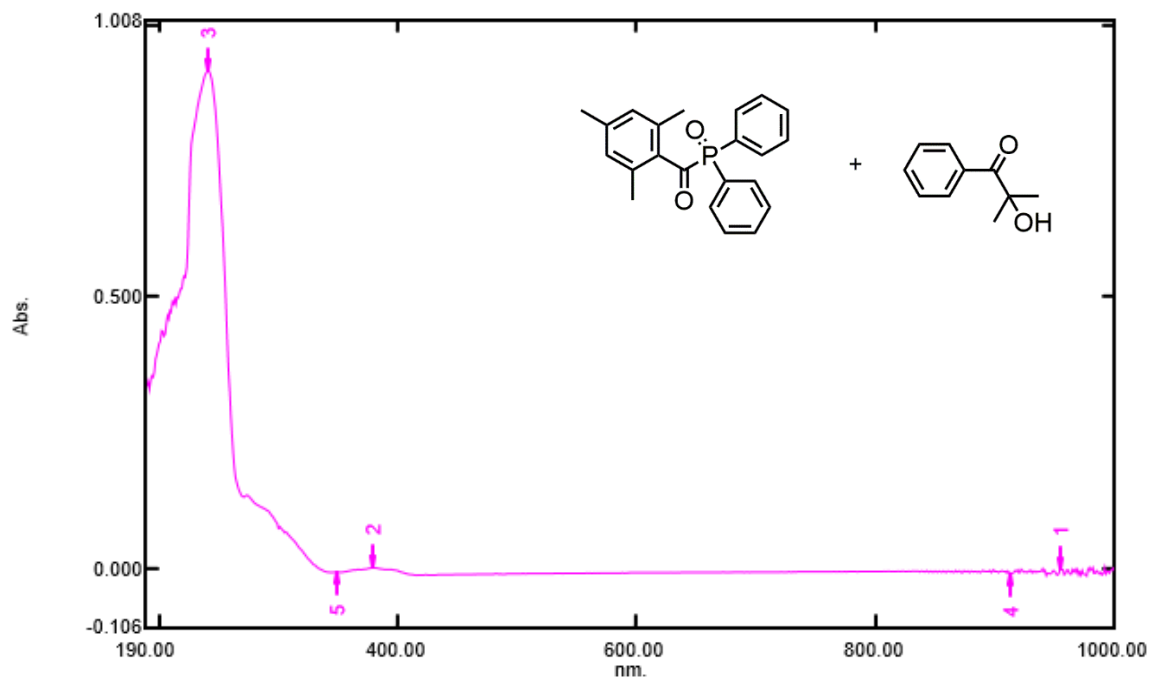


Figure 7.15: UV-Vis absorption spectrum and structure of Darocure 4265.

7.1.3.10: UV-Analysis of CGI1300

Another potential initiator that could be used is CGI1300. This particular initiator has a rather more complex UV-Vis spectrum, with three significant absorbances, see Figure 7.16. The most significant absorbance occurs at 320 nm which is outside of the absorbance of Compound **22**. Despite this absorbance at 320 nm it is not known if it has a significant role in photolysis.

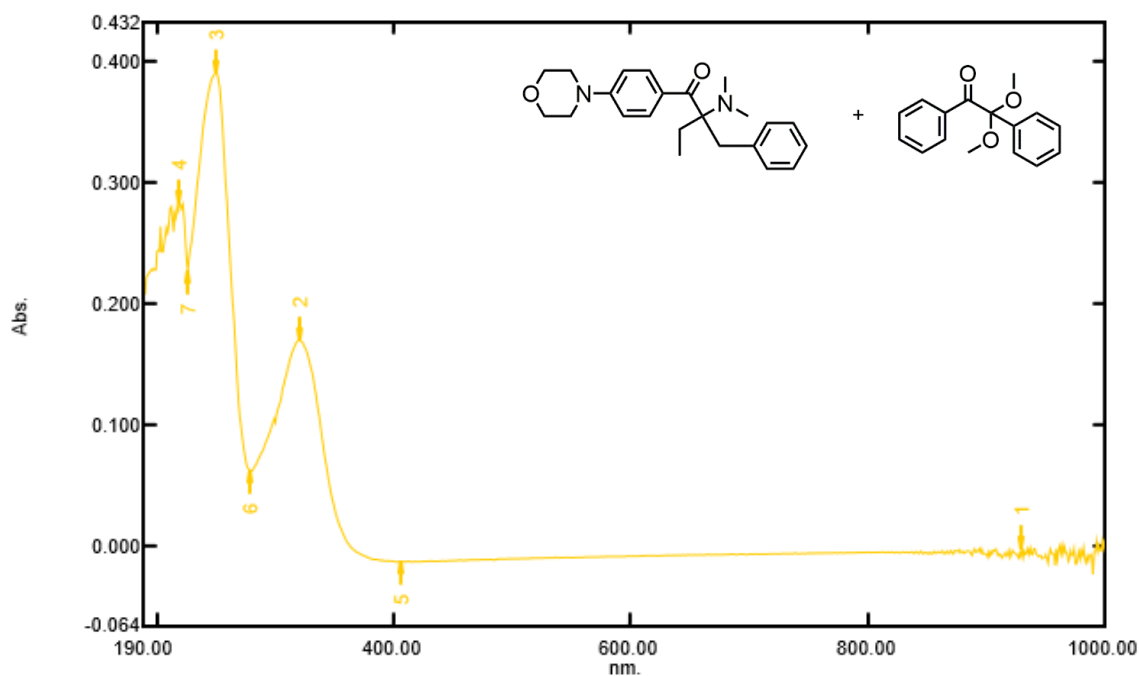


Figure 7.16: UV-Vis absorption spectrum and structure of CGI1300.

7.1.4: Selection of Initiator for Polymerisation of Monomers

Having examined each potential photoinitiator it can be concluded that those that possess absorptions which overlap with those exhibited by the monomer will be of reduced use. This is because they will not be able to undergo photolysis so readily due to a lack of penetration of photons at the appropriate wavelengths and energies.

Among the photoinitiators examined, CGI1300 and a handful of Irgacure initiators, namely 369 and to a lesser extent 819 and 907, possessed absorbances in the regions not obscured by Compound **22** i.e., above 300 nm. However, the nature of the peaks is not fully known in relation to the initiation process. The nature of the secondary peaks is thus of great importance almost as a tie-breaker scenario between these candidates.

From the natures of the primary peaks of interest, i.e. peaks of lower energies and wavelengths greater than those observed in the spectrum of compound **22**, the primary candidates for the initiator system are Irgacure 369 and CGI1300. Of these, the latter was preferred due to the lesser degree of overlap in the peaks observed at higher energies, where Irgacure 369 features a strong absorption at 234 nm, which is mired in the region of intense absorptions for compound **22**. This is in contrast with the 250 nm peak observed for CGI1300, which more closely aligns with the minimum observed, shown in Figure 7.17.

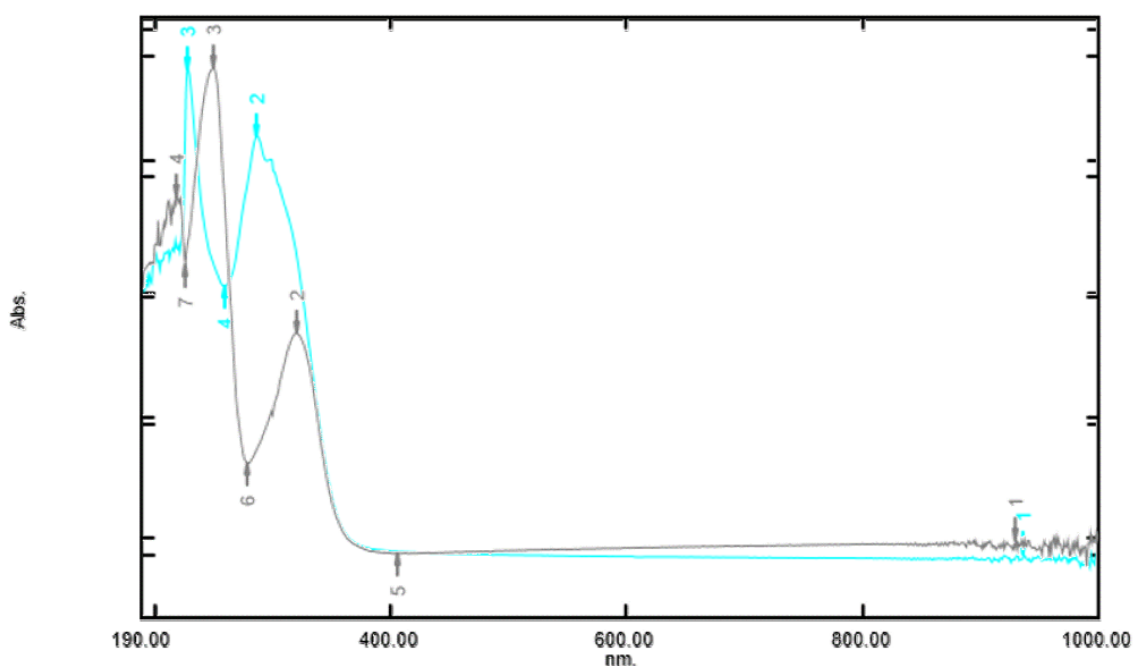


Figure 7.17: UV-Vis absorption spectra of CGI1300 (brown) and Compound **22** (blue).

7.2: UV-Polymerisation Analysis

For subsequent polymerisation studies, it was decided that 5 wt % (allowing a balance between the rapid initiation of 8 % and the longer polymer chains afforded by 2 %) of CGI1300 would be

used to investigate polymerisation of the chloride salt of Compound **22** in each of its different phases, E and SmA, including the isotropic liquid state.

Carrying out the polymerisation too close to a phase transition could result in the polymerisation taking place in different phases resulting in mixed domains within the system, for example part of the sample being organised in a smectic A phase and the rest in a disorganised liquid state as a result of localised heating. Since the nature of the local structures within the phases could affect the rate of polymerisation the closest point chosen, in terms of temperature, was decided to be ± 5 °C. These limits allowed for multiple measurements to be made for polymerizations in each of the liquid crystal phases.

Analysis at different temperatures should have the obvious effect of increased rate of reaction due to increased energy within the system. However, the degree of organisation within a phase will also have a significant impact by holding reactive groups in close proximity to one another and in an organised way. This suggests that there may be a non-linear increase in the rate of polymerisation, or even a reduction at the boundaries of different phases, meaning that studies closer to phase transitions would be important such that the temperature change doesn't mask the phase change in terms of the effects seen.

One potential problem to be considered is that of the high temperatures used for the studies. Compound **22** possesses very high transition temperatures with a clearing point close to 200 °C which may result in thermal degradation of the sample if it is exposed to temperatures that are too high for too long. Furthermore, this may be exacerbated by the presence of UV-irradiation. Despite this potential issue the terphenyl compounds **19** to **23** are still preferable to the biphenyl compounds **14** to **18** as they retain mesophase behaviour when converted to their quaternary ammonium salts, which is vitally important for investigating the impact of phase structure on the rate of polymerisation.

For each polymerisation, the UV lamp in the UV-DSC instrument was set to 80% intensity, and the sample was allowed to settle at the required temperature for two minutes before initiation of the reaction. At lower intensity the polymerisation proceeded at a much slower rate but UV photodegradation of the polymer occurred at higher intensities.

7.2.1: Initiator Test

Photoinitiator CGI1300 was initially tested on Compound **2** to ensure that it was activated by the lamp, as well as to determine a basic profile of the energetics of polymerisation. The photoinitiator was mixed at 5 wt % with Compound **22** a DCM. The solvent was removed under reduced pressure and then the polymerisation was conducted at 25 °C under a nitrogen atmosphere.

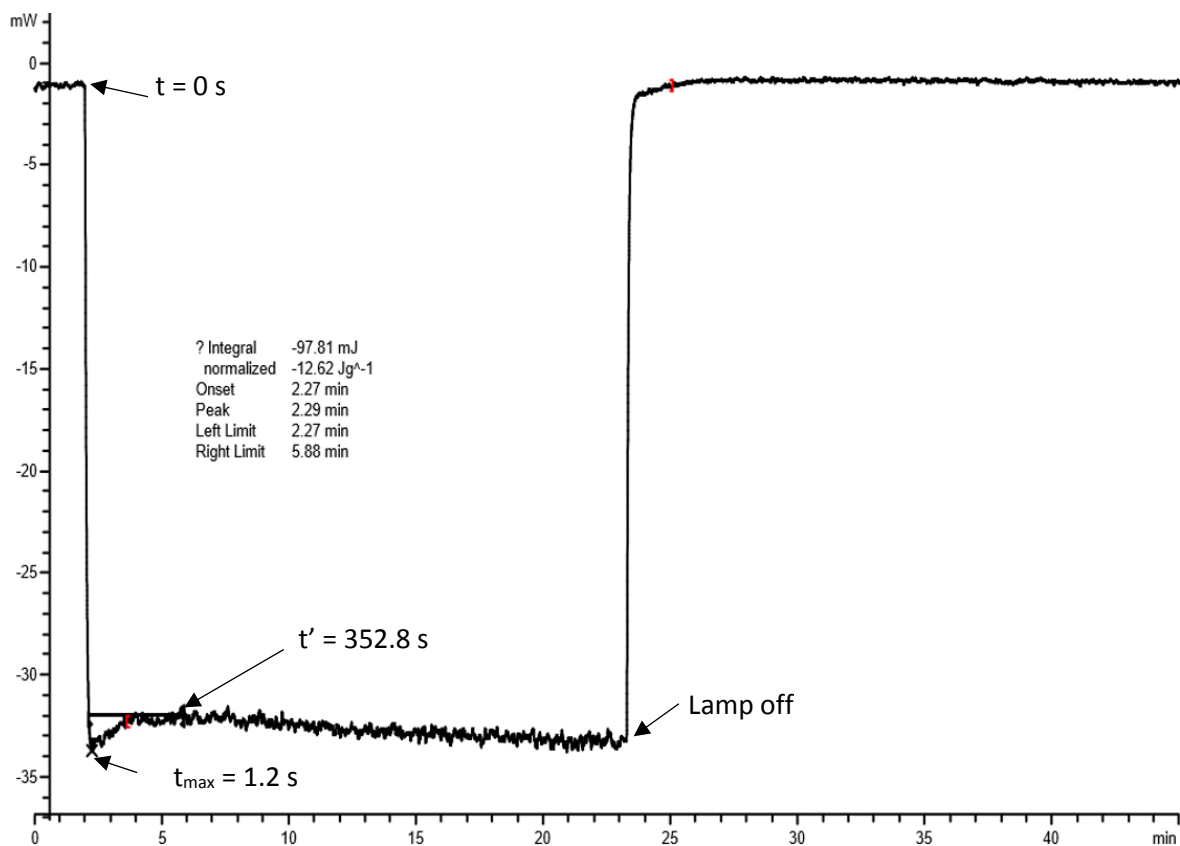


Figure 7.18: UV-DSC profile for the polymerisation of Compound **2** initiated by CGI1300.

The UV-DSC profile for the polymerisation is shown in Figure 7.18. The lamp was turned on after 136.2 s, with the minimum in the reaction profile reached by 137.4 s, ($t_{\max} = 1.2$ s). The reaction reached a stable baseline after 352.8 s. Subsequently, there was a slow downturn in the profile of the reaction due to partial degradation of the sample by UV-irradiation. After 24 min the lamp was turned off, and the profile returned to baseline levels.

These results show comparable behaviour to that of Irgacures 184 and 369 but with a faster initiation and comparable polymerisation times. One significant difference was the enthalpy associated with the reaction (only 12.62 J g^{-1}) compared to vastly larger values seen for both Irgacures 184 and 369. Despite this reduced enthalpy, it is evident that polymerisation occurred using CGI1300 because an insoluble product was produced.

7.2.1.1: Determination of Temperatures for Analysis

Based on the phase profiles of the chloride salt of Compound **22**, it was determined that polymerisation at two temperatures in each phase would be explored. The chloride salt exhibited transition temperatures at $190 \text{ }^{\circ}\text{C}$ (isotropic liquid to smectic A), $148 \text{ }^{\circ}\text{C}$ (smectic A to smectic B) and $35 \text{ }^{\circ}\text{C}$ (crystallisation).

For the isotropic liquid, it was decided that temperatures of $194 \text{ }^{\circ}\text{C}$ and $199 \text{ }^{\circ}\text{C}$ would be studied because higher temperatures lead to a significant risk of degradation of the samples.

Studies in the smectic A phase were made at temperatures of 169 °C and 174 °C, allowing for a gap of at least 5 °C either side of these temperatures from the phase transitions into either the isotropic liquid phase or the soft crystal phases below. These transitions were very broad, and so a significant buffer was allowed.

For the previously mentioned soft crystal phase, significantly lower temperatures were possible, so to reduce the possibility of decomposition these lower temperatures were used. A broader gap was also used in this study, with temperatures of 100 °C and 120 °C determined for the polymerization in order to observe a wider range of data.

7.2.1.2: Polymerization in the Isotropic Liquid

Studies were initially conducted in the isotropic liquid phase because it is the least ordered phase to be examined. Although the molecules are least ordered in the liquid phase they possess greater freedom of motion and greater free energy to promote reactions between the molecules. Due to these multiple factors it is not easy to predict the impact of temperature changes on the rate of polymerisation. Broer has previously observed that the nature of the mesophase has dramatic effects upon the rate. Indeed, Broer noted that the rates of polymerisation were found to be higher in the isotropic liquid phase than in the more ordered nematic and smectic phases, i.e. energetics outweighed the proximity of the polymerisable groups. This trend was reversed when the monomers contained more than one polymerisable moiety.

The initial test was conducted at 194 °C to determine if photodecomposition would occur just above the clearing point. If photodecomposition occurred and it was rapid, then measurements further into the liquid state would not be attempted.

The sample was mixed with 5 wt % of CGI1300 and exposed to UV-irradiation. The experiment was carried out over 15 min whereby the UV lamp was turned on after 2 min. The UV-DSC result is shown in Figure 7.19.

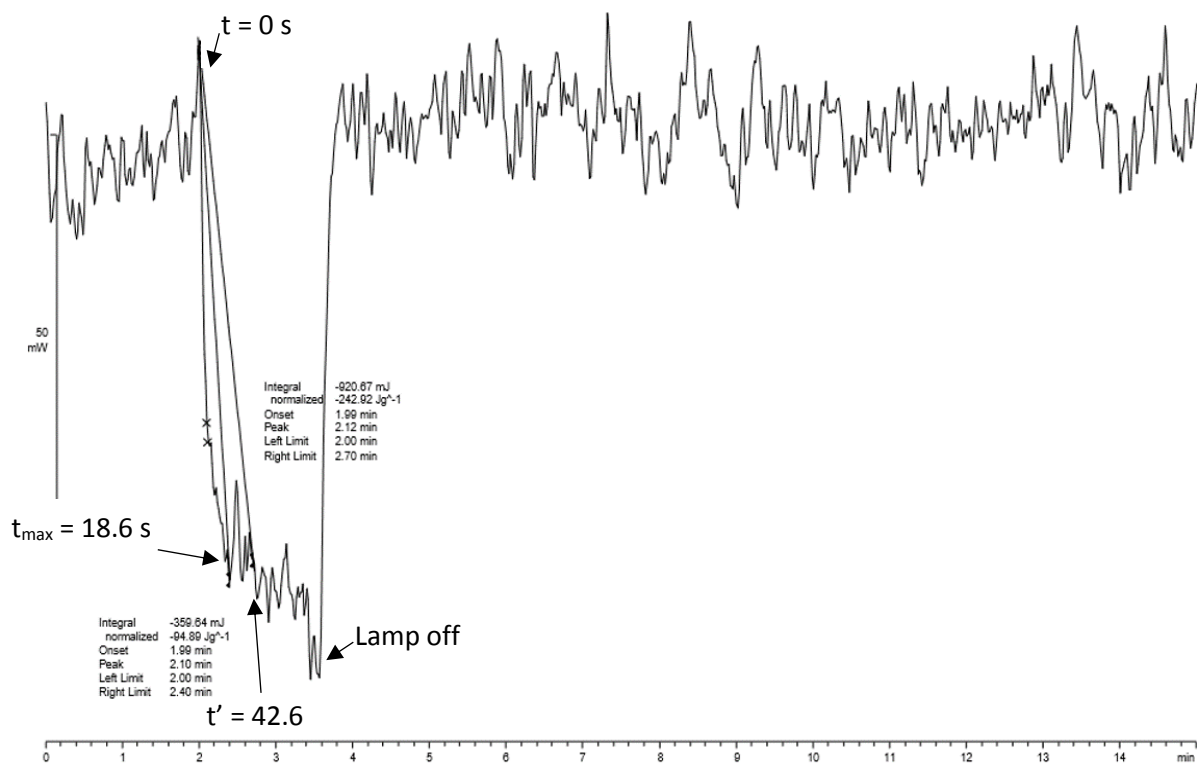


Figure 7.19: UV-DSC profile of the polymerisation of Compound **22** initiated by CGI1300 at 194 °C, isotropic liquid phase.

As can be seen in Figure 7.19, the initiation of the reaction was rapid ($t_{\text{max}} = 18.6 \text{ s}$), and the reaction profile was determined to be complete after approximately 42.6 s. After this time the profile of the reaction began to show a sustained downward progression, suggesting photodecomposition of the polymer. The UV lamp was switched off at this point and the polymer sample was removed from the instrument. On examination of the polymer it was found that significant yellowing of the sample had occurred which indicated a degree of photodecomposition.

Despite evidence of photodecomposition at 194 °C, it was deemed worthwhile examining the effects at slightly higher temperature. Figure 7.20 shows the UV-DSC result for the polymerization taking place at 199 °C.

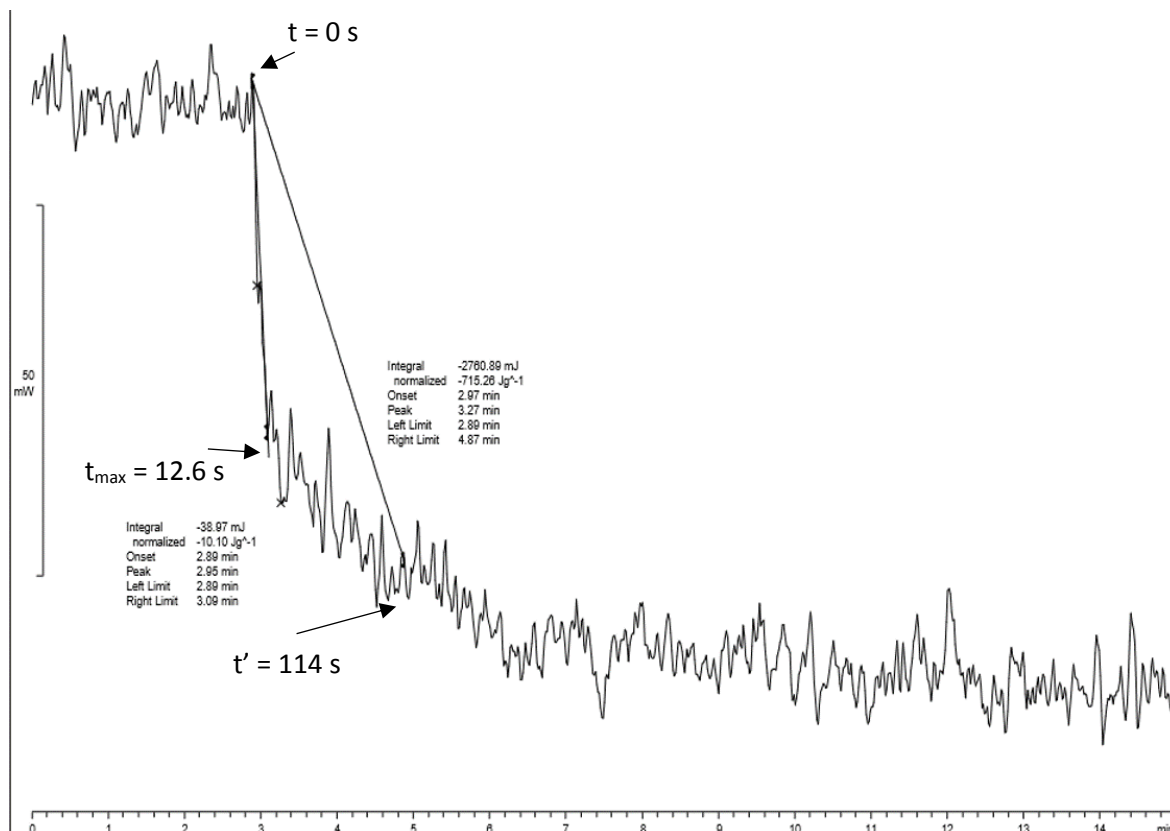


Figure 7.20: UV-DSC profile of the polymerisation of Compound **22** initiated by CGI1300 at 199 °C, isotropic liquid phase.

At 199 °C the initiation occurred at a slightly faster time of 12.6 s (t_{\max}), with t' being before 114 s. The determination of the completion of the reaction became significantly more difficult to analyse in this reaction profile due to the photodegradation of the sample. In order to determine the extent of photodegradation, the UV lamp was only turned off after 15 minutes, and unsurprisingly the sample had fully degraded into a brown/black powder.

7.2.1.3: Polymerization in the Smectic A Phase

The smectic A phase is more ordered than the isotropic liquid phase, wherein the molecules retain a slight degree of freedom, largely in the rotation of the molecules which are organised in a weak layered structure. This organisation should, in theory, allow for rapid polymerisation as the functional units are held close together thereby promoting reaction. Conversely, the lack of translational freedom may lead to the monomers being held further apart, and there is lower thermal energy than in the isotropic liquid phase which may restrict polymerisation. One significant advantage of the lower energy in the system is that there is less tendency for photodecomposition.

The initial study in the smectic A phase was conducted at 174 °C which was 5 °C below the onset of the transition to the isotropic liquid. The UV-DSC result is shown in Figure 7.21.

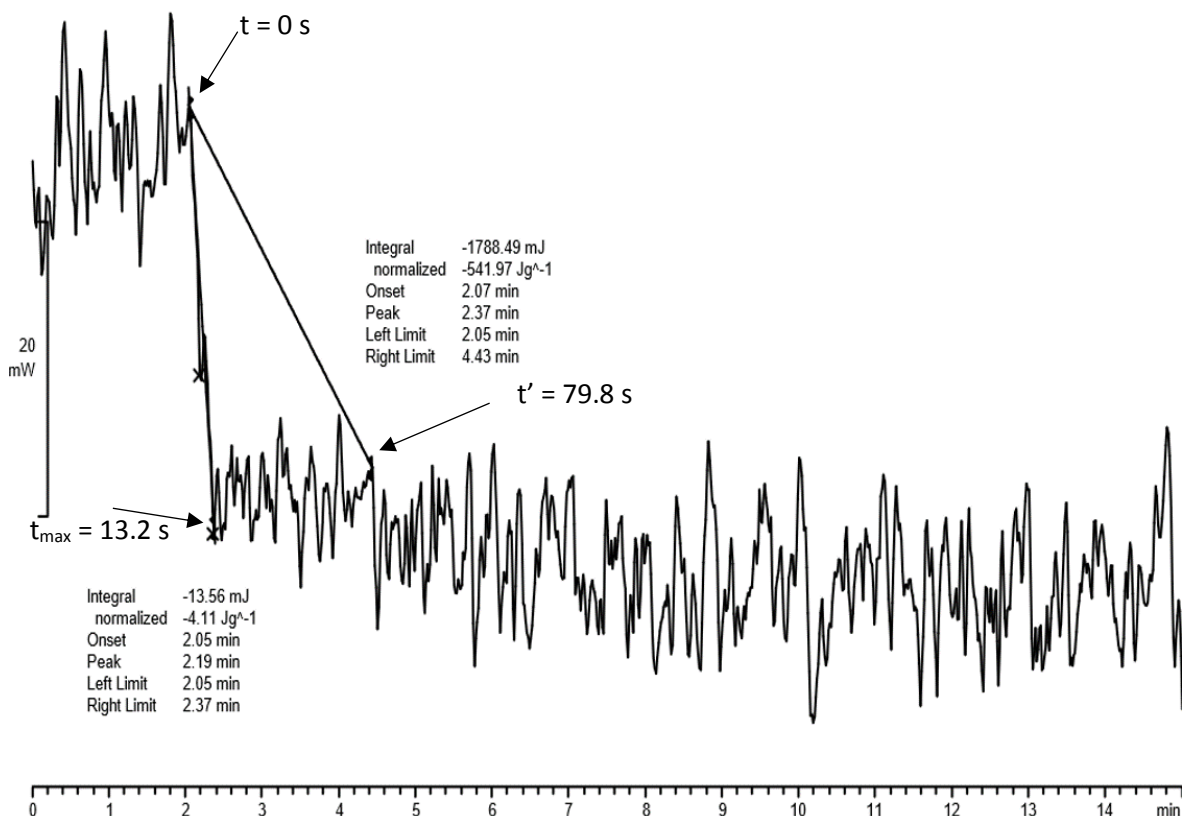


Figure 7.21: UV-DSC profile of the polymerisation of Compound **22** initiated by CGI1300 at 174 °C, smectic A phase.

The initiation of the reaction was completed after 13.2 s and photodecomposition began to occur after 141.6 sec. The reaction was determined to have reached completion after 79.8 s. At this temperature there was not a significant different in initiation time compared to the isotropic liquid although photodecomposition was slightly delayed. Again, the lamp was not switched off until the 15 min experiment time had elapsed and the sample was observed as a brown solid.

Subsequently, a second measurement was carried out in the smectic A phase at 169 °C where the order parameter was expected to be higher as the sample approached the smectic B phase. The UV-DSC results are shown in Figure 7.22.

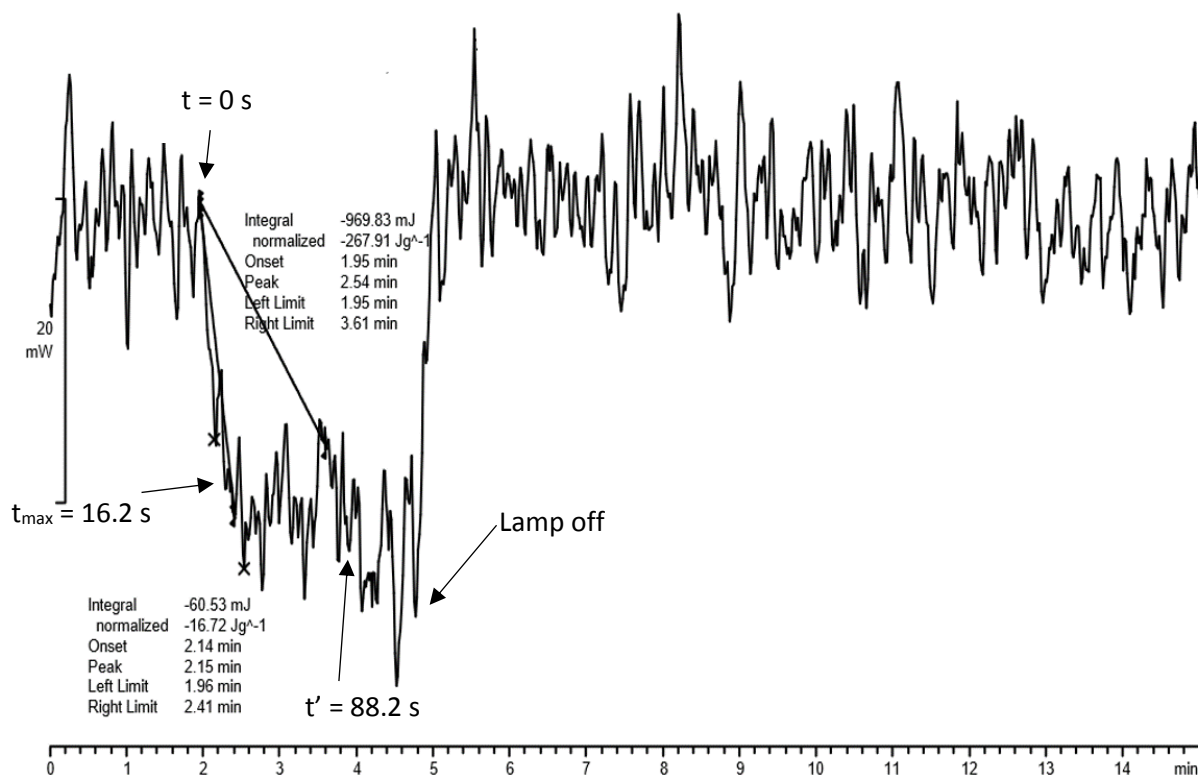


Figure 7.22: UV-DSC profile of the polymerisation of Compound **22** initiated by CGI1300 at 169 °C, smectic A phase.

At this lower temperature the initiation of the reaction (t_{\max}) was completed after 16.2 s which is slightly slower than at higher temperatures. The reaction reached a plateau in the profile after 88.2 s indicating completion of the reaction. Upon observation of the sample after reaction only slight yellowing was observed which indicated less photodecomposition compared to higher temperature experiments. The reduced energetic profile of this reaction, as well as the greater noise observed, was due to the lower mass of sample used in this experiment (approximately 0.7 mg rather than 1 mg).

7.2.1.4: Polymerization in the Smectic B Phase

The final set of analyses were conducted in the more ordered smectic B phase. The increase in order of the system again was expected to have a marked impact on the rate of polymerisation, whereby the molecules are held together through organisation, which may promote reaction. Alternatively, due to the soft crystal nature of the phase the polymerisable groups may be located away from each other hindering the reaction.

The initial study was conducted at 120 °C, and the sample was prepared in the same way as for those studied in the isotropic liquid and smectic A studies. The UV-DSC results are shown in Figure 7.23.

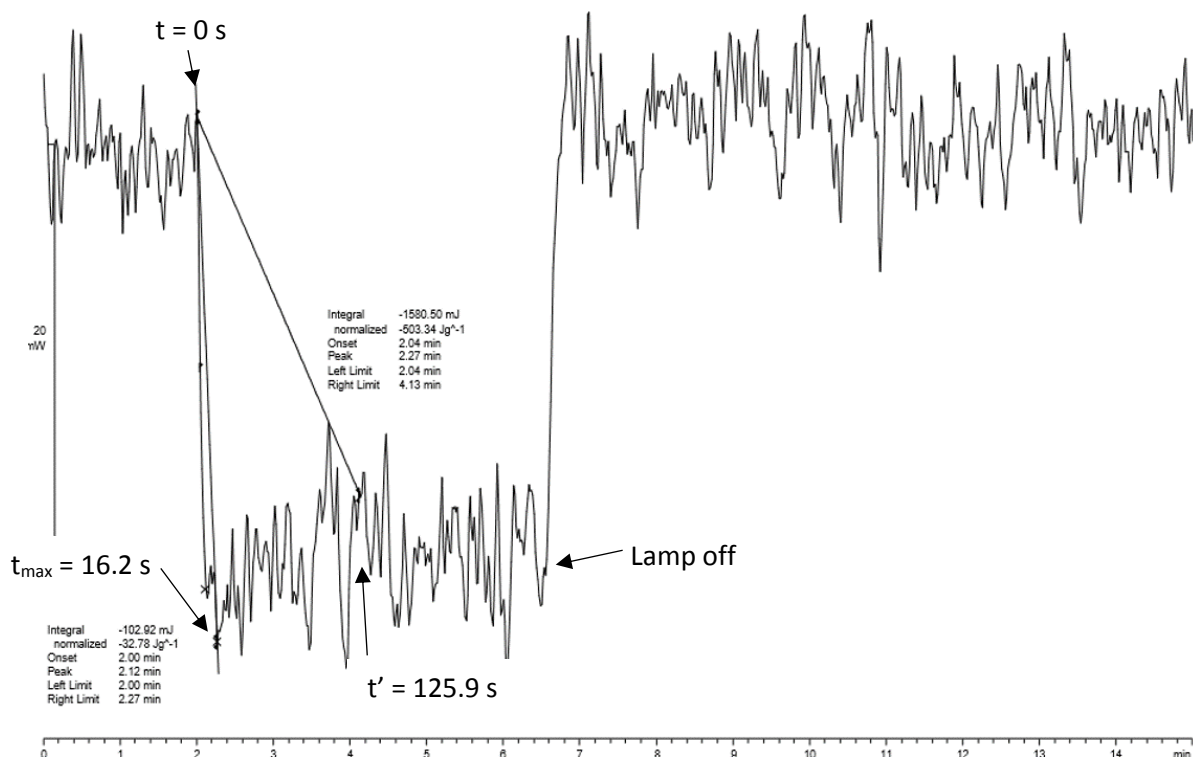


Figure 7.23: UV-DSC profile of the polymerisation of Compound **22** initiated by CGI1300 at 120 °C, smectic B phase.

The initiation of the reaction (t_{\max}) occurred in 16.2 s which was comparable to that observed in both the smectic A and isotropic liquid states. The reaction tended to plateau after 125.9 sec (t') indicating complete reaction. At this temperature the sample showed only a mild degree of discolouration after the experiment indicating that very little photodecomposition had occurred.

The second analysis within the smectic B phase was conducted at a significantly lower temperature of 100 °C in order to broaden the observation of the impact of temperature on the system. With the significantly lower temperature, it was expected that the rate of the reaction would be substantially lower. UV-DSC results for Compound **22** at 100 °C are shown in Figure 7.24.

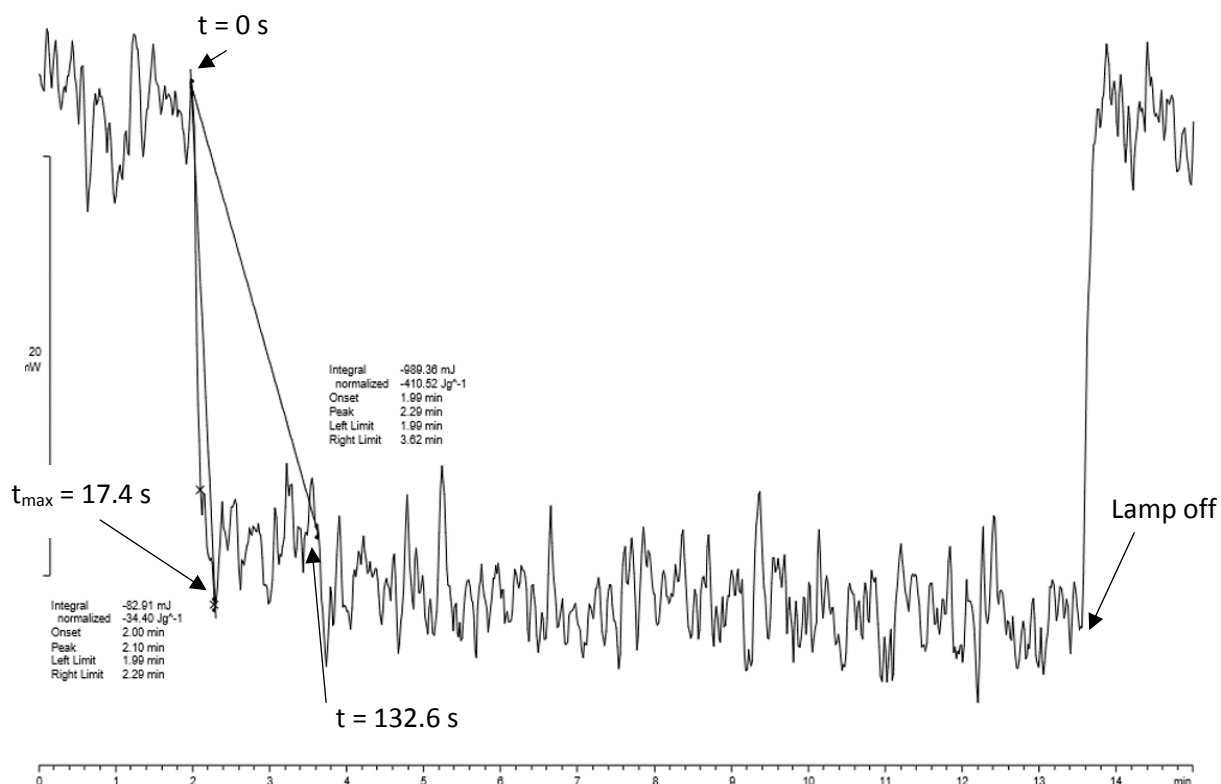


Figure 7.24: UV-DSC profile of the polymerisation of Compound **22** initiated by CGI1300 at 100 °C, smectic B phase.

At this temperature the initiation of the reaction was completed at $t_{\max} = 17.4$ s after irradiation was commenced and completion of polymerisation occurred at 132.6 s, which is slower than observed at 120°C, but not significantly slower.

7.3 Comparison of Polymerisations in Phases

From initial observations, the polymerisation of mono-functionalised quaternary diallylammonium salts appears to follow the trends described by Broer on mono-acrylate systems. The greater rates of polymerisation tended to be seen at higher temperatures, ie, when there is greater thermal energy in the system, rather than as a function of the degree of organisation of the system. The experimental results for the chloride salt of Compound **22** are summarised in Table 7.2.

Phase	Temperature (°C)	T_{\max} (s)	t' (s)
Isotropic Liquid	199	12.6	114
Isotropic Liquid	194	18.6	42.6
Smectic A	174	13.2	79.8
Smectic A	169	16.2	88.2
Smectic B	120	16.2	125.9
Smectic B	100	17.4	132.6

Table 7.2: Kinetic analysis of polymerizations related to temperature and phase variation.

The initiation of polymerisation for this system appears to be generally independent of the conditions of the reaction although potentially it could be argued that slightly faster initiation occurred with increase in temperature. There was definitely a correlation with completion of the reaction and temperature although this was also restricted by the increased tendency of the system to undergo photodecomposition at higher temperatures. These results are presented graphically in Figure 7.25.

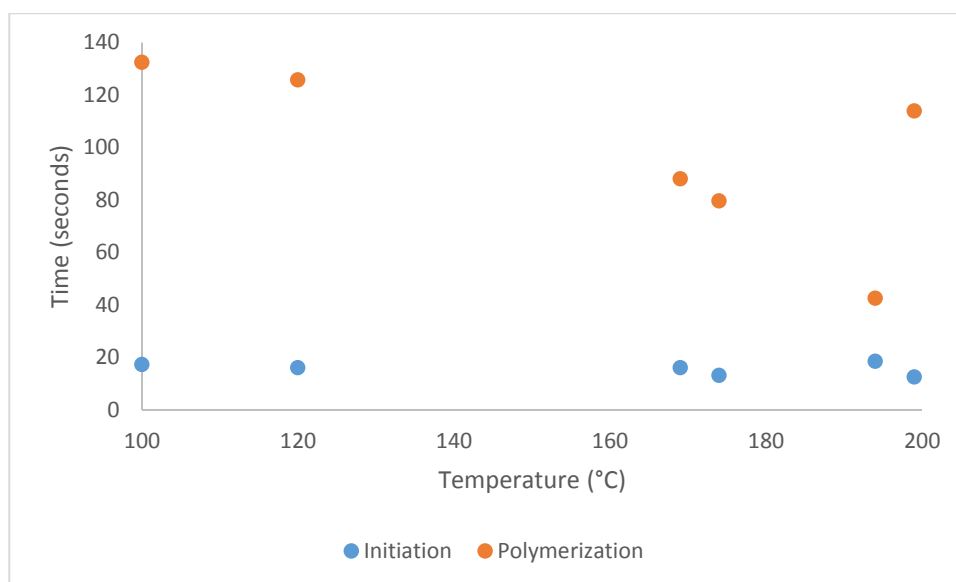


Figure 7.25: Initiation time and completion time as a function of temperature for the polymerisation of the chloride salt of Compound **22**.

According to the trend for the polymerization times shown in Figure 7.25 it is clear that the rate of initiation and polymerisation time show significantly greater rates of change for less ordered phases, i.e., those at elevated temperatures. This result is consistent with the findings of Broer for acrylate monomers.

The change in the rates of polymerization is likely to be due to the organisation of the molecules as well as the thermal energy of the system. The greater energy to promote reactions is an obvious impact, with more energy resulting in faster reactions. However, the organisation of the reactants could be thought of as a factor to increase the reactivity of the mixture, where a more organised system would tend towards greater rates of reaction owing to the reactive groups being held together.

An alternative view of the polymerisation profile in relation to the temperature is presented below in Figure 7.26. This graph uses a calculated rate of reaction obtained from the following calculation (Equation 7.1):

$$rate = \frac{1}{t' - t_{max}} \quad \text{Equation 7.1}$$

From this calculation, the true rate of reaction is determined, also negating the effect of initiation. The different phases are also separated, with trends extrapolated to show the change in rate through each transition. This confirms that there is not a consistent change in relation to temperature exclusively, and that the nature of the phase present during polymerization bears a marked impact on the rate of polymerization.

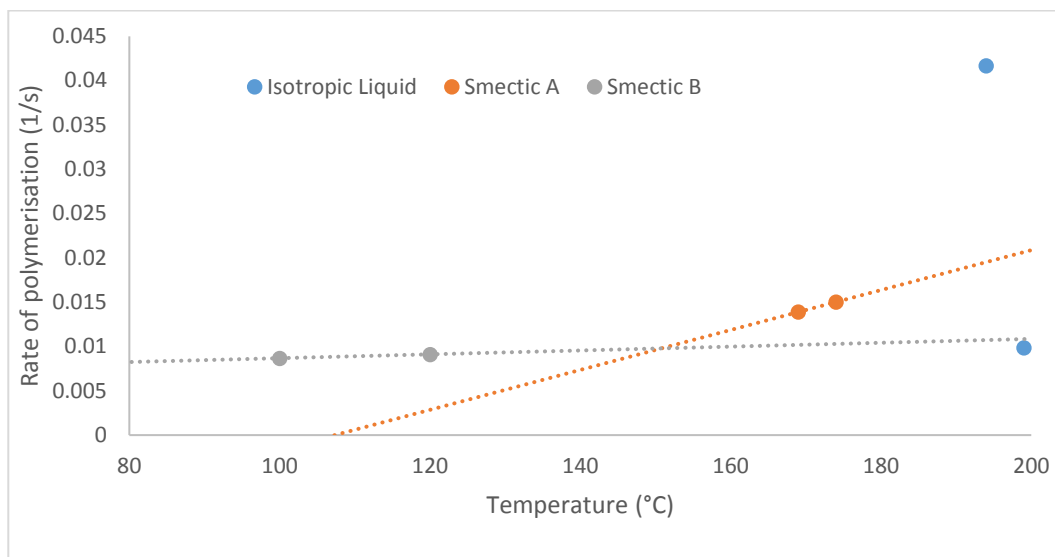


Figure 7.26: Rate of polymerisation as a function of temperature for the polymerisation of Compound **22**.

Generally, the impact of the temperature on a reaction would be a logarithmic increase in rate with regards to the increase of temperature. The rate of a reaction will tend to double with the addition of 10 °C, beyond the activation temperature of the reaction.

8: Conclusions

The bromo-terminated intermediate compounds **4-13** behaved in a manner expected when compared to analogous materials previously published by Gray⁸¹, Davis⁷⁵, Mandle⁷⁶ and Itahara⁷⁷, with comparable transition temperatures observed between the previous publications and compounds **4-7**, with the same phases being identified at comparable temperatures in the region of 75 °C to 80 °C. Each of compounds **4-8** exhibited nematic phases in temperatures in agreement with those displayed by the contemporary work, whereas the transition temperatures of the terphenyl-based compounds featured initial melting points into a B phase at comparable temperatures to the clearing points of the biphenyl compounds. In addition to the elevated initial melting transitions, additional phases were observed, including the B phase, as well as a shorter thermal range smectic A before the nematic phase was observed. It should be noted, however, that the clearing points of these compounds approximated temperatures at which the compounds decomposed.

The nature of the amino-terminated compounds **14-23** were also investigated and compared both between themselves as well as with the intermediate compounds previously discussed. Compounds **15, 16** and **18** showed thermal behaviours clearly different from their parent compounds, with reduced transition temperatures, as well as a loss of the nematic phase and replacement with a smectic A phase. The suppression of the transition temperatures also resulted in not being able to witness the recrystallization of compounds **16** and **18** from the smectic A phases. Compounds **14** and **17**, however, were not synthesised in a sufficient purity and quantity for thermal studies.

Compounds **19-23** showed different changes in behaviour from their parent compounds than were witnessed in compounds **14-18**, with same array of phases displayed at comparable temperatures to those exhibited by compounds **9-13**. Generally there was a slight suppression of the transition temperatures, most notably in the clearing points, which no longer overlapped with the decomposition of the molecules.

The study of the benzoate-ester compounds **39-43** resulted in minimal thermal results produced, with dramatic suppression of transitions to below where they could be visualised clearly, as well as low stability of the compounds, and the difficulty of synthesis and purification required.

From these studies it suggests that the thermal behaviours can be heavily affected by both the core and the terminal groups involved, with the impacts of the larger terphenyl core outweighing the effects of the changing terminal group. The nature of the terminal group leads to a suppression of the transition temperatures due to their larger steric nature, which disrupts the packing of the molecules within a sample, however it is clear to see that in the biphenyl compounds **14-18** it influences the formation of a more organised smectic A phase in place of the nematic phase observed for the bromide-terminated samples (**4-8**).

The larger terphenyl core leads to a change in the length to breadth ratio of the molecules, as well as leading to a significant increase in the number of pi-electrons which influence the organisation of the phases. This leads to more organised phases for the terphenyl compounds **9-13** than for the comparable biphenyl compounds **4-8**. Furthermore, due to the increased length-to-breadth ratio, the change in packing by the introduction of a larger terminal group is negated to a degree, leading to only a minor suppression in the thermal behaviours.

With regards to the proposed odd-even effect, it can be argued from the data provided that there are suppressions of the transition temperatures of odd-chain compounds where compared to the surrounding even-chain compounds that are one methylene unit shorter or longer. This relative suppression that causes significant non-linearity of the trends for each class of compounds can potentially be attributed to the change in the relative angle between the terminal group and the core of the molecules in question.

Further study of the diallylamino-compounds **14-23** showed the behaviours with respect to acidification and polymerisation. The smaller biphenyl core compounds showed complete loss of phase behaviour when acidified to form the quaternary ammonium salts which were required for polymerisation. This loss of all phase behaviour shows that these compounds cannot meet the specifications outlined in the aims section of this thesis when acting as either the sole material or the primary component of a mixture. However, the larger terphenyl core compounds revealed a small suppression of their thermal behaviours when acidified to the quaternary ammonium salts, with thermal behaviours rather elevated when compared to an ideal temperature range for a display device, with smectic A and smectic B phases exceeding 180 °C and 145 °C respectively.

Variation of the salt content of the compound mixture led to minor variations in the transition temperatures, with a slight suppression of the clearing point when salt content approached 40% by weight. However, these differences were fairly minimal (in the range of 5 °C), and so variation of salt content cannot overcome the elevated temperatures compared to the ideal ranges for device applications.

Consideration of the polymerisation behaviours showed that the functionalised compounds polymerised at a significantly reduced rate when compared to the bis-diallylamino standards also considered, which can be partially attributed to the reduction of the density in polymerisable groups, as well as potential kinetic barriers that have to be overcome. The exploration of the reaction rates in different phases and at different temperatures within phases showed that the nature of the phase had an impact on the rate of polymerisation independent of the temperature, meaning that the organisation of the phase and how the molecules are held within a structure can outweigh the energy within the system.

The formation of compounds **4-23** exhibited acceptable yields from straightforward synthetic procedures when compared to the multi-step procedures used to synthesise compounds **39-43**. The syntheses of compounds **4-23** would require some alterations to make them viable for bulk synthesis.

The work conducted within this thesis suggests the possibility for ionic liquid crystal polymer structures to be synthesised for their application in display devices. There is room for alteration of composition of mixtures, or the addition of lateral substituents in the motifs incorporated to alter the thermal properties of the compounds. This potentially allowing for ambient temperature phases that could be used in device construction.

9: References

- 1: S.C Jain and D.K. Rout; *J. App. Phys.*, 1991, **70**, 6988
- 2: D.S. Fredley and R.W. Pennisi; US Patent 5847787, 1996
- 3: T. Kato; *Science*, 2002, **295**, 2414
- 4: A.D. Bendrea; L. Cianga and I. Cianga; *J. Biomat. App.*; 2011, **26**, 3
- 5: P.D. DeGennes, *Compt. Rend. Acad. Sci.*, 1968, **266B**, 571
- 6: A. de Vries, *Mol. Cryst. Liq. Cryst.*, 1970, **10**, 219
- 7: S. Chandrasekhar, in *Liquid Crystals (Second Edition)*, Cambridge University Press, 1992, p86
- 8: A.J. Leadbetter and E.K. Norris; *Mol. Phys.*, 1979, **38**, 3
- 9: J.W. Goodby and G.W. Gray, in *Smectic Liquid Crystals: Textures and Structures*, Blackie Academic & Professional, 1984
- 10: S.J. Cowling, in *Handbook of Liquid Crystals – 9 Optical Microscopy Studies of Liquid Crystals*, Wiley, 2014, 1 Part III:9:1-38
- 11: P. Martinot-Lagarde, R. Duke and G. Durand, *Mol. Cryst. Liq. Cryst.*, 1981, **75**, 249
- 12: A. Angioletti, S. Eccher, O. Polvara and V. Zerbini, *Rub. Chem. and Tech.*, 1965, **38**, 1115
- 13: P.J. Collings and M. Hird, in *Introduction to Liquid Crystals Chemistry and Physics*, Taylor & Francis, London, 1997
- 14: W.H. Bragg and W.L. Bragg, *Proceedings of the Royal Society of London. Ser. A Containing Papers of a Mathematical and Physical Char.*, 1913, **88**, 605
- 15: W.C. Marra, P. Eisenberger and A.Y. Cho, *J. App. Phys.*, 1979, **50**, 6927
- 16: D.M. Agra-Kooijman and S. Kumar, in *Handbook of Liquid Crystals – 10 X-Ray Scattering Investigations of Liquid Crystals*, Wiley, 2014, 1 Part III:10:1-38
- 17: B.I. Ostrovkii, *Sov. Sci. Rev. A. Phys.*, 1989, **12**, 85
- 18: J. Wendorff, in *Handbook of Liquid Crystals – 9 Main-Chain and Side-Chain LC Polymers with Dislike Segments*, Wiley, 2014, 7 Part III:9:1-34
- 19: H Finkelmann, *Angew. Chem. Int. Ed. Eng.*, 1987, **26**, 816
- 20: G.B. Butler and R.J. Angelo, *J. Am. Chem. Soc.*, 1957, **79**, 3128
- 21: V.N. Tsvetkov, E.I. Riumstev, I.N. Shtennikova, E.V. Korneeva, B.A. Krentsel and Y.B. Amerik, *Euro. Poly. J.*, 1973, **9**, 481
- 22: M.J. Earle and K.R. Seddon, *Pure Appl. Chem.*, 2000, **72**, 1391
- 23: G.F. Starkula, S. Klenk, M. Butschies, S. Tussetschläger and S. Laschat, *J. Mater. Chem.*, 2012, **22**, 21987
- 24: V. Perez-Grégorio, I. Giner, M.C. López, I. Gascón, E. Cavero and R. Giménez, *J. Coll. Int. Sci.*, 2012, **375**, 94
- 25: C.J. Bowlas, D.W. Bruce and K.R. Seddon, *Chem. Commun.*, 1996, **14**, 1625

- 26:** T. Ichikawa, M. Yoshio, A. Hamasaki, S. Taguchi, F. Liu, X. Zeng, G. Ungar, H. Ohno and T. Kato, *J. Am. Chem. Soc.*, 2012, **134**, 5, 2364
- 27:** K. Hoshino, M. Yoshio, T. Mukai, K. Kishimoto, H. Ohno and T. Kato, *J. Polym. Sci. Part A Polym. Chem.*, 2003, **41**, 22
- 28:** M. Yoshio, T. Kagata, K. Hoshino, T. Mukai, H. Ohno and T. Kato, *J. Am. Chem. Soc.*, 2006, **128**, 16
- 29:** T. Ichikawa, M. Yoshio, A. Hamasaki, J. Kagimoto, H. Ohno and T. Kato, *J. Am. Chem. Soc.*, 2011, **133**, 7
- 30:** J. Chiefari, Y.K. Chong, F. Ercole, J. Krstina, J. Jeffrey, T.P.T. Le, R.T.A. Mayadunne, G.F. Meijs, C.L. Moad, G. Moad, E. Rizzardo, S.H. Thang, *Macromolecules*, 1998, **31**, 5559
- 31:** Y. Takimoto, in *Radiation Curing in Polymer Science and Technology*, Vol. 3, Springer, 1993, pp269-297
- 32:** S.R. Sandler, in *Polymer Syntheses*, Vol. 1, Academic Press Inc., San Diego, 1974, p6
- 33:** D.R. Miller, E.M. Valles and C.W. Macosko, *Polym. Eng. Sci.*, 1979, **19**, 272
- 34:** J. Zhang, Z. Chen, Z. Wang, W. Zhang, N. Ming, *Mater. Lett.*, 2003, **57**, 4466
- 35:** S.M. Kelly, *Liquid Crystals Today*, 1996, **6**, 4
- 36:** A.S. Hashim, B. Azahari, Y. Ikeda and S. Kohjiya, *Rubber Chem. Tech.*, 1998, **71**, 2
- 37:** J.M.G. Cowie, in *Polymers: Chemistry & Physics of Modern Materials (2nd Edition)*, Blackie Academic & Professional, 1991
- 38:** R. Ishige, K. Osada, H. Tagawa, H. Niwano, M. Tokita and J. Watanabe, *Macromolecules*, **31**
- 39:** D. Liu, C.W.M Bastiaansen and D.J. Broer, in *Handbook of Liquid Crystals – 14 Liquid Crystal Polymer Networks: Toward Soft Actuators and Dynamic Surface Reliefs*, Wiley, 2014, 7 Part IV:14:1-16
- 40:** R.A.M. Hikmet, "Display Device Comprising Liquid Crystalline Material Locally Formed Into a Polymer Network", U.S. Patent 5,333,074, issued July 26, 1994
- 41:** F.R. Mayo, *Berichte der Bunsengesellschaft für Physikalische Chemie*, 1966, **70**, 3
- 42:** E. Hecht and H. Hoffmann, *Colloids and Surfaces A: Physiochemical and Engineering Aspects*, 1994, **96**, 1-2
- 43:** M.W. Matsen and M. Schick, *Phys. Rev. Lett.*, 1994, **72**, 16
- 44:** P. Alexandridis, U. Olsson and B. Lindman, *Langmuir*, 1998, **14**, 10
- 45:** G. Moad, *Prog. In Polym. Sci.*, 1999, **24**, 1
- 46:** A.E.A. Contoret, S.R. Farrar, M.O'Neill, J.E. Nicholls, G.J. Richards, S.M. Kelly and A.W.Hall, *Chem. Mater.*, 2002, **14**, 1477
- 47:** D.J. Broer, H. Finkelmann and K. Kondo, *Makromol. Chem.*, 1988, **189**, 185
- 48:** D.J. Broer, G.N. Mol and G. Challa, *Makromol. Chem.*, 1989, **190**, 19
- 49:** C.C. Wu and W.J. Lee, *J. App. Polym. Sci.*, 2010, **116**, 4

- 50:** G.B. Butler and R.L. Bunch, *J. Am. Chem. Soc.*, 1949, **71**, 3120
- 51:** G.B. Butler and F.L. Ingley, *J. Am. Chem. Soc.*, 1951, **73**, 895
- 52:** A.L.J. Beckwith, A.K. Ong and D.H. Solomon, *J. Macromol. Sci. Chem.*, 1975, **A9**, 115
- 53:** A.W. Hall, M.J. Godber, K.M. Blackwood, P.E.Y. Milne and J.W. Goodby, *J. Mater. Chem.*, 2004, **14**, 2593
- 54:** M.R. Bhalla and A.V. Bhalla, *Int. J. Computer Apps.*, 2010, **6**, 12
- 55:** R. Downs, *Analog Apps. J.*, 2005, **3Q**, 5
- 56:** D.S. Hecht, D. Thomas, L. Hu, C. Ladous, T. Lam, Y. Park, G. Irvin and P. Drzaic, *J. SID*, 2009, **17**, 941
- 57:** G. Barrett and R. Omote, *Inform. Display.*, 2010, 19
- 58:** F.P. Nicoletta, G. Chidichimo, D. Cupelli, G. De Filippo, M. De Benedittis, B. Gabriele, G. Salerno and A. Fazio, *Adv. Funct. Mater.*, 2005, **15**, 995
- 59:** D. Cupelli, F.P. Nicoletta, S. Manfredi, M. Vivacqua, P. Formoso, G. De Filippo and G. Chidichimo, *Solar Energy Mater. Solar Cells*, 2009, **93**, 2008
- 60:** J. Lee, P. Lee, H.B. Lee, S. Hong, I. Lee, J. Yeo, S.S. Lee, T-S. Kim, D. Lee and S.H. Ko, *Adv. Funct. Mater.*, 2013, **23**, 4171
- 61:** C.M. Lampert, in *Chromogenic Switchable Glazing: Towards the Development of the Smart Window*, U.S. Department of Energy, 1995
- 62:** C.M. Lampert, *Solar Energy Mater. Solar Cells*, 1998, **52**, 207
- 63:** H. Mori and P.J. Bos, *Jpn. J. Appl. Phys.*, 1999, **38**, 2837
- 64:** H. Mori, Y. Itoh, Y. Nishiura, T. Nakamura and Y. Shinagawa, *Jpn. J. Appl. Phys.*, 1997, **36**, 143
- 65:** C.D. Hoke, H. Mori and P.J. Bos, *Jpn. J. Appl. Phys.*, 1999, **38**, 642
- 66:** B.K. Winker, W.J. Gunning, D.B. Taber and L.G. Hale, "Optical Compensator for Improved Gray Scale Performance in Liquid Crystal Display", U.S. Patent 5,504,603, issued April 2, 1996
- 67:** K. Nomoto, N. Hirai, N. Yoneya, N. Kawashima, M. Noda, M. Wada and J. Kasahara, *IEEE Trans. On Electron Devices*, 2005, **52**, 7
- 68:** M. Oh-e and K. Kondo, *Appl. Phys. Lett.*, 1995, **67**, 26
- 69:** I. Yang-En Wu, J.-S. Yu and F.-J. Ko. "Pixel Structure of Dual Mode Liquid Crystal Display", U.S. Patent 6,351,078, issued June 13, 2006
- 70:** D.R.H. Jones and G.A. Chadwick, *J. Crys. Growth*, 1971, **11**, 3
- 71:** E.P. Raynes and I.C. Sage, *Liquid Crystals*, 2014, **42**, 5-6
- 72:** L. Chen, Y. Chen, W. Zhou, F. Li, X. He and B.Z. Tang, *Mol. Liq. Cryst.*, 2010, **518**, 70
- 73:** H.H. Freedman and R.A. Dubois, *Tet. Lett.*, 1975, **16**, 38
- 74:** L. Zhang, X. Wang, J. Wang, N. Grinberg, D.K. Krishnamurthy and C.H. Senanayake, *Tet. Lett.*, 2009, **50**, 24
- 75:** E.J. Davis, R.J. Mandle, B.K. Russell, P.Y. Foeller, M.S. Cook, S.J. Cowling and J.W. Goodby,

Liquid Crystals, 2014, **41**, 1635-1646

76: R.J. Mandle, E.J. Davis, C.-C. A. Voll, D.J. Lewis, S.J. Cowling and J.W. Goodby, *J. Mater. Chem. C.*, 2015, **3**, 2380

77: T. Itahara and H. Tamura, *Mol. Cryst. and Liq. Cryst.*, 2007, **474**, 17-27

78: O. Mitsunobu, *Synthesis*, 1981, **1**

79: R.W. Taft, *J. Am. Chem. Soc.*, 1952, **74**, 11

80: B. Neises and W. Steglich, *Angew. Chem. Int. Ed.*, 1978, **17**, 7

81: G.W. Gray and D.G. McDonnell, "Liquid Crystal Compounds", U.S. Patent 4,261,651, issued April 14, 1981

82: P.S. Pershan, G. Aeppli, J.D. Luster and R.J Birgeneau, *Mol. Cryst. and Liq. Cryst.*, 1981, **67**, 1